Microstructural Control during Three Dimensional Printing of Polymeric Medical Devices

by

Benjamin M. Wu

D.D.S., Dentistry
University of the Pacific, 1987

Specialty Certificate in Advanced Prosthodontics
Harvard University, 1997

Submitted to the Department of Materials Science and Engineering in
Partial Fulfillment of the Requirements for the Degree of

DOCTOR OF PHILOSOPHY
in Materials Engineering

at the
MASSACHUSETTS INSTITUTE OF TECHNOLOGY

January 1998

Signature of Author:

Department of Materials Science and Engineering
January 9, 1998

Certified by:_____

Professor Michael J. Cima
Sumitomo Electric Industries Professor of Materials Science Engineering
Thesis Supervisor

Accepted by:_____

Professor Linn W. Hobbs
John F. Elliott Professor of Materials
Chairman, Committee for Graduate Students

Microstructural Control during Three Dimensional Printing of Polymeric Medical Devices

by

Benjamin M. Wu

Submitted to the Department of Materials Science and Engineering
on January 9, 1998 in Partial Fulfillment of the
Requirements for the Degree of Doctor of Philosophy in
Materials Engineering

ABSTRACT

Four types of primitive formation mechanisms were observed during 3D Printing™ of biomedical materials. The type of binding mechanism was found to have practical implications on printing strategy and device performance. Dissolution-re-precipitation is the predominant binding mechanism for bioerodable polymers, and four important stages have been identified in this mechanism. Time scale analysis and experimental observations revealed that droplet impact ($\sim 10^{-4}$ sec) and binder migration ($\sim 10^{-2}$ sec) are completed before significant particle dissolution ($\sim 10^{0}$ to 10^{2} sec) occurs. Two mechanisms of particle dissolution were observed. Some polymer-solvent combinations required a minimim dissolution time, which was found to scale with polymer molecular weight. Significant binder evaporation was found to occur as soon as the liquid exits the nozzle, but complete evaporation from the powder bed can require up to 10^{0} to 10^{3} sec after impact. The extent of particle dissolution depended on the relative timescale of dissolution and evaporation. Dissolution-evaporation plots were constructed from simple analytical models for predicting microstructure based on materials properties such as dissolution rate and evaporation kinetics, as well as printing parameters such as flow rate, printspeed, and line spacing. Studies with printing dense structures showed increased sintering defects with larger particles for which the evaporation timescale is shorter than that required for complete particle dissolution. The dissolution-evaporation plots derived from the dissolution and evaporation experiments were also found to be relevant during printing of micro porous structures. Simple drug delivery devices and tissue engineering scaffolds were fabricated to illustrate the effects of microstructure on device performance.
This fundamental understanding of primitive binding process during 3D Printing™, and its affects on microstructure, will have real implications on printing strategies and clinical performance of future 3DP™ polymeric medical devices.

Thesis Supervisor: Professor Michael J. Cima
Title: Sumitomo Electric Industries Professor of Materials Science Engineering

ACKNOWLEDGMENTS

This thesis would not have been possible without the guidance of Prof. Michael Cima, who always asks the right questions. I am grateful for the insightful comments from the thesis committee members, Prof. Linda Griffith, Prof. Chris Scott, and Prof. Robert Langer. Their constructive inputs made this thesis more coherent and practical.

Everyone in 3DP™ Biomaterials group deserves special thanks for being so considerate whenever I needed to bump someone off the machine. Scott Borland made the best looking microspheres, and Russ Giordano set the record for SEM time. I would still be waiting for my devices to dry if Wendy hadn't build the Koeg (CO_2 reactor). Ann Hirahara sure left her mark all over the lab, although she was only on the amaranth project for a short time. Bill Rowe's LabView VI's simplified data collection, but his Jurassic Park CD made the data meaningful. Bugra's mushy impersonation of his soul mate always made me laugh. Stampede cadet Bob Palazzolo deserves much credit for upgrading the machine and taking the ODF project to its current stage. It was great to have someone else staying up late, and BFTing during those final months. Best of luck to Wendy', who just inherited la machine.

Everyone in 12-005 can now breath easier since Chloe and Sarah won't be leaving their voicemail here anymore. Thanks for all the legible phone messages over the years. I will miss all those deep discussions with Jason the MAN on important issues such as sports and financial investment. Chapter 3 would not be possible without Lynne's excellent video equipment. Chicago Pizza would file for Chapter 11 after Scott graduates. I am indebted to Dai for translating those Japanese article for me.

The entire CPRL cast made my MIT experience enjoyable. Chunging, coffee stampedes, Chinatown trips, and other holy excursions are just some of the fond memories (names were deleted to protect the guilty). I couldn't have spent all that sponsored research money without the rapid PO number response from Barb. Lenny deserves special thanks for training me on the equipment and finally ordering the FTIR. Thanks to John C. for milling powder and ordering supplies for me. Hey Santini, Wutini lives!

I am grateful for all the help from Jim Serdy and other fellow 3DP'ers in Building 35. I am also grateful to members of Dr. Jay Vacanti's Liver Research Team at Boston Children's Hospital for taking such good care of my devices, and trying so hard to make things work.

My greatest debt belongs to Betty, whose love and understanding throughout these past years made this journey meaningful.

Everyone: I wish you all health, success, and happiness.

TABLE OF CONTENTS

LIST OF FIGURES

LIST OF TABLES

1. INTRODUCTION

1.1 BACKGROUND

Conventional industrial prototyping techniques are labor intensive, inflexible, expensive, and require extensive lead time. Even with advanced computer-aided design (CAD) packages prepared specifically for rendering 3D objects and verifying dimensional fit, prototype tooling parts must still be fabricated prior to actual manufacturing. Integration of CAD with numeric controlled (NC) machining represented the first direct prototyping approach from CAD model-to-part. The subtractive nature of NC machining, however, poses rigid constraints on shape complexity due to path requirements and limitations on shaping tools. Features such as internal cavities and narrow tortuous channels are nearly impossible.

1.2 SOLID FREEFORM FABRICATION

Increasing global competition lead to the demand for better prototyping technologies which would drastically reduce the cost and time of the product development cycle. This demand has resulted in the emergence of a new class of CAD based technologies which fabricate complex objects in a laminated fashion by sequential addition of patterned thin layers. Complicated 3D features such as internal voids, cantilevers, undercuts, and narrow tortuous paths are simply reduced to a stack of common 2D features such as circles, lines, and points. Exempted from tooling path restrictions, these additive technologies offer much higher levels in shape complexity. The freedom in form is the basis for the term solid freeform fabrication (SFF).

Numerous SFF technologies are currently available,[1,2] and many classification systems exist. Yoo[3] recently presented a convenient system for categorizing the various SFF technologies based on the manner in which each layer is patterned. Although these technologies were developed primarily for industrial applications, their flexibility make them attractive candidates for biomedical engineering.[4,5] The following section reviews some of the more popular SFF technologies, and highlights their strengths and weaknesses in terms of their applicability for medical device manufacturing.

1.2.1 Removal of matter

Examples of SFF technologies which pattern each layer by removing matter are laminated object manufacturing (LOM) and computer aided manufacturing of laminated engineering materials (CAM-LEM). A CO_2 laser is used in LOM to cut out 2D patterns from pre-formed sheets of build material, usually paper (Figure 1.1). The extraneous sheet material is cut into rectilinear tiles to facilitate part retrieval. Upon completion of each layer, a fresh sheet of material is pressed and laminated to the previous layer, and the appropriate pattern for the next layer is cut[6]. LOM has been used extensively to make paper prototypes, but any material which can be processed into sheets, and can be cut efficiently, are candidates for LOM. Bioceramic parts, for example, can be made by tape casting slurries and cutting the sheet into the appropriate 2D patterns. The LOM structure is ready for heat treatment after complete binder burn-out. Solids content and sintering conditions may be varied to exert control on the porosity of the final part. Compositional gradients along the z-axis can be easily produced by varying the composition of sheet material for different layers. Compositional gradients along the x-y plane is not possible during the LOM process, but it may be possible, although impractical, to stack sheets with compositional gradients which were prepared *a priori*.

CO_2 lasers are also used in CAM-LEM to trace out the 2D patterns from pre-formed sheets. Each layer is then assembled robotically to reconstruct the 3D structure. Lamination can be achieved by conventional joining techniques such as warm isostatic pressing. The laminated structure is then sintered to achieve full density. Surface finish along the build axis is reportedly superior with CAM-LEM since bevels can be traced along the edges for each layer. This layered build style virtually eliminates the previous constraints with conventional NC machining on shape complexity due to tooling path limitations. Powder materials, such as alumina, silicon nitride, nickel-iron, and stainless steel, have been used in CAM-LEM by mixing the powders with the appropriate binder and forming sheets. The principles involved are similar to those in LOM, as are the limitations in terms of compositional gradients. Another important constraint is that

microstructure cannot be specified during LOM or CAM-LEM, and it must be either built into the original sheet materials, or introduced during post-processing steps.

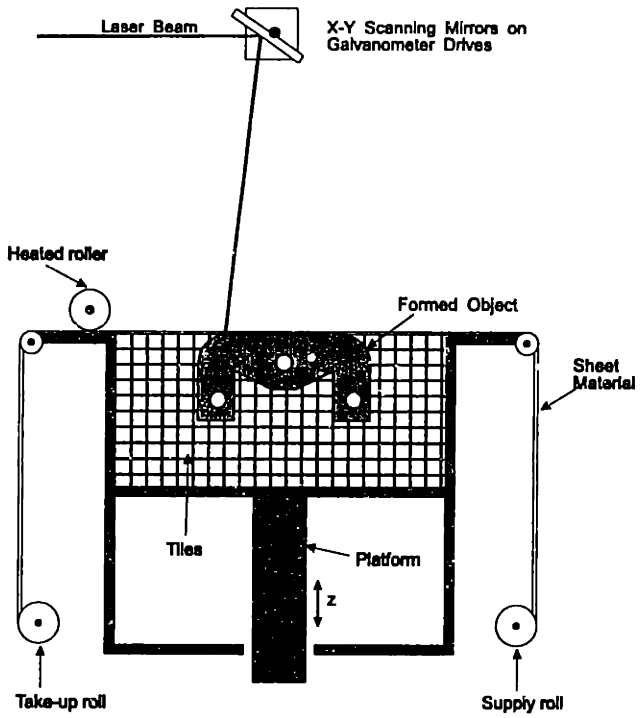

Figure 1.1: Laminated object manufacturing (LOM)

1.2.2 Deposition of energy

Examples of SFF technologies which pattern each layer by depositing energy to fuse the starting material together are stereolithography (SLA) and selective laser sintering (SLS). Stereolithography uses HeCd-lasers to polymerize photocurable liquid resins to form 2D patterns (Figure 1.2). The entire structure is lowered into the liquid resin reservoir at the end of each layer. The drop distance represents the thickness of the un-cured liquid resin which spreads over the top. This fresh layer of liquid is polymerized to pattern the new slice. Part retrieval is much simpler than LOM, since any uncured resin simply flow away from the polymerized structure. Postcure is usually necessary since complete polymerization is usually not achieved during SLA. Temporary support structures must be incorporated into the CAD model in order to produce unsupported features such as cantilevers, since polymerization is not instantaneous during SLA. Resins with and without ceramic dispersions have been processed by SLA.

Compositional gradients are even more restrictive than LOM and CAM-LAM, unless the reservoir resin is replaced in between layers. Gradients along the horizontal planes are virtually impossible. Biocompatible resins with the proper SLA processing properties are also scarce. These constraints have limited the use of SLA in biomedical applications. The main medical applications of SLA seems to be the fabrication of anatomical models for pre-surgical planning,[7,8] and indirect fabrication of medical devices by using the SLA pattern in the molding process. Titanium dental implant components have been fabricated by electrical discharge machining of titanium ingot based on a SLA-derived template.[9]

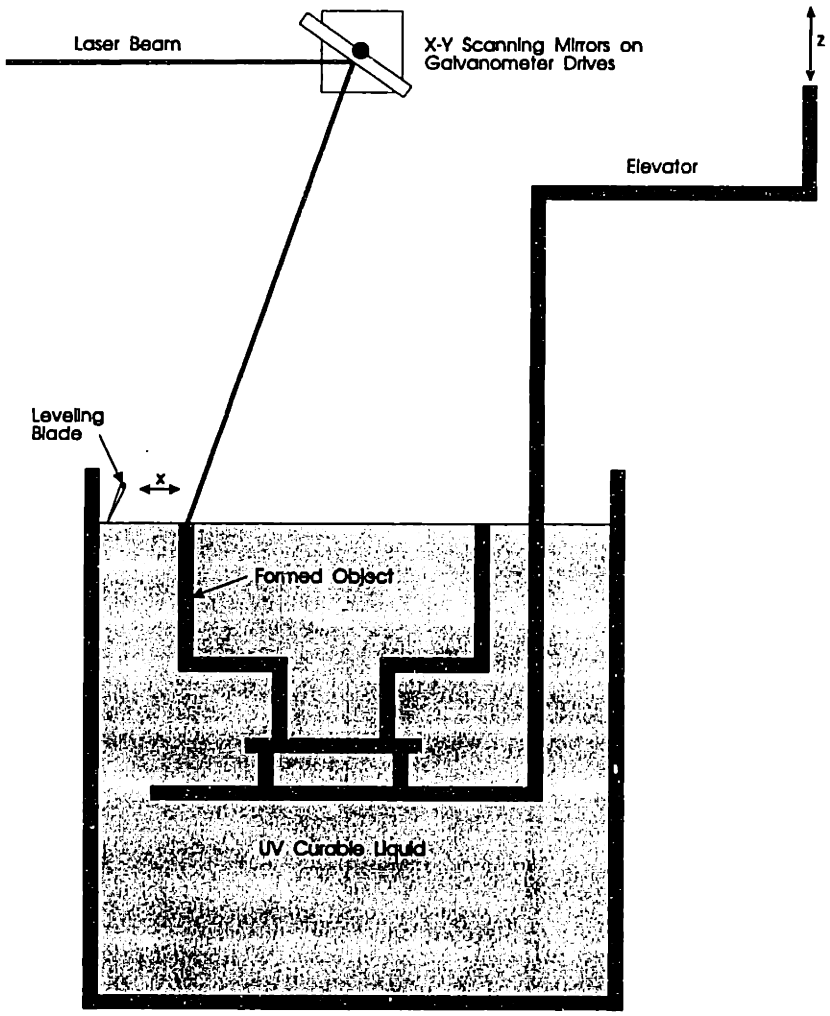

Figure 1.2: Stereolithography (SLA)

Selective laser sintering (SLS) directs a laser to pattern each layer by partially fusing thermoplastic particles together (Figure 1.3). The piston is lowered at the end of

one layer, a fresh layer of powder material is rolled evenly across the top surface, and the laser binds the fresh particles to form the appropriate 2D pattern. Loose, unbound powder is brushed away upon completion of the entire part, and heat treatment is performed to achieve full density.[10,11] Unlike SLA, temporary support structures are not needed since unbound solid particles can serve as supporting struts under cantilevers. It is slightly easier to achieve compositional gradients in SLS than in SLA, but they are limited to vertical axis. Compositional gradients along the horizontal planes are virtually impossible in these approaches. Microstructural control is possible by controlling the laser energy, scan speed, and total exposure time. Most of the microstructural control with SLS has relied on post-processing heat treatments, however. SLS has been used to fabricate polycarbonate pre-surgical models from converted CT data.[12]

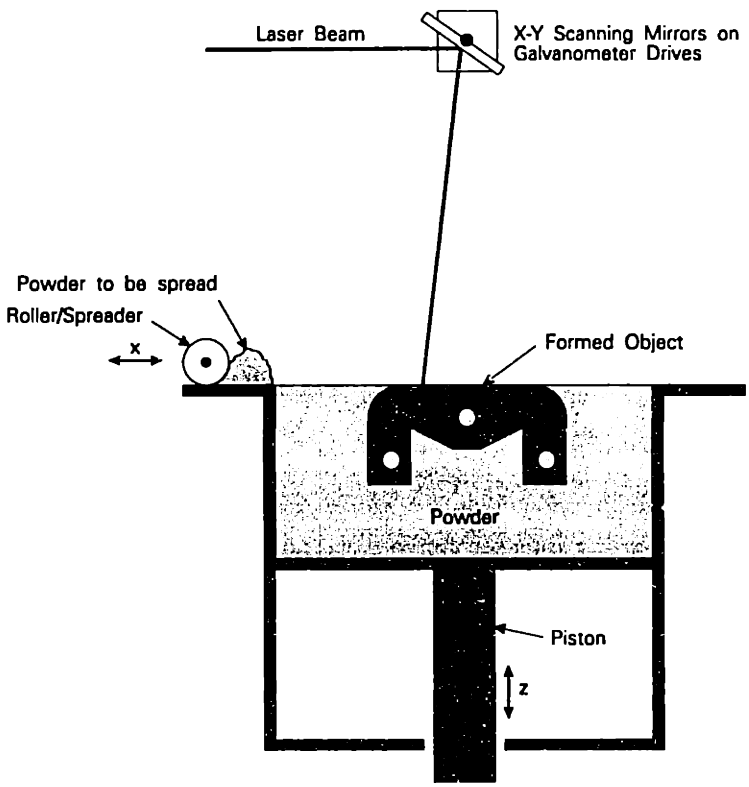

Figure 1.3: Selective laser sintering (SLS)

1.2.3 Deposition of matter

Fused deposition modeling[13] (FDM) constructs 2D patterns by selective extrusion of molten thermoplastic materials through two heated extrusion tips (Figure 1.4). One

nozzle deposits the filament modeling material, and the second deposits a temporary material to support cantilevers. No supporting structures need to be added to the CAD model. No theoretical restriction on compositional gradients exist for FDM, although this process has not been exploited for fabricating functional gradient material. One variation of FDM utilizes inkjet printheads to deposit plastic models in a laminated fashion. The use of additional extrusion nozzles for multiple build materials, each depositing different matter, should allow flexible compositional variation in all three dimensions. Some control on microstructure may be possible during FDM by manipulating the relevant FDM parameters.

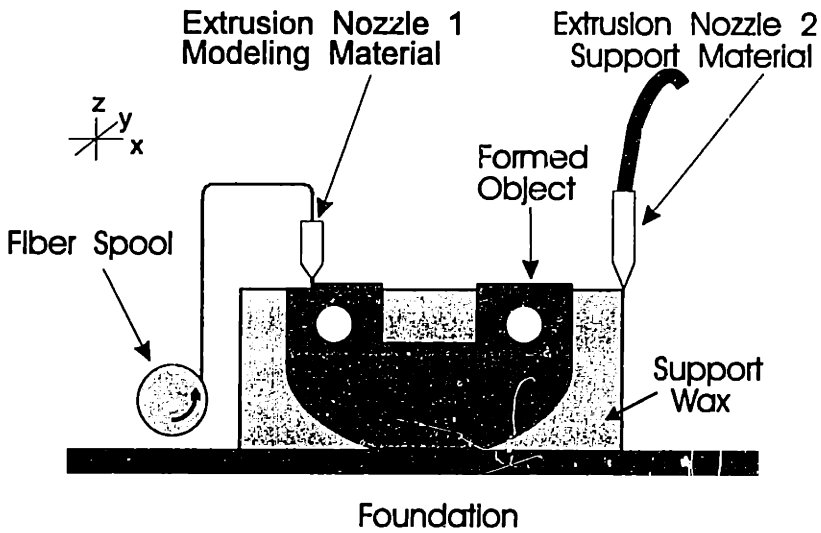

Figure 1.4: Fused Deposition Modeling (FDM)

Despite the flexibility in shape and composition, FDM has found little use in direct biomedical applications due to materials related issues. Heat transfer characteristics and rheology are critical for proper material selection for FDM. Thermoplastics such as PVC, nylon, ABS, and investment casting wax, have been successfully used in FDM. The molten droplet must be hot enough to rapidly induce fusion with previously extruded beads, yet solidify fast enough to minimize flow and feature size. The viscosity must be low enough during the molten stage for reliable extrusion through a fine nozzle in order to minimize feature size, yet high enough during

the burnout stage to avoid large scale collapsing in the furnace. Chemical modifiers may be required to facilitate the use of other thermoplastics. Biocompatibility requirements, however, impose constraints on the type of rheological modifiers which can be used.

Three dimensional printing™ (3DP™) constructs 2D patterns by selective printing liquid droplets onto a thin layer of powder material to bind neighboring particles together.[14,15] The process is very similar to SLS, but the nature by which 3DP™ builds primitives - by selective deposition of *matter*, makes it possible to achieve compositional gradients in all 3 dimensions. Selective deposition of matter is easily achieved by various inkjet technologies, which are described in detail in later sections. 3DP™ is, in fact, the only SFF technology with demonstrated ability to fabricate functionally gradient materials (FGM). Material selection is also much more flexible than all remaining SFF technologies[16], since virtually any material which can be processed into either powder or liquid form can be used. Selective deposition of matter can be accomplished by either dissolving the material in the appropriate solvents, or dispersing material in a slurry, or extruding the molten material through a heated extruder. Besides materials flexibility, 3DP™ is also much more efficient than FDM because extrusion of supporting material is unnecessary with 3DP™, where unbound solid particles serve as supporting struts for cantilevers. The actual 3DP™ process will be described in more detail in section 1.3. It should be pointed out that limitations exist for the types of FGM which are possible with 3DP™. It is not feasible, for example, to achieve *fully dense* FGM's with localized regions composing purely of one component, and other regions within the same build layer consisting only of a second component. Such FGM's are possible if the *porous* structure are allowed, by depositing different components via separate printheads onto particles which will be dissolved away after printing. This approach is the basis for fabricating microporous tissue engineering scaffolds by 3DP™.

1.2.4 Combination of energy & matter deposition, and matter removal

There are many other SFF methods which will not be described here, but they are essentially variations of the approaches described above. Solid ground curing (SGC), for example, involves all three approaches in one machine. It is similar to SLA in its use of a photocuring resin, but SGC requires much less curing time since the entire resin layer is

completely cured at once by flooding the area with a mercury UV lamp. Selective polymerization is achieved by sliding a custom patterned glass mask in between the UV lamp and the uncured resin, and aligning the mask precisely over the previous layers. The pattern is generated on the glass plate according to a process similar to that utilized in common laser printers. Unlike SLA, four additional steps must occur prior to the next curing cycle. The pattern on the glass plate is first erased, and the appropriate pattern is generated for the next layer. The uncured resin is then vacuumed away and replaced by spreading a thin layer of liquid wax. The entire layer is solidified by contacting the wax and resin with a chilling plate. The next step involves the repositioning of the entire assembly to a milling station for removal of the excess wax. Finally, the assembly moves back into the curing station, dips beneath the surface of the uncured resin, and the patterned glass plates slides over the assembly for the next curing cycle. The relevant SGC components are diagrammed in Figure 1.5.

The wax serves as temporary supporting material, eliminating the need to modify the CAD design. The wax can be eliminated at the end by mild heating. SGC is less labor intensive than conventional SLA because SGC eliminates the post-processing curing step and the need to remove any supports manually. As complicated as the process is, the current state of the technology is not amenable for controlling microstructure or producing compositional gradients. This deficiency is due to the fact that unlike FDM or 3DP™, deposition of matter in current SGC is not truly selective in nature. Although it is possible to further modify this complex process to achieve greater control over composition and microstructure, the use of photocurable polymers have limited applications in biomedical device manufacturing.

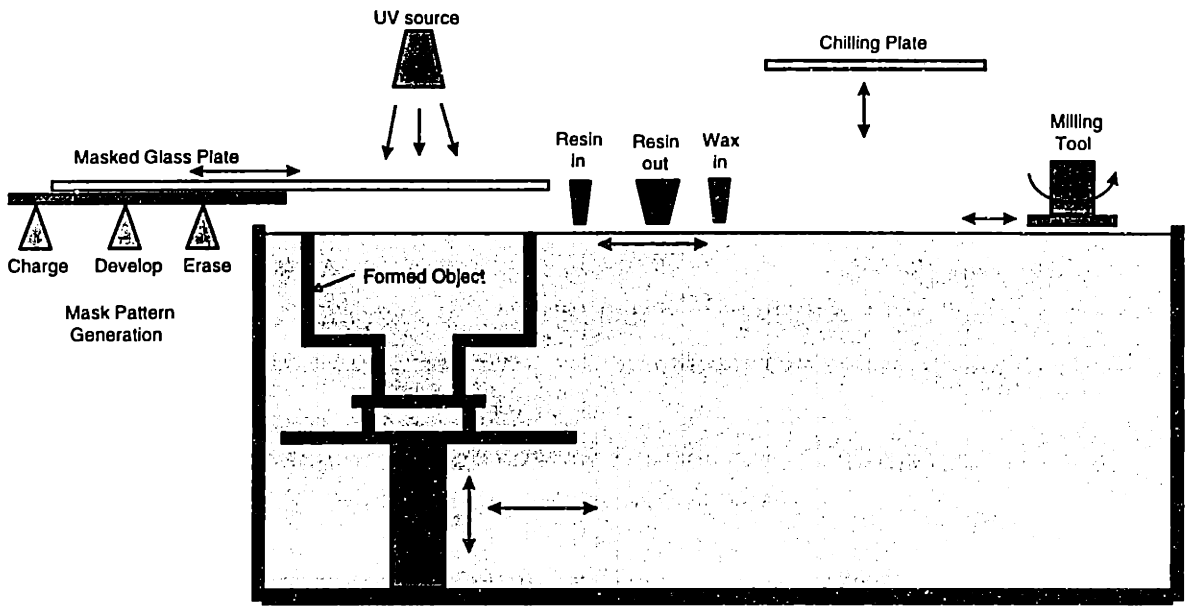

Figure 1.5: Solid ground curing (SGC)

1.3 THE 3DP™ PROCESS

1.3.1 General concepts

3DP™ builds 3D structures by ink-jet printing liquid binder onto loose fine powder in a laminated printing fashion. Because the liquid phase and powder phase can have different compositions, a large number of material combinations can be processed. The relevant machine components are shown in Figure 1.6. The computerized X-Y positioning system directs the 2D horizontal motion of the printhead, which in turn controls the fate of each liquid binder droplet. Binding occurs only where binder droplets contact the powder material below.

The sequence of operation is illustrated in Figure 1.7. The process begins by spreading a layer of fine powder material evenly across the piston. The X-Y positioning system and the printhead are synchronized to print the desired 2D pattern by selective deposition of binder droplets onto the powder layer. The piston, powder bed, and part are lowered, and the next layer of powder is spread. The drop-spread-print cycle is repeated until the entire part is completed. Removal of the unbound powder reveals the fabricated part. The local composition can be manipulated by specifying the appropriate printhead to

deposit the predetermined volume of binder. The local microstructure can be controlled by either modulating the binder composition,[17] or by altering the printing parameters during component construction.[18]

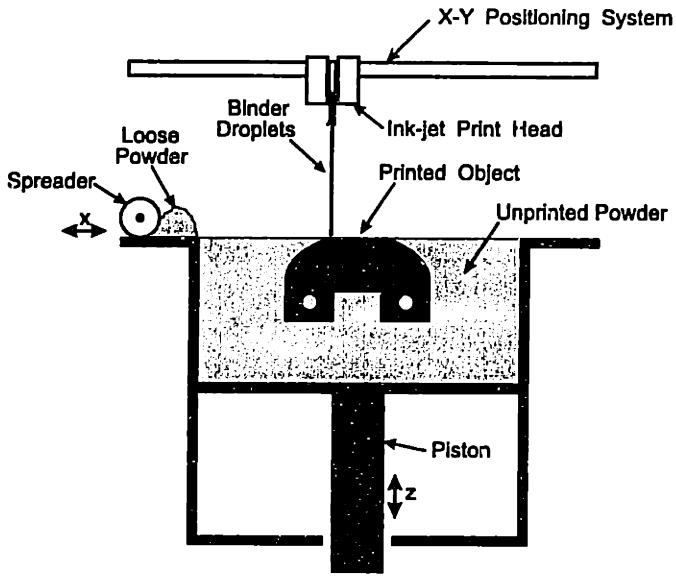

Figure 1.6: Three dimensional printing™ (3DP™)

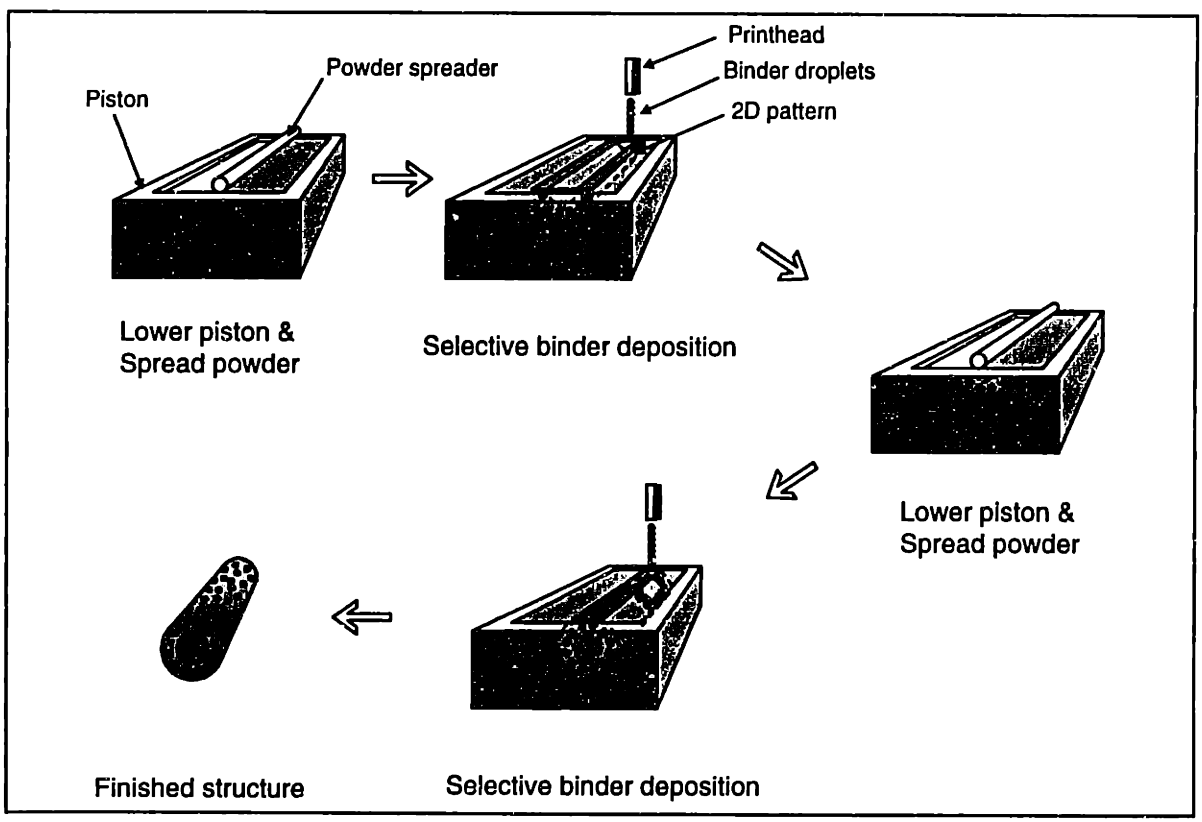

Figure 1.7: The 3DP™ sequence

1.3.2 Continuous jet printing

Continuous jet printing is the most commonly practiced mode of liquid matter deposition in 3DP™. Pressurized liquid binder is forced through a filter into a conical entrance nozzle during continuous jet printing. A small piezoelectric element provides the excitation energy to break the jet up into uniform droplets at the desired frequency and phase. Selective charging of the droplets occur during droplet formation due to charge induction by the charging cell. Charged droplets are deflected by a set of deflection plates downstream, into a catcher under negative-pressure. Uncharged droplets pass undeflected to interact with the loose powder below. The printhead assembly and the relevant components are shown on Figure 1.8. The material properties which affect these important steps of continuous jet printing are presented in this chapter. The appropriate material and machine design modifications for overcoming the constraints are discussed.

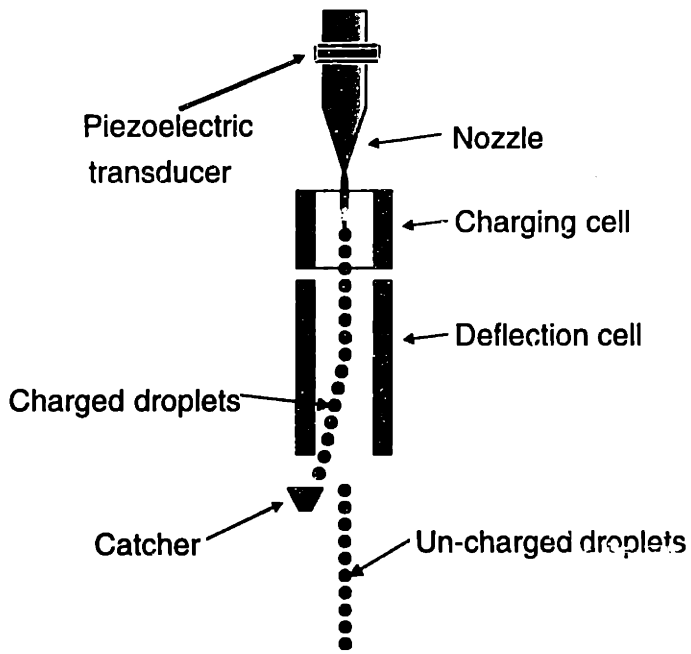

Figure 1.8: 3DP™ continuous jet printhead

1.3.2.1 Droplet formation

The aspect ratio of the nozzles used in 3DP™ continuous jet printing are chosen for print resolution and laminar-flow. Savart[19] showed that continuous laminar-flow jets tend to break up into discrete droplets since the surface energy of a liquid sphere is less

than that of a cylindrical jet with the corresponding volume. Rayleigh showed that jet oscillations develop upon nozzle exit and increase in amplitude with increasing distance from the orifice. Rayleigh related the oscillation frequency to a growth factor q, and reasoned that the wavelength (λ_{max}) with the largest growth factor predominates. The mechanical vibration from the piezoelectric element must be significantly greater than the spontaneous instability. λ_{max} for the inviscid case is given by the following equations.[20]

$$q = 0.97 \sqrt{\frac{\sigma}{\rho d_o^3}}$$

$$\lambda_{max} = 4.51 d_o$$

where σ = surface tension of the liquid

ρ = density of liquid

d_o = nozzle diameter

The droplet velocity, u, and droplet volume, d_{drop}, can be obtained by mass balance:

$$u = \frac{4 \cdot F}{\pi d_o^2}$$

where F = binder flowrate (m^3/s)

$$d_{drop} = \left(\frac{6 \cdot F}{\pi \upsilon}\right)^{1/3}$$

where υ = droplet frequency = $\frac{u}{\lambda}$

The droplet radius (r_{drop}) for natural (unmodulated) breakoff can be shown by combining the above equations to depend only on orifice diameter:

$$r_{drop} = 0.945 d_o$$

A jet of liquid exiting a 45 μm nozzle at 1 cc/min travels at 10.48 m/s, and breaks off into 85 μm droplets at a natural droplet frequency is 51.66 kHz with droplet wavelength of 202.9 μm (2.38 droplet lengths). The droplet formation frequency can be modulated by adding a piezoelectric element. The distance, L, below the orifice at which break-off occurs for Newtonian fluids can be estimated by:[21]

$$L = d \ln\left(\frac{d_o}{2\zeta_o}\right) We^{0.5}(1+3Z)$$

where ζ_o = estimated jet disturbance ($\sim 1.1\times10^{-6}\cdot d$)

$We = \frac{\rho u^2 d}{\sigma}$ is the Weber number of the jet

$Z = \frac{\sqrt{We}}{Re}$ is the Ohnesorge number of the jet

$Re = \frac{du\rho}{\mu}$ is the Reynolds number of the jet

u = jet velocity = $4F/\pi d_o^2$

μ = viscosity of liquid

solvent	density 25°C ρ (g/cc)	viscosity 25°C μ (cp)	surface tension, 25°C σ (dyne/cm)	Weber, *We*	Reynolds, *Re*	Ohnesorge, *Z*	Breakoff length, *L* (m)
water	1.00	1.00	73.05	67.7	471.8	1.7E-02	5.1E-03
N-methyl-2-pyrrolidone	1.02	1.67	40.70	124.0	288.9	3.9E-02	7.3E-03
dimethyl sulfoxide	1.095	2.00	42.98	126.0	258.3	4.3E-02	7.4E-03
toluene	0.86	0.55	27.92	152.8	736.3	1.7E-02	7.6E-03
acetone	0.79	0.30	23.70	164.5	1239.3	1.0E-02	7.8E-03
ethanol	0.79	0.55	22.75	171.6	676.8	1.9E-02	8.1E-03
ethyl acetate	0.89	0.43	23.90	185.0	990.1	1.4E-02	8.3E-03
methyl tertiary butyl ether	0.74	0.35	18.30	200.0	997.5	1.4E-02	8.6E-03
dichloromethane	1.32	0.40	27.89	233.6	1536.9	9.9E-03	9.2E-03
chloroform	1.47	0.54	26.53	274.8	1298.2	1.3E-02	1.0E-02

Table 1.1: *We, Re, Z,* and *L* of common 3DP™ solvents (1 cc/min, 45 μm nozzle)

We, Z, Re, and *L* for common 3DP™ solvents at 25°C are listed in Table 1.1. The break-off lengths for chloroform (1 cm) is therefore almost twice that of water (0.51 cm)

for identical flow conditions. Break-off lengths of common 3DP™ solvents can be seen to fall between those of water and chloroform ($0.5 < L < 1$ cm).

The equations above are adequate for Newtonian fluids. Goldin et al. reported that the addition of 0.25% sodium carboxy-methyl cellulose significantly increased the break-off distance, and showed that viscoelastic jets develop more rapid growth of axisymmetric wave disturbances than Newtonian jets of the same zero shear viscosity.[22] The mechanical excitations from typical piezoelectric elements are not sufficient to overcome the spontaneous disturbances of such fluids. These disturbances were observed in this laboratory with high speed CCD video as "stringers" or "threads" which connect the droplets into continuous strands (Figure 1.9). Similar observations were made with polymer solutions containing < 1 % polymers (PCL, PLGA, PLA). Reynolds number of the jet decreases with increasing viscosity, resulting in extensive breakoff lengths. A jet of polymeric solution with a viscosity of 15 cP, for example, requires 2 cm of breakoff length. Droplets were obtained from low viscosity solutions with low MW polymers.

Many polymeric binders are necessary for constructing dense 3DP™ structures. There are many other applications where polymeric matter need to be deposited in the liquid state. These binders contain polymer in sufficiently high concentrations that droplet break-off is not attainable due to viscoelastic fluid behavior. The inability to form individual droplets interferes with proper charging and deflection of these polymeric solutions.

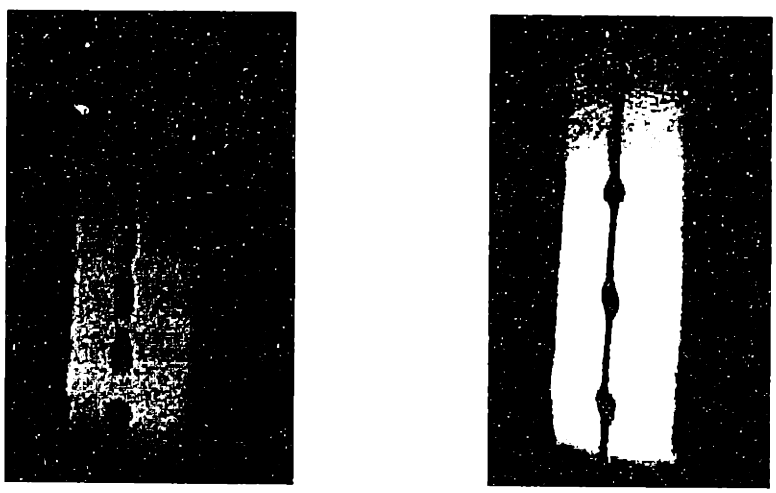

Figure 1.9: Normal droplet formation (left) vs. stringer development (right)

1.3.2.2 Droplet charging

Droplet charge Q is determined by the applied charging voltage V_c, and the capacitance between the liquid stream center electrode and the conductive charging electrode.

$$Q = -CV_c$$

For a parallel plate configuration with a small center conductor relative to the plate spacing, the capacitance C is given by the following equation:[23]

$$C = \frac{2\pi\varepsilon_o\lambda}{\ln\left(\frac{4\xi}{\pi d}\right)}$$

where ε_o = permittivity of free space

λ = droplet wavelength

ξ = separation distance between parallel plates

Permittivity of air is 8.81×10^{-12} F/m, and the separation distance between the parallel charging plates is typically 1 mm. The droplet wavelength (λ) is 2×10^{-4} m, for typical droplet velocity of 10 m/s, formation frequency of 50 kHz, and nozzle diameter of 45 μm. The capacitance is hence 3.5×10^{-15} F. The typical applied voltage to the charging cell is 50 V, resulting in a theoretical droplet charge of 1.75×10^{-13} C.

There are two phenomena which can limit droplet charge. There is a critical charge Q_c, above which the droplet will disintegrate if electrostatic repulsive forces acting on the droplet surface exceed the surface tension of the liquid.[24] The unstable droplet breaks into smaller droplets to distribute the charge and mass such that the resultant droplets are stable. Rayleigh[20] first determine the maximum charge to be:

$$Q_c = \sqrt{64\pi^2\varepsilon_o r^3\sigma}$$

where r = droplet radius

σ = surface tension

The maximum charge for 86 μm diameter water droplets is 5.68×10^{-12} C, corresponding to a maximum charging cell voltage of over 1600 volts. The surface tensions of common 3DP™ solvents are listed in Table 1.1. Surface tension of many organic solvents are about one third that of water, and hence the maximum charge for solvents are expected to be significantly lower due to droplet instability. Non-conductive solvents, such as chloroform, are exempt from such limitations since they can not be charged at all.

A second, and more commonly encountered limitation is due to electrostatic repulsion in between two adjacent droplets. This phenomenon can affect the linearity of the droplet train, resulting in a spray of droplets. It can occur at a charging voltage Q_m which is much lower than Q_c. Q_m is given by:[25]

$$Q_m = \frac{1.05 \cdot 10^{-3} u d_o \lambda^2}{z_i}$$

where z_i = distance from breakup to the point at which average deflection is d_{drop}

The Q_m for droplets exiting a 45 μm nozzle at 1 cc/min is hence 5.09×10^{-12} C, corresponding to a maximum charging voltage of appoximately 1400 volts.

1.3.2.3 Droplet deflection

The charged droplets are deflected by a pair of parallel deflection plates in 3DP™. The horizontal deflection can be obtained by the following equation:[25]

$$\text{Horizontal deflection } X_d = \frac{q_d V_{deflect}}{m_d v_d^2} L\left(Z - \frac{L}{2}\right)$$

where q_d = droplet charge

$V_{deflect}$ = deflection cell voltage

m_d = droplet mass

v_d = droplet velocity

L = length of deflection field

Z = vertical distance between top of deflection plate to catcher

A deflection distance of 3.4 mm can be achieved with 500 volt $V_{deflect}$, using typical values of 16 mm for L and Z, and 43 μm droplet radius, and 10 m/s droplet velocity. It can be seen that the horizontal deflection can be improved by increasing the deflection voltage, increasing the vertical distance of deflective motion, improving the charge-to-mass ratio, decreasing the droplet velocity, and lowering the droplet formation frequency. Another approach is to shorten the horizontal deflection that is required to practice selective printing. This can be accomplished by re-locating the fluid catcher closer to the un-deflected jet, reducing the amount of horizontal deflection that is required. The catcher morphology can also be modified to further reduce the deflection distance. All of these mechanical modifications were incorporated in the recent design of the deflection and catcher assembly. The white arrows in Figure 1.10 show the position of the undeflected (left photo), and partially deflected (middle photo), and deflected acetone droplets (right photo) using the modified deflection and catcher assembly.

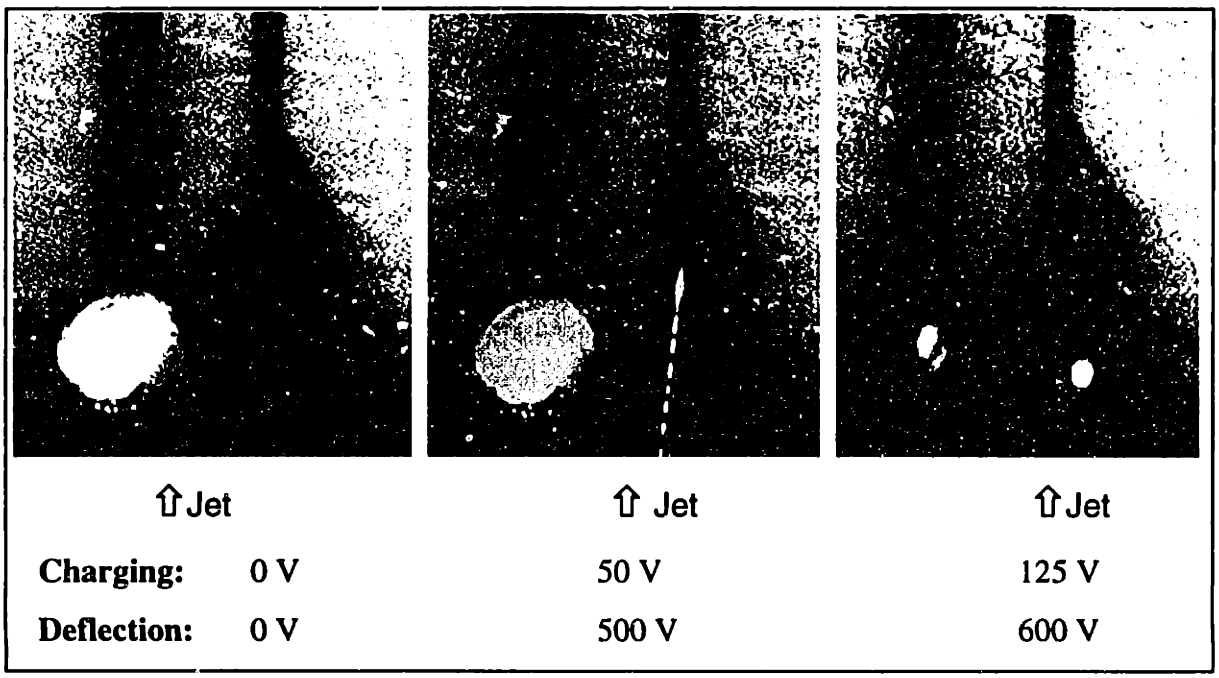

Figure 1.10: Deflection of acetone droplets

1.3.2.4 Sequential stencils

Polymeric binders are necessary for constructing dense 3DP™ structures (see Chapter 5). There are other applications where polymeric matter needs to be deposited in the liquid state. One example is the deposition of polymeric solution onto a powder bed

of pure salt for producing highly porous structures and eliminating powder removal problems. Another common reason for printing with polymeric solutions is to control binder migration and improve structural resolution during 3D Printing™.

These binders contain polymer in sufficiently high concentrations that droplet break-off is not attainable due to viscoelastic fluid behavior. The inability to form individual droplets precludes the selective charging and deflection of many polymeric binder solutions. Even at 1 w/w%, polycaprolactone (10,000 MW) / chloroform solutions form an unstable but continuous jet, upon exit from printhead orifice. Although binders with no or insignificant polymer content can form droplets, many pure organic solvents used for 3DP™ are electrically non-conductive. Non-conductive solvents such as chloroform and methylene chloride cannot be charged and deflected during printing. The inability to deflect the binder droplets results in continuous, semi-selective deposition of binder into the powder bed, effectively limiting the printed features to continuous lines and sheets. This material limitation poses a severe constraint on the geometric complexity of the parts.

A sequential stencil indexing system *(Wutini™)* was developed to overcome the limitation and allow the fabrication of complex three dimensional parts with non-conductive solvents. Initial, proof-of-concept stencils were fabricated by patterning the "unprinted" regions of thin copper sheets by photolithography and selectively removing the "printed" regions by chemical etching. An indexing system was developed to reproducibly reference the stencils to the powder bed. Tissue scaffolds with complex channel patterns were fabricated with the prototype copper stencils. It was determined that isolated islands of unprinted regions require two complimentary patterns, and that a maximum of two stencils may be required for each binder material in any given layer. The second iteration of sequential stencils were fabricated by computer-assisted laser cutting of tempered stainless steel plates according to CAD files (Figure 1.11) of the stencils. The appropriate CAD files can be generated on PC-based CAD software such as TurboCAD® or AutoCAD®.

Resolution as low as 5 μm can be obtained with 0.020 inch thick tempered steel (Rache Corp, Camarillo, CA). Thicker stencils are stiffer but the resolution deteriorates

to >25 μm. Thinner stencils are too compliant for repetitive removal and insertion during use in 3DP™. Figure 1.12 shows the first polymeric structures which were derived from the stencils using the 3DP™ operating parameters listed in Table 1.2.

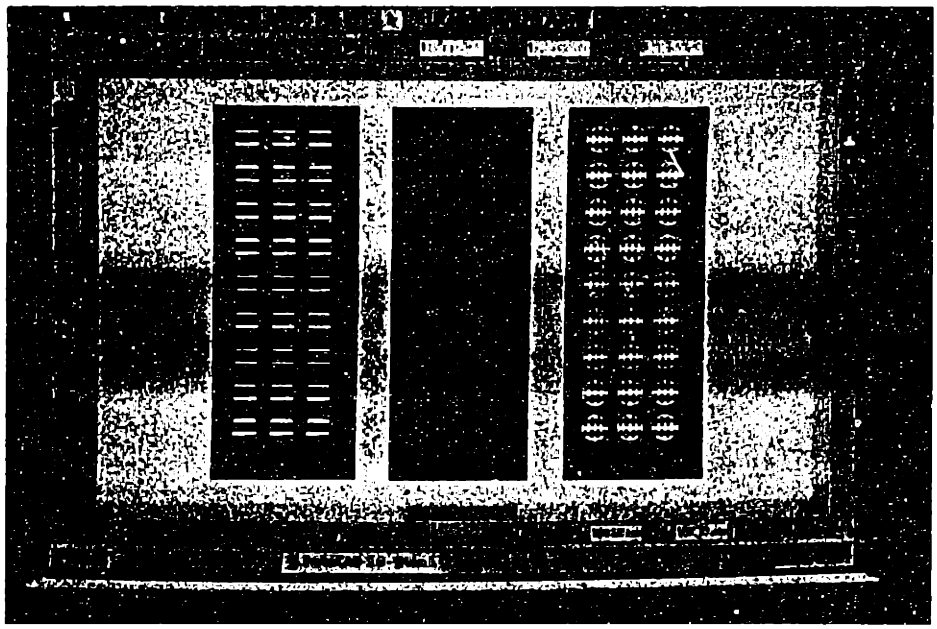

Figure 1.11: CAD images of stencils

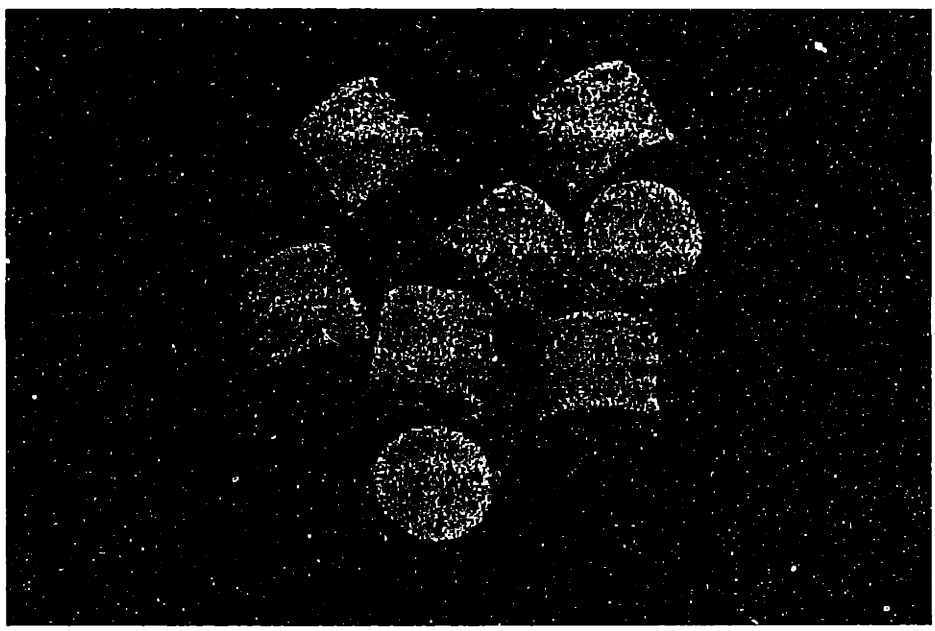

Figure 1.12: Devices constructed by sequential stencils

3DP™ parameters	
Powder	45-75 μm PLGA (85:15 100,000MW)
Binder	Chloroform
Printspeed	90 cm/s
Line spacing	100 μm
Layer thickness	150 μm
Flowrate	1.5 g/min

Table 1.2: 3DP™ parameters for printing the devices shown in Figure 1.12

1.3.2.5 Background

Drop on demand (DOD) printing is the second method for printing in 3DP™. DOD systems use electrical signals to generate individual droplets. Selective droplet formation during DOD printing differs from continuous jet printing, in which liquid is continually released. Selective droplet generation is advantageous for depositing biological actives because of reduced waste. The modular nature of DOD systems is also important because of reduced cross-contamination.

An electrical signal is used in DOD printing to trigger either heat generation or piezoelectric element excitation, depending on the system. In both cases, the associated sudden increase in chamber pressure results in the ejection of a liquid droplet through the nozzle. DOD systems work at lower frequency range (below 10 kHz) than continuous jet systems because the meniscus at the nozzle must be restored and the chamber refilled with liquid from the main reservoir before the next droplet can be fired. DOD printing can be very efficient despite the above limitations.

Commercial DOD printheads (Hewlett Packard 51626A) were emptied, cleaned, and filled with various biological actives. Electrical signals were generated by a data acquisition board (National Instruments AT-MIO-E2) and a LabView® VI (virtual instrument) was written to control the relevant signal pulse parameters. Calibration curves for various materials indicate good reproducibility of droplet generation. DOD printing was successfully integrated with three axes motion on the 3DP™ machine. A file format (TDF) was established to standardize instructions for DOD printing. An

algorithm was developed with LabView® to convert bitmap files from most popular graphic applications.

1.3.3 Chamber and droplet volume

One obvious question is the relation between chamber volume and droplet volume. If the chamber is large relative to the droplet, then re-filling the chamber and local heating are less important. If the two volumes are similar, then the re-filling and heating issues may constrain the materials that can be used with this technology. An "off-the-shelf" printhead cartridge (HP 51626A) was disassembled and analyzed to compare the chamber volume and the characteristic droplet volume. Figure 1.13 shows the magnified external views of the nozzle plate, and Figure 1.14 shows the magnified internal view of the nozzle plate. There are two long rows of 27 nozzles (54 total) and two sets of three mounting indices. Two of the 54 nozzles have non-printing functions since there are only 52 signal connectors (plus four common connectors).

(37.5 x) 375 x

Figure 1.13: External view of DOD nozzles

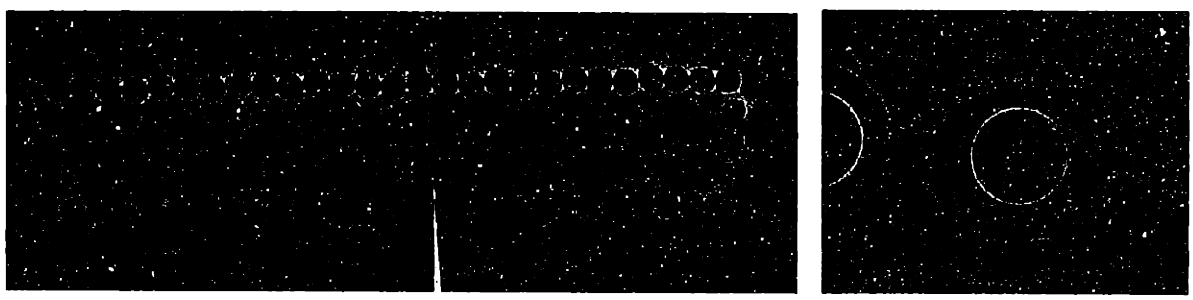

(37.5 x) 375 x

Figure 1.14: Internal view of DOD nozzles

Note that the nozzles are aligned in a staggering/alternating pattern. Energy-dispersive X-ray spectroscopy (EDS) reveals Ni as the main constituent of the nozzle

plate material (Figure 1.18). The total chamber volume is composed of the nozzle plate volume and the chamber-reservoir volume. The nozzle resemble a cylindrical cone with a 50.7 μm external diameter, 130.7 μm internal diameter, and 70 μm height (Figure 1.15).

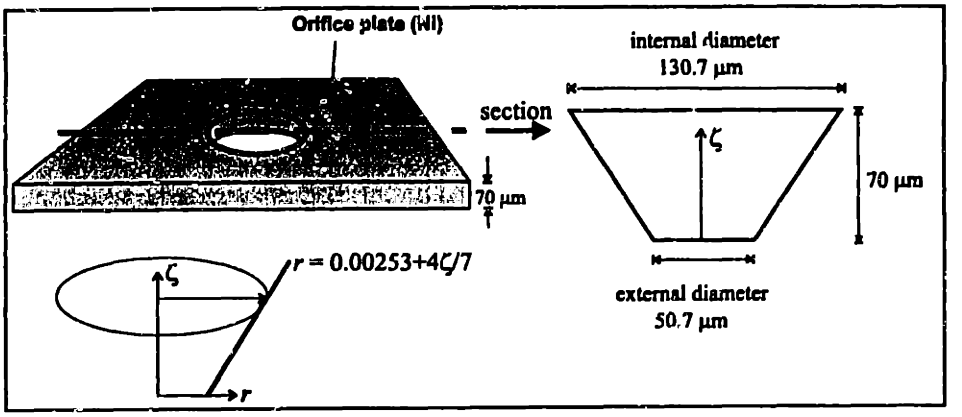

Figure 1.15: Diagram of one DOD nozzle in orifice plate

The nozzle plate volume can be obtained with the volume equation of the cone by integrating from 0 to 70 μm:

$$v_{nozzle} = \int_0^{0.007} \pi \left(0.00253 + \frac{4}{7}\zeta\right)^2 d\zeta \qquad = 4.8 \cdot 10^{-7}\ cm^3$$

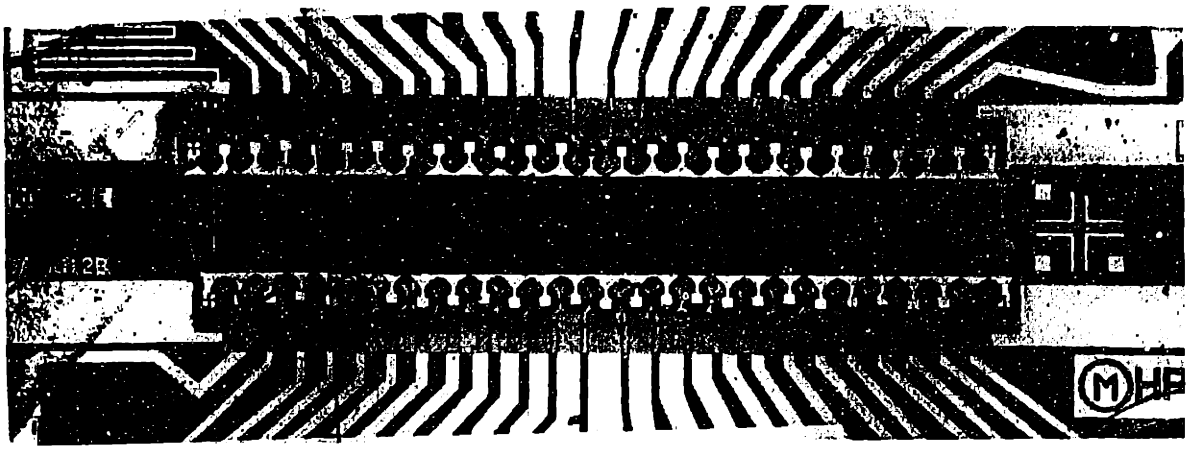

Figure 1.16: Optical micrograph of firing chambers (37.5 x)

The chamber-reservoir can be seen on the high-magnification optical micrographs (Figures Figure 1.16 and Figure 1.17). The walls are 94 μm wide, and 30

μm high. Thus, the chamber-reservoir volume is approximately 265 pl. The total chamber volume is thus 746 pl. The characteristic droplet diameter is 52 μm, corresponding to a typical droplet volume of 73.6 pl. This small volume represents only 10% of the total chamber volume (73.6÷746 ~ 10%).

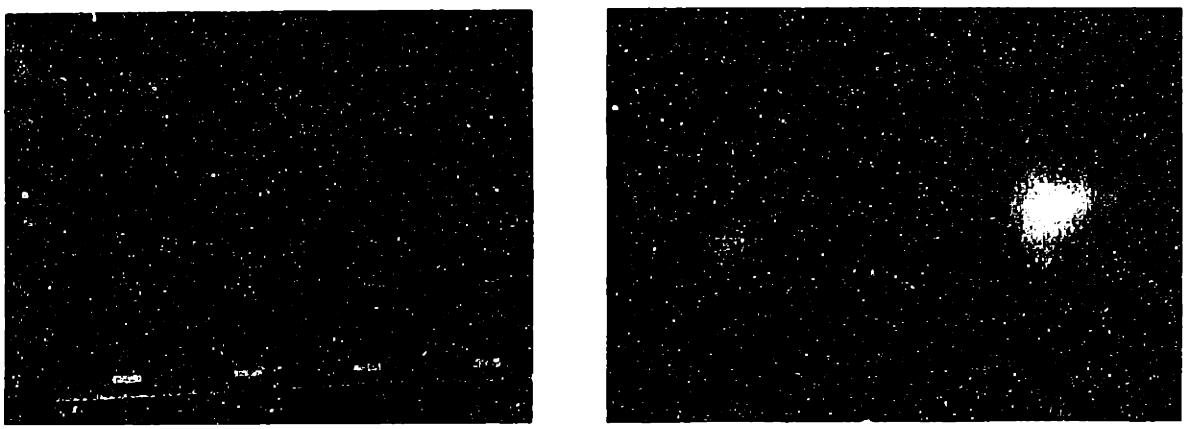

Figure 1.17: Optical micrograph of firing chambers (150x and 375x)

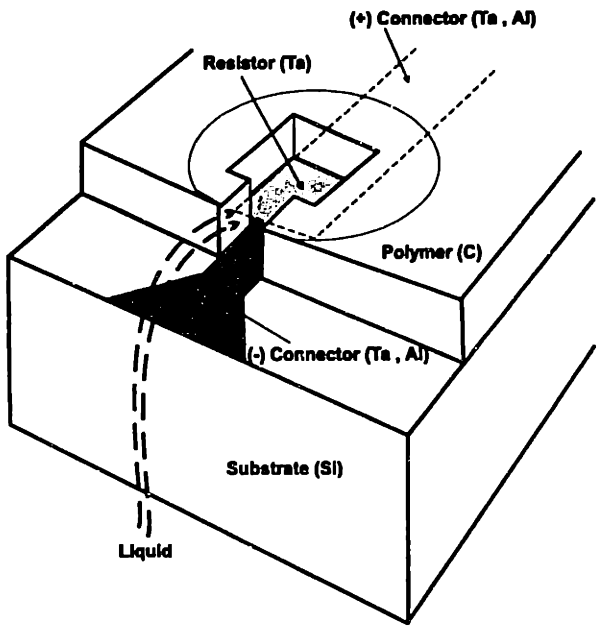

Figure 1.18: Firing chamber of DOD nozzle

Figure 1.18 illustrates the construction of the chamber. EDS was used to determine the composition of the relevant components. A tantalum resistor is patterned on a silicon substrate and forms the "floor" of the chamber. The resistor is connected to

the external electrical connector plate by a tantalum/aluminum lead which is also patterned on the silicon substrate. The "walls" of the chamber are constructed with a polymeric material. An electrical signal is carried through the lead to heat the tantalum resistor. The heat is quickly transferred to the liquid between the resistor and the orifice, resulting in vaporization and bubble generation. The net result is droplet ejection. The liquid is subsequently replenished from the main reservoir by capillary driven flow.

1.4 3DP™ AND BIOMEDICAL APPLICATIONS

3DP™ is unique among SFF technologies by offering selective spatial deposition of multiple materials, and consequently the ability to manipulate local composition and microstructure. These unique features present many new possibilities for the fabrication of biomedical devices. While other SFF technologies are limited to pre-surgical models and anatomical molds for secondary processing, 3DP™ can fabricate novel biomedical devices *directly*. Controlling spatial distribution of multiple drugs, matrix modifiers, and matrix binder offers unprecedented flexibility to design chronopharmacological drug delivery systems. Controlling spatial distribution of porosity, cell adhesion modifiers, and growth factors offers unparalleled versatility to design microporous anatomical tissue engineering scaffolds with the proper microarchitecture for maximizing cell density and regeneration.

Dense, defect free structures are required for most drug delivery devices in which uncontrolled printing defects lead to adverse complications. Highly dense structures are also necessary for many orthopedic fixation devices in which random defects can deteriorate mechanical integrity and result in premature clinical failure. Highly porous matrices with interconnected microporosity and controlled channel dimensions are critical for successful engineering of thick tissues. Release kinetics of many drug delivery systems are based drug diffusion through porous matrices. The ability to control feature size, or optimize print resolution, is critical for all types of devices. The common theme for controlling feature size, microstructure, and spatial distribution of printed matter is to understand the fundamental binding mechanisms during 3D Printing™.

1.5 THESIS OBJECTIVES

The main objective of this thesis is to understand the mechanisms responsible for primitive formation during 3D Printing™ of polymeric structures. The second objective is to identify the key parameters for controlling microstructure formation. The third objective is to establish the relation between 3DP™ microstructure and biomedical device performance.

1.6 SCOPE OF THESIS

3DP™ was originally developed for industrial processing of ceramic and metal materials. Chapter 2 describes the four general binding mechanisms during 3D Printing™, and delineates the four binding stages during primitive formation. The implications of binding mechanism on microstructure control and device performance are discussed. Particle dissolution is studied in detail in Chapter 3, since it is the predominant particle-solvent interaction during 3D Printing™ of bioerodable polymers. Two distinct dissolution modes were observed, and the four key stages are also described for the predominant dissolution mode. A key finding is the existence of a minimal dissolution time for some particle-solvent combinations. The relative kinetics of particle dissolution and solvent evaporation are important since they represent competing parameters which affect microstructure formation. Chapter 5 divides the problem of solvent evaporation into three problems - solvent evaporation from droplet in flight prior to binder-particle contact, evaporation from non-dissolving particles, and evaporation from dissolving particles. A kinetics model for predicting particle dissolution is proposed. The implications of these findings on 3D Printing™ of bioerodible particles are discussed.

The materials-processing-microstructure relationships are studied in Chapters 5 and 6. Chapter 5 summarizes the experiments for the fabrication of highly dense, defect-free structures. Chapter 6 describes the fabrication of highly porous structures. The microstructure-performance relationships are studied in Chapters 7 and 8. Chapter 7 demonstrates the application of 3DP™ for controlling drug release profiles by manipulating spatial distribution of the drugs, and by modulating local composition and

microstructure. Chapter 7 also illustrates how 3DP™ utilized USP grade excipient materials to fabricate oral dosage forms, and FDA approved polymers to fabricate implantable drug delivery devices. By offering simultaneous control over macroscopic shape, oriented channels, microporosity, and local composition, 3DP™ offers unique opportunities to fabricate complex scaffolds with intrinsic vascular network for engineering of thick organs. Chapter 8 reviews the liver regeneration data from preliminary experiments in collaboration with the Laboratory for Transplantation and Tissue Engineering at Boston Children's Hospital.

2. 3DP™ Binding Mechanisms

2.1 BACKGROUND

The first objective of this thesis is to understand the fundamental binding mechanisms during 3D Printing™ of polymeric materials. Such an understanding would facilitate control over feature size, microstructure, and local distribution of printed matter. These are particularly important issues for medical device manufacturing, where uncontrolled microstructural defects may lead to life threatening complications and grave legal ramifications. Controlled microstructure, on the other hand, allows the fabrication of a new generation of chronopharmacological drug delivery systems, customized high-performance orthopedic fixation devices, and novel tissue engineering scaffolds. It turns out that there is another practical benefit for the mechanistic approach.

One of the most important attributes of 3DP™ is its flexibility in material selection. Virtually any powder material and low viscosity liquid can be processed by 3DP™. Some material combinations, of course, are more amenable for the process than others. This tremendous level of flexibility separates 3DP™ from all other SFF technologies. Materials flexibility, however, also presents a minor problem: it is virtually impossible to comprehensively describe the powder-binder interactions for each specific material combinations which have been attempted in 3DP™. It would be a formidable task even if the description was limited to biodegradable polymers. It is more meaningful to categorize all the observed powder-binder interactions into specific mechanisms, and report each mechanism in detail. The mechanistic approach can also be utilized in the future to formulate printing strategy and predict device performance of untested material combinations.

Section 2.2 describes four general classes of primitive formation mechanisms which have been observed during 3D Printing™ of polymeric parts: adhesion, dissolution/re-precipitation, swell-sinter, and chemical reaction/cross-linking. The practical implications of binding mechanism on printing strategy and device performance are highlighted in section 2.2.5. One binding mechanism, dissolution-re-precipitation, is the predominant binding mechanism for bioerodable polymers. Four important stages

have been identified during dissolution-re-precipitation: droplet impact, imbibition and drainage, dissolution/swelling, and re-precipitation. Each of the 4 stages are considered in detail in section 2.3. The time and length scale for feature formation are discussed in section 2.4.

2.2 MECHANISMS OF POWDER-BINDER INTERACTIONS

2.2.1 Adhesion

The powder-binder interaction during conventional 3D Printing™ of ceramic and metal parts involve the selective adhesion of neighboring loose particles by binder droplets.[26] The particles are coated by the liquid binder and joined together when the binder solidifies. The size of the resultant primitive is related to the extent of liquid migration through the porous powder bed.[27] The adhesion mechanism is also valid for many polymeric systems, such as microcrystalline cellulose powder and aqueous latex binders. The common theme among these materials systems is that the solid powder particles retain their original size and shape during powder-binder interaction, and are not physically altered by the liquid binder.

The scanning electron micrograph in Figure 2.1 shows 2 intersecting perpendicular lines which were constructed by printing an aqueous pharmaceutical latex of methacrylic acid copolymers (Eudragit L30D) into a powder bed of calcium carbonate crystals (<10 μm particle size). The coarse surfaces of the lines appear to be composed of small granules. The individual cubic particles are clearly visible at higher magnification in Figure 2.2. The sharp edges and corners indicate that the particles underwent no morphological changes, and the inter-particle binding is purely adhesive in nature.

The adhesion mechanism is also used to construct tissue engineering structures. It is the basic binding mechanism when polymer-chloroform solution is printed into a powder bed of sodium chloride particles. The resultant structure is then immersed in water to dissolve away the salt particles, leaving behind an interconnected porous matrix.

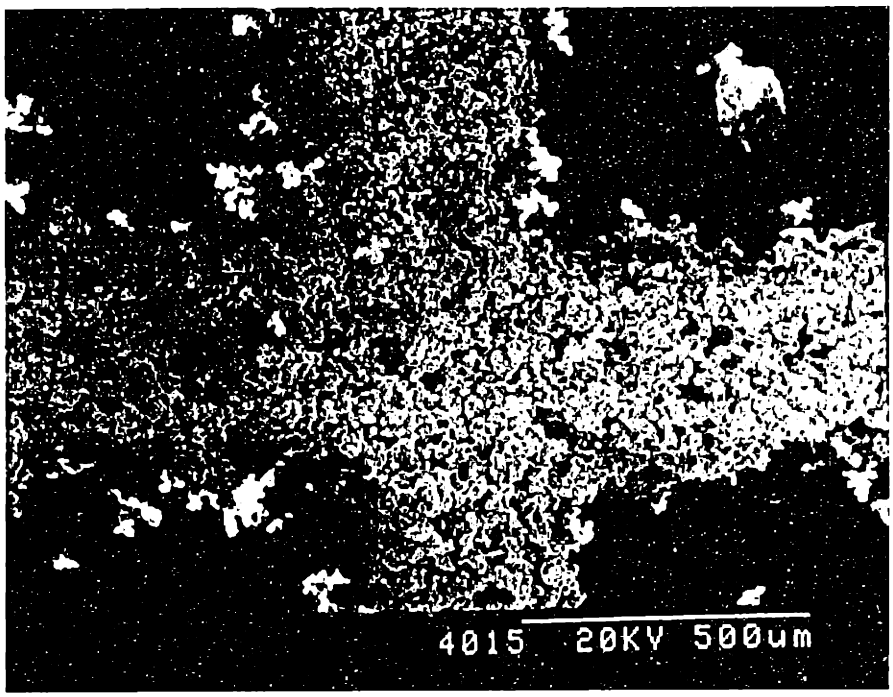

Figure 2.1: Lines constructed with acrylic latex into calcium carbonate powder

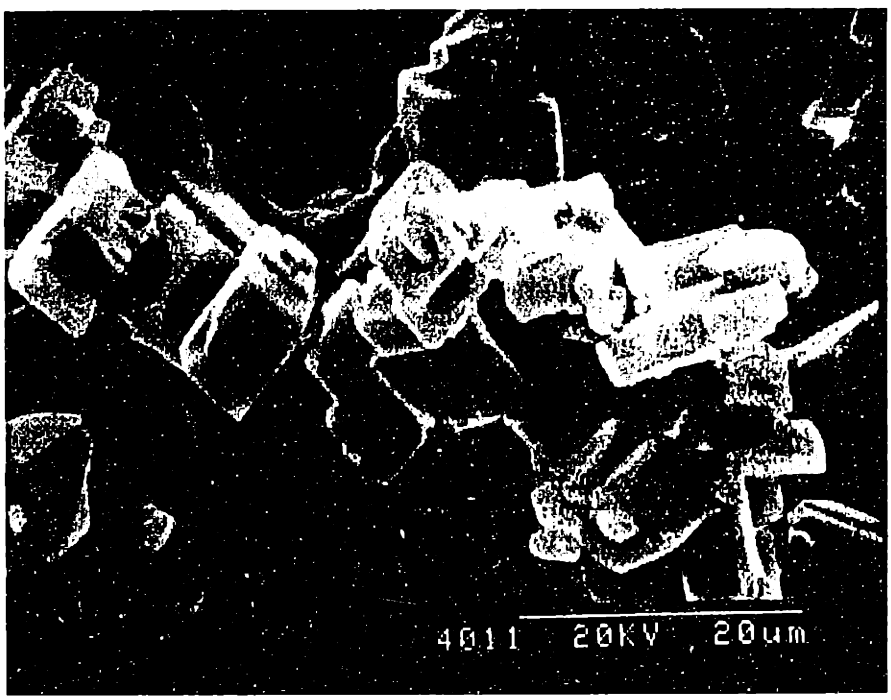

Figure 2.2: Adhesion of cubic calcium carbonate particles

2.2.2 Dissolution and re-precipitation

Bioerodable polyesters are used extensively for the construction of implantable drug delivery devices and tissue matrices. The dominant 3DP™ binding mechanism for these materials is dissolution and re-precipitation. The initial stage of the binding process involves the dissolution of neighboring loose particles after they are wetted with solvent. 3D structures are produced by re-precipitation of the solvent-polymer gel-mix due to solvent evaporation. The particles may be partially or completely dissolved, and are joined together when the dissolved portions of the particles re-solidify.

Figure 2.3 shows a single droplet primitive formed by dissolution/re-precipitation. This primitive was produced by depositing a single droplet of methylene chloride through a 26 gauge intradermal beveled syringe (i.d. = 400 μm) into a powder bed of loose polycaprolactone particles (PCL 45,00, 75-150 μm). The top of the droplet primitive appears smooth and dense, and unlike Figure 2.2, no particles are visible. These observations are indicative of complete particle dissolution and subsequent re-precipitation into one cohesive mass. Partially dissolved particles can be observed along the outer surface which was in contact with loose powder. Solvent migration may be responsible for delivering enough solvent to attach, but inadequate amount of solvent to dissolve these particles. It is possible, however, that particle binding along the outer edge may be due to adhesion of dissolved solvent-polymer gel-mix to the particles, without dissolving them. These extra particles can deteriorate print resolution, regardless of etiology, and the effect is more dramatic with increasing particle size.

Another important observation can be made from Figure 2.3. Note the concavity at the top surface of the single droplet primitive. The sources of the concavity are radial and basal binder migration, complete particle dissolution, and re-distribution of the particle material (PCL in this case) into the void space. This observation suggests that in order to achieve fully dense structures by cohesive binding without incurring gross volume changes, polymeric solutions should be considered for binder selection. Use of polymeric solutions should reduce binder migration due to higher binder viscosity, and the dissolved polymer also contributes to void filling. This observation has direct implications in developing 3D Printing™ strategies.

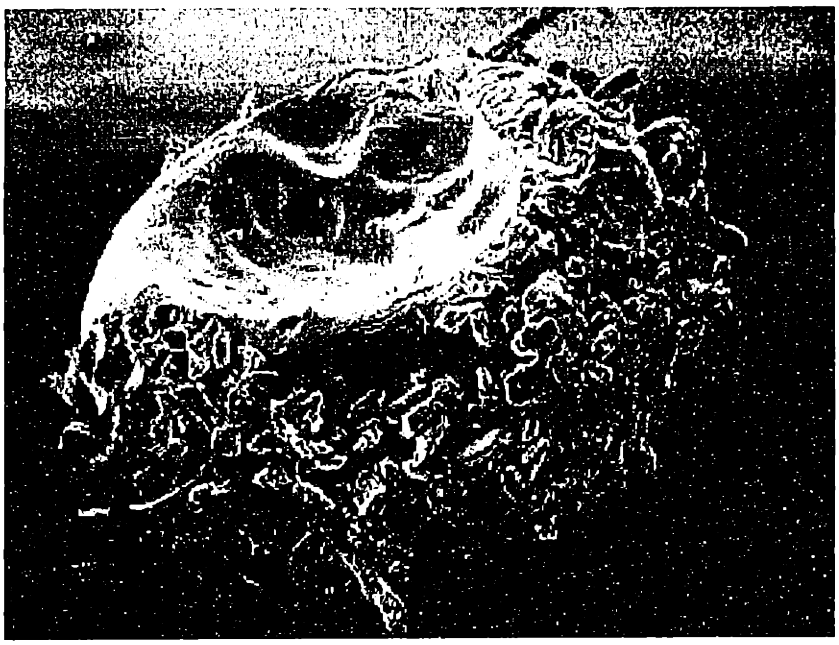

Figure 2.3: Single droplet primitive (PCL particles and methylene chloride)

The following two figures illustrate that besides materials properties, printing parameters can also affect the printed features. The highly smooth surface in Figure 2.4 is achieved by printing chloroform under the proper printing parameters (150 cm/s, 1 mm line spacing) into polycaprolactone PCL (45,000) particles. The use of less aggressive solvents and less soluble particles is expected to result in partial dissolution. Partial dissolution may also occur with highly soluble material combinations if the printing parameters are inappropriate.

The "bumpy" surface in Figure 2.5 was achieved by using the same materials which made up the smooth surface in Figure 2.4, but at different printing conditions (150 cm/s, 7 mm line spacing). It appears that printing parameters affect the extent of chemical and physical interactions between the liquid binder and the solid particles. In this illustration printing parameters affected the extent to which the particles dissolve, decrease in size, and undergo morphological changes during printing. Printing parameters must therefore affect the rate of polymer dissolution and rate of solvent evaporation.

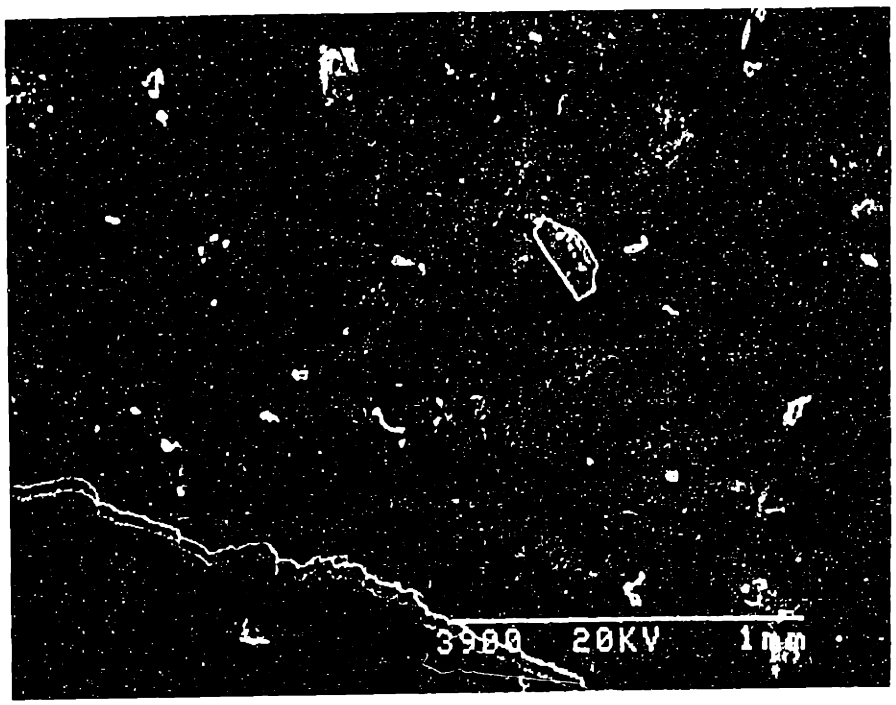

Figure 2.4: Complete particle dissolution

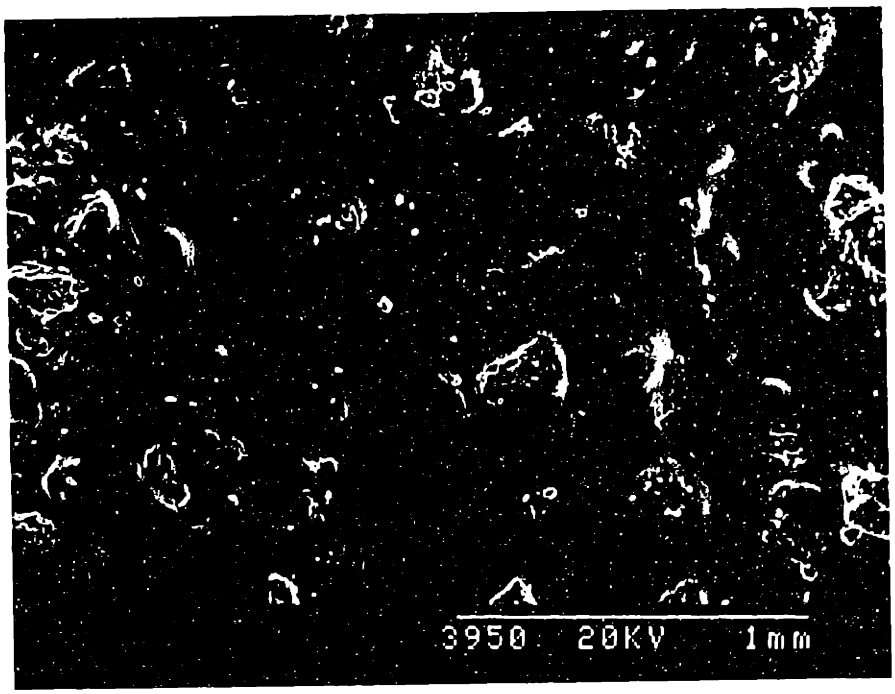

Figure 2.5: Partial particle dissolution

2.2.3 Swell and sinter

The swell and sinter model describes another possible polymer-binder interaction for the polyester particles. The initial stage involves wetting and absorption of liquid binder into the polymeric particles, resulting in swelling and softening. If the absorbed binder sufficiently lowers the polymer T_g, adjacent swelling particles may join together by a creep deformation mechanism. This binding mechanism is operative if the liquid binder exhibits very low solvency for the polymer, or if the dissolution rate is much slower than evaporation rate. This mechanism requires the rate of solvent penetration into polymer particles to be faster than that of solvent evaporation. Viscosity build-up in this model is expected to be less significant than in the dissolution model, and binder migration may be more extensive than the dissolution model.

It should be emphasized that particle binding can also occur in this model if sufficient portions of the particle surfaces are dissolved by the weak solvent. Figure 2.6 shows partial binding of PLGA (85:15 100,000) particles by printing a 70:30 v/v mixture of ethanol:acetone. Extensive swelling of the printed lines was observable within minutes. The swollen structure reverts completely to the unswollen dimensions after placement in an flushed nitrogen environment for 24 hours. The final feature size depends on the amount of shrinkage that occurs within the polymeric particles during drying. Structures derived from the swelling mechanism tend to exhibit poor mechanical integrity, as suggested by Figure 2.6. The key difference between this swelling mechanism and the gel layer formation observed during particle dissolution is that in the latter case, the gel layer will dissolve away, and the gel layer will not revert to the original particle dimensions after solvent evaporation. Swelling is not a commonly observed mechanism, and it may find limited applicability in biomedical device manufacturing.

Figure 2.6: Partial binding of PLGA (85:15 100,000) particles

2.2.4 Chemical reaction/cross-linking

A fourth class of binding mechanism involves various *in situ* chemical reactions between the binder and powder particles. A significant number of biomaterial combinations can be processed in 3DP by this mechanism. The formation of antigen-antibody complex can be utilized, for example, by printing an antigenic binder onto polymer particles which are chemisorbed with the appropriate antibodies. Another example is the formation of fibrin clot by depositing a dilute thrombin solution onto fibrinogen powder. One interesting application of this binding mechanism is to print a 20U/ml solution into a powder bed of fibrinogen bone particle mixture (Figure 2.7). Polymerization is also possible by depositing initiators and accelerators only in selective regions of each layer, and then exposing the entire layer surface to heat or UV. This approach can be utilized to fabricate novel scaffolds from polymerizable hydrogels.

Figure 2.7: Device built with thrombin solution and fibrinogen/bone particles

2.2.5 Practical implications of binding mechanisms

The type of binding mechanism can have a major impact on the degradation mechanism of the printed structure, which plays a crucial role in determining release rate of drug delivery devices. Bulk erosion due to simultaneous binder dissolution and particle disassociation would result in rapid drug release. Slower, Fickian transport is expected for devices with intact matrices. Intermediate release rate is expected for devices with evolving porosity.

Selective dissolution of the binder from printed structures which were formed by the adhesion mechanism results in unbinding and scattering of the particles. An example of this is the water dissolution of aqueous latex binder and subsequent scattering of microcrystalline cellulose particles. Selective dissolution of the particles, on the other hand, from "adhesive" bound structures leaves behind a porous matrix composed only of the binder material. An example of this is the water dissolution of sodium chloride

particles and development of an interconnected, porous polylactide structure. Particle scattering is unique to the adhesion mechanism.

The other three binding mechanisms are considered to be cohesive binding mechanisms, as they involve chemical and physical alteration of the powder particles. Selective dissolution of the binder from cohesively bound structures does not result in scattering of the bound particles. In fact the binder used in most cohesive binding may be a pure solvent, which dissolves the particles and evaporates. In cohesive binding, therefore, presence of the binder is not necessary for particle binding. Selective dissolution of the particles from cohesively bound structures also leaves behind a porous matrix with higher inter-pore connectivity than can be derived from adhesive bound structures. An example of this is the water dissolution of low molecular weight polyethylene glycol particles and formation of an interconnected porous polylactide structure.

Binding mechanisms also have important implications on printing strategies. It may be much more difficult to achieve full density *directly* during printing if the binding mechanism is adhesive in nature. The inter-particle void space must be completely saturated with binder material in order to achieve fully dense structures, since the particles do not contribute to void filling. Repeated printing over the same layer is also mandatory, since the solid content in the binder is limited. Repetitive printing is inefficient because the printhead must raster over the same region multiple times, and adequate time must be allotted for liquid drying between successive repetitions in order to preserve print resolution. Drying time may be reduced by heating, increasing ventilation rate, or choosing binders with higher evaporation rates.

Achieving full density *directly* during printing may be possible with cohesive binding mechanisms. There are two sources of void filling material in cohesive mechanisms - binder and particles. The key contribution here is the re-distribution of physically modified particle materials into the adjacent void spaces. Repetitive printing may still be required to introduce additional volume of materials, depending on the packing density of the powder and solid concentration in the binder. The contribution from dissolved particles should, however, reduce the number of repetitions. Repetitive

printing alone is not likely to fill all the voids if the particles do not dissolve, since the solids in the binder are carried with a solvent which occupy finite volume. Dissolution/re-precipitation is expected to contribute the most material to void filling among the three cohesive mechanisms, since the dissolved polymer can flow and redistribute. The contribution to void filling for the swelling and chemical reaction mechanisms depend on the flowability of the swollen state, and the nature and extent of the chemical reaction, respectively.

2.3 4 STAGES OF BINDING DURING DISSOLUTION/RE-PRECIPITATION

This section describes in detail the predominant binding mechanism for bioerodable polymers, dissolution-re-precipitation. The important stages which occur during this binding mechanism are diagrammed in Figure 2.8. The four stages are droplet impact, binder imbibition and drainage, particle dissolution/swelling, and re-precipitation.

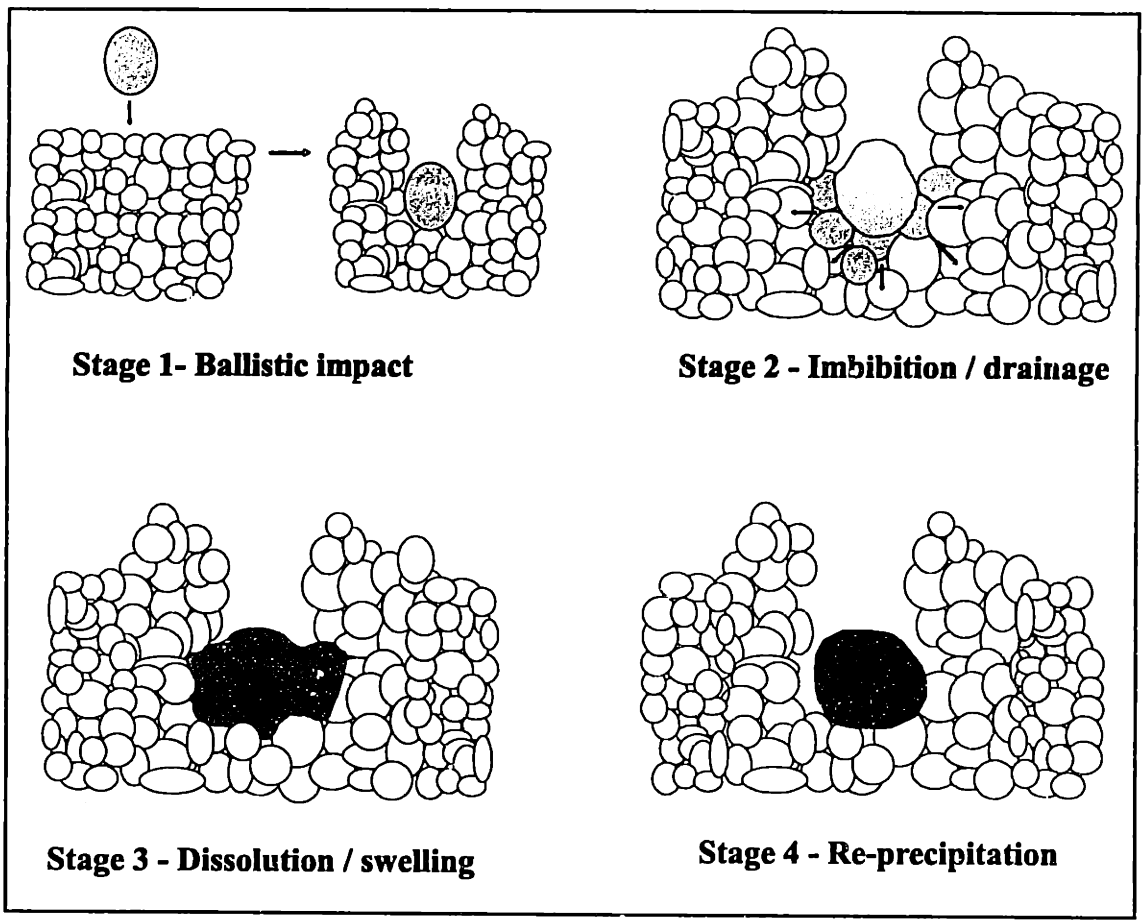

Figure 2.8: 4 stages of binding during dissolution/re-precipitation

2.3.1 Stage 1 - Ballistic impact

The ballistic impact between liquid droplets with loose powder particles was first characterized by Lauder[26], and recently analyzed by Fan[28]. Droplet velocity, u, for continuous jet printing can be determined by mass balance:

$$u = \frac{4 \cdot F}{\pi d_o^2}$$

where F = binder flow rate

d_o = orifice diameter

The dependence of droplet velocity on binder flow rate is plotted in Figure 2.9 for three common nozzle dimensions used in 3DP™ (45μm, 70 μm, and 127 μm). Continuous jet printing droplets exiting a 45 μm nozzle at 1 cc/min typically travel at a velocity of 10.5 m/sec. It can be seen that for the same flowrate, droplets exiting from larger nozzles travel at much lower speed than those from smaller nozzles. The larger droplets are also less sensitive to flowrate changes.

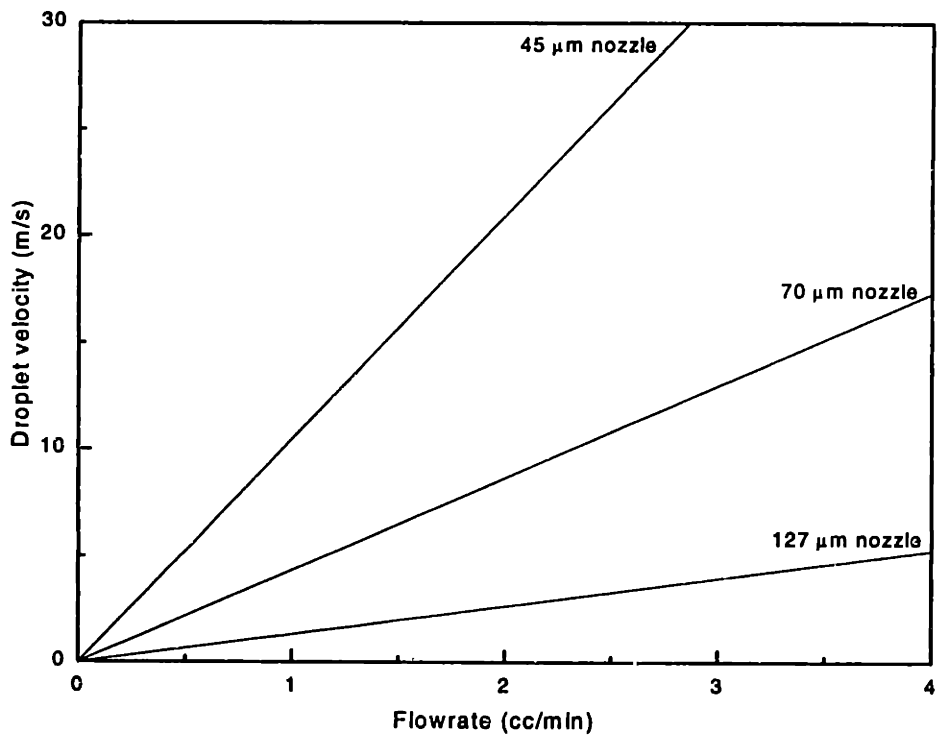

Figure 2.9: Effect of nozzle size and flowrate on CJ droplet velocity

The kinetic energy dependence on flowrate is plotted in Figure 2.10 for continuous jets undergoing natural breakoff with three common nozzle dimensions (45μm, 70 μm, and 127 μm). It can be seen that for the same flowrate, jets exiting from larger nozzles are less energetic than those exiting from smaller orifices. This is expected from the square dependence of energy on velocity. In practice, however, much higher flowrates are required to eliminate jet-wandering for the larger jets. Flowrates of 3 to 4 cc/min are commonly used for 127 μm nozzles, whereas only 1 cc/min is typically adequate for 45 μm nozzles. The typical kinetic energy for the 127 μm jet is $1x10^{-7}$ Nm, and that for the 45 μm jet is $1.7x10^{-8}$ Nm. The additional energy associated with increased flowrate is responsible for the observed extensive ballistic damage with the larger nozzles.

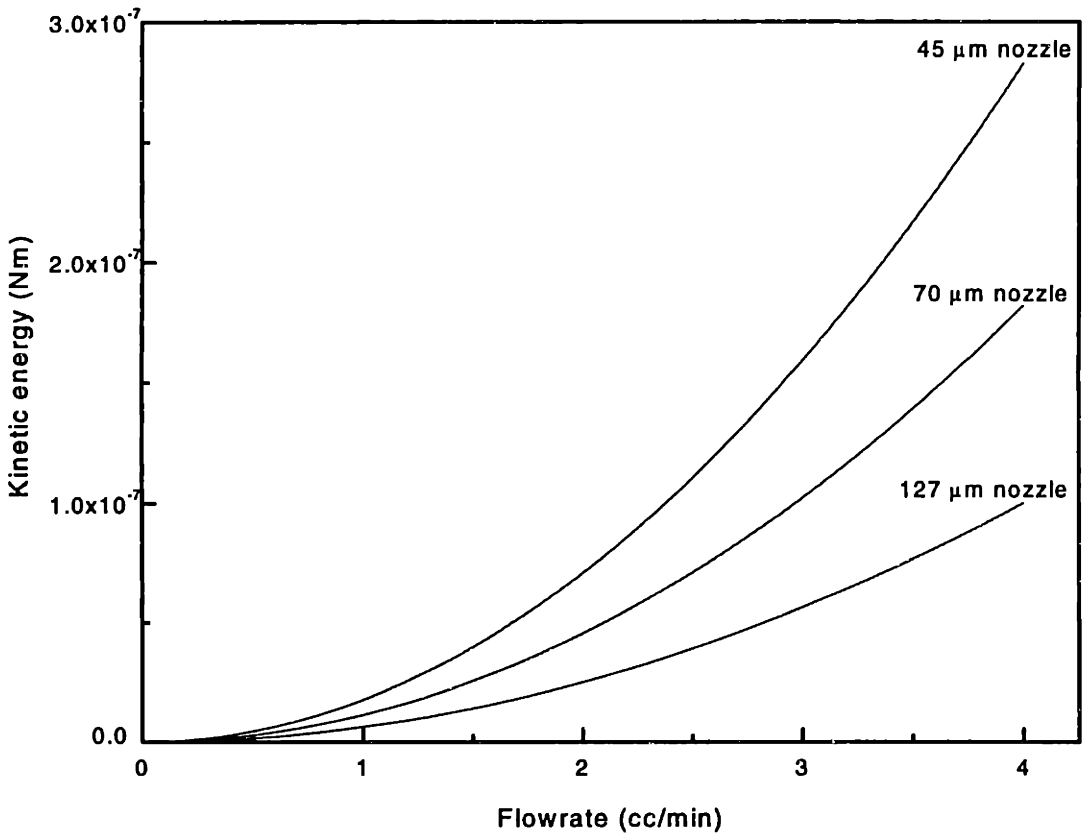

Figure 2.10: Kinetic energy for CJ jets at natural breakoff

The choice of droplet velocity is based on several considerations. The demand for higher manufacturing throughput requires greater binder flow rate. The demand for better print resolution, however, requires the use of finer particles and smaller droplets. Droplet velocity must be sufficiently high to meet both competing requirements, since droplet velocity is determined by volumetric flow rate and orifice dimensions. Another benefit associated with increased droplet velocity is improved jet stability. Improved jet stability is particularly important during 3D Printing™ of polymers, where the use of organic solvents mandates adequate ventilation. The main drawback of increased droplet velocity is the formation of deep craters and deterioration of powder bed uniformity. The energy expended in crater formation results in deceleration of the binder droplets.

It should be noted that DOD-derived droplets produce significantly less ballistic damages. The kinetic energy of DOD droplets traveling at typical speed[29] of 5 m/sec is 1.4×10^{-9} Nm, which is two orders of magnitude less than that of typical CJ droplets.

Crater dimensions have been reported by several investigators. Fan reported that when a 90 μm water droplet impacts alumina powder (10-25 μm particle size, 40% packing density) at 10 m/s, the resultant crater is approximately 300 μm in diameter, and 200 μm in depth. Fan reported the time scale for crater formation to be less than 1 msec.[28] Bredt reported that the typical crater depth for alumina particles is approximately 500 μm.[27] Giritlioglu reported crater dimensions in spray dried alumina powder foundation layers to range from 500 μm to 800 μm in depth, and about 1000 μm in width[30]. Similar crater dimensions are commonly observed in polymeric powder beds due to lower density and low cohesive strength. Detrimental ballistic impact damage can also be produced at lower droplet velocity if the droplet size is too large. This is the case when larger nozzles are used to achieve reliable jetting of viscous polymeric solutions. Craters become progressively shallower and narrower with increased impact resistance, which can be achieved by decreasing layer thickness, or by printing onto regions where foundation layer below has been printed. Fan showed that the bearing capacity of a powder bed scales linearly with the depth of the powder layer.[28] It has been demonstrated that cratering can be virtually eliminated by printing into a highly cohesive powder bed.

Cohesive powder beds can be achieved by tape casting, spraying the powder as a slurry, or jetting the powder as a slurry dispersion through a separate nozzle.[31]

Two other important events occur during ballistic impact, besides cater formation. They are best illustrated by comparing droplet impact onto paper, versus that into loose powder. The paper is analogous to a rigid powder bed with low powder bed compliance. When a droplet impacts the hard paper surface, the droplet itself undergoes extensive deformation. The droplet diameter may increase to 4 times the original size. The paper, in contrast, suffers little distortion. This sudden impact results in rapid deceleration of the droplet, usually within a microsecond.[28] The flattened droplet then begins to penetrate the paper by capillary flow. The paper industry manipulates the capillary characteristics to control printing resolution. The key point here, with paper printing, is that ballistic impact and droplet penetration are separate events.

When a droplet impacts the surface of a loose powder bed, both the droplet and the powder bed deform. The droplet deforms up to 1.2 times in diameter, at the same time that crater formation commences.[28] As the crater develops, the liquid binder penetrates the inter-particle void space, resulting in mixing of the liquid and solid phases. This inertial mixing results in mass accumulation for the droplet, leading to deceleration and arrest. Crater formation is complete at this point, and the initial powder-binder mixture is ready for the next stage. The key point here is that ballistic impact and droplet penetration are inseparable events for loose powder impact. Table 2.1 summarizes the differences between the two substrates.

	Rigid bed	Loose bed
Bed distortion	none	extensive
Deceleration energy	droplet deformation	mass accumulation
Deceleration time	10^{-6} s	10^{-3} s
Droplet diameter	~ 4x	~ 1.2x
Initial infiltration	capillary	inertial

Table 2.1: Effects of bed compliance on ballistic impact

2.3.2 Stage 2 - Imbibition and drainage

Stage 2 commences as the liquid from the initial powder-binder mixture migrates away from the saturated core, and drains into surrounding pores. Smaller pores tend to exert larger capillary forces for the binder, and larger pores tend to offer less resistance against binder drainage. The problem of liquid transport through a porous capillary has been studied by numerous investigators.[35-40]

Capillary migration in alumina systems can be arrested by one of two ways. The liquid migration may cease when binder gelation causes the binder-powder mix to solidify. The time scale for gelation (10^{-1} to 10^{2} sec) for colloidal silica binder is, for example, much longer than the time scale for its capillary equilibrium (10^{-2} to 10^{-1}sec) in alumina powder.[27] The observed feature size is also too small for the gelation effect to be responsible for migration arrest. A second cause for migration arrest involves the establishment of pressure equilibrium between the moist, printed region and the surrounding dry, un-printed porous powder. The feature size of the printed primitive in conventional materials systems is reportedly governed by the capillary characteristics of the powder bed.

A hysteretic relationship exists between capillary pressure and binder saturation, depending on flow direction (Figure 2.11). For a given binder saturation, capillary pressure is higher during drainage than imbibition. Capillary pressure equilibrium exists when drainage pressure in more saturated regions equal imbibition pressure in less saturated regions. Capillary pressure equilibrium is also likely to be responsible for migration arrest during dissolution-re-precipitation. Figure 2.11 shows that for liquid drainage from a packed bed, there is a irreducible saturation of discontinuous, immobile liquid which can only be removed by evaporation. This irreducible saturation is not found in capillary tubes, which drain completely.[32]

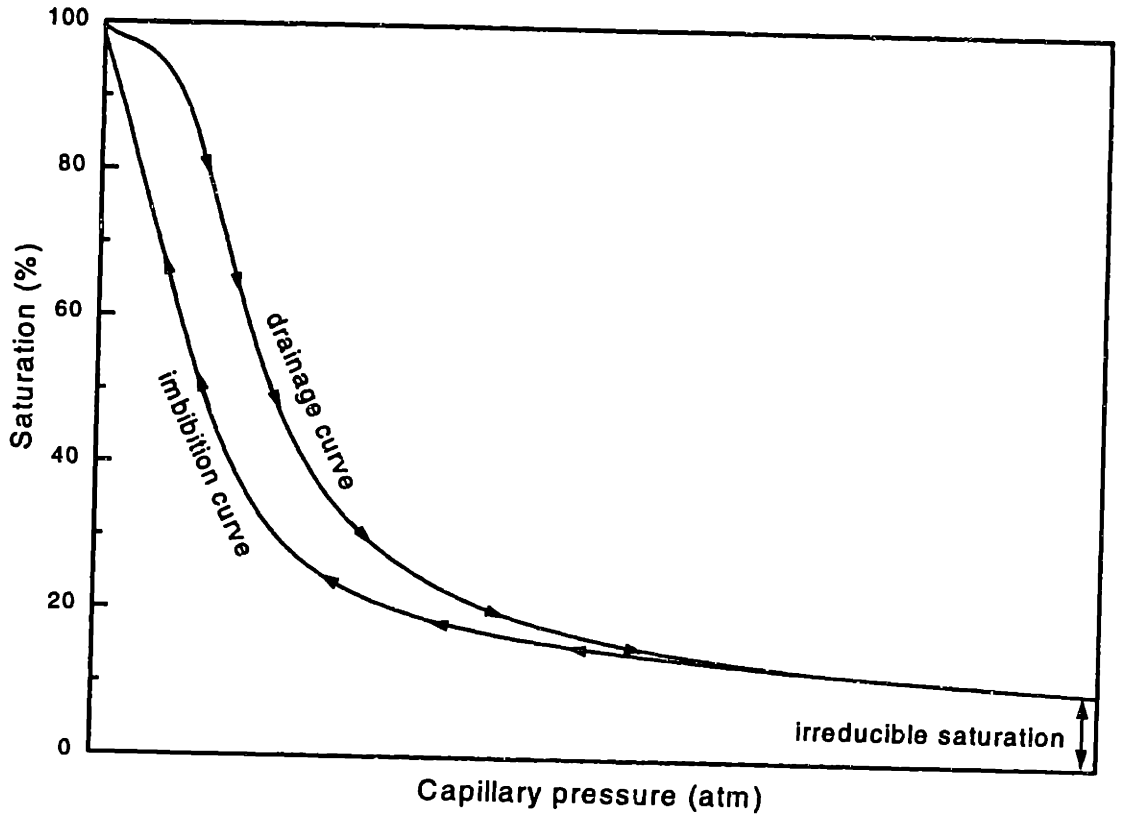

Figure 2.11: Effect of capillary hysteresis on drainage and imbibition curves[32]

2.3.3 Stage 3 - Dissolution/swelling

Powder binding involves the momentary dissolution/swelling of neighboring loose particles after they are wetted with solvent. The particles undergo size and morphological changes. The extent of these changes depends on degree of dissolution/swelling, which in turn depends on the rate of polymer dissolution and rate of solvent evaporation. Joining of neighboring particles occurs if the time scale for polymer dissolution is shorter than that for solvent evaporation. The dissolution rate of the powder depends on the aggressiveness of the solvent for the particular polymer, and powder particle size. Non-aggressive solvents can also result in swelling of polymer particles. If the time-scale for dissolution and swelling is significantly longer than the time scale binder evaporation, no 3DP primitives can form. Particle dissolution is studied in the next chapter.

2.3.4 Stage 4 - Re-precipitation/drying

The subsequent stage involves the re-precipitation of the solvent-polymer gel-mix due to solvent evaporation. The evaporation kinetics depends on the solvent vapor pressure, gas transport through porous media, and the equilibrium pressure of the operational area. Another major distinction between the adhesion and dissolution-re-precipitation models is that the final primitive size in the latter model may be larger than that predicted by considering only liquid transport. Solvent vapor diffusing away from the printed region may also possess adequate solvency to bind (or swell) un-printed powder particles together, effectively increasing the feature size. This undesirable phenomenon can be extensive since it may continue to occur for days after printing, if the printed structures are left in the powder bed. Solvent evaporation is studied in Chapter 5.

2.4 TIME AND LENGTH SCALE FOR FEATURE FORMATION

The four physical and chemical processes described in the previous section are distinct events, but they overlap each other in time. Evaporation, for example, begins as soon as droplets form outside the nozzle, and continues to occur throughout the 4 binding stages. The actual time scale for each stage is very important in understanding feature formation. The relative time scale between binder imbibition and particle dissolution are critical in determining relative parameters which govern feature size. Binder viscosity is expected to increase significantly during binder migration if the time scale for particle dissolution is short relative to binder imbibition and drainage. Binder viscosity can be assumed to be constant during binder imbibition, however, if the opposite is true. The relative time scale between solvent evaporation and particle dissolution can affect microstructure formation. If the time scale for typical solvent evaporation is significantly shorter than that for particle dissolution, poor particle binding is achieved. It is critical to determine the time scale during which these events occur.

2.4.1 Ballistic impact

The deceleration time for 3DP™ droplets after powder bed impact has been estimated by Bredt to be 10^{-4} sec, based on an initial droplet velocity of 10 m/sec and a typical cratering depth of 500 μm.[27] Fan studied droplet ballistic impact with high speed

photography and reported that the time scale for crater formation was less than 1 msec when a 90 μm water droplet impacts alumina powder (10-25 μm particle size, 40% packing density) at 10 m/s. The resultant crater was approximately 300 μm in diameter, and 200 μm in depth.[28] Similar time-scales of ballistic impact and binder migration for polymeric systems are expected, even though these estimates were derived for ceramic systems.

One contribution to the arrest of ballistic impact is momentum transfer from the high speed droplet for crater development. Interparticle friction must also be overcome during penetration. Penetration resistance of soil was reported to be an exponential function of the penetration depth ($q \propto z^n$). Fan showed that $n \sim 0.63$ for the intrusion of a 1 mm diameter pin into alumina powder. [28] It should be noted that the crater depths listed above were obtained by printing into fresh powder beds, which are strictly valid only for the foundation layer during 3DP™. The crater depth for ballistic impact is expected to be less for the subsequent layers, since the typical layer thickness is only approximately 150 μm. The time scale for ballistic impact should also be shorter for the non-foundation layers.

2.4.2 Imbibition/drainage

Bredt used three approaches to estimate the time scale of binder migration into surrounding pores. The migration time was approximated to be about 2 msec using the Washburn infiltration model, approximately 5 msec based on pressure equilibration calculations,[27] and roughly 90 msec with Chang's modified Richards infiltration model.[33] Capillary migration during dissolution/re-precipitation can be arrested according to one of two ways. Binder migration may cease when the solvent-polymer mix becomes more polymer-rich due to solvent evaporation, if the time scale for evaporation is shorter than the that for capillary migration. A more probable cause for migration arrest involves the establishment of pressure equilibrium between the moist, printed region and the surrounding dry, un-printed porous powder. An analytical relationship between polymer line primitive diameter and printing parameters has been proposed based on available binder and accessible pore volume.[34] The model does not consider ballistic impact and

materials-specific properties such as binder viscosity. Primitive size prediction may be better achieved by considering the initial saturated core volume due to inertial mixing during ballistic impact, and then calculating the extent of binder migration through the porous media.

Many theoretical models treat liquid penetration into porous medium as liquid transport through a system of capillaries. The Lucas-Washburn equation, which predicts a $t^{1/2}$ dependence on the penetration distance, is commonly used to describe the unidirectional penetration kinetics of a liquid into a horizontal capillary. The Washburn approach is not applicable in 3DP™ because it was derived for liquids undergoing Hagen-Poiseuille flow from an infinite liquid reservoir through an infinite porous media.[35] There is another major difference between capillary transport and porous medium flow. Figure 2.12 illustrates that in capillary transport, the liquid-vapor interface may fluctuate, but does not continually increase. Liquid transport through porous medium involve continual creation of liquid-vapor interface by re-exposing the liquid to vapor inside the porous medium and at its boundaries. Thin porous media, such as paper or textile yarns, may enhance the re-exposure effect by imposing a high surface to volume ratio on the liquid. Thermodynamic analysis and kinetic models have shown that the penetration of a limited amount of liquid into a capillary is different from that of an infinite reservoir. Ink-jet printing, spray painting, and yarn wicking, involve the penetration of finite size liquid reservoir into finite thickness of porous medium. Kinetic studies of penetration into paper supported the capillary models. Thermodynamic analysis by Murmur showed that the finite dimensions of the porous medium and liquid reservoir are important in determining the conditions for penetration and phenomenology.[36]

The binder volume in 3DP™ is finite, typically on the order of 110 nl per centimeter of printed line length under typical printing conditions (binder flow rate = 1 cc/min, printspeed = 150 cm/s). The typical powder bed layer thickness is also finite, ranging from 10 to 200 μm. Several investigators considered the problem of liquid penetration into finite porous media. Marmur extended the Lucas-Washburn approach to consider radial penetration kinetics of a liquid from an infinite liquid reservoir between

two parallel disks. Radial penetration rate was found to be slightly slower than that of unidirectional penetration for the case of infinite liquid reservoir ($R \propto t^{\kappa/2}$, where $\kappa \sim 0.9$).[37] Borhan and Rungta recently reported the penetration rate of various liquids into filter paper, and observed similar time dependence.[38] Experimental data for droplet penetrations into paper, however, suggested much slower radial penetration rate ($R \propto t^{\kappa/2}$, where $\kappa \sim 0.3$).[39,40] This discrepancy suggests that although geometry (radial penetration vs. unidirectional) is partially responsible for decreased penetration rate, another factor must contribute to the large difference in time-dependence.

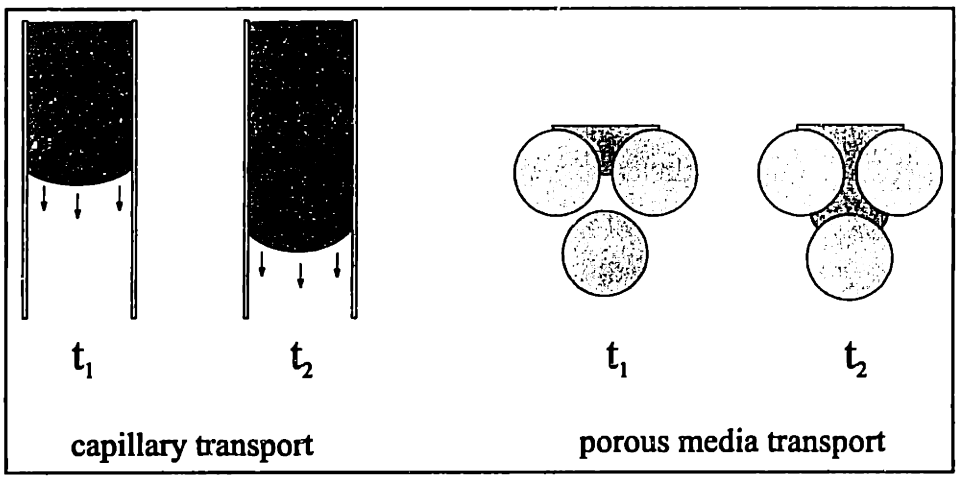

Figure 2.12: Fluctuating liquid-vapor interface in capillary transport (left) vs. increasing interfacial surface area in porous media

The other major difference between capillary transport and porous medium flow is the finiteness of the infiltrating liquid volume. The models presented by Washburn, Marmur, and Borhan are all based on infinite liquid reservoirs. The $R \propto t^{1/6}$ dependence was obtained for droplets, which have finite volume. Marmur considered two limiting regimes to account for the combined effects of geometry (radial spreading) and a shrinking liquid reservoir. In the "no hysteresis" regime, where a constant contact angle exists between droplet and outside disk surface while the basal area of the droplet decreases, penetration rate of a finite droplet was predicted to be faster than that of an infinite liquid reservoir, particularly for higher contact angles. In the "contact angle hysteresis" regime, where the basal area remains constant while the contact angel

decreases during liquid penetration, a slower penetration rate was predicted for the finite droplet. Marmur reasoned that the actual penetration rates fall somewhere between the two limiting cases.[37] Gillespie proposed a two stage penetration model to describe the penetration of low vapor pressure droplets into filter paper.[40] Phase I starts at t=0 and covers the entire period where some portion of the liquid droplet remains above the porous substrate. Phase II commences when all liquid is contained within substrate. Gillespie assumed a constant pressure gradient and derived a $t^{1/6}$ time-dependence from Darcy's law for the ratio of instantaneous stain dimension to initial droplet dimension during phase II radial spreading. The instantaneous stain dimension was determined by high speed photography, and was found to increase with time during radial penetration of the liquid into surrounding substrate. This $t^{1/6}$ time-dependence for spreading factor was confirmed experimentally by syringing drops of undyed liquids onto filter paper strips, and recording the stain size over time.[40] Borhan and Rungta modified Gillespie's expression for the radial penetration distance and obtained similar results.[40] Kissa modified Gillespie's model to predict stain area dependence over time, and also reported $t^{1/6}$ dependence for penetration of alkanes into fabrics. Kissa reasoned that stain area provided more meaningful measurement for penetration rate into anisotropic pore structures found in textile fabrics.[39]

These models are consistent with experimental observations that radial penetration of finite droplets into finite porous media is much slower than Washburn kinetics. They were, however, derived for infiltration of single droplets into a completely porous substrate. It should be emphasized that the total surface area for binder drainage depends the spatial position of the feature within the 3DP™ powder bed. Binder from the saturated core of first printed line has three surfaces for draining (Figure 2.13a). The adjacent line has only two surfaces for drainage (Figure 2.13b). A similar line on the layer above has only one surface for drainage (Figure 2.13c). The third case is representative of most the actual features in 3DP™. Efforts to model binder migration should consider the initial saturated core as a cylindrical mixture of binder and powder, with a one dimensional binder flux.

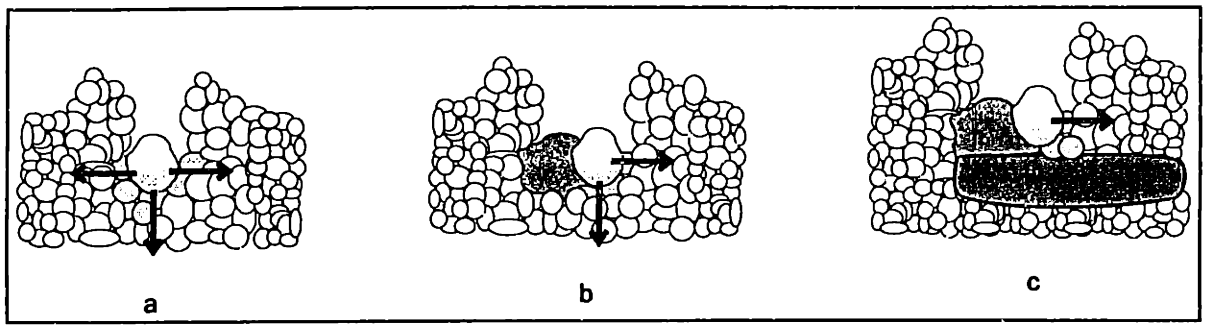

Figure 2.13: Effect of feature position on binder drainage

Other important assumptions for the above models are that the liquid is not evaporating significantly during infiltration, and that the liquid do not react with the porous substrate materials. Neither assumptions are true for the dissolution/re-precipitation mechanism, where volatile organic solvents are used to dissolve polymeric particles. These assumptions may be justified, however, if the time scale for binder infiltration is much shorter than that for particle dissolution and evaporation. A time-dependent viscosity term would need to be introduced to the appropriate model, if the time scale for binder migration is similar to that of dissolution and evaporation. Increasing binder viscosity is expected as the polymer-solvent mixture becomes more polymer-rich. The rate of viscosity increase is then a function of the dissolution kinetics. Rapid viscosity build-up should result in reduced capillary migration if the dissolution rate is very high. Solvent evaporation is also expected to increase the viscosity of the polymer-solvent mixture.

2.4.3 Dissolution/swelling

The importance of the dissolution time scale was described above. Particle dissolution is expected to have negligible effects on binder viscosity during binder transport if the timescale for binder migration is much shorter than the timescale for particle dissolution. Particle dissolution and swelling have not been studied in 3DP™, and will be presented in chapter 3.

2.4.4 Re-precipitation

Inadequate particle dissolution is expected if the time scale for solvent evaporation is much shorter than that for particle dissolution. Poor feature size would be expected if the evaporation rate is too slow. Print resolution may be increased by addition of an extra drying step between layers, but decreased 3DP™ build rate is expected. Re-precipitation kinetics of the solvent-polymer gel mixture depends on evaporation kinetics of the solvent from the powder bed, as well as the solvent diffusivity out of the bulk particles. Solvent evaporation kinetics are studied in chapter 4.

3. Particle Dissolution

3.1 BACKGROUND

The predominant particle-solvent interaction during 3D Printing™ of bioerodable polymers is dissolution/re-precipitation of loose particles by the printed solvent. The relative rates of dissolution and evaporation are important since they represent competing parameters which affect microstructure formation during 3D Printing™. The problem of polymer dissolution has been studied for numerous industrial applications such as microlithography,[41,42] waste water treatment,[43] polymer recycling,[44,45] and polymer modification reactions.[46,47] Dissolution of bioerodable polymers is also relevant in biomedical applications such as drug delivery[48,49,50] and tissue engineering.[51] Polymer dissolution have been studied, but most reports focus on the dissolution of thin polymeric films. There is no investigation on the actual dissolution of bioerodable particles. Section 3.2 describes an experimental set-up which facilitates direct observation of particle dissolution. The subsequent sections summarize the experimental observations of various polymeric particles undergoing dissolution. Two mechanisms of particle dissolution were observed. Some polymer-solvent combinations required a minimim dissolution time, which was found to scale with polymer molecular weight. The implications of these findings on 3D Printing™ of bioerodable particles are discussed.

3.2 MATERIALS AND METHODS

A dissolution cell was designed and constructed to contain the particles to be dissolved, allow solvent flow, and permit direct microscopic observation. The dissolution cell must allow simple and reproducible sample mounting, and be small enough to fit between the microscope eyepiece and sample stage. The actual dissolution cell used for these experiment is shown in Figure 3.1. The holder assembly, which contains the main housing, top metal block, and 3 tightening screws, was fabricated by modifying a commercial FTIR sample cell (Beckman Quick-mount Multicell, Columbia, OH). Two 1 mm-thick glass plate (1.5cm x 3cm) were cut from a microscope slide to fit into the main housing. One glass plate is used to form the "bottom" of the dissolution

cell. 2 holes (2 mm diameter) were drilled into the second glass plate to form the "top" boundary of the dissolution cell. The holes were positioned to correspond with the solvent inlet and outlet ports of the metal block above. A thin Teflon spacer is placed between the two 1 mm-thick glass plates to control the inter-plate distance and maintain the seal for the dissolution cell. The various components of the dissolution cell are depicted in Figure 3.2.

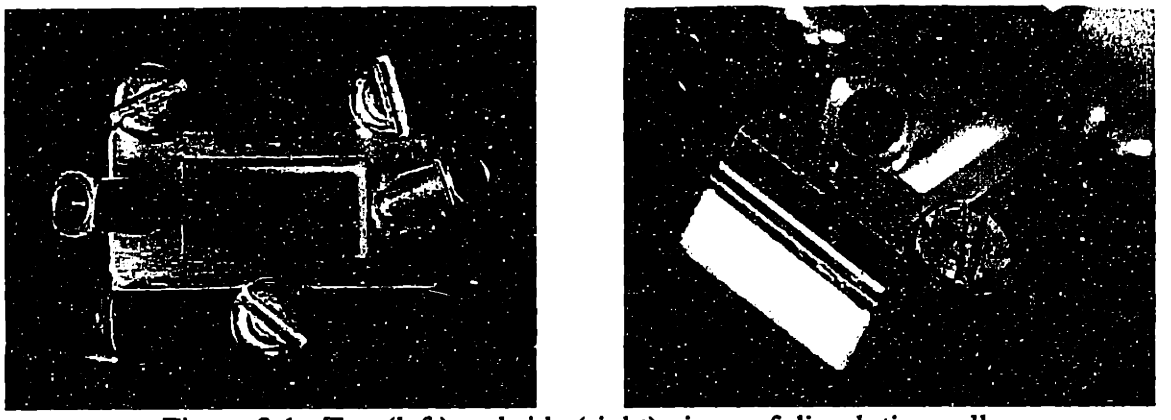

Figure 3.1: Top (left) and side (right) views of dissolution cell

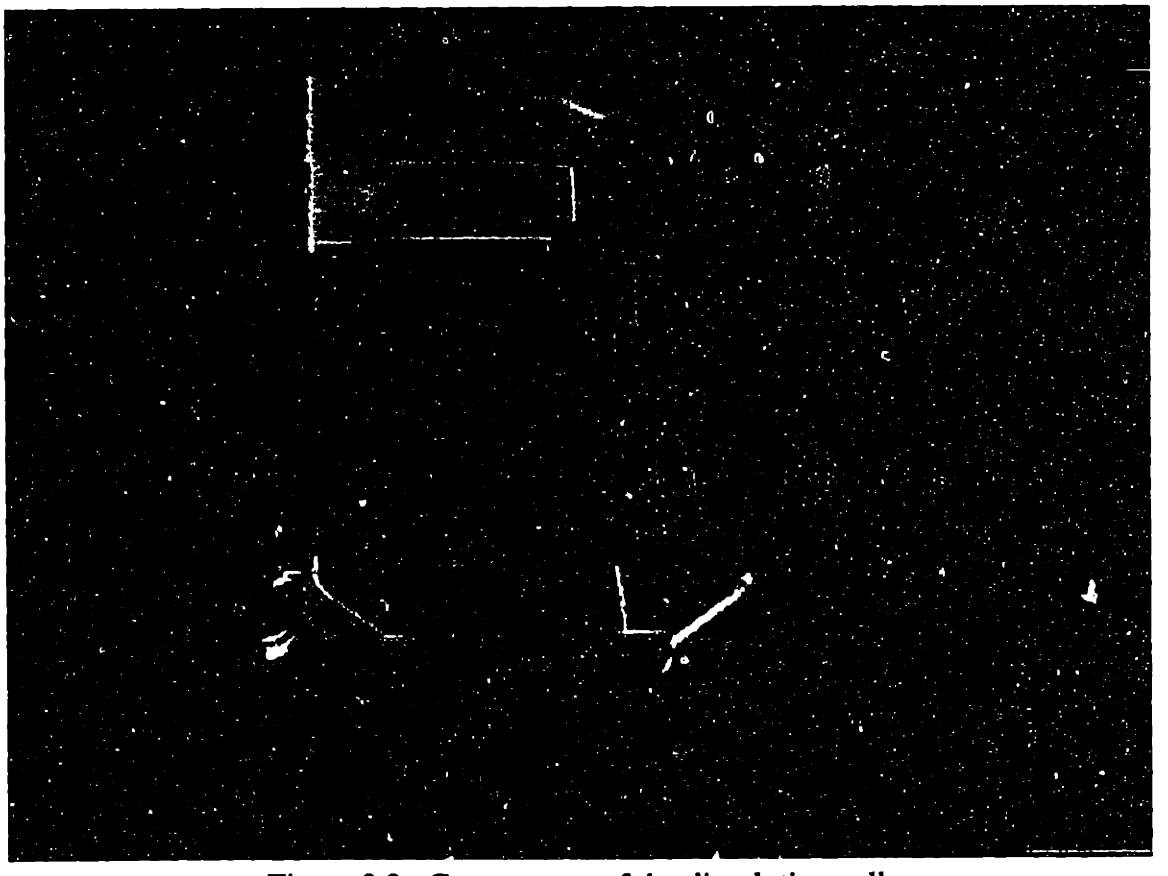

Figure 3.2: Components of the dissolution cell

Polymeric particles were placed in between the glass plates within the confines of the thin Teflon spacer. The 3 screws shown in Figure 3.1 were tightened slightly in order to secure the various components together, and prevent leakage during the experiment. Excessive tightening could result in cracking and fracturing of the top and/or bottom glass plates. Cracking of the top glass plate was prevented by cushioning a thin Teflon spacer between the glass plate and top metal block. Another thin Teflon spacer was placed between the bottom glass plate and the Teflon block for similar purposes. The entire assembly was placed under an objective lens of an optical microscope (Olympus BH-2, Japan) outfitted with a color CCD video camera (Toshiba Image Master SIK-636S, Japan). A monochromatic light source (512 nm wafer QC lamp, American Scientific Products, McGaw Park, IL) was projected at a mirror which directs the monochromatic light at the dissolution cell at approximately 20° angle. The entire experimental set-up is diagrammed in Figure 3.3. At time zero, solvent is introduced at 0.1 cc/min into the dissolution cell through the metal block in-port. Particle dissolution was observed on a 20" monitor (Toshiba CM1900A, Japan) in real time, and captured on a video cassette recorder (JVC BR-S600U, Japan) at 30 frames/sec for later analyses.

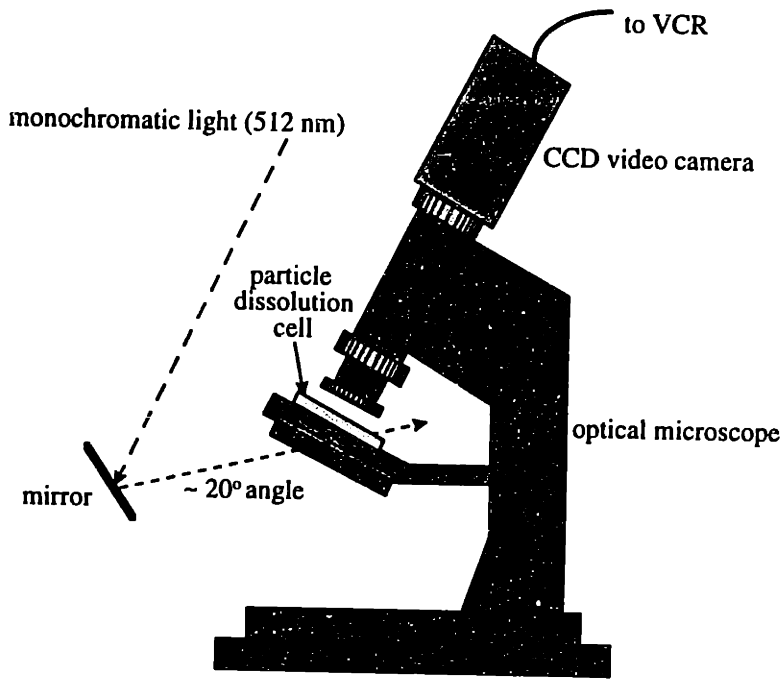

Figure 3.3: Experimental set-up for observing polymer dissolution

3.3 OBSERVATIONS

Two general types of dissolution behavior were observed. Gel layer formation was seen in many, but not all, of the polymer-solvent systems used in 3DP™. Crack formation, propagation, and particle fragmentation was observed for other polymer-solvent systems. The actual observations for both dissolution behavior are detailed in this section. In all cases, the solvent front motion is usually completed in less than 33 msec. The time required for the solvent front to reach the particles may be much less, since 33 msec only represents the time between successive video frames. Negligible dissolution was observed during the initial few frames (~100 msec). A time scale on the order of 10^0-10^2 seconds was required for complete particle dissolution, depending on the polymer-solvent system of interest.

3.3.1 Complete dissolution with gel formation

Highly soluble particles-solvent systems tend to exhibit gel formation during dissolution. The interaction begins with solvent penetration into the polymer particle. The external polymer layer undergoes rapid transformation from the solid state to the gel state when a critical solvent concentration in the polymer is reached. The gel state is characterized as the swollen mass of entangled polymer chains. The diagram in Figure 3.4 describes this mode of particle dissolution. Two distinct interfaces are identifiable during the initial stages of dissolution. An internal solid-gel interface divides the inner solid (low solvent volume fraction) and gel layer. An external gel-solvent interface separates the gel layer from the surrounding solvent (low polymer volume fraction).

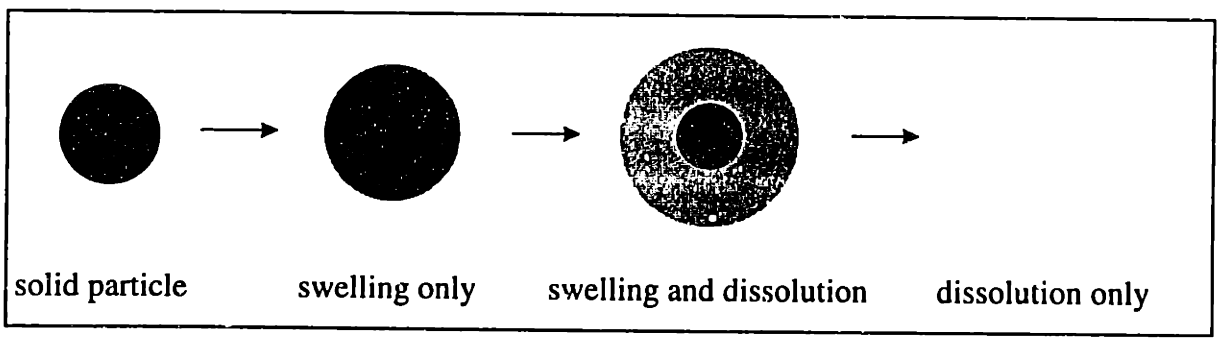

Figure 3.4: 4 stages of the dissolution process (with gel formation)

Chloroform is one of the most common solvents used in 3DP™ for the bioerodable polymers. Polymers such as PLGA (85:15 108,000), PLGA (65:35 53,000), PLLA (<130,000) and PCL (30,000), etc., are known to be highly soluble in chloroform. Dissolution of a PCL (30,000) particle in chloroform is shown in Figure 3.5. A gel layer can be observed shortly after solvent flow, and grows to appreciable size after only 1 second. The solid-gel interface moves radially inwards. The gel-solvent interface expands to almost twice the initial particle diameter after only 5 seconds, while the solid-gel interface continues to shrink. The gel-solvent interface remains visible after 15 seconds, beyond which time the solid-gel interface converges to the center of the particle. No solid polymer remains at that point.

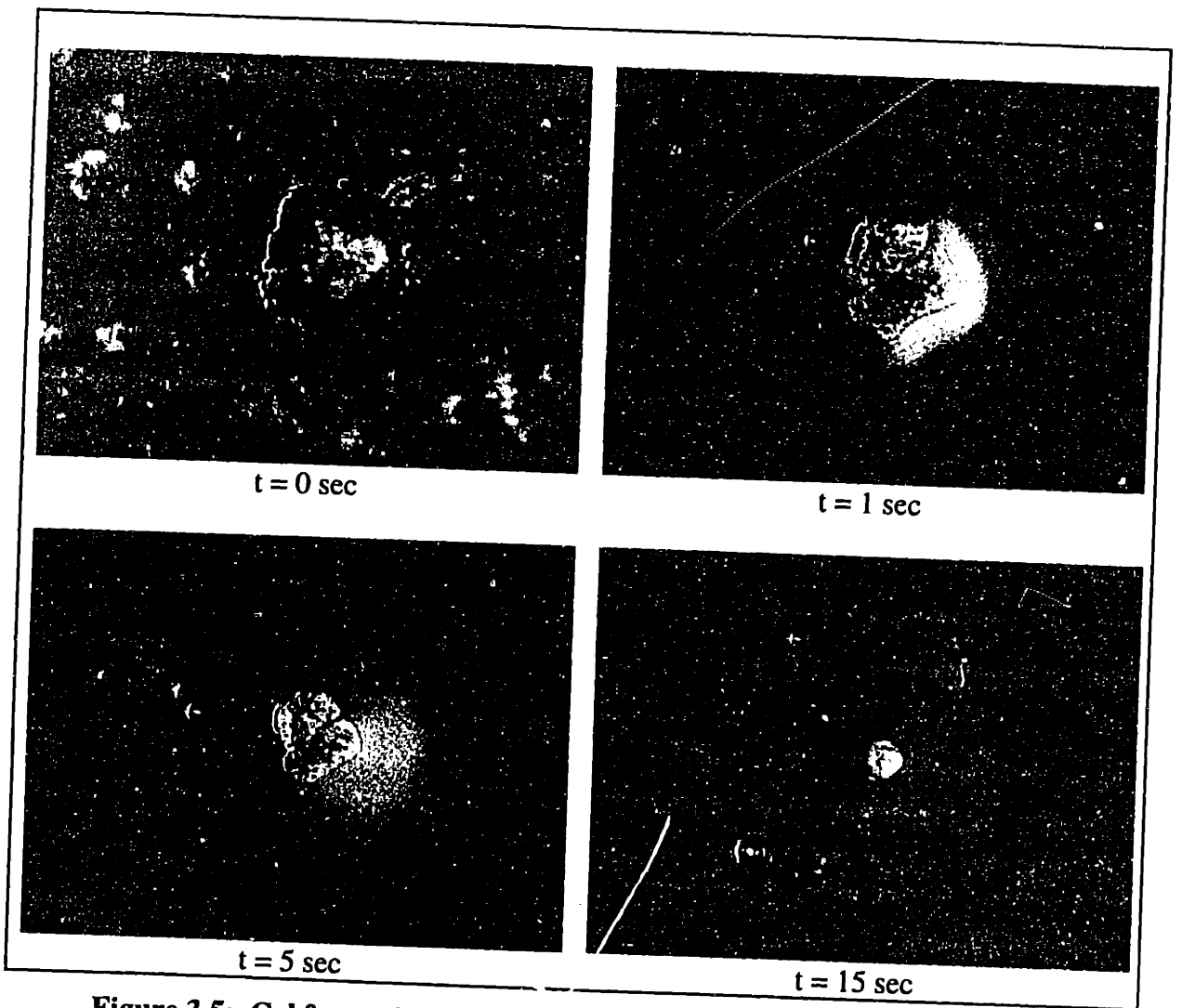

Figure 3.5: Gel formation during dissolution (PCL 30,000 in chloroform)

Positions of the two moving interfaces during dissolution of six PLGA (85:15 108,000) particles in chloroform are plotted versus time in Figure 3.6. The solid-gel interface moves toward the center of the particle with time, and disappears when the last solid fraction becomes swollen. The solid-gel interfaces of these six PLGA particles vanished after 15 seconds. The external gel-solvent interface moves radially away from the center during the first second, and then levels off between t=1 sec and t=2 sec. The gel-solvent interfaces becomes indistinguishable from the surrounding solvent after 2 seconds. The distance between the two interfaces is the gel layer thickness. The gel layer thickness increases rapidly during the first second, then expands slowly as the gel-solvent interface levels off, and the solid-gel interface continue to shrink. The gel layer becomes indiscernible when the gel-solvent interfaces becomes indistinguishable.

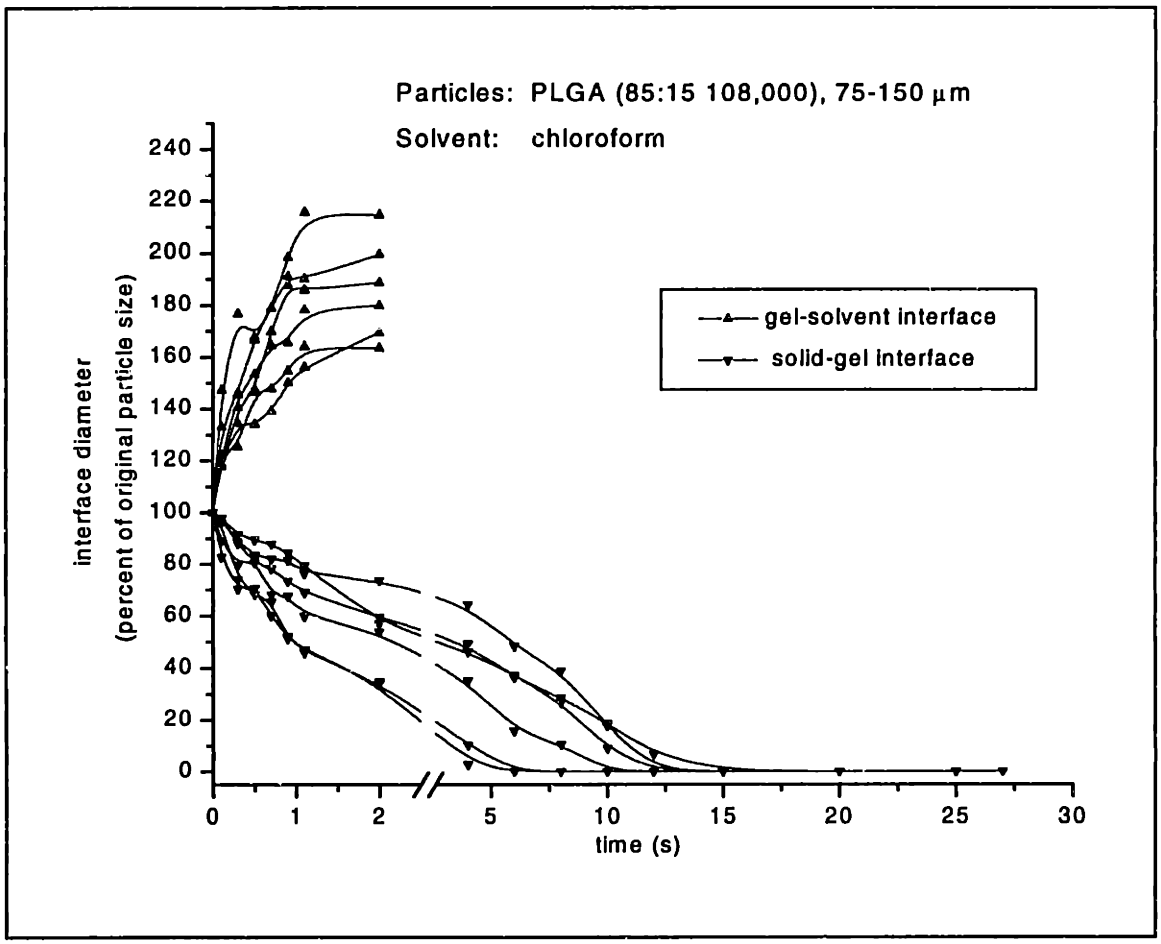

Figure 3.6: Positions of moving interfaces during dissolution (with gel formation)

One interesting finding with polymer-solvent systems which dissolve with gel formation is the existence of a "minimal" dissolution time and an "optimal" particle size". The dissolution time of fifty PLGA (85:15 108,000) particles in chloroform is plotted against their initial particle dimensions, which are idealized for spherical particles in Figure 3.7. Two dissolution regimes can be observed, suggesting a change in controlling mechanism. In the first regime, the dissolution time of larger particles decreases with decreasing particle size. In the second regime, the dissolution time becomes independent of particle dimension for particles below 75 μm. This critical dissolution time (t_{min}=1.25 sec) may represent the "minimal" time required for the dissolution of small PLGA (85:15 108,000) particles.

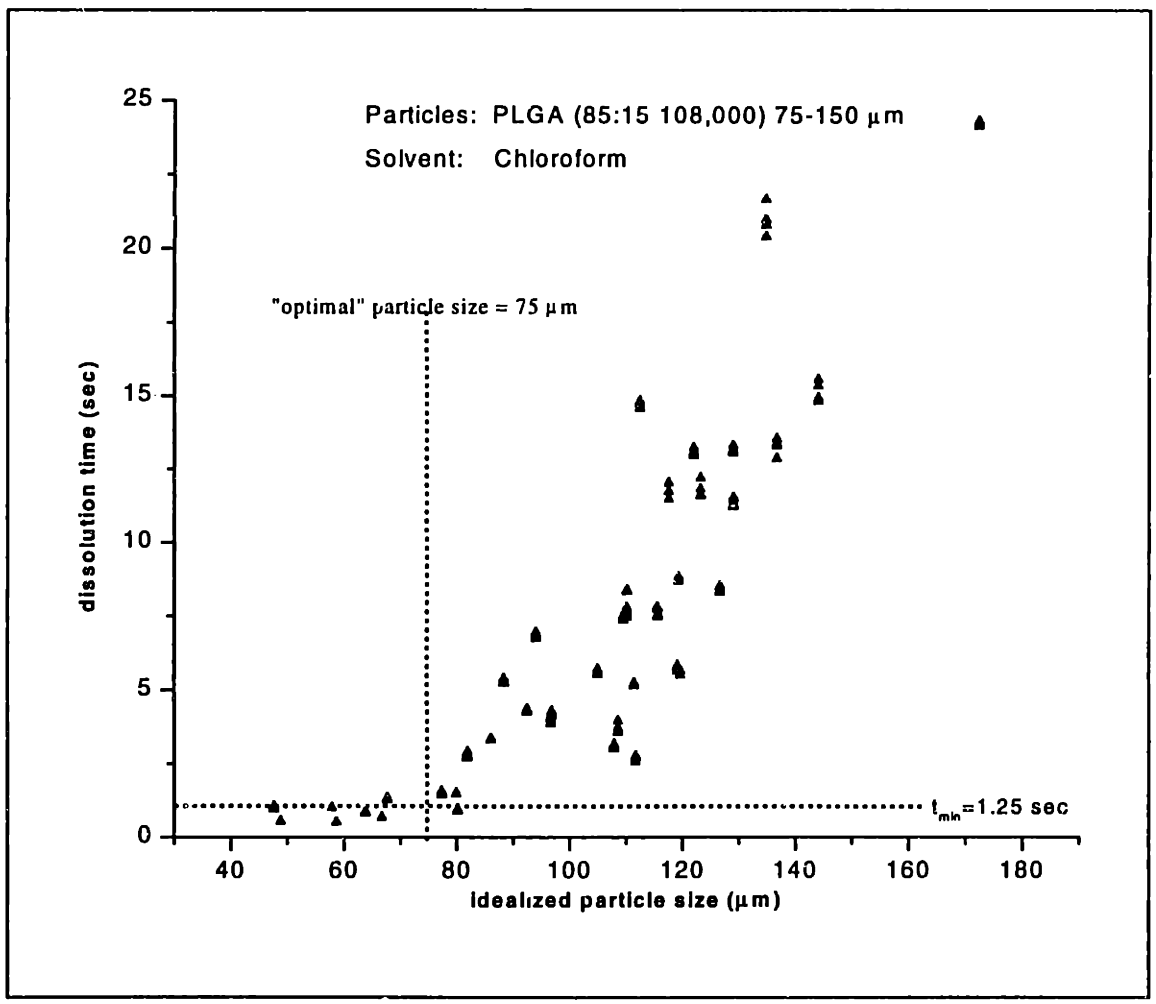

Figure 3.7: Dissolution time vs. particle size (PLGA 85:15 108,000 in chloroform)

3.3.2 Partial dissolution with gel formation

Figure 3.8 shows the dissolution of PLGA (85:15 108,000) particles in acetone. This polymer-solvent combination also dissolves with gel formation. Many PLGA (85:15 108,000) particles dissolved completely in acetone, but some particles did not completely dissolve, even after 5 minutes. At t=0.5 sec (Figure 3.8), the particles appear to be dissolving similar to those in Figure 3.5, with two distinct interfaces. At t=5 sec (Figure 3.8) the solid-gel interface of many particles vanished, but the gel-solvent interface is still distinguishable. Some particles (arrow), or portions of some particles, remained un-dissolved. At t=30 sec (Figure 3.8), the gel-solvent interface of the dissolving particles vanished, but the un-dissolved regions remained. These fractions remained un-dissolved after 5 minutes. The insoluble regions may be blocky domains or crystalline portions of the PLGA particles.

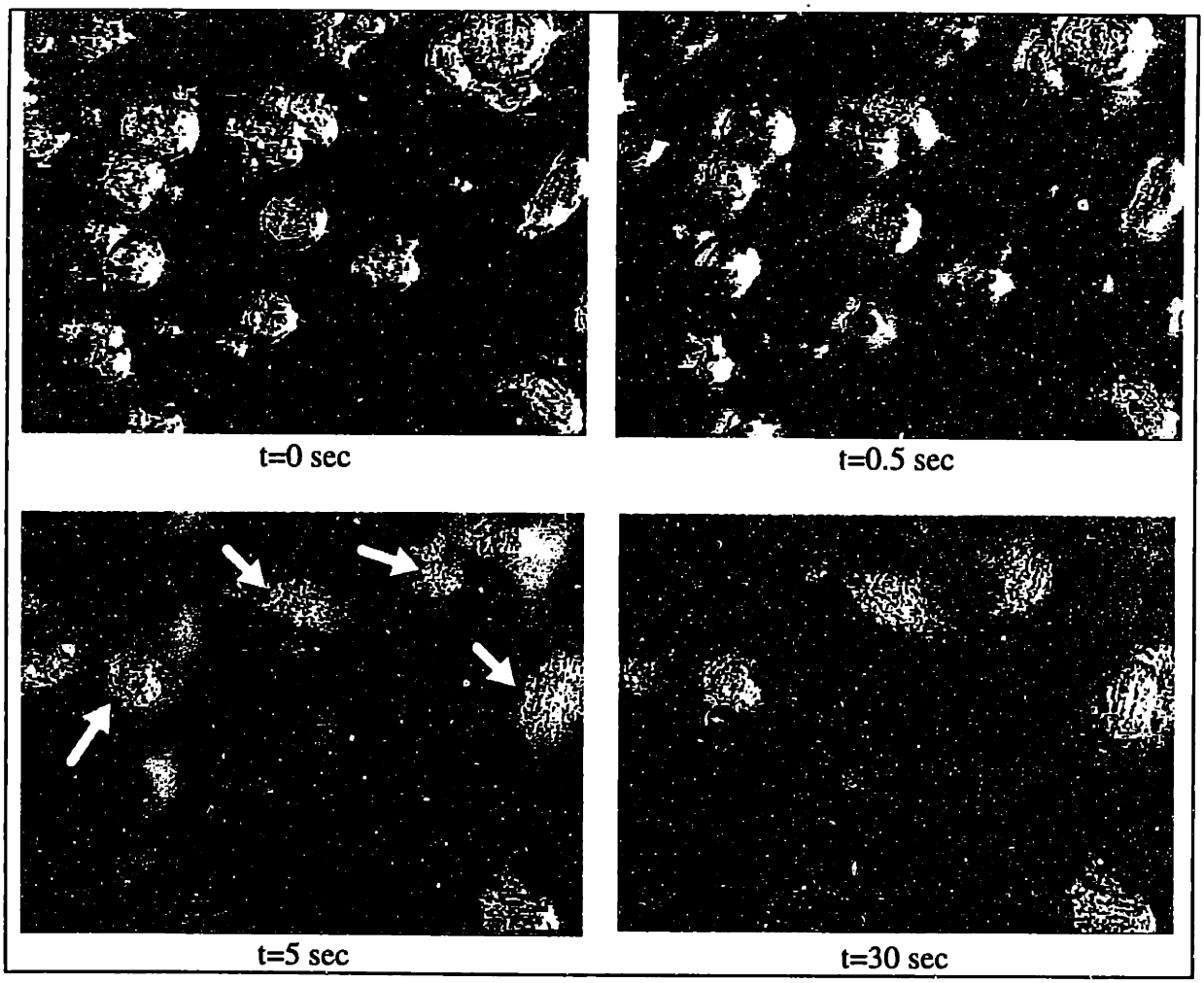

Figure 3.8: Incomplete dissolution (PLGA 85:15 108,000 in acetone)

The dissolution time of twenty-seven *dissolving* PLGA (85:15 108,000) particles in acetone is plotted against their initial particle dimensions, which are idealized for spherical particles in Figure 3.9. The plot is very similar to that in Figure 3.7. Two dissolution regimes are also observed for these *dissolving* particles. The dissolution time appears to become independent of particle dimension for particles below 60 μm. This is slightly smaller than that obtained for PLGA (85:15 108,000) particles in chloroform. The "minimal" dissolution time (t_{min}=2.5 sec) in acetone is also slightly longer than in chloroform. It must be emphasized that Figure 3.9 does not completely represent all PLGA (85:15 108,000) particles in acetone, since some particles do not dissolve completely.

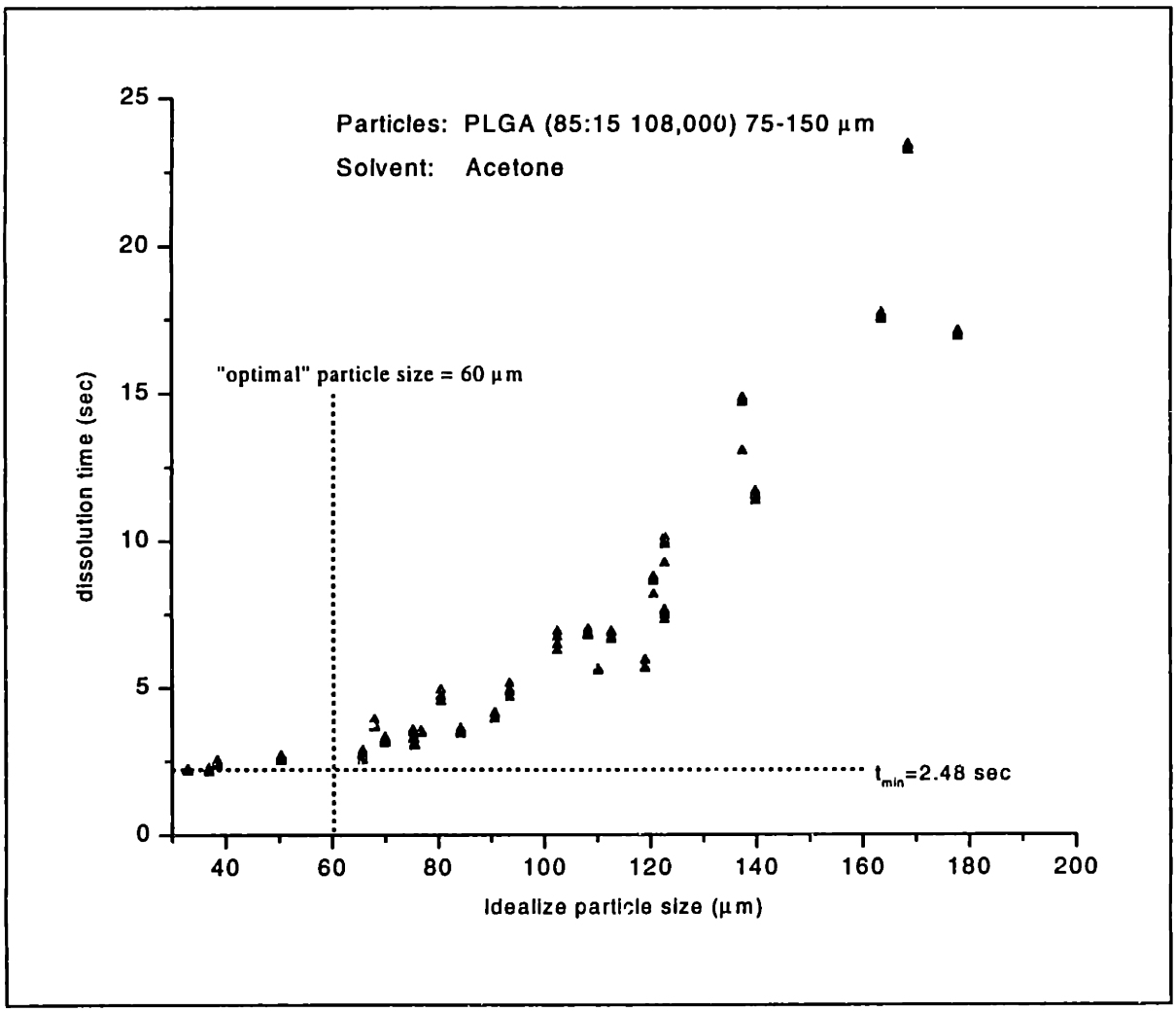

Figure 3.9: Dissolution time vs. particle size (PLGA 85:15 108,000 in acetone)

Some particles are only slightly soluble, even in chloroform. The dissolution of PLLA (301,000) particles in chloroform is shown in Figure 3.10. It can be seen that although smaller particles dissolved completely within seconds, some portions of the larger particles remained un-dissolved even after 150 seconds. Dissolution of the similar PLLA particles in acetone was also observed to be negligible (Figure 3.11).

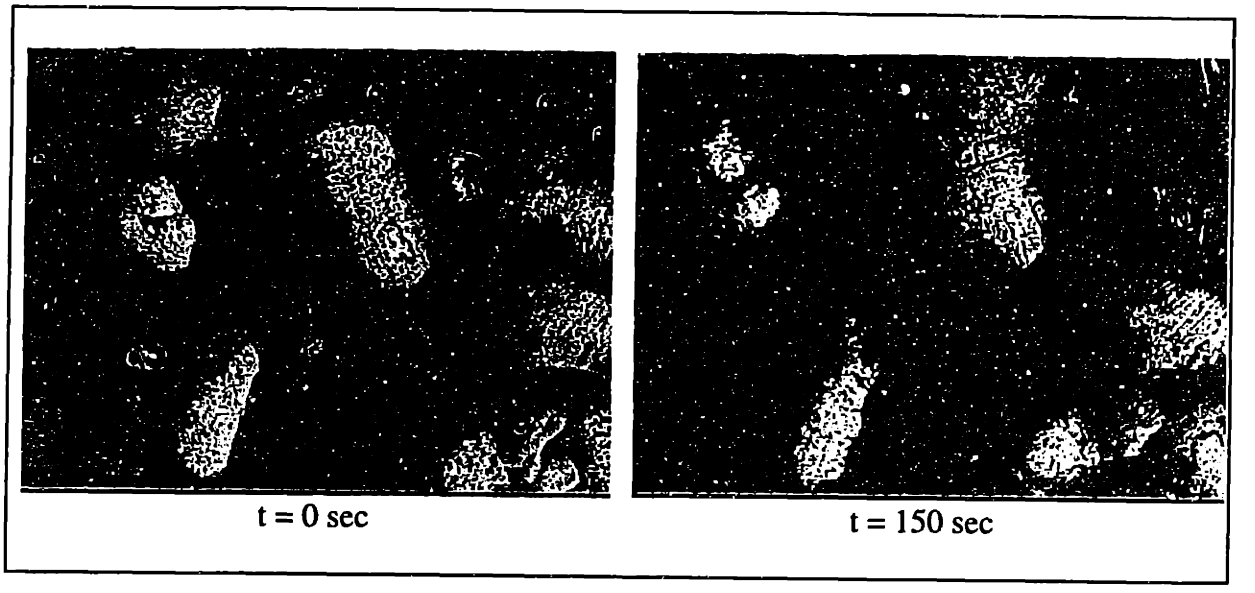

Figure 3.10: Incomplete dissolution (PLLA 301,000 in chloroform)

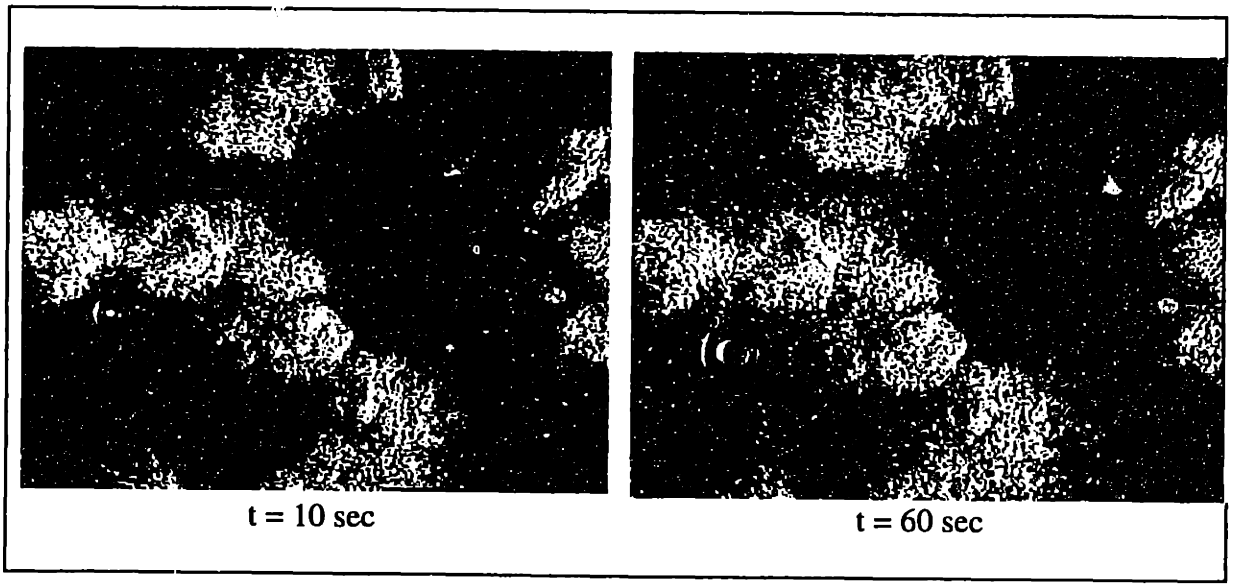

Figure 3.11: Incomplete dissolution (PLLA 301,000 in in acetone)

The minimum dissolution time and optimal particle size for various polymers in chloroform and acetone are summarized in Table 3.1 below. It should be emphasized that the data for PLGA (85:15 108,000)/acetone and PLLA (301,000)/chloroform only applies to those particles which dissolved *completely*.

Polymer	Solvent	minimum time (s)	optimal size (μm)
PLGA (85:15 108,000)	chloroform	1.25	75
PLGA (85:15 108,000)	acetone	2.48	60
PLLA (53,000)	chloroform	0.2	95
PLLA (132,000)	chloroform	2.1	60
PLLA (301,000)	chloroform	18.1	30

Table 3.1: Minimum dissolution time and optimal particle size for various polymers

3.3.3 Dissolution by crack propagation and no gel formation

Not all polymers-solvent systems dissolve according to Figure 3.4. Powder-solvent systems which do not dissolve readily, such as poly-ε-caprolactone (PCL) and acetone, exhibit negligible gel layer formation during dissolution. Crazing, cracking, and fragmentation of the polymer particle characterize this type of dissolution. The diagram in Figure 3.12 describes this mode of particle dissolution.

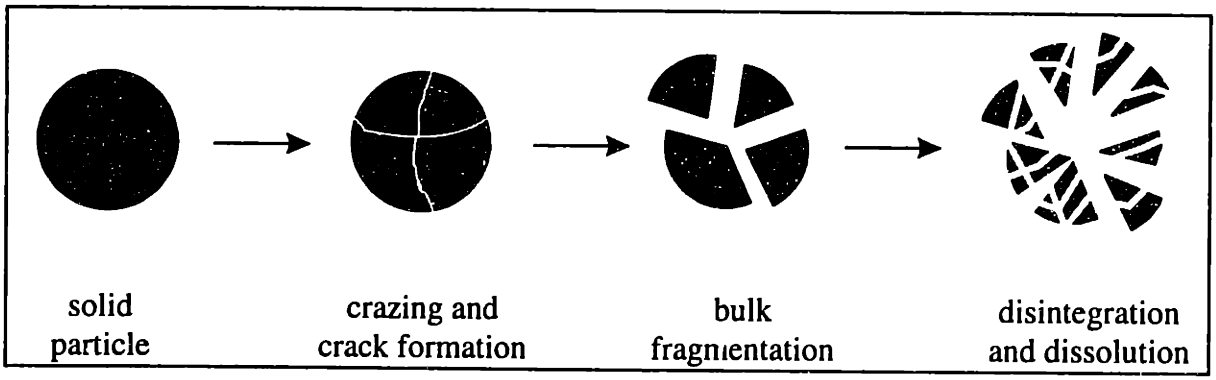

Figure 3.12: 4 stages of the dissolution process (no gel formation)

Dissolution of PCL (30,000) particles in acetone is shown in Figure 3.13. A gel layer was not observed at any time during the experiment. Crazing and cracking of the bulk particle developed during the first second. The only observable interface in this dissolution mode is the solid-solvent interface, which increased in surface area as particle fragmentation proceeded. More cracks developed with increasing time, but the particle remained mostly un-dissolved even after 15 seconds. The original solid-solvent interface did not move significantly during this time. Cracking and fragmentation continued until the particle disintegrated into numerous smaller fragments. These small fragments eventually became indistinguishable in the solvent. Their disappearance may be due to either complete dissolution, or further disintegration into mini-fragments of undetectable dimensions. It should be noted that PCL (30,000) particles dissolve in chloroform with gel layer formation, and no crack propagation (see Figure 3.5).

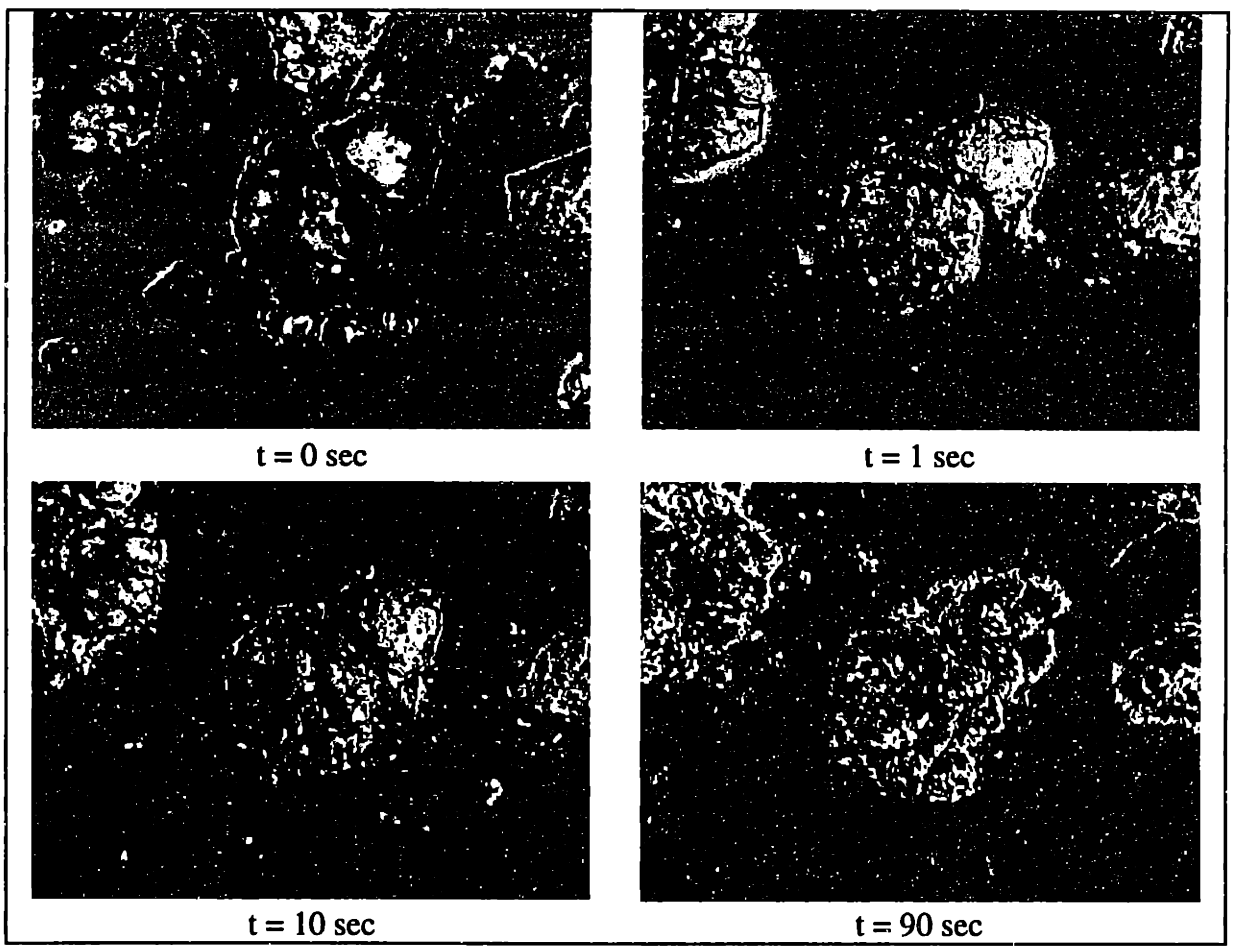

Figure 3.13: Crack propagation mode of dissolution (PCL 30,000 in acetone)

3.3.4 No dissolution

No dissolution occurs if the solvent and the polymer are thermodynamically incompatible. Ethanol, for example, is known to be a poor solvent for most bioerodable polymers used in 3DP™. PLGA (85:15 108,000) particles and ethanol were monitored in the setup to determine if there were any artifacts in Figure 3.5 and Figure 3.13 due to changes in solvent level within the dissolution cell during the experiment. Figure 3.14 shows clearly that the particles remained unchanged even after 90 seconds, with no observable swelling or dissolution. It appears that solvent level within the dissolution cell did not result in any artifacts. Similar results were obtained with other combinations.

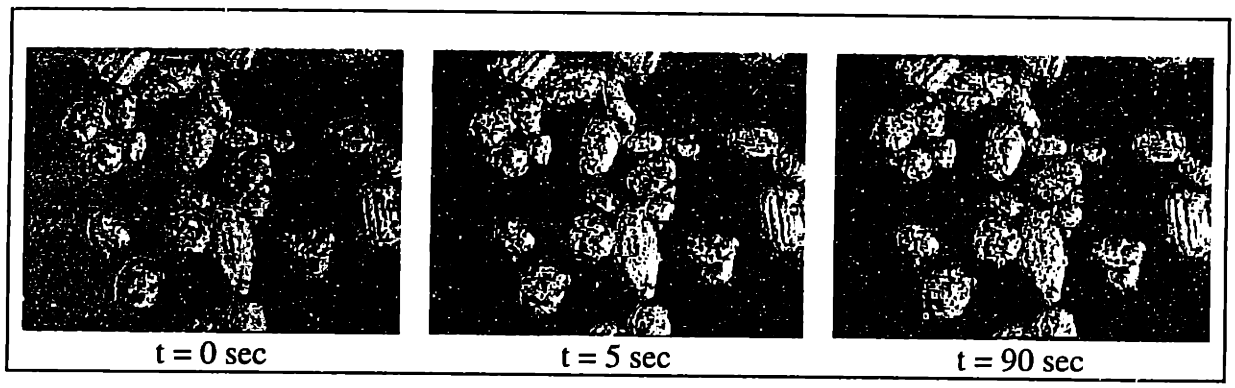

Figure 3.14: Images for no dissolution (PLGA 85:15 108,000 in ethanol)

3.4 DISCUSSION

3.4.1 Time scale

The deceleration time for 3DP™ droplets after powder bed impact has been estimated by Bredt[52] to be 10^{-4} sec, based on an initial droplet velocity of 10 m/sec and a typical cratering depth of 500 μm. Fan[53] studied droplet ballistic impact with high speed photography and observed no further growth in crater diameter after 0.9 msec. Bredt used three approaches to estimate the time scale of binder migration into surrounding pores. The migration time was approximated to be about 2 msec using the Washburn infiltration model,[54] approximately 5 msec based on pressure equilibration calculations,[52] and roughly 90 msec with Chang's modified Richards infiltration model.[55] Similar time-scales of ballistic impact and binder migration for polymeric systems are expected, even

though these estimates were derived for ceramic systems. The particle dissolution process is expected to commence as soon as solvent contacts the polymer particle, but it had been assumed that the negligible dissolution occurs during the initial few milliseconds. This important assumption implies that binder impact and migration are not significantly affected by the dissolution process. A high speed video recorder capable of capturing images at >1000 frames/second would be useful to determine the actual solvent penetration time into the powder bed, but the current set-up (30 frames/sec) suffices to demonstrate that negligible dissolution occurs during the initial few frames (~100 msec), and complete particle dissolution time required 10^0 to 10^2 seconds. This work provides the first experimental validation of this assumption.

3.4.2 Dissolution with gel formation

Ueberreiter and Asmussen[56] observed four distinct surface structures during dissolution of some polymers: a liquid boundary layer, a gel layer, a solid swollen layer, and an infiltration layer. "Normal" dissolution was said to occur when all four structures, particularly the gel layer, were present. Only swelling may occur and no true dissolution would takes place if the solvent and the polymer are thermodynamically incompatible. True dissolution occurs only when a thermodynamically compatible solvent reaches a critical volume fraction in the gel, and disentangled molecular chains diffuse away from the gel-solvent interface, and into the solvent. An initial induction time, or reptation time, is often associated with the disentanglement process.[57] Reptation refers to the molecular disentanglement process of individual chains. Once dissolution commences, the motion of gel-solvent interface depends on the relative difference between swelling and disentanglement rates. The gel-solvent may continue to expand outwards if the swelling rate is much faster than the disentanglement rate ($k_s > k_d$). The gel-solvent interface may reverse direction and move radially inwards toward the center, however, if the disentanglement rate is sufficiently fast ($k_d > k_s$). The gel-solvent interface will eventually become indistinguishable from the solvent phase, when the entire gel layer is dissolved. The relevant polymeric parameters are molecular structure, crystallinity, and molecular weight. The important parameters are the solvent diffusivity in the solid

polymer, solvent-polymer interaction parameter (χ), polymer diffusivity in the solvent, temperature, and stir rate.

At least 5 distinct phenomena are involved with this type of dissolution: 1) solvent ingression into the polymer particle, 2) particle swelling, 3) chain disentanglement (reptation), 4) chain disengagement from the solvent-gel interface, and 5) chain diffusion across the liquid boundary layer. Reptation is the process by which individual polymeric chains "free" themselves from the entangled swollen polymer network. Ranade and Mashelkar[58] developed a two dimensional transport model to describe the dissolution of a spherical polymer particle under a uniform solvent convective field:

$$\frac{\partial \phi_p}{\partial t} + \frac{1}{r^2}\frac{\partial}{\partial r}\left(r^2 N_{\phi r}\right) + \frac{1}{r\sin\theta}\frac{\partial}{\partial \theta}\left(N_{\phi\theta}\sin\theta\right) = S_\phi \tag{3.1}$$

where ϕ_p = volume fraction of polymer

$N_{\phi r}$ = polymer flux in r - direction

$N_{\phi\theta}$ = polymer flux in θ - direction

S_ϕ = source term

Time dependence of the polymer-gel interface during swelling was modeled according to a power law kinetic model first proposed by Astarita and Sarti:[59]

$$\alpha\frac{dR_{pg}}{dt} = k\left(\phi^* - \phi_g\right)^n \tag{3.2}$$

where $\alpha = \frac{R_c}{t_c U_c}$; (subscript c denotes characteristic values, U denotes rate)

R_{pg} = distance from polymer - gel interface to center of particle

k, n = glass transition kinetics parameters

ϕ^* = threshold polymer volume fraction for glass transition

ϕ_g = polymer volume fraction on gel side of polymer - gel interface

Ranade and Mashelkar modeled the movement of the gel-solvent interface as:

$$\alpha\frac{dR_{gs}}{dt} = -\frac{1}{Pe_c}\left(D_s\frac{\partial \phi}{\partial r}\right) - \frac{R_{eff}}{\phi_B} \tag{3.3}$$

where R_{gs} = distance from gel - solvent interface to center of particle

$Pe_c = \frac{R_c U_c}{D_c}$; (Peclet number; subscript c denotes characteristic values)

D_s = dimensionless diffusivities of solvent in gel

R_{eff} = effective disengagement rate of polymer at gel - solvent interface

ϕ_B = polymer volume fraction at gel - solvent interface

The first term on the RHS in equation 3.3 accounts for the swelling, while the second term represents disengagment. The initial and boundary conditions are:

$$
\begin{aligned}
&t = 0, \qquad R_{gs} = R_o \text{ (initial particle radius)} \\
&t < t_{rep}, \qquad R_{eff} = 0 \\
&t > t_{rep}, \qquad R_{eff} = -\frac{1}{Pe_R}\left(D_p \frac{\partial \phi_p}{\partial r}\right) = k_d \phi_B \qquad (3.4) \\
&r = R_{pg}, \qquad \frac{1}{Pe_c}\left(D_s \frac{\partial \phi_p}{\partial r}\right) = \alpha\left(1 - \phi_g\right) \frac{dR_g}{dt} \\
&r = R_{gs}, \qquad \phi = \phi_B \\
&r = 0, \qquad \frac{\partial \phi_p}{\partial r} = 0
\end{aligned}
$$

Numerical calculations revealed that a 10-fold deviation in glass transition kinetics resulted in only 6% modification in dissolution time. Sensitivity analysis revealed that gel formation and swelling kinetics are governed by reptation time (t_{rep}) and solvent diffusivity in the gel (D_s). These two parameters were therefore used as t_c and D_c, respectively. R_c is therefore $(D_s t_{rep})^{1/2}$, and U_c is R_c / t_{rep}. Particle dissolution time was found to depend primarily on polymer diffusivity in solvent (D_p), the external velocity (U_∞), and the disengagement rate (k_d). Their model predicted that dissolution time decreases with increasing particle size for larger particles, while dissolution time is particle size independent for smaller particles, and converges to t_{rep}. Dissolution time was found to decrease, as expected, with increasing mass transfer kinetic parameters (D_p and U_∞).

Ranade and Mashelkar presented several limiting cases for which analytical solutions can be obtained. Particle dissolution is glass transition controlled if the glass

transition kinetics is very slow relative to reptation, disengagement, and external mass transfer. Negligible gel layer is expected in such cases, and ϕ_g becomes essentially ϕ_B. Integration of equation 3.2 shows that for glass transition controlled dissolution, the particle dissolution time, t_D, scales linearly with initial particle size, R_o:

$$t_D = \frac{\alpha R_o}{k\left(\phi^* - \phi_B\right)^n} \tag{3.5}$$

The observation of a distinct gel layer suggests that the dissolution process is not glass transition controlled. The process is disengagement (k_d) controlled if chain disentaglement and external mass transfer are fast relative to chain disengagement. Equation 3.3 can be simplified in such cases by ignoring the swelling term (first term on the RHS):

$$\alpha \frac{dR_{gs}}{dt} = -\frac{R_{eff}}{\phi_B} \tag{3.6}$$

Substituting equation 3.4 for R_{eff}, the particle dissolution time, t_D is again found to vary linearly with the initial particle radius, R_o, and inversely with disengagement rate (k_d):

$$t_D = t_{rep} + \frac{\alpha R_{gs}\Big|_{t=t_{rep}}}{k_d} \tag{3.7}$$

$$\text{where } R_{gs}\Big|_{t=t_{rep}} = \frac{R_o}{\sqrt[3]{\phi_B}} \text{ for } R_o < R_c \tag{3.8}$$

$$R_{gs}\Big|_{t=t_{rep}} = R_o \text{ for } R_o >> R_c \tag{3.9}$$

The particle dissolution process is mass transfer controlled if chain reptation and disengagement are fast relative to the external mass transfer. The polymer concentration on the solvent side of the gel-solvent interface remains essentially ϕ_B in such cases, and the effective disengagement rate becomes:

$$R_{eff} = k_{SL}\left(\phi_B - \phi_\infty\right) \tag{3.10}$$

where k_{SL} = external mass transfer coefficient

ϕ_∞ = polymer volume fraction in bulk solvent

k_{SL} can be estimated by the Ranz's correlation for a sphere:

$$Sh = \frac{k_{sc} R_{gs}}{D_s} = 2 + 0.6(\mathrm{Re})^{1/2}(Sc)^{1/3} \tag{3.11}$$

Sh, in turn, is related to the Peclet number, *Pe*, as follows:[60]

$$Sh = 1 + (1 + Pe)^{1/3} \tag{3.12}$$

Pe is sufficiently large for polymeric particles under external mass transfer control:

$$Sh = Pe^{1/3} \tag{3.13}$$

Combining equations 3.6 and 3.8 through 3.13, Ranade and Mashelkar showed that the particle dissolution time scales with initial particle radius to the 5/3 power if the process is mass transferred controlled:

$$t_D = t_{rep} + \frac{3\alpha(2Pe_c)^{2/3}}{5\phi_B^{4/3}} \frac{(R_o)^{5/3}}{D_P^{2/3} U_\infty^{1/3}} \quad \text{for } R_o < R_c \tag{3.14}$$

$$t_D = t_{rep} + \frac{3\alpha(2Pe_c)^{2/3}}{5\phi_B} \frac{(R_o)^{5/3}}{D_P^{2/3} U_\infty^{1/3}} \quad \text{for } R_o > R_c \tag{3.15}$$

The dissolution process is reptation controlled if the particles are small, and the disentaglement rate is much slower than that for disengagement and mass transfer. The dissolution time is hence the reptation time:

$$t_D = t_{rep} \tag{3.16}$$

The dissolution time can be approximated for mixed control as t_{rep} if the second term on the RHS of equations 3.7, 3.14, and 3.15 are small relative to t_{rep}.

These existing models are quite useful for interpreting the observations presented earlier in this chapter. Two important distinctions should be pointed out, however, before applying these models for actual 3D Printing™. The external solvent velocity (U_∞), in 3DP™ is practically zero during most of the dissolution process, hence dissolution time is expected to be higher than model prediction. More importantly, these models were based on infinite volume of liquid solvent, and solvent evaporation during dissolution was not considered. It was pointed out in section 2.4.2 that finite quantities of particles and liquids are involved during 3DP™, and solvent evaporation during 3DP™ is expected to decrease the amount of time and solvent available for particle dissolution.

3.4.3 Minimum dissolution time

The existence of a "minimum" dissolution time and an "optimal" particle size has important implications for 3DP™. Powder processing for polymeric materials is inefficient at best, particularly for very fine powder. Table 3.2 lists the yield for various particle size distribution of PLGA (85:15 108,000) from cryogenic milling. A 75 μm "optimal" particle size for this polymer implies that there is no need to expand great efforts in producing sub-45 micron powder (3.1% yield) from this polymer, since no improvement in particle dissolution will be achieved. The use of sub-45 micron powder of this polymer may also cause powder spreading problems due to electrostatic charging, resulting in poor powder bed uniformity.

Polymer	<45 μm	45-75 μm	75-150 μm	>150 μm	Total collected
PLGA (85:15 108,000)	3.1%	8.3%	42.0%	35.4%	88.9%

Table 3.2: Yield for various particle size distribution from cryogenic milling

Brochard and de Gennes[57] analyzed the dissolution of a semi-dilute polymer solution of various droplet sizes and reported the existence of a critical droplet size, below which the dissolution time is droplet size independent. This minimum dissolution time was termed the reptation time, t_{rep}, and was dependent on the molecular weight and structure of the polymer. The critical droplet size was found to be on the order of $\sqrt{D_{coop}\, t_{rep}}$, where D_{coop} is the cooperative diffusion coefficient. Devotta et al. extended the analysis to solid particles, and found that dissolution time of polymeric particles also becomes size-independent for particles smaller than a critical size.[61] This finding is in marked contrast with the dissolution behavior of non-polymeric solid particles and low molecular weight particles, which are primarily mass transfer limited, and are strongly dependent on particle size. Non-polymeric particles shrink continually during dissolution, while polymeric particles first swell, and then shrink, during dissolution. The particle size dependence for the dissolution of monodispersed, non-polymeric particles can be described by the Hixon-Crowell equation:[62,63]

$$m_o^{\frac{1}{3}} - m^{\frac{1}{3}} = \frac{m_o^{\frac{1}{3}}}{D_o} kt$$

where m_o = initial mass of particle

m = remaining mass at time t

D_o = initial particle diameter

k = reaction rate constant

The Hixon-Crowell equation is similar in form to equation 3.5, and it suggests that a plot of dissolution time of non-polymer and low molecular weight polymers vs. particle size should consist of a straight line passing through the origin ($D_o \propto t$). A similar plot for high molecular weight polymer, as shown in Figure 3.7, intercepts the temporal axis at a finite minimum dissolution time. Devotta et al. added 60 mg of polymer particles of known "average" particle size into a beaker containing 80 ml solvent and used a stopwatch to determine the dissolution time according to visual observation. The authors reported that the readings were reproducible to within ±5 sec.[61] Although their set-up was adequate for their polymers of interest, it would be inadequate for the polymer-solvent systems used in 3DP™, where the t_{min} was found to be 1.25 sec. The experimental set-up described in this report represents a much more sensitive technique for observing polymer particle dissolution, and a reproducibility of ±33 msec. This reproducibility and sensitivity can be further improved, if necessary, by simply upgrading the video recorder with a high-speed video recorder.

DeGennes[64] estimated the molecular weight dependence of minimum reptation time to scale with molecular weight to the third power ($t_{rep} \propto M_w^3$). Other investigators[65] predicted a stronger dependence, with $t_{rep} \propto Mw^{3.4}$. Devotta et al. reported a molecular weight dependence to be 3.2 for polystyrene-cyclohexane, and 2.9 for poly(methyl methacrylate)-benzene. The data in Table 3.1 is plotted in Figure 3.15 to illustrate the molecular weight dependence of reptation time for a range of MW for PLLA (53,000, 132,000, and 301,000). The best curve fit was obtained with $t_{rep} \propto M_w^{2.6}$. It should be emphasized that Figure 3.15 represents only those high molecular weight PLLA particles which dissolved completely.

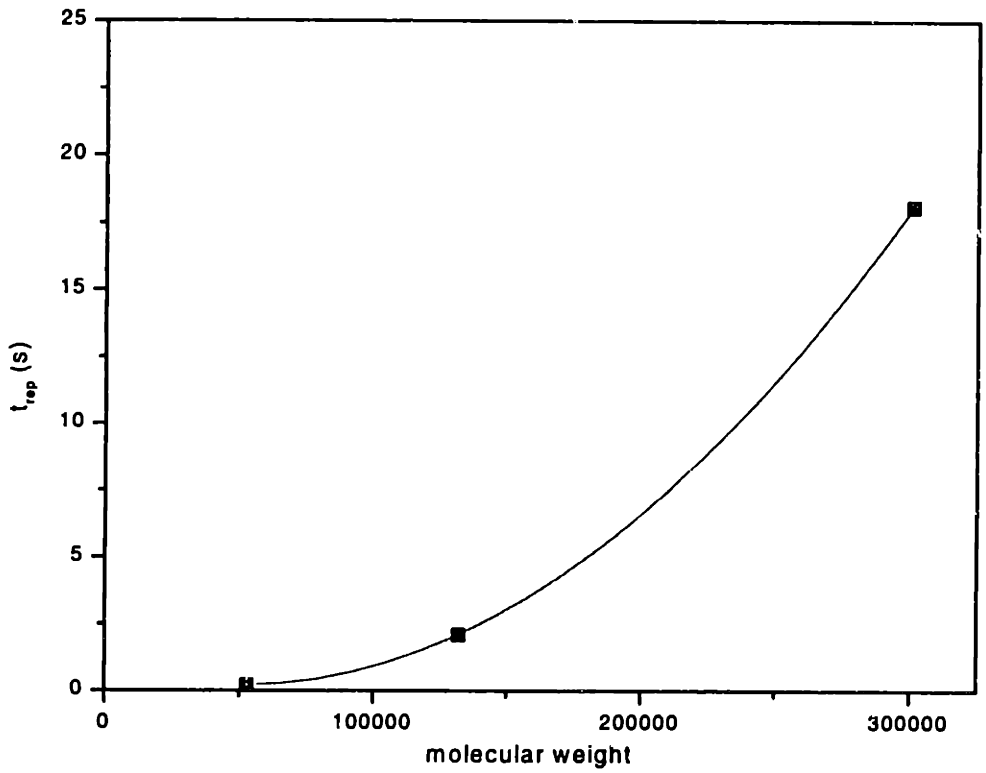

Figure 3.15: Molecular weight dependence of t_{rep} for PLLA

3.4.4 Dissolution without gel formation

Ueberreiter and Asmussen[56] also observed a crack propagation type of dissolution where the gel layer was absent, and proposed that there is a critical gel temperature below which gel formation is too slow and the polymer cracks before sufficient relaxation occurs. "Normal dissolution" was observed with polymers with low critical gel temperature, such as polystyrene (PS). Polymers with higher critical gel temperature, such as poly(methyl methacrylate) (PMMA), can be made to dissolve in the crack propagation mode by decreasing the experimental temperature to below the critical gel temperature. Peppas et al. dissolve PMMA (M_n=153,000) in MEK at 27°C and observed crack propagation as the predominant mechanism. Peppas et al. reasoned that crack propagation occurs for low temperature because the polymer relaxation (swelling) rate is much slower than the disentanglement rate ($k_d >> k_s$). The polymer relaxation rate should

be similar to the disentanglement rate ($k_d \sim k_s$) at higher temperatures since the relaxation processes generally involve higher activation energies.[66] Ouano and Carothers proposed that cracks tend to develop faster with smaller molecular weight solvents than with those with larger molecular weight, since the latter have much slower diffusivity in the polymer.[67] The molecular weight of acetone, C_3H_6O, and chloroform, $CHCl_3$, are 58 and 119 g/mole, respectively. This 2 fold difference in molecular weight, and lower solubility of PCL (30,000) in acetone, may contribute to the cracking seen with PCL-acetone and the gelling observed with PCL-chloroform. Manjkow et al. studied the crazing problem and showed that crazing occurs when a polymer critical crazing stress is exceeded.[68] Both dissolution rate and critical stress were found to scale with molecular weight for low molecular weight PMMA (<100,000). It appears that crazing may not occur with higher molecular weight polymers due to the combined effects of slower solvent diffusivity and higher critical crazing stresses.

3.4.5 Limitations of experimental techniques

Figure 3.5 shows that during dissolution, the particle remained relatively stationary within the dissolution cell. This lack of mobility is indicative of contact and adhesion between the exterior surface and the glass plates. Particles are adhered to the bottom plate during initial dissolution, but can also contact the top plate if the gel layer grows to sufficient dimensions. This geometric effect must be considered in any length scale analysis during dissolution. Particle dissolution may be slightly faster if the particles were placed under true three dimensional convective flow, since polymer diffusion cannot occur through the top and bottom planes in this case. The laminated fashion by which 3DP™ constructs parts, however, does not involve true three dimensional convective flow. The restricted diffusion path and the adhesion effect between layers and may be more representative of the actual 3DP™ process. It should be noted that these effects are irrelevant to the measurement of initial particle dimensions.

4. SOLVENT EVAPORATION

4.1 BACKGROUND

The importance of time scale for evaporation was discussed in chapter 2. The objective of this chapter is to establish a more complete understanding of the evaporation process during 3DP™. Section 4.2 analyzes the amount of evaporation a typical chloroform droplet undergoes from the time it exits the nozzle orifice to the time of powder bed impact. This is important in determining the amount of solvent which actually reaches the powder bed. Section 4.3 summarizes the evaporation rates of common 3DP™ solvents in air for vented and non-vented cases. Section 4.4 studies the problem of solvent evaporation from a thin layer of non-dissolving particles. This scenario applies to materials systems which bind by the adhesion mechanism. Section 4.5 studies the problem of solvent evaporation from a thin layer of dissolving particles, which applies to materials combinations which bind by dissolution/re-precipitation. Section 4.6 considers the relative rates of solvent evaporation and particle dissolution.

4.2 DROPLET EVAPORATION DURING FLIGHT

4.2.1 Background

The common equation to determine the volume of binder deposited into the powder bed is based on volumetric flow rate as determined by mass loss in the binder reservoir. The equation assumes that all binder which was pressurized out through the nozzle would reach the powder bed. While the assumption is valid for aqueous based systems which have low vapor pressure, its validity is questionable for the common 3DP™ organic solvents which are highly volatile. This section analyzes the amount of evaporation a typical chloroform droplet undergoes from the time it exits the nozzle orifice to the time of powder bed impact. The analysis would be important in determining the amount of solvent which actually reaches the powder bed.

4.2.2 Materials and method

Chloroform was pressurized out of a 45 μm continuous jet nozzle. The dimensions of the chloroform droplets during flight were measured using a high magnification charge-coupled device (CCD) video camera which was mounted to a rack and pinion adjustable height post. The piezo frequency used for droplet generation was used to control the on-off of a LED, which was attached to the camera such that the image zone is constantly illuminated for all camera positions. The experiment began with the initial jet column as chloroform exits the orifice (z=0). The camera and the attached LED was then lowered, and volume loss was quantified by measuring the droplet image sizes at various vertical positions along the droplet flight path. The camera was connected to a video recorder, and the images replayed for subsequent analysis.

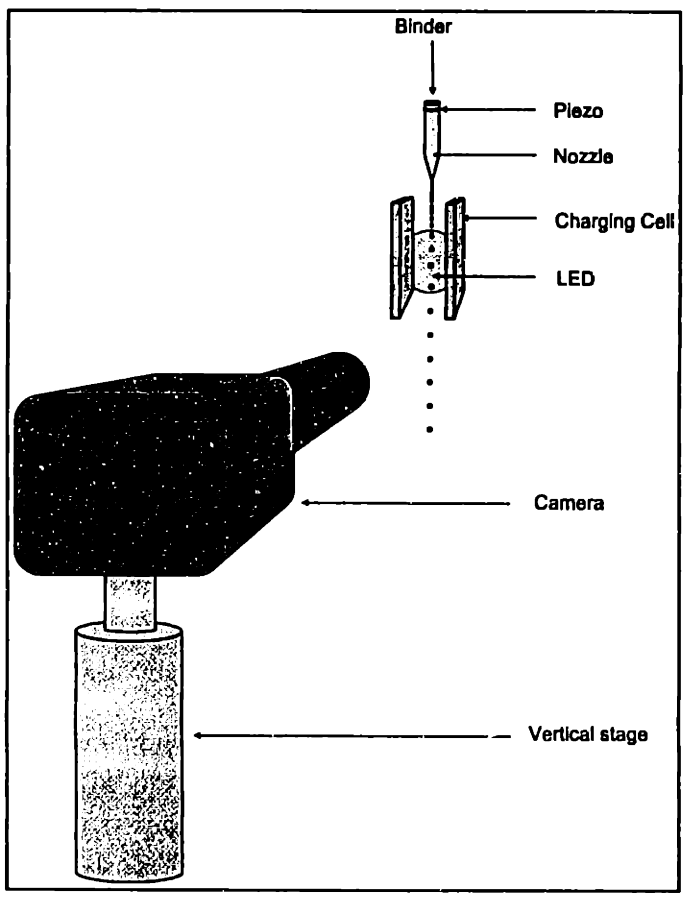

Figure 4.1: Experimental set-up for determining droplet evaporation

4.2.3 Droplet evaporation model

The time of flight between droplet formation and droplet impact with the powder bed can be determined from the flight distance and droplet velocity. The *initial* droplet velocity can be assumed to approximate that of the jet velocity, which can be modeled as a differential cylindrical element with height dz passing through the orifice with cross-sectional area A. The jet velocity is therefore obtained by a mass balance:

$$\frac{dm}{dt} = \frac{dz}{dt} A\rho$$

where $\frac{dz}{dt} = velocity$

A = area of orifice opening = πr^2

r = orifice radius = 45.7 μm

ρ = density of chloroform

thus, $\frac{dz}{dt} = 1034.0 \frac{\text{cm}}{\text{sec}}$

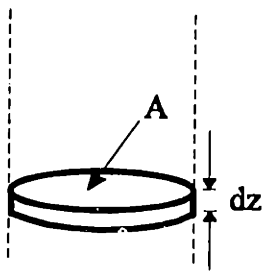

The time required for each droplet to travel 3 cm at 10m/s is approximately 2.9 msec. This initial velocity of 1,034 cm/sec, however, is not expected to remain constant due to the effect of a drag force acting on the surface of the moving droplet. This drag force, or friction force, may result in significant deceleration of the droplet, thereby increasing its time of flight. The net result is increased evaporation due to increased flight time. The significance of the drag force must be determined:

$$W - D = m\frac{dv}{dt}$$

where W = weight of the droplet with radius r

D = drag force or friction force

m = mass of droplet

$$\frac{4}{3}\pi r^3 \rho g - \frac{F_r \rho_{air} v^2 2\pi r^2}{2g} = m\frac{dv}{dt} = \frac{4}{3}\pi r^3 \rho \frac{dv}{dt}$$

where ρ = density of chloroform

ρ_{air} = density of air

g = gravitation constant

F_r = drag / friction coefficient

v = velocity of droplet at time t

r = radius of droplet at time t

Collecting terms, and integrating from t=0 to t= time at impact

$$\int_0^t \left(g - \frac{3\rho_{air}}{8\rho} F_r r \right) dt = \int_{v_o}^{v_f} v^{-2} dv \tag{4.1}$$

The time dependence of radius r must first be solved in order to evaluate the drag force on the droplet. The droplet is expected to shrink due to vapor pressure driven chloroform evaporation during this short amount of time. The vapor pressure is temperature dependent. The released latent heat of vaporization results in a temperature drop within the evaporating droplet, and corresponding vapor pressure reduction. The cooling droplet also absorbs heat from the ambient air. A steady state temperature, commonly referred to as the wet-bulb temperature, will be reached when the latent heat of vaporization is balanced by ambient heat transfer if the droplet travels for long enough time. It is doubtful that the wet-bulb temperature is ever reached during 3DP™, however, since the time of flight is only on the order of milliseconds. It is necessary to calculate the amount of temperature drop (ΔT) during evaporation to determine the vapor pressure variation during flight. The rate of evaporation can reduce significantly if ΔT is large. The assumption can be made that the evaporation rate remains roughly constant during the 2.9 msec flight time if ΔT is small. The assumption of Newtonian cooling can be made due to the small size of these droplets. ΔT can be estimated from heat balance:

$$N_A \Delta H_{vap} At = \rho C_p V \Delta T$$

where N_A = chloroform flux on droplet surface (see Table 4.2)

ΔH_{vap} = heat of vaporization for chloroform at 25° C (29 kJ / mol)

A = surface area of droplet

ρ = density of chloroform at 25° C (1.474 g / cm^3)

C_p = heat capacity of chloroform at 25° C (109.96 J / mol · C)

V = droplet volume

ΔT = temperature change

ΔT is found to be significantly less than 1°C. The droplet is not expected to undergo significant cooling. The droplet temperature is, thus, assumed to remain quite close to 25°C during flight over a distance of 3 cm. The theoretical dimension change and corresponding volume loss can be obtained by mass balance:

$$\frac{dm}{dt} = -NM_w A$$

$$\frac{dm}{dt} = \rho \frac{dV}{dt} \quad \pi r^2 \frac{dr}{dt}$$

$$-N_A M_w A = -k_g C X_s M_w A$$

where r = droplet radius at time t

k_g = mass transfer coefficient

$= \frac{S_h D_{AB}}{2r}$ where

S_h = Sherwood number

D_{AB} = diffusion coefficient of chloroform vapor through air

M_w = molecular weight of chloroform = 119.4 $\frac{g}{mole}$

C = average concentration of chloroform

X_s = mole fraction of chloroform on droplet surface

Rearranging the terms, and integrating,

$$r \frac{dr}{dt} = \frac{- S_h D_{AB} C X_s M_w}{2\rho}$$

$$\int_{r_o}^{r} r\,dr = \int_{0}^{t} \frac{-S_h D_{AB} C X_S M_W t}{2\rho}\,dt$$

where r = droplet radius at time t

S_h = Sherwood number

D_{AB} = diffusion coefficient of chloroform vapor in air

C = average chloroform concentration in vapor $\left(C=\frac{P}{RT}\right)$

where $P \equiv$ vapor pressue of cholоform at temperature T

$R \equiv$ gas constant

X_S = mole fraction of chlorform on droplet surface

The constant of integration can be determined from the initial condition, i.e., at t=0, r=r_o. The radius of the shrinking droplet at time t becomes:

$$r = \sqrt{r_o^2 - \frac{S_h D_{AB} C X_S M_W t}{2\rho}} \tag{4.2}$$

The Sherwood number for mass transfer of a moving sphere can be approximated by

$$S_h = 2 + 0.6 R_e^{0.5} S_c^{0.33}$$

where R_e = Reynolds Number

$$= \frac{2Vr}{\nu} = \frac{\left(1034\frac{\text{cm}}{\text{sec}}\right)\left(79.28\times10^{-4}\text{cm}\right)}{3.68\frac{\text{cm}^2}{\text{sec}}} = 2.227$$

S_c = Schmidt Number

$$= \frac{\nu}{D_{AB}} = \frac{3.68\frac{\text{cm}^2}{\text{sec}}}{0.0861\frac{\text{cm}^2}{\text{sec}}} = 42.74$$

$$S_h = 2 + 0.6 R_e^{0.5} S_c^{0.33} = 5.131$$

The diffusion coefficient of chloroform in air can be estimated from the Chapman-Enskog kinetic theory for diffusivity

$$D_{AB} = \frac{\left(1.8583\times10^{-3}\right)(T)^{\frac{3}{2}}\left(\frac{1}{M_A}+\frac{1}{M_B}\right)^{\frac{1}{2}}}{P\sigma_{AB}{}^2\Omega_{AB}}$$

where σ_{AB} = collision diameter

Ω_{AB} = dimensionless function of T and intermolecular potential field for one molecule of A and one of B

M_i = molecular weight of species i

$$D_{AB} = \frac{\left(1.8583\times10^{-3}\right)(298)^{\frac{3}{2}}\left(\frac{1}{119.4}+\frac{1}{29}\right)^{\frac{1}{2}}}{(1)(4.550)^2(1.111)}$$

$$= 0.0861\ \frac{\text{cm}^2}{\text{sec}}$$

The mole fraction of chloroform on the surface of the droplet is determined as follows:

$$X_s = \frac{P_{saturation}}{P_{ambient}}$$

where $\log\left(P_{saturation}\right) = A - \frac{B}{T+C}$

for chloroform, $A = 6.903$, $B = 1163.03$, and $C = 227.4$

Therefore, $X_s = 0.26$.

These physical constants can be applied into equation 4.2, which can be substituted into equation 4.1:

$$\int_0^t \left[g - \frac{3\rho_{air}}{8\rho}F_r\left(r_o^2 - \frac{S_h D_{AB} C X_s M_w t}{2\rho}\right)\right]dt = \int_{v_o}^{v_f} v^{-2}dv \qquad (4.3)$$

The final droplet velocity at 3cm below the orifice, v_f, is found to be 1018.4 cm/sec. The drag force appears to cause some deceleration of the chloroform droplet. The assumption of constant velocity can be still be made, however, since the drag effect is small (only 1% decrease in velocity). This assumption is reasonable, considering that the total flight time is only approximately 2.9 msec.

4.2.4 Observations

Figure 4.2 shows the droplet diameter variation with z. It can be seen that for a 45 μm orifice, the diameter of the initial jet column is approximately 45 μm (z = 0). Breakoff of the continuous liquid column into discrete droplets was observed at 0.2 cm below the orifice plate. The initial droplet size at breakoff was approximately 67 μm at z = -0.2 cm. Droplet dimensions decreased gradually with increasing distance below the orifice.

4.2.5 Discussion

The model predicted a radius of the shrinking droplet at z = 3 cm is 32.5 μm, or a droplet diameter of 65 μm. This corresponds to a 3% shrinkage in droplet size, and a 9.7% volume loss. Volume loss at z = -4.8 cm is approximately 11.5%. This analysis is in excellent agreement with the experimental observations, in light of the fact that the average standard deviation for diffusion coefficient as predicted from the Chapman-Enskog kinetic theory is approximately 6%.

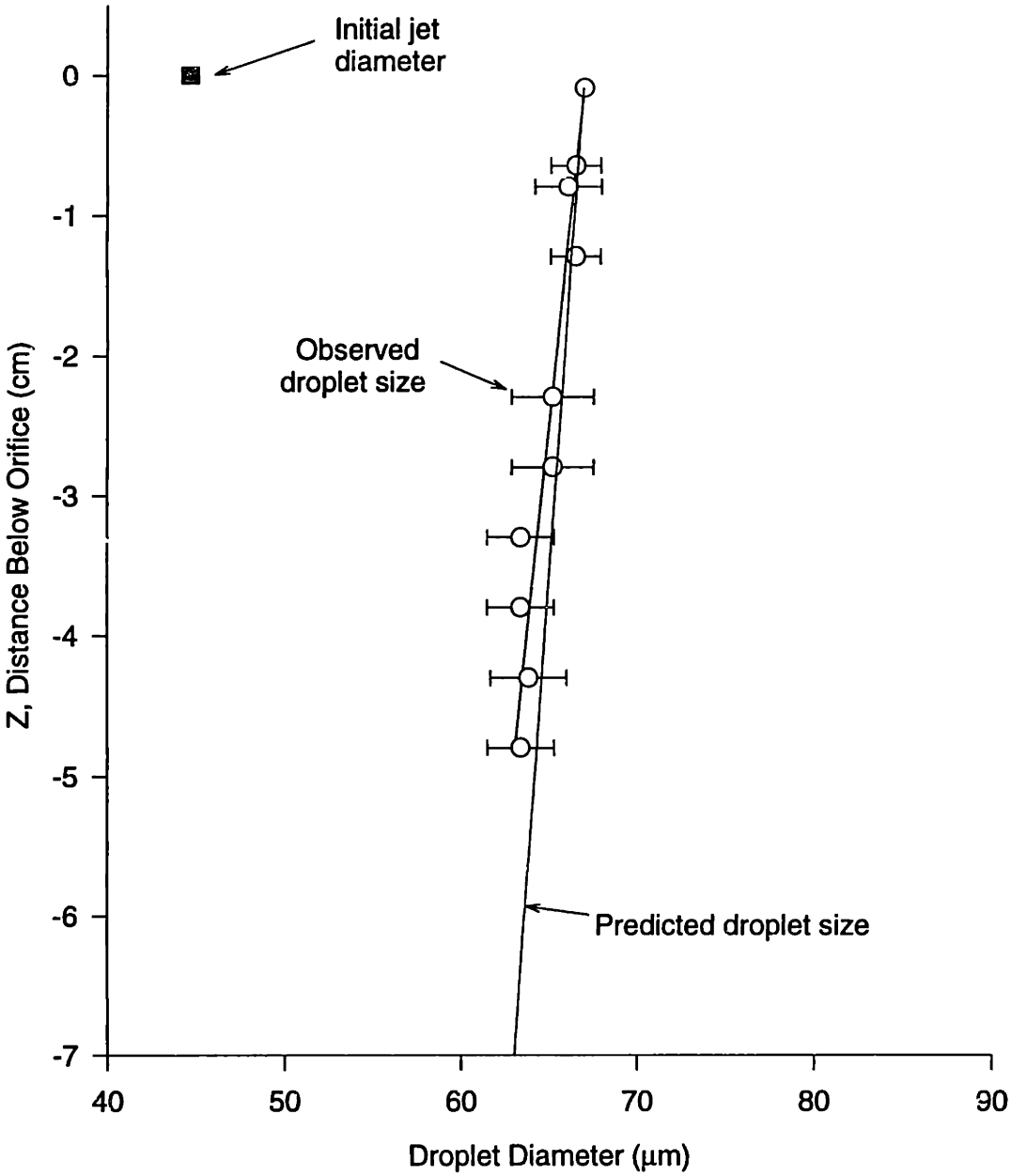

Figure 4.2: Chloroform droplet evaporation: droplet size vs. travel distance

4.3 SOLVENT EVAPORATION FROM THIN LAYER OF LIQUID

4.3.1 Background

The previous section demonstrated that significant solvent evaporation can occur from chloroform droplets during the 2.9 msec flight time. Of great interest is the time scale for evaporation from the powder bed after ballistic impact. One objective of this study is to determine the actual evaporation rates of common 3DP™ solvents under typical operational conditions. The solvents used in 3DP™ are not suitable for human inhalation, hence ventilation is typically required during operation. The second objective is to ascertain the actual effects that ventilation have on solvent evaporation rates, since air current is expected to affect the mass transfer coefficient. The rate data obtained from these simple experiments will be compared with that obtained from solvent evaporation in powder beds.

4.3.2 Materials and methods

A list of common 3DP™ solvents is provided in Table 4.1. Solvents were selected from the list to represent a broad range of vapor pressure. Fresh solvents were obtained from various suppliers. 100 cc aliquots of each solvent were filled into clean evaporation dishes, 14.66 cm diameter, 1.5 cm height, and placed on an analytical balance (Mettler PM4800) in the 3DP™ machine. The piston was removed from the 3DP™ machine, and the balance was positioned such that the liquid level in the dish corresponded to the typical powder bed surface level. This attempt to simulate actual mass transfer conditions during 3DP™ was necessary because the 3DP™ machine itself occupied a large volume of the ventilation hood. The analytical balance was outfitted with a data communication module. The selected solvents were allowed to evaporate under vented and un-vented (air) conditions, and mass data were transmitted from the balance to the computer at 1 second intervals for 20 minutes. The data was collected by a LabView virtual instrument and saved as spreadsheet files for subsequent analysis. Evaporation experiments were repeated 5 times for each solvent, vented and unvented. The ventilation switch is simply turned off for the "unvented" case, but some recirculation

of the ambient air is expected. All experiments were conducted at approximately 25°C and relative humidity of 35%.

solvent	molecular weight (g/mol)	vapor pressure 25°C (mm Hg)	solubility parameter, δ $(cal/cm^3)^{1/2}$	boiling point at 1 atm (°C)
propylene carbonate	102.10	0.02	13.3	242
gamma-butyrolactone	86.09	0.3		204
N-methyl-2-pyrrolidone	99.13	0.3	11.3	202
dimethyl sulfoxide	78.13	0.46	12.00	189.00
water	18.00	26	23.5	100
toluene	92.14	30	8.91	110.63
ethyl acetate	88.11	100	9.1	77.111
ethanol	46.07	140	12.92	78.5
chloroform	119.38	214	9.49	61.178
methyl tertiary butyl ether	88.15	245	7.4	55
acetone	58.08	299	9.77	56.5
dichloromethane	84.94	466	9.88	39.64

Table 4.1: Vapor pressure and solubility parameters of common 3DP™ solvents

4.3.3 Observations

A typical mass loss profile for chloroform evaporation into air (unvented) is shown in Figure 4.3. A constant evaporation rate can be seen for the entire 20 minutes, even for this relatively volatile solvent. A slope was obtained from this profile by linear regression analysis. Slopes from all 5 trials of chloroform evaporation in air were averaged. Average evaporation rates were determined similarly for each solvent under vented and unvented conditions. All slopes had r^2 values >0.99. It should be pointed out that mass loss was not detected in non-volatile solvents such as propylene carbonate, gamma-butyrolactone, and N-methyl-2-pyrrolidone. All of them had vapor pressures below 1 mm Hg, and boiling points exceeding 200°C. Table 4.2 summarizes the evaporation rates for various solvents under unvented conditions, with units expressed in micromoles and nanoliters.

The effect of solvent vapor pressure on evaporation rate is shown in Figure 4.4. Evaporation rate was significantly affected by venting, as expected, for all solvents. It is interesting that besides shifting the curve upwards, venting also increased the evaporation rate dependence on vapor pressure as indicated by the increased slope. The vented evaporation rates for all solvents were normalized with the unvented evaporation rates and plotted in Figure 4.5.

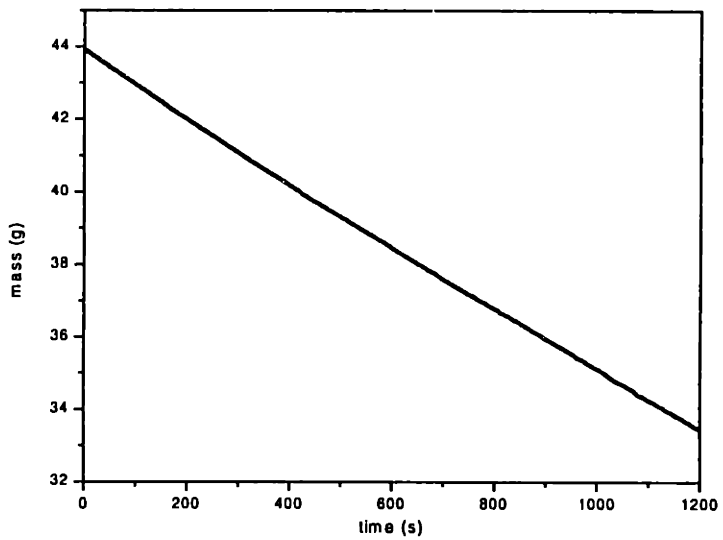

Figure 4.3: Chloroform evaporation profile (in air)

solvent	vapor pressure 25°C (mm Hg)[69,70]	evaporation rate (nl/s*cm^2)	evaporation rate (μmol/s*cm^2)
propylene carbonate	0.02	(not detected)	(not detected)
gamma-butyrolactone	0.3	(not detected)	(not detected)
N-methyl-2-pyrrolidone	0.3	(not detected)	(not detected)
water	26	2.85 ± 0.78	0.16 ± 0.04
ethyl acetate	100	21.74 ± 1.04	0.22 ± 0.01
ethanol	140	10.00 ± 0.06	0.17 ± 0.001
methyl tertiary butyl ether	204	68.77 ± 0.85	0.58 ± 0.01
chloroform	214	34.46 ± 1.71	0.43 ± 0.02
acetone	299	42.49 ± 1.38	0.58 ± 0.02
dichloromethane	466	62.59 ± 1.91	0.97 ± 0.03

Table 4.2: Evaporation rates for 3DP™ solvents in air (unvented)

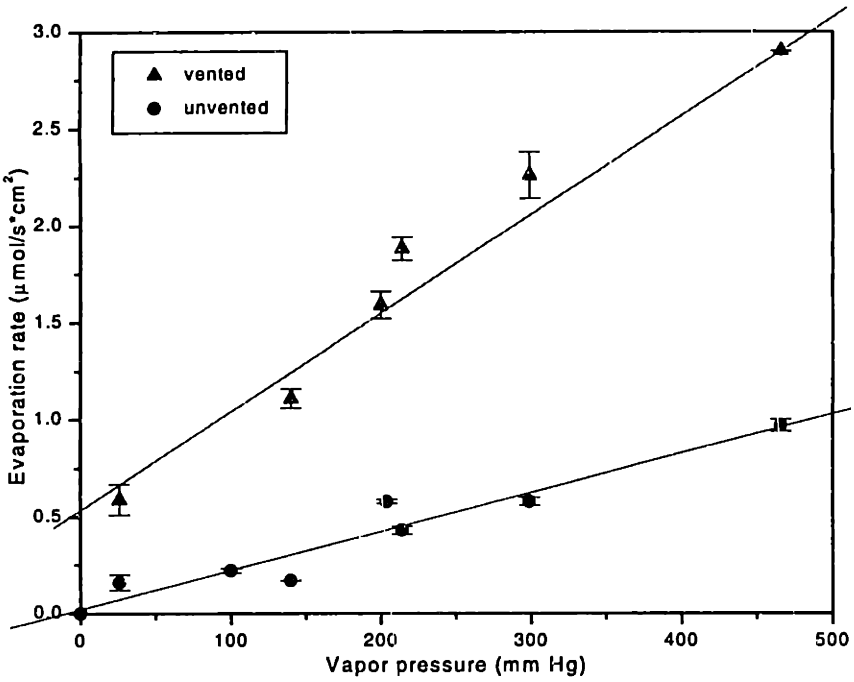

Figure 4.4: Evaporation rates for common 3DP™ solvents

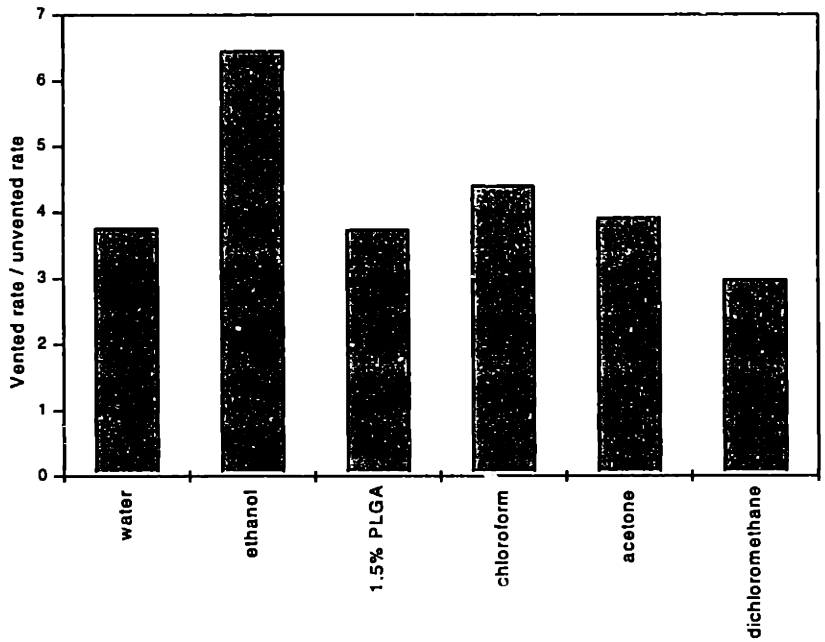

Figure 4.5: Effect of ventilation on evaporation rate

4.3.4 Discussion

Evaporation of a liquid solvent from a planar surface represents the simplest case of drying. Solvent molecules vaporize from the liquid-vapor interface, diffuse across a boundary layer, and mix with ambient gases. This process is controlled by external diffusion across the boundary layer. The evaporation rate, J, is proportional to the difference between the liquid vapor pressure (p_l) and ambient vapor pressure (p_v).

$$J = h\left(p_l - p_v\right)$$

where h is the mass transfer coefficient which characterizes the geometry of the system, air current, temperature, etc. The aspect ratio of the dish (14.6 cm diameter, 1.5 cm height) was selected to minimize the affects of a potential stagnant boundary layer. Calculations in Appendix A showed that the stagnant boundary layer did not affect the evaporation rate significantly. This indicates that even under "unvented" conditions, the recirculating room air is adequate to decrease the stagnant boundary layer thickness. The boundary layer becomes thinner with increasing air current, resulting in a corresponding increase in h, and hence evaporation rate. Figure 4.5 shows that three-fold to six-fold increases in mass transfer coefficient were achieved with venting in the current 3DP™ setup. Evaporation rate can also be enhanced by raising the ambient temperature, which increases p_l. Evaporation rate can also be increased by reducing the relative humidity, p_v, particularly if the liquid is water, Temperature and humidity were monitored for all experiments to minimize their effects on evaporation rate.

The latent heat of vaporization must be supplied from the liquid in the form of sensible heat. This cooling during evaporation results in reduced p_l, which leads to lower evaporation rate, and ultimately reduced cooling. At some point the equilibrium wet-bulb temperature, is reached. No further reduction in liquid vapor pressure is expected at that point. The constant slope in Figure 4.3 suggest that, for the time scale of these experiments, the thermal mass in the sample was sufficient to provide the heat of vaporization without significant cooling and lowering of p_l.

4.4 EVAPORATION FROM THIN LAYER OF NON-DISSOLVING PARTICLES

4.4.1 Background

This section considers solvent evaporation from 3DP™ structures composed of solvent-particle systems which bind by the adhesion mechanism. 3 stages of drying have been described in the literature for drying of granular solids. One objective of this study is to determine if the 3 drying stages can be observed for thin porous structures. Of interest is the time scale for transition between successive stages, if they are observed. Another objective is to determine the effects of particle size on evaporation rate from these structures.

4.4.2 Materials and methods

Salt particles were manually spread to uniform 200 μm thick layers on a stainless steel plate by first leveling the plate with the piston roller guides and then lowering the piston actuator by the desired distance. The plate is then placed on an analytical balance which was outfitted with a data communication module and connected to a computer. A stainless steel stencil with a rectangular opening was placed over the plate, exposing the salt particles below. The bottom side of the stencil has a milled recess around the stencil opening so as to avoid contact with the particles during the experiments. A LabView VI was activated at this point to establish the baseline weight. 200 μl chloroform were deposited through the stencil and directly onto the salt particles. Data was collected from the balance at a rate of 1 sample per second. Two particle size ranges were used for the salt particles: <45 μm and 75-150 μm. 5 samples were tested for each size range.

4.4.3 Observations

A typical mass loss profile during chloroform evaporation from a powder bed of <45 μm salt is shown in Figure 4.6. 2 regimes are clearly discernible after the solvent peak. A linear regime, labeled as "constant rate period" in Figure 4.6, can be seen immediately after solvent deposition. A non-linear regime can be seen on the right side. The time scale for transition from the constant rate period to the non-linear period was found to be on the order of 100 seconds for chloroform and salt particles.

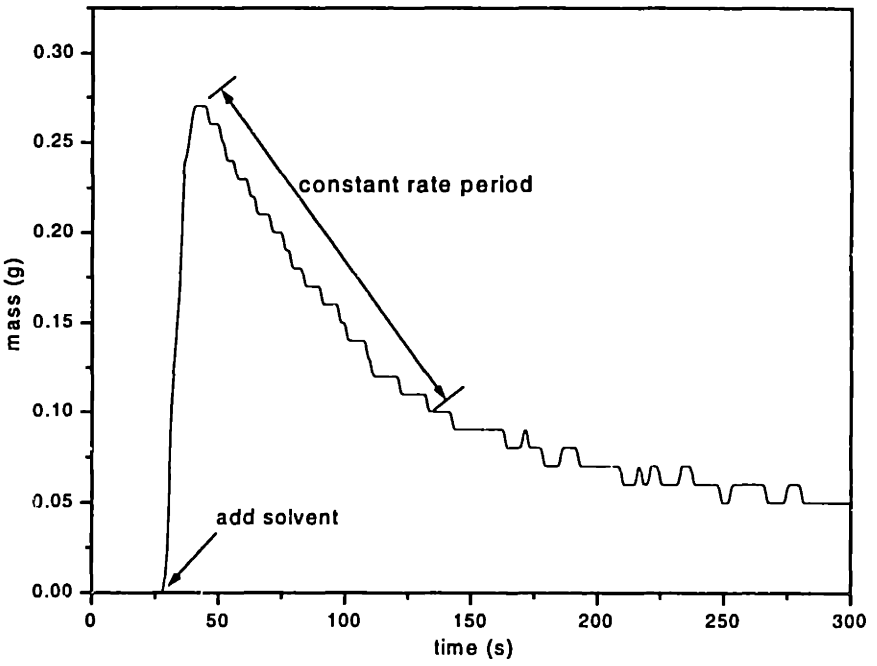

Figure 4.6: Mass loss profile of chloroform from salt particle bed (<45 μm)

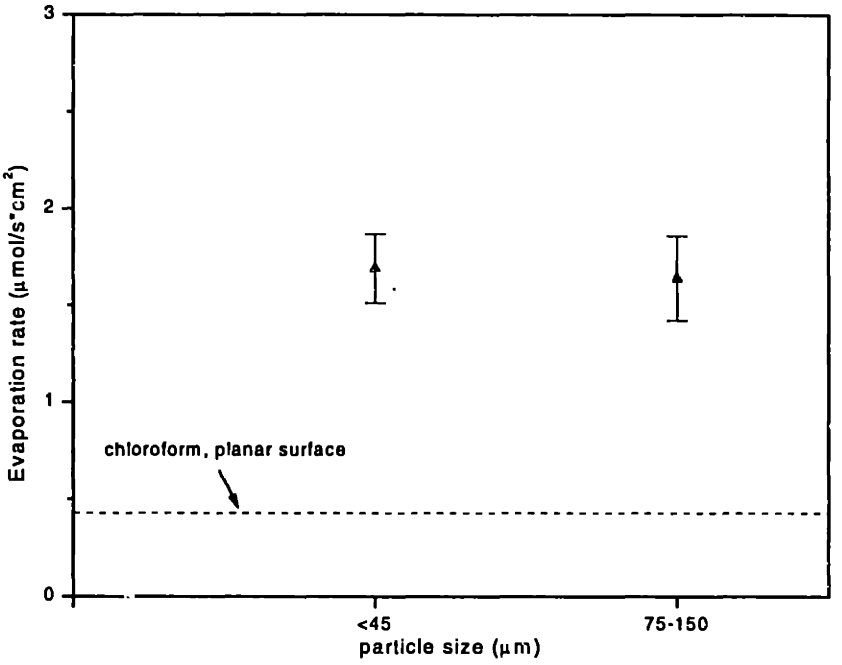

Figure 4.7: Effects of salt particle size on chloroform evaporation rate

The extend of the linear region was determined by using linear regression analysis and identifying the limits where $r^2 > 0.99$. The slope value as determined in this manner was converted into evaporation rate, expressed as $\mu mole/s*cm^2$. Evaporation rates for all samples were determined similarly, and the averages and standard deviations are plotted in Figure 4.7. It can be seen that solvent evaporation from a particulate surface is three times faster than that from a planar, smooth surface. The dotted line shown corresponds to the chloroform evaporation rate as listed in Table 4.2. The data also seem to suggest that particle size has minimal effects on the kinetics of chloroform evaporation from a thin layer of non-dissolving powder. This may be attributed to the cubic crystalline structure of the salt particles, for which variations in particle size do not result in changes in radii of curvature. The salt particles were prepared by mechanical milling, which tend to produce particles with flat surfaces.

4.4.4 Discussion

The problem of solvent evaporation from non-dissolving 3DP™ powder beds is analogous to the problem of drying from a porous substrate. The latter process is frequently encountered in sol-gel processing, tape casting, and many coating applications. Briefly, three drying stages have been described. The initial drying stage is termed "constant rate period", in which the evaporation process is similar to that observed with pure liquid layers. Evaporation *rate* is expected to be higher from a powder bed due to increased surface area as the surface liquid conform to the particle morphology. The planar, non-textured surface of the pure liquid case has less surface area, but equal evaporation *flux*. The curvature of the liquid may also contribute to the increased evaporation rate. The additional thermal mass of the salt particles may also help to maintain the solvent temperature at constant levels, hence maintaining evaporation rate. Solvent molecules in both cases vaporize from the liquid-vapor interface, diffuse across a boundary layer, and mix with ambient gases. This stage is controlled by external diffusion across the boundary layer, and is expected to dominate the process if the boundary layer is large. As the initial surface liquid layer is depleted, a constant evaporation rate can be maintained by replenishing the evaporated volume with liquid

from the interior of the porous body. Isolated dry regions develop on the exterior surface as drying continues, but constant rate may still be maintained initially by lateral diffusion of vapor molecules within the boundary layer. This is particularly true if lateral diffusivity within the boundary is much faster than that *through* the boundary. Liquid redistribution due to capillary migration is expected to be a minimal effect for thin powder layers, especially if the particle dimensions are on the same order of magnitude as the layer thickness. The constant rate period for chloroform evaporation from a powder bed is labeled in Figure 4.6.

The second stage of drying commences when the evaporated volume is no longer replenished adequately by capillary migration of liquid from the interior to the surface, or when lateral diffusion inside the boundary layer is insufficient to compensate for the loss in surface area. The second drying stage is termed "first falling rate period", and the evaporation process is controlled by the capillary migration kinetics of bulk liquid to surface. The final stage of drying is termed "second falling rate period". This stage is characterized by solvent vapor diffusion from isolated wet pores to the surface through the interconnected dried pores. Pathways in thin powder layers for vapor diffusion are expected to be more straight-forward than those in thick granular structures.

4.5 EVAPORATION FROM THIN LAYER OF DISSOLVING PARTICLES

4.5.1 Background

This section considers solvent evaporation from 3DP™ structures composed of solvent-particle systems which bind by the dissolution/re-precipitation mechanism. This is a very different problem than that described in the previous section. Evaporation rate in the dissolving case is expected to be lower than the non-dissolving case, if the particles dissolve and the rough particulate surface is reduced to a more planar surface. Evaporation rate may be reduced even if particle dissolution is much slower than evaporation rate, if solvent penetration into the particles is fast. The objective of this section is to determine the evaporation rate during dissolution/re-precipitation.

4.5.2 Materials and methods

PLGA (85:15 108,000) particles were manually spread to uniform 200 μm thick layers as described in section 4.4.2. Two particle size ranges were used for the PLGA particles: <45 μm and 75-150 μm. 5 samples were tested for each size range.

4.5.3 Observations

Mass loss profile during chloroform evaporation from a powder bed of <45 μm PLGA (85:15 108,000) is shown in Figure 4.8. This constant rate period appears to be longer than that in Figure 4.6. A non-linear regime can be seen on the right side. The time scale for transition from the constant rate period to the non-linear period was found to be over 200 seconds. The extend of the linear region was determined by using linear regression analysis and identifying the limits where $r^2 > 0.99$. The slope value as determined in this manner was converted into evaporation rate, expressed as $\mu mole/s*cm^2$. Evaporation rates for all samples were determined similarly, and the averages and standard deviations are plotted in Figure 4.9. Evaporation is lower than the case of non-dissolution. Solvent uptake into the polymer particles may account for the differences. Another contributing factor may be better wetting between the polymer and chloroform, than it is between the salt and solvent. The dotted line shown corresponds to the chloroform evaporation rate as listed in Table 4.2. It can be seen that solvent evaporation from a dissolving particulate surface is significantly faster than that from a planar, smooth surface. The data indicate that particle size has minimal effects on the kinetics of chloroform evaporation from a thin layer of dissolving powder.

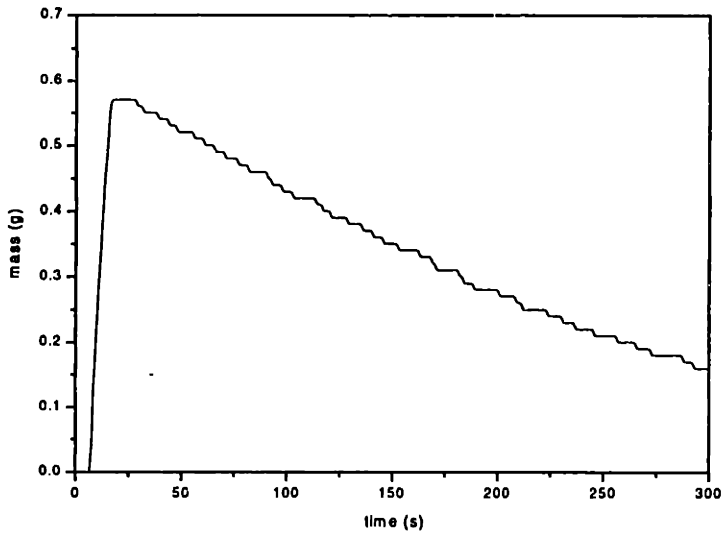

Figure 4.8: Mass loss profile during chloroform evaporation from PLGA particles

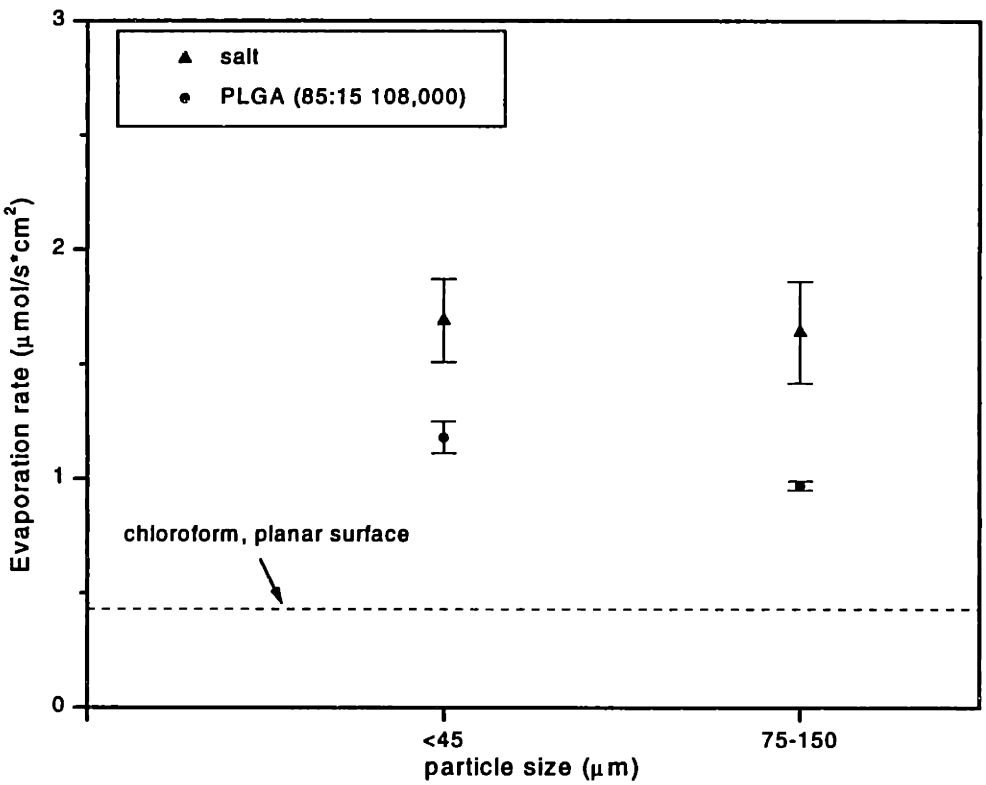

Figure 4.9: Dissolving vs. non-dissolving particles on evaporation kinetics

4.5.4 Discussion

It was shown in section 4.2.4 that for drying of liquids, increase in vapor pressure of the evaporating gas phase effectively lowers the driving force for evaporation, hence decreases evaporation rate. The opposite had been reported for drying gels, where decreased solvent vapor in gas phase resulted in reduced solvent evaporation rate. This observation was attributed to concentration dependence of diffusion coefficient. Crank[71] investigated one diffusivity-concentration relationship and argued that the concentration dependence of diffusion coefficient cannot be responsible for the observed anomaly. Crank suggested that other non-Fickian processes may be involved. Vrentas and Vrentas investigated the effects of various diffusivity-concentration relationships and surface concentrations on solvent evaporation rate, and developed an analytical perturbation solution for the nonlinear problem. A dimensionless quantity W was defined as the ratio of amount of solvent evaporated at time τ for various surface concentration ($0<\alpha<1$), to that at time τ for zero surface concentration ($\alpha=0$). W was seen to decrease monotonically with increasing surface concentration, for a large range of diffusivity-concentration dependence (from zero dependence to very high dependence). The authors suggested that the analysis support Crank's conclusions that evaporation rate is independent of solvent concentration at the liquid surface. The analysis also suggested that the presence of a significant solvent concentration at the liquid surface does not affect drying efficiency. This may be advantageous in preventing surface solidification.

4.6 EVAPORATION VS. DISSOLUTION

The evaporation rates obtained from the previous sections can be used to estimate the time scale for complete solvent evaporation from typical 3DP™ features. The binder per unit line length (*BPULL*) is the volume delivered to print a 1 cm long line:

$$BPULL = \frac{f}{v} \text{ [cc / cm]}$$

where f = volumetric flowrate of binder solution [cc/sec]

v = printspeed [cm/sec]

The volume of solvent delivered per unit area of powder bed is:

$V = \varepsilon \cdot BPULL$ [cc]

where ε = correction factor accounting for evaporation in flight

The time scale for solvent to evaporate from the top surface of a printed line is:

$$\tau_{evap} = \frac{\varepsilon \cdot BPULL \cdot 10^6}{J_{evap} \cdot A} = \frac{\varepsilon \cdot f \cdot 10^6}{J_{evap} \cdot v \cdot A} \text{ [s]} \quad (4.4)$$

where A = area of top surface of printed line [cm^2]

The correction factor for chloroform evaporation in flight is 0.9. The 10^6 is for unit conversion from nl to ml. Typical 3DP™ lines range from 300 to 500 μm, depending on packing density and extent of capillary migration. A typical 3DP™ single line is approximately 300 μm wide, while a typical wall comprised of a vertical stack of single lines is typically 500 μm wide. The time scale can be estimated by using representative operational flow rates of 0.8 cc/min, and chloroform evaporation rates determined in earlier sections for PLGA (85:15 108,000) particles.

The unvented evaporation time scale for three line widths are plotted in Figure 4.10. It can be seen that the time scale of evaporation is not significantly affected by changes in printspeed for speeds above 60 cm/s, and is highly sensitive to printspeed below 30 cm/s. Widths of the printed lines, hence evaporating surface area, appears to have more influence on evaporation time scale than printspeed under typical 3DP™ operational conditions. The plot shows that even at the lowest saturation, the minimum evaporation time is approximately 17 seconds.

The effect of ventilation on evaporation rate was shown in section 4.3 to be extensive. The time scale for solvent evaporation is expected to be significantly less. The vented evaporation time scale for three typical line widths are plotted in Figure 4.11. It can be seen that the time scale of evaporation is not significantly affected by changes in printspeed for speeds above 30 cm/s, and is highly sensitive to printspeed below 15 cm/s. Less dependence on primitive dimension is also observed. Figure 4.11 shows that even at maximum printspeed (lowest saturation), the minimum evaporation time is approximately 3 seconds. This is within the time scale for PLGA particle dissolution, as reported in chapter 3. It should be emphasized that the plots in and Figure 4.10 and Figure 4.11 are

based on calculations which do not account for capillary migration of the solvent into adjacent pores, and become unavailable for particle dissolution. An additional assumption is that evaporation occurs only from the top surface, but in reality some evaporation is expected along portions of other surfaces. The evaporation rates used to generate Figure 4.10 and Figure 4.11 were measured from solvent evaporation from a large area. The plots were based on evaporation from thin lines, which have larger surface area to volume ratio. The combined effect of these conditions is that the evaporation time scales predicted in Figure 4.10 and Figure 4.11 represent upper limits.

The effects of ventilation on evaporation time scale can be better appreciated by combining the two previous figures, as shown in Figure 4.12. Significant reduction in time scale is achieved with ventilation. It should be noted that although the plot shows that approximately 3 seconds are needed for complete evaporation, it does not suggest that 3 seconds are available for dissolution. The solvent-polymer gel mixture becomes increasingly polymer-rich during initial evaporation and dissolution. Dissolution may cease when enough chloroform has evaporated, or enough polymer has dissolved, to exceed the solubility limit for PLGA (85:15 108,000) in chloroform. The actual time available for particle dissolution are expected to be less than predicted by the evaporation time scales.

The previous three plots showed a dramatic dependence of time scale on printspeed for the low printspeed regimes. It should be emphasized that those extremely low printspeeds are not practical in 3DP™, as they tend to deteriorate print resolution. A better approach to maximize particle dissolution is to decrease line spacing between adjacent lines, but preserve print resolution by staying on the high printspeed regime.

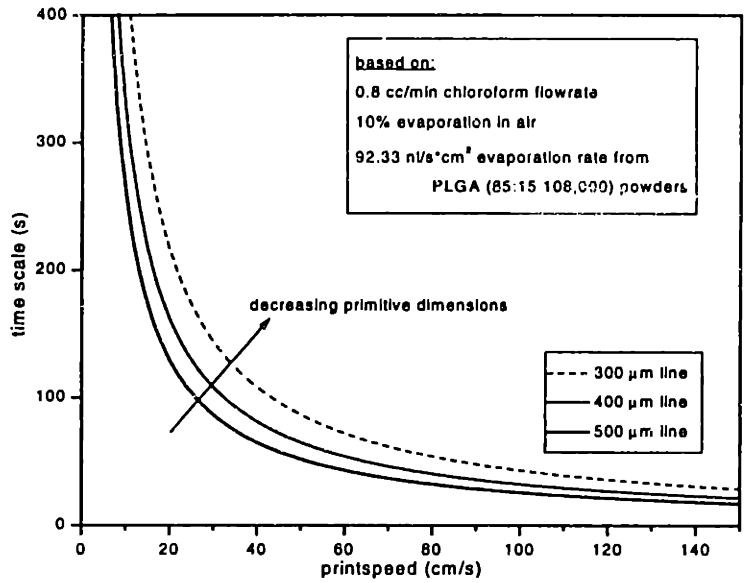

Figure 4.10: Chloroform evaporation time scale from PLGA bed (unvented)

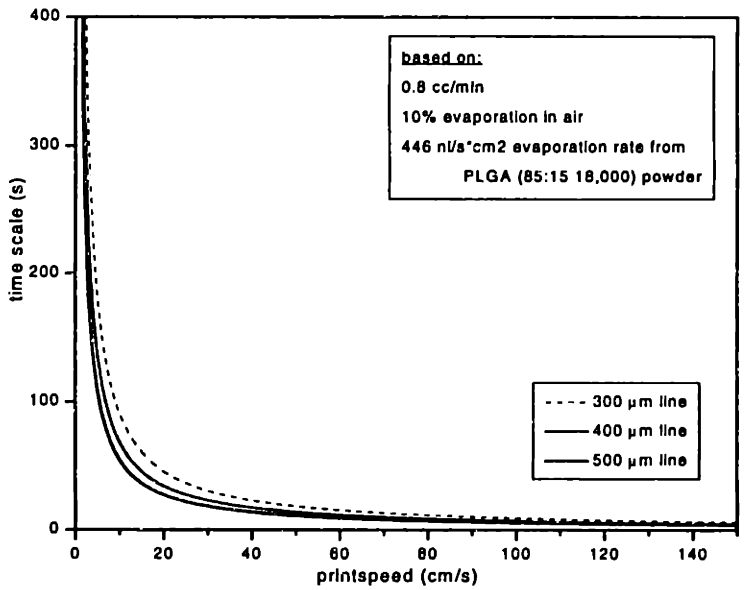

Figure 4.11: Chloroform evaporation time scale from PLGA bed (vented)

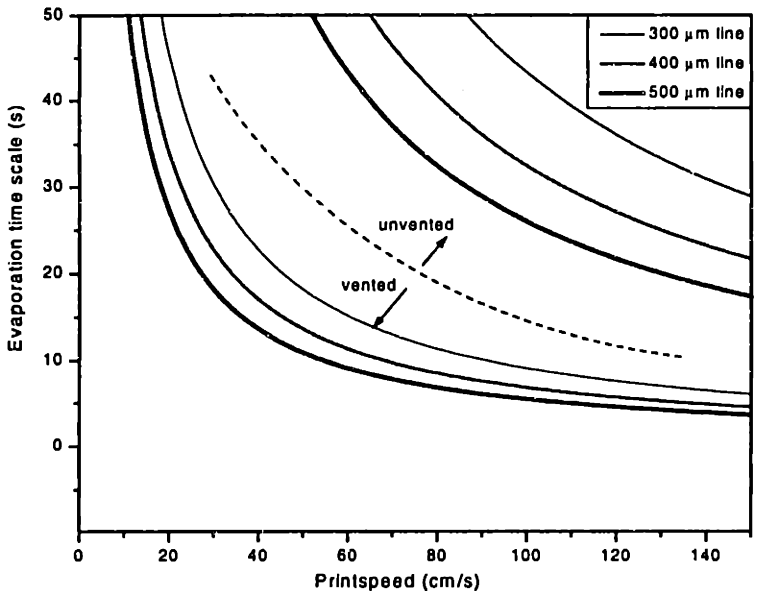

Figure 4.12: Effect of venting on chloroform evaporation timescale

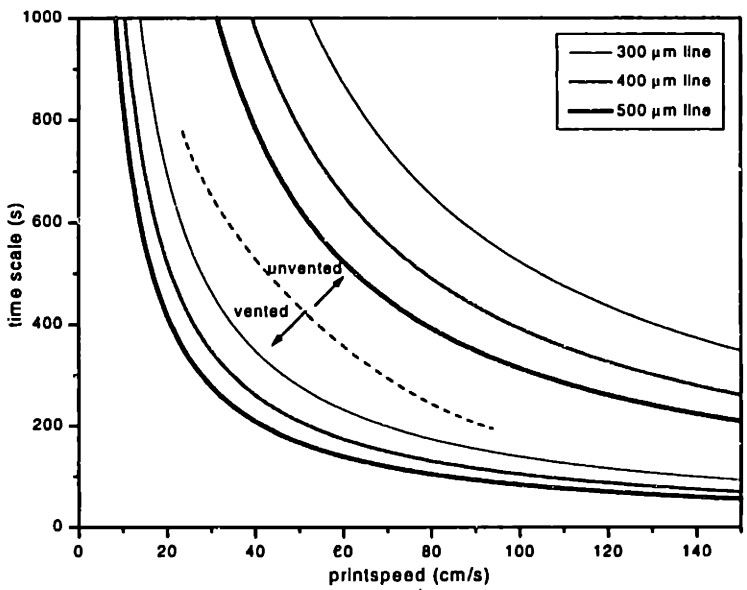

Figure 4.13: Evaporation timescale for water from 3DP™ powder bed

Aqueous binders represent the opposite extreme in terms of evaporation kinetics. Table 4.2 shows that the evaporation rate of water (2.85 nl/s*cm^2) is less than 9% that of chloroform (34.46 nl/s*cm^2). Evaporation of water droplet in flight can be evaluated as shown in section 4.2.3 to be less than 1% in volume over a flight distance of 3 cm. Lines printed with aqueous binders are expected to require significantly longer drying time (Figure 4.13). In practice the drying of aqueous binders may be accelerated by increasing the ventilation rate, and/or by raising the powder bed surface temperature with a heat source. The contrast between Figures 4.12 and 4.13 is significant. The evaporation timescale for chloroform is less than 10 seconds at printspeed above 100 cm/s, while the timescale under similar printing conditions for water is approximately 100 seconds. The minimum time required for dissolution was presented in Table 3.1.

Table 3.1 suggests that the 10 seconds evaporation timescale for chloroform may be sufficient to allow complete dissolution of PLGA (85:15 108,000) particles below 75 μm and PLLA (MW < 132,000) particles below 60 μm. This is in good agreement with experimental observations from actual 3DP™ structures. Giordano et al.[80] printed chloroform (binder flowrate = 0.83 cc/min) into two molecular weight groups (53,000 and 312,000) of PLLA particles at various printspeed (45 -150 cm/s). 75-150 μm particles were used for the experiments. PLLA (53,000) particles were found to dissolve well with typical printspeed (75 - 100 cm/s). Giordano et al. reported that PLLA (301,000) did not dissolve well in chloroform, even under very low printspeed (45 cm/s) with excessive binder migration. [80] This is not surprising since, according to Table 3.1, over 18 seconds are required to dissolve even sub-30 μm PLLA (301,000) particles. It should be re-emphasized that finite quantities of particles and liquids are involved during 3DP™, and solvent evaporation during 3DP™ is expected to decrease the amount of time and solvent available for particle dissolution.

The dissolution time vs. particle size for PLGA (85:15 108,000) in chloroform can be superimposed onto Figure 4.12 to illustrate the influence of dissolution-evaporation on microstructure formation (Figure 4.14). Chloroform was delivered under identical printing conditions (shaded circle) into powder bed mixture containing 60% v/v salt and 40% v/v PLGA particles of various dimensions. The samples were sectioned for

SEM analysis after particulate leaching. It can be readily seen that complete dissolution is achieved for <45 μm PLGA particles (SEM #1), and 45-75 PLGA particles (SEM #2). The different pore sizes are due to different initial salt particle size. The dotted horizontal line shows that at 150 cm/s, the evaporation time is greater than that required for complete dissolution of particles smaller than 90 μm. SEM #3 shows that the larger particles are connected to each other, but they are not completely dissolved. This is not surprising, since the dissolution-evaporation plot shows that the time scale for dissolution of large particles is much greater than that for evaporation. Dissolution of these larger particles can be improved by varying the printing parameter (shaded square). SEM #4 shows that by decreasing the printspeed by 50%, the dissolution time scale in increased, and more particles are dissolved. The micrograph shows that not all of the particles are dissolved, as predicted by the dissolution-evaporation plot. The dissolution plot suggests that complete dissolution of the large particles can be achieved by turning off the ventilation, or by decreasing the printspeed. Such slow printspeeds are impractical for 3DP™ since they deteriorate feature resolution. Future, completely automated versions of the 3DP™ machine can be placed into dedicated chambers in which ventilation rates can be carefully controlled.

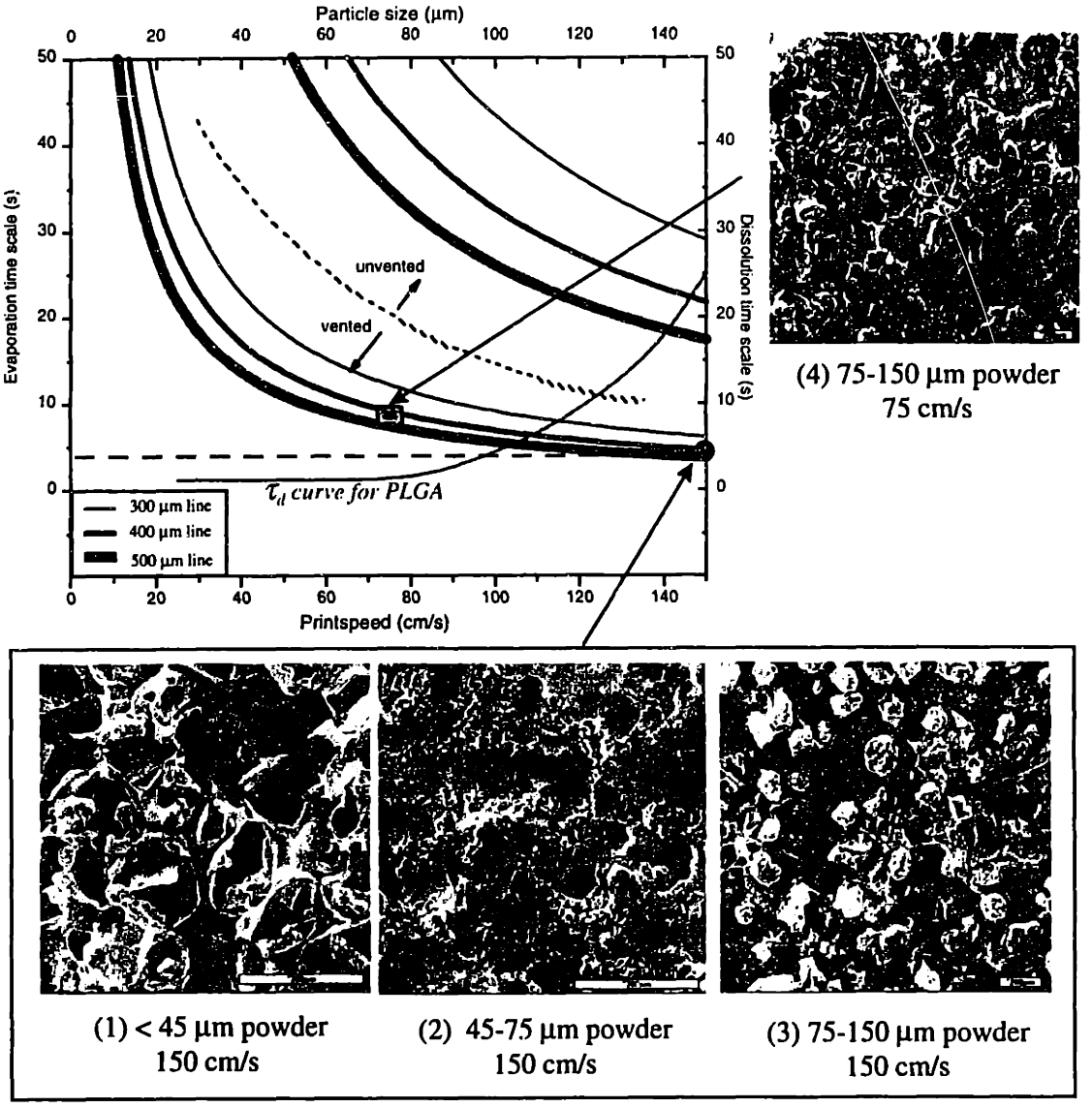

Figure 4.14: Dissolution-evaporation plot for PLGA (85:15 108,000) in chloroform

5. DENSE STRUCTURES by 3DP™

5.1 BACKGROUND

Highly dense ceramic parts have been produced by 3DP™, but they are obtained only with appropriate post-processing procedures. The green density of ceramic and metal 3DP™ parts is highly dependent on the powder type, and ranges from 40 to 55%. The green density can be increased to approximately 60% by isostatic pressing[72], but structures with complicated internal geometry may undergo anisotropic densification. An alternative approach to improve the green density is to increase the initial density of the powder bed prior to binder deposition. Powder beds with ~56% theoretical density have been reported by spray deposition of ceramic slurry layers[73]. Even higher green density can be achieved by tape casting of the slurry (~68% dense). Highly dense ceramic parts are then achieved after binder burn-out and sintering (>99%). Another strategy is to obtain partial sintering of ceramic particles, and then infiltrate the porous ceramic network with glass to form dense structures[74]. This approach has the added benefit of producing near net-shape structures directly from 3DP™, since sintering shrinkage is virtually eliminated. The infiltration approach is also used to achieve high density metal parts by infiltrating a partially sintered stainless steel matrix with molten bronze. Direct dense green ceramic and metal parts are not possible because the highest theoretical packing density is only 74%, and are also undesirable. Excessive dimensional distortion and stresses can develop if a porous (~50% dense) powder bed is rapidly densified during printing. The stresses associated with such large dimensional distortions can result in cracking and failure of the pre-fired ceramic or metal part. Highly dense parts have not been achieved by *directly* printing binder into metal or ceramic powder beds. Most post-printing densification techniques are inappropriate for biopolymers.

Dense, defect free microstructure is required for most drug delivery devices in which uncontrolled, random processing defects can adversely and unpredictably affect the drug release kinetics. The ability to minimize random printing defects may be important even for delivery systems which are based on drug transport through porous matrices[75,76,77]. Highly dense structures are also necessary for maximum mechanical

properties in high strength orthopedic fixation devices, such as bone screws[78], plates, and rods[79]. Random processing defects can also significantly reduce the mechanical properties of these structural devices[80], resulting in clinical complications.

Dissolution of polymer particles was reported in Chapter 3. The competing parameters in particle dissolution were analyzed in Chapter 4. One oversimplified approach to create dense structures is to increase particle dissolution by over-saturating the powder bed with polymeric solvents. This approach is unacceptable since it would sacrifice print resolution and dimensional accuracy. The need to simultaneously minimize defect formation and maximize printing resolution requires further understanding of the primitive formation process. Section 5.3 describes the common defects observed in actual printed structures, and summarizes the efforts to identify the relevant materials properties and processing parameters which affect defect formation. The final section will discuss strategies to fabricate highly dense polymeric medical devices *directly* from 3DP™, without forfeiting print resolution.

5.2 MATERIALS AND METHODS

3DP™ specimens for microstructural analysis were designed to be square in cross section, no greater than 1.5 mm in width and height, and 35 mm in length (Figure 5.1). A typical specimen is printed in 8 successive layers. Layers 1 to 3 are identical, and are built by printing 3 successive sheets to form the "base layers" on the bottom of the specimen. Layers 4 and 5 form the channel layers, which are constructed by printing 2 narrow sheets separated by a reservoir channel approximately 300 μm in width. This results in 2 "solid" side walls, and an un-printed channel along the center of the specimen. Layers 6 to 8 on the top comprise the so called "top layers", and are essentially 3 successively printed sheets, similar to layers 1 to 3 in terms of print strategy. The top layers differ from the non-releasing layers only in composition of the binder used to construct the layers. Specimens were constructed by 3DP™ with various combinations (see Table 5.1) of processing parameters and materials properties. Powder materials tested include polylactides, polylactide-co-glycolides, and polycaprolactones. Each polymer type is available in different molecular weights and particle size distributions. The polylactide-co-glycolides are also available in different blend ratios (lactide:glycolide

ratios). In addition, polylactides and polylactide-co-glycolides can be mixed mechanically in various proportions of PLLA:PLGA mixture ratios. Interesting binder parameters include composition of the solvent used in the binder, composition, molecular weight, and blend ratio of the polymer in the binder.

Important printing parameters are layer thickness, printhead velocity (or print speed), line spacing, and print style. Non-printing parameters which may affect drying defects include drying protocol between layers, and drying treatment after printing. Table 5.1 contains a list of important parameters. An important advantage of 3DP™ is its ability to rapidly fabricate a large number of devices out of different materials and printing variables. The devices were dried, sectioned, and prepared for microstructural analysis in scanning electron microscopy.

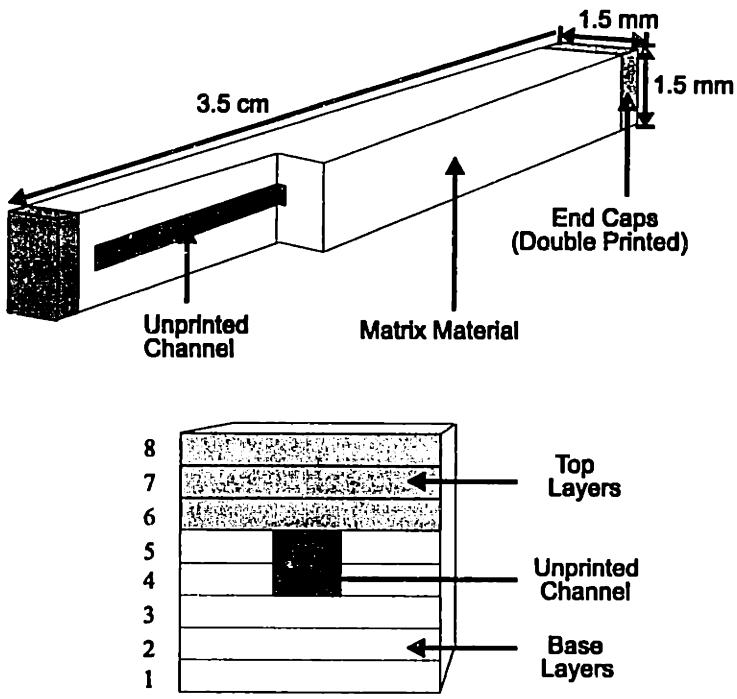

Figure 5.1: Diagram of specimens used for defect analysis

Powder Composition
Composition
Molecular Weight
Mixture Ratio (PLLA:PLGA)
Blend Ratio (L:G)
Particle Size
Binder Composition
Composition of Solvent
Composition of Polymer
Molecular Weight
Blend Ratio (L:G)
3D Printing Parameters
Layer Thickness
Print Speed
Line Spacing
Print Style
Drying Parameters
Air Drying in Between Layers
Heating in Between Layers
Drying Treatment after Printing

Table 5.1: Relevant material and machine parameters

5.3 OBSERVATIONS

5.3.1 Defect classification

Microstructural analysis revealed 3 categories of recurring processing defects: lamination defects, sintering defects, and drying defects. Lamination defects (Figure 5.1) are irregularly shaped defects which lie along the horizontal interface between the successive layers. Vertical spacing, approximating that of the powder layer height, can be seen between rows of lamination defects. Sintering defects (Figure 5.2) are irregularly shaped defects which are distributed randomly within each layer. Incomplete particle dissolution is thought to be responsible for both defect types. Drying defects (Figure 5.3) are well-defined pores with smooth, round borders, and can be easily distinguished from the other two defect types. Drying defects are generally observed when little or none of the other defects are observed, suggesting that their formation is limited to highly soluble polymer-solvent systems. Their well-defined borders also suggest an association with a surface tension driven phenomena during the initial stages of solvent evaporation, when the polymer is still soft enough to flow.

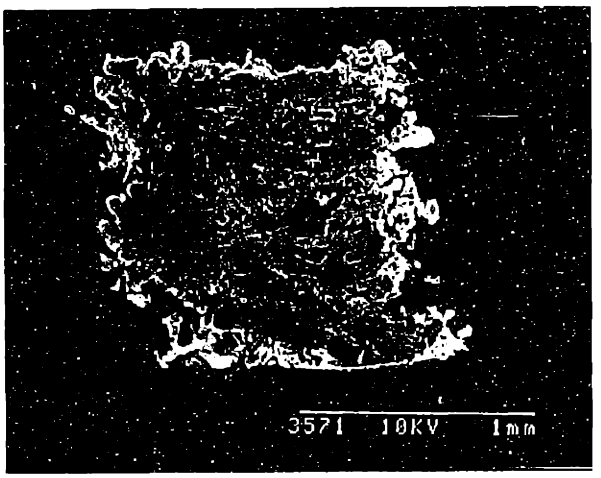

Figure 5.1: Cross sectional view of specimen device showing lamination defects

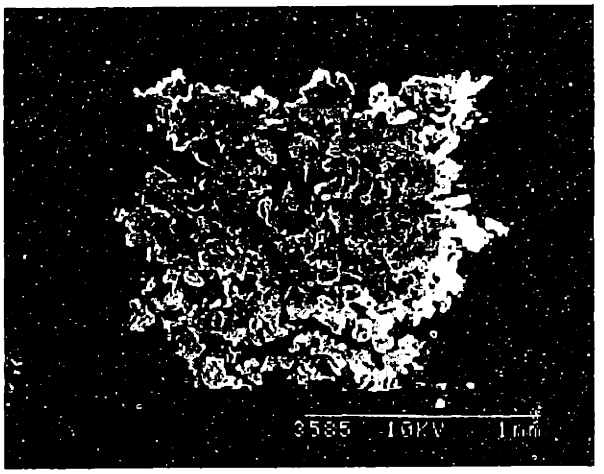

Figure 5.2: Cross sectional view of specimen device showing sintering defects

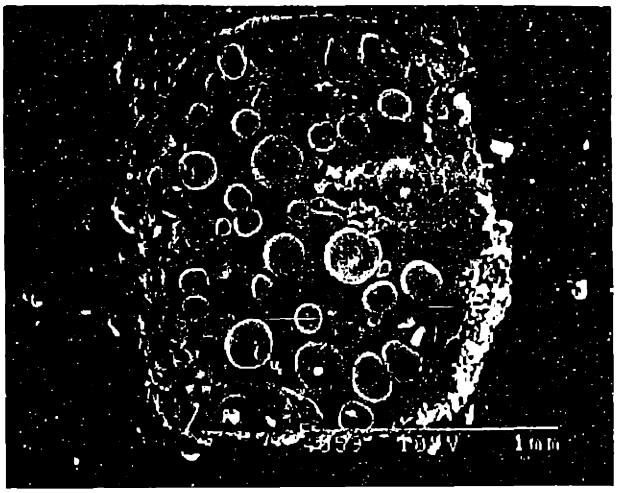

Figure 5.3: Cross sectional view of specimen device showing drying defects

5.3.2 3DP™ terminology

Familiarity with several popular 3DP™ terms would facilitate the data analysis in the following sections. A common term among 3DP™ practitioners is "binder per unit line length", or BPULL. BPULL the volume of binder deposited onto the powder bed per unit length of printed length. It is a function of the volumetric flowrate of the binder through the nozzle, and the printhead travel velocity. It does not account for binder evaporation during flight, and liquid splashing upon impact, although these can be easily included.

$$\text{BPULL} = \frac{f}{v\rho_b} \text{ [cc/cm]}$$

where f = mass flowrate of binder solution [g/sec]

v = printspeed [cm/sec]

ρ_b = binder density [g/cc]

Another term used often in 3DP™ saturation. It is a dimensionless ratio of the volume of binder deposited per unit length and the available inter-particle void volume in the powder bed:

$$\text{Saturation} = \frac{\text{BPULL}}{(1-\rho_p)\Delta x \Delta z}$$

where ρ_p = powder packing density

Δx = line spacing

Δz = layer thickness

One of the drawbacks with the term saturation is that the actual void volume is not known. The actual amount of loose powder, for example, cannot be accurately determined due to ballistic ejection, which is generally more extensive with polymeric powder. Horizontal and vertical binder migration into surrounding pores can be quite unique to each binder-powder combination. Another complicating factor for polymer system is the changing particle dimensions during printing. Swelling from a previously printed line can intrude into the void space of the new line. Solvent uptake by the

particles from the previous layer can also affect the actual volume of binder available for the current layer. The calculated saturation values are hence less meaningful, but can be used with caution to compare samples made with the same powder-binder combinations, and similar printing conditions.

A new quantity, β_x, can be defined by dividing BPULL by Δx (line spacing). β_x represents the volume of binder deposited per unit horizontal area, when all the other printing parameters are kept constant. The use of β_x allows more meaningful data analysis since it is less sensitive to ballistic effects. More importantly, the effect of line spacing on defect formation can be isolated by simply plotting defect scores to β_x. Higher values of β_x are less desirable, since they can result in deteriorated resolution. One objective of the data analysis is to simply identify the minimum β_x which results in defect-free parts.

5.3.3 Defect scoring system

An ordinal defect scoring system was developed to allow efficient evaluation of the scanning electron micrographs. Each micrograph was visually analyzed and assigned "defect scores" for each of the three categories of defect types described in section 5.3.1. A defect score of "4" represents a failure, and is assigned to devices which are too weak to be sectioned for SEM. A score of "3" signifies the presence of numerous defects and/or large defects (>300 μm). These devices are unacceptable because the defects are likely to dominate release profile. A defect score of "2" represents the presence of a moderate number and/or smaller defects (<300 μm). The release profile of these devices is not likely to be dominated by the defects. A score of "1" is assigned to those devices with very few small defects (<200 μm), while a score of "0" is assigned to devices with none of the defect type. The scoring guidelines are summarized in Table 5.2. Sample micrographs with defect scores ranging from 0 to 3 for lamination defects are shown in Figure 5.4. Examples of sintering and drying defect scores are shown in Figure 5.5 and Figure 5.6, respectively. An SEM with a composite defect score of 0-0-1, for example, represents a cross-section of the device with no lamination and sintering defects, but some non-critical size drying defects.

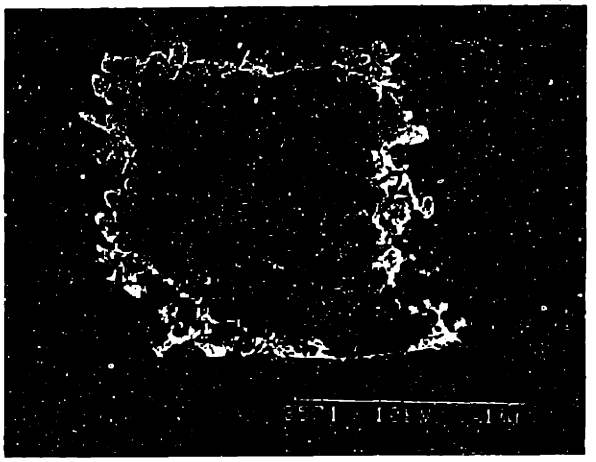

Lamination Score = 3

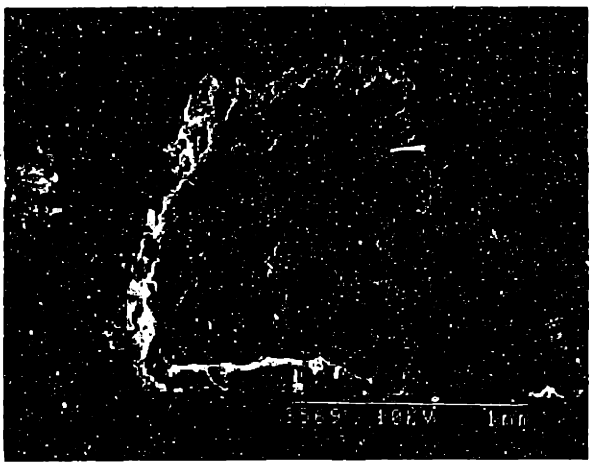

Lamination Score = 2

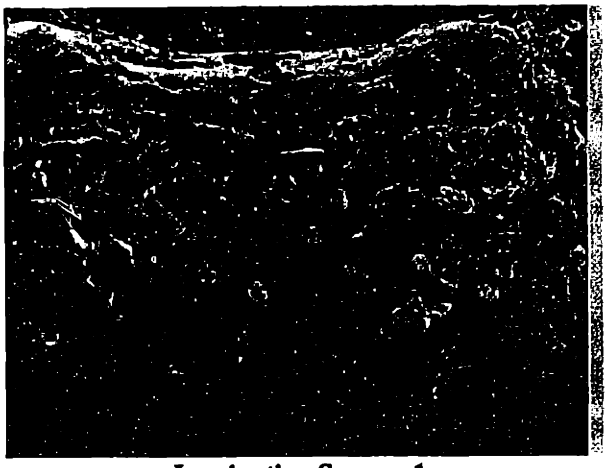

Lamination Score = 1

Lamination Score = 0

Figure 5.4: Lamination defect scores

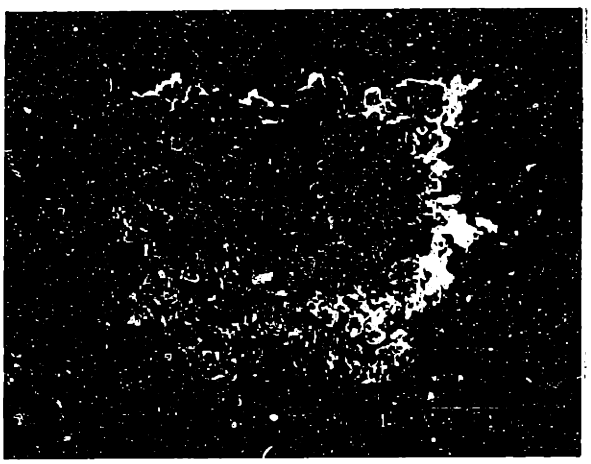

Sintering Score = 3

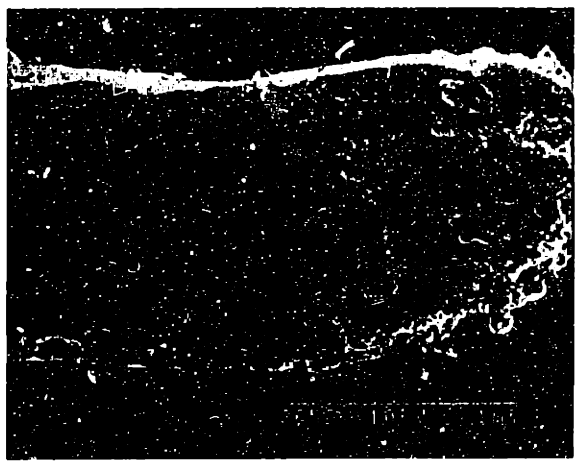

Sintering Score = 2

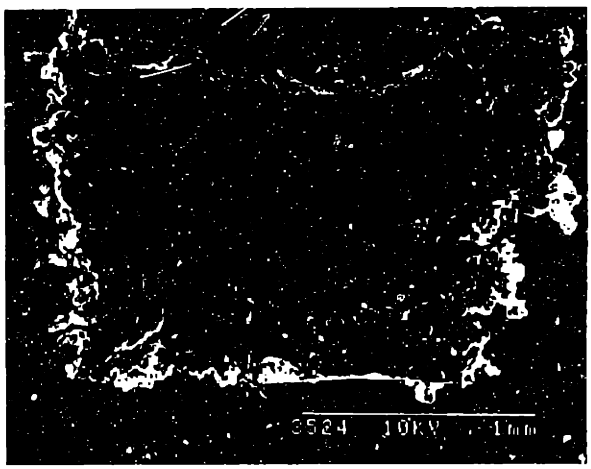

Sintering Score = 1

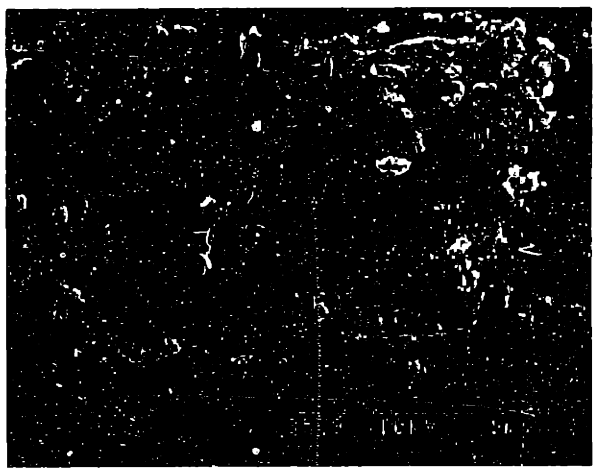

Sintering Score = 0

Figure 5.5: Sintering defect scores

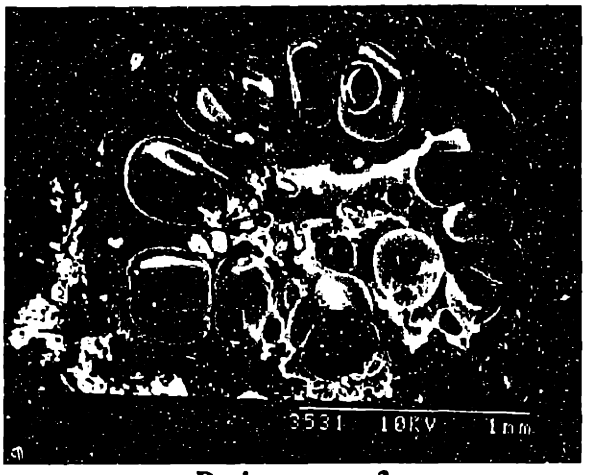

Drying score = 3

Drying Score = 2

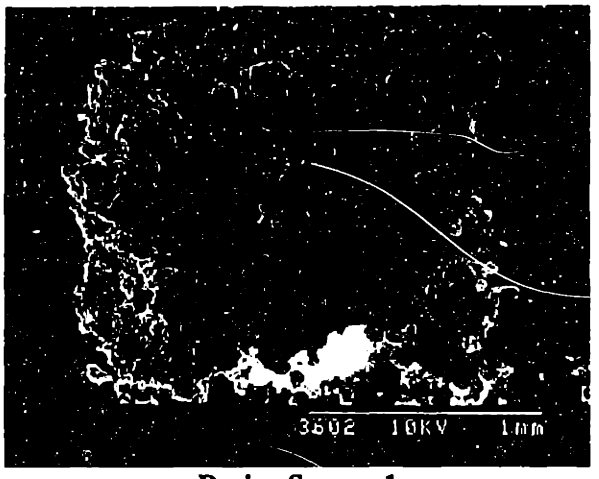

Drying Score = 1

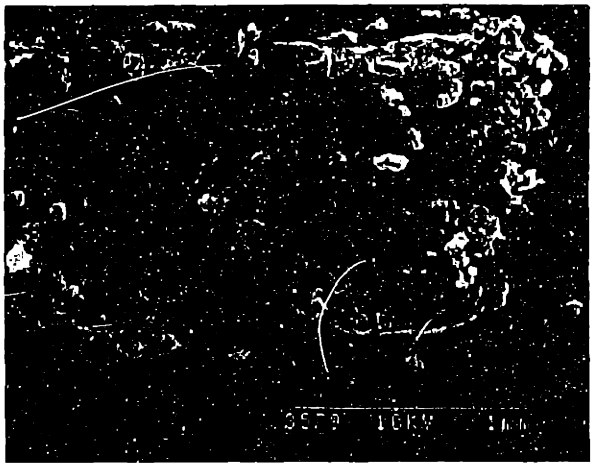

Sintering Score = 0

Figure 5.6: Drying defect scores

All micrographs were analyzed independently by two investigators. The composite defect scores from both investigators were then combined, and compared to assess the frequency and severity of defect formation. Despite the qualitative nature of the defect scoring system, it has proven to be practical for comparing various parameters when they are plotted against the appropriate processing variables. Print resolution was evaluated by comparing the actual printed dimensions with the intended dimensions. The un-printed channel along the center of each sample can also serve as an indicator for resolution control. Complete obliteration of the channels, for example, would indicate poor resolution.

Score		Description
4	Failure	too fragile to section
3	Unacceptable	>300 μm
2	Okay	200 - 300 μm
1	Good	<200 μm
0	Excellent	zero

Table 5.2: Defect scoring system

5.3.4 Data representation

Plots such as that shown in Figure 5.7 can be very useful for relating materials properties to processing parameters when similar plots from different material systems are compared. The shaded region in Figure 5.7 can be thought of as the "sweet spot", where defect free devices can be made with optimal print resolution. The "sweet spot" may represent the processing window in which minimum defect formation and maximum printing resolution can be produced.

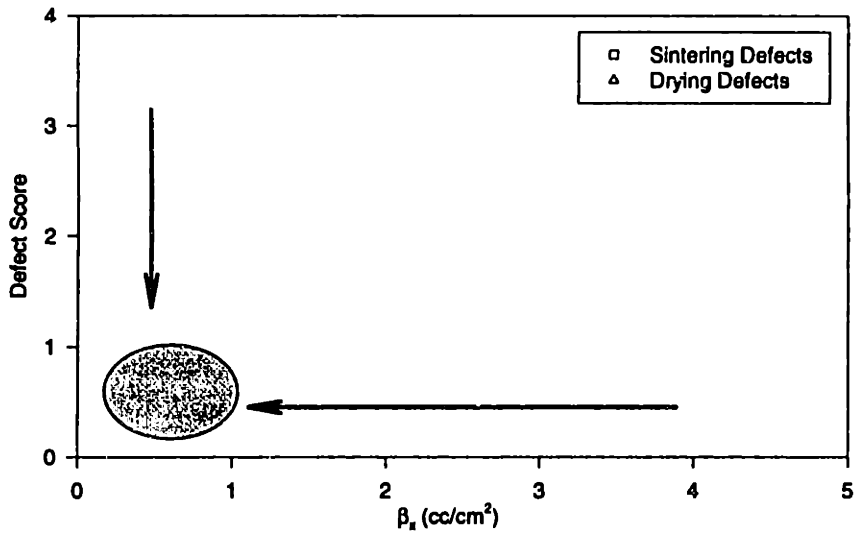

Figure 5.7: Defect score vs. βx

5.3.5 Effect of material properties

Low molecular weight polylactide-co-glycolide (65L:35G 53,000) were observed to be highly susceptible to developing drying defects, but not sintering defects. Figure 5.8 shows a cross sectional SEM of a specimen produced by printing acetone into PLGA (65L:35G 53,000MW) particles. Large drying pores, on the order of 700 μm in diameter, can be seen. No sintering or lamination defects are noticeable. This observation was generally true for all pure-solvent binders, such as chloroform and acetone. Figure 5.9 represents the drying and sintering defect scores of all PLGA (65L:35G 53,000) specimens which were printed with chloroform and acetone, under various printing conditions. Figure 5.9 shows that severe drying defects (drying defect score = 3) can develop in this polymer even at very low values of β_x. The plot also shows that very small amounts of binder are required to eliminate sintering defects (sintering defect score = 0). These observations may be due to the high solubility of the polymer in organic solvents. It should be emphasized that the formation of drying defects in these specimens are not caused by binder over-saturation during printing, since severe drying defects were observed even at very low values of β_x. A more likely explanation is that these polymers have lower T_g and can creep under the pressure of small solvent bubbles during the initial

stages of dissolution/re-precipitation, when the primitive is still flowable. The permeability of solvent may also be sufficiently low enough that the retained solvent can lead to bubble formation due to increased pressure.

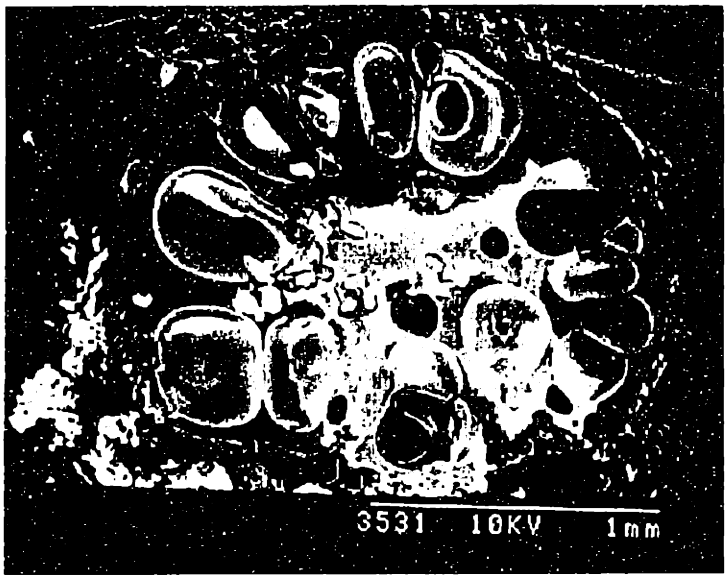

Figure 5.8: Drying defects in PLGA (65:35 53,000)

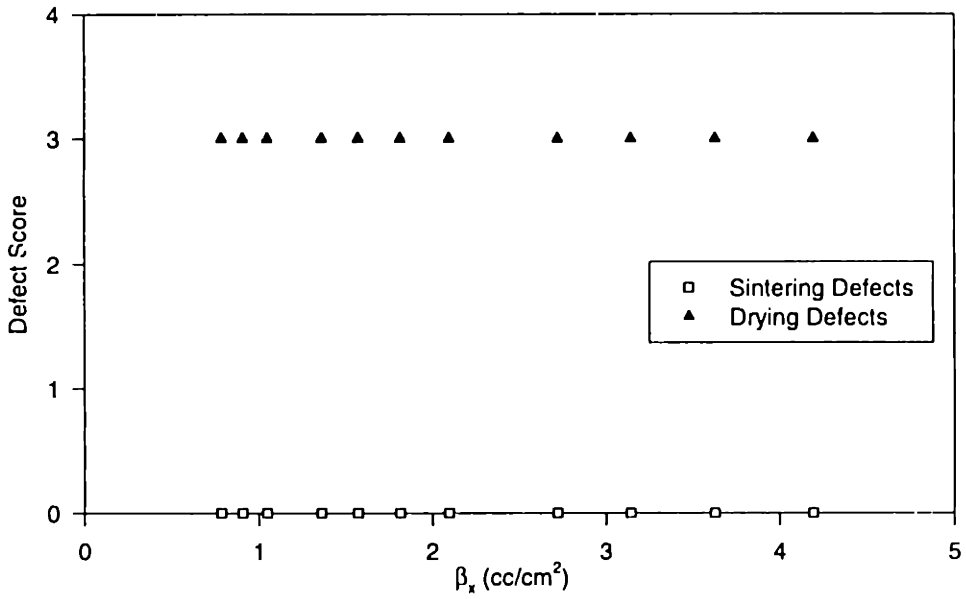

Figure 5.9: Defect vs. βx for PLGA (65:35 53,000)

On the other end of the solubility spectrum, high molecular weight poly-*l*-lactides (PLLA 301,000 MW) are associated with severe sintering defects, but no drying defects (Figure 5.10). These polymeric particles are barely soluble in acetone, and only slightly soluble in chloroform. Figure 5.11 compares the defect scores from SEMs of devices printed with either pure chloroform, pure acetone, or a polymeric binder solution containing 20% (w/w) of a low molecular weight polycaprolactone (PCL 9,000 MW). The data reveal that chloroform-printed devices are associated with severe sintering defects (score = 3), and those printed with polymeric binders have slightly less sintering defects (score = 2). Drying defects are generally not observed (drying defect scores =0) in devices made with high MW PLLA, regardless of binder used, since drying defects can only develop in regions of dissolved polymeric particles. The severity of sintering defects may worsen when less aggressive solvents are used. Large increases in β_x did not significantly reduce defect scores.

Lamination and sintering defects are associated with the poly-*l*-lactides (PLLA), and increase in severity with increasing molecular weight. This finding is not unexpected since the polymer solubility, as well as rate of dissolution, decreases with increasing molecular weight. Polylactide-co-glycolides (PLGA) are less prone to sintering defects, since they tend to dissolve more readily than PLLA. These findings further support the concept that sintering and lamination defects are caused by incomplete dissolution of neighboring particles during printing. Polymer binder solution may reduce sintering and lamination defect by filling the initial void volume in the powder bed. Binders containing pure solvents do not eliminate pore spaces because they rely only on particle dissolution. The use of polymeric binders in PLGA (65:35 53,000), however, resulted in negligible reduction of drying defects (Figure 5.12). This observation suggest that inter-particle void space is not the origin of drying defects.

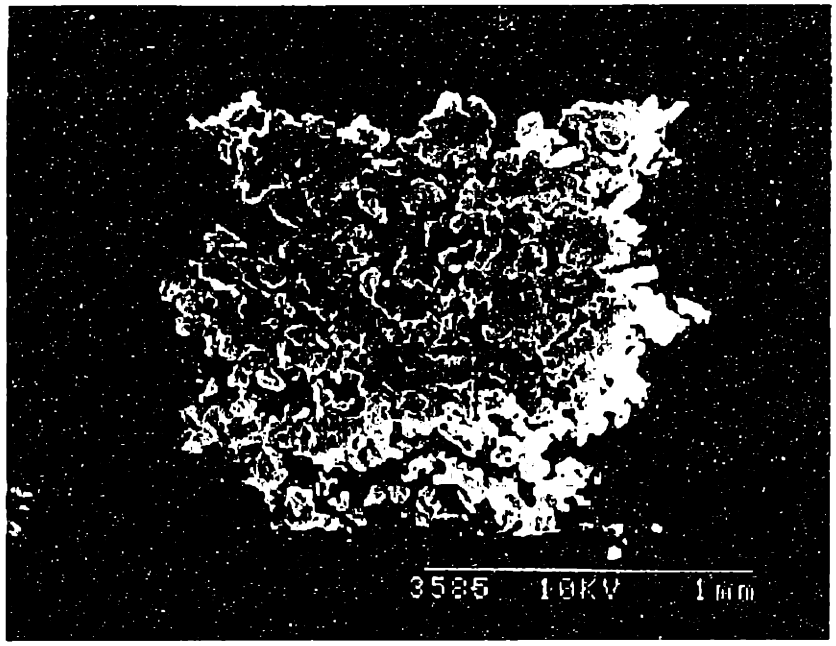

Figure 5.10: Severe sintering defect associated with PLLA (301,000)

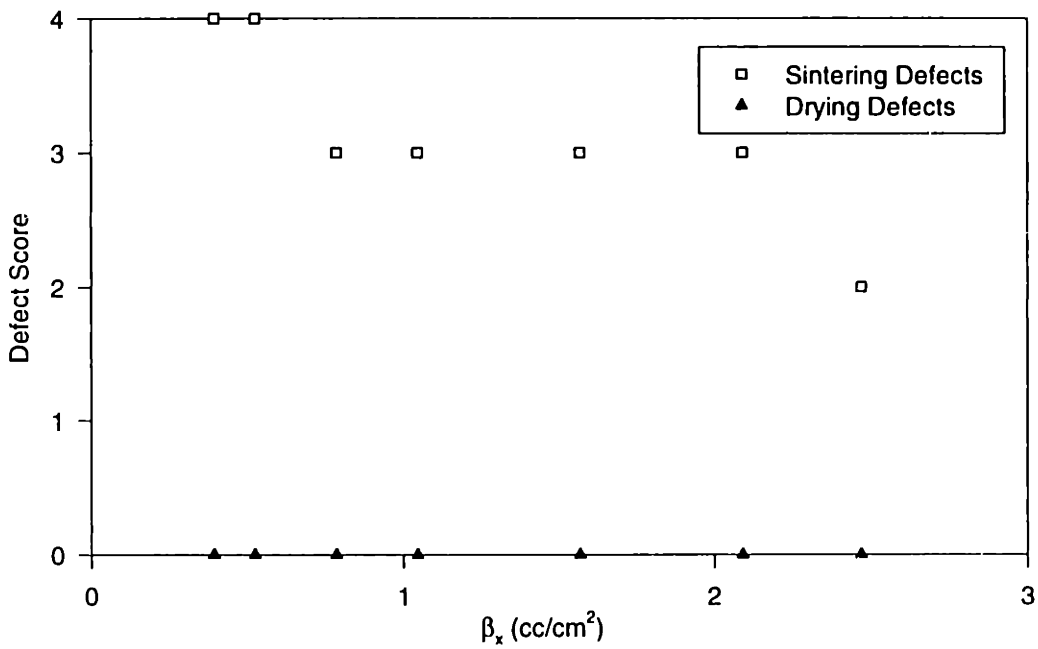

Figure 5.11: Defect vs. βx for PLLA (301,000)

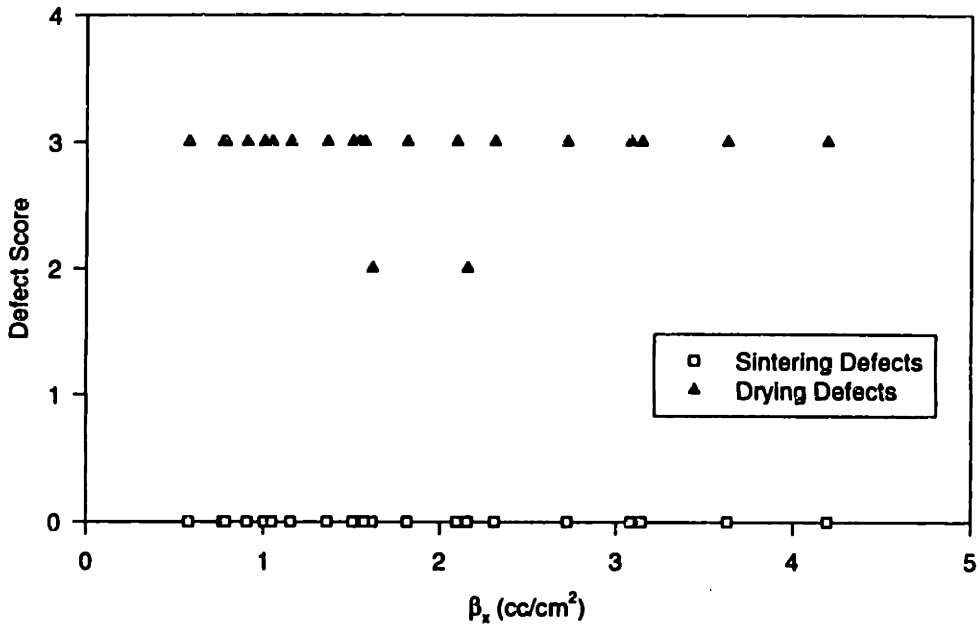

Figure 5.12: Defect vs. βx for PLGA (65:35 53,000) & polymeric binders

The materials systems cited above represent the two extremes in terms of defect formation. Many polymer systems exist in between the two extremes, and exhibit far less severe defects. In may cases, sintering and drying defects can coexist within the same device. PLLA (132,000 MW) is such an example. Devices constructed from this lower molecular weight PLLA contain all three types of defects. Figure 5.13 suggests that while the use of polymeric binders with PLLA (131,000) resulted in only a slight reduction of sintering defects, drying defects were significantly reduced.

Printing of chloroform into PLGA (85:15 100,000) particles also resulted in all three defect types. The use of polymeric binders, however, significantly reduced all defect. Figure 5.14 represents devices made from PLGA (85:15 100,000) with four different binders: chloroform only, 2.5% PCL (45,000) in chloroform, 20% PCL (9,000) in chloroform, and 12.5% PLLA (2,000) in chloroform. A new quantity, polymeric β_x, was used in Figure 5.14 to facilitate data analysis. Polymeric β_x is the volume of polymer deposited through the nozzle per unit area of printed structure. It is a useful quantity for

comparing various polymeric binders with differing concentrations of polymer content. The introduction of this term allow better differentiation between binders which contain varying amounts of polymer, such as 2.5% PCL (45,000) in chloroform, 12.5% PLLA (2,000) in chloroform, and 20% PCL (9,000) in chloroform. Such differentiation would not be possible if the axes were plotted as "defect score vs. β_x". Note that the chloroform-only binder has a polymeric β_x value of zero, therefore all data points for chloroform-only binder are represented on the vertical axis. The data suggest that the composition of polymeric binder solution is important for 100,000 MW PLGA (85L:15G). Devices printed with 2.5% PCL (45,000) and 20% PCL (9,000) solutions in chloroform contain less defects, whereas those printed with 12.5% PLLA (2,000) in chloroform actually increased drying defects. The concept that only certain polymeric binders are useful in defect elimination is further demonstrated in Figure 5.15, which compare devices made by printing acetone and 7.5% PLGA (65:35 53,000) in acetone into PLGA (85:15 100,000) powder. The data clearly shows that the use of 7.5% PLGA (65:35 53,000) polymeric binder did not result in defect reduction.

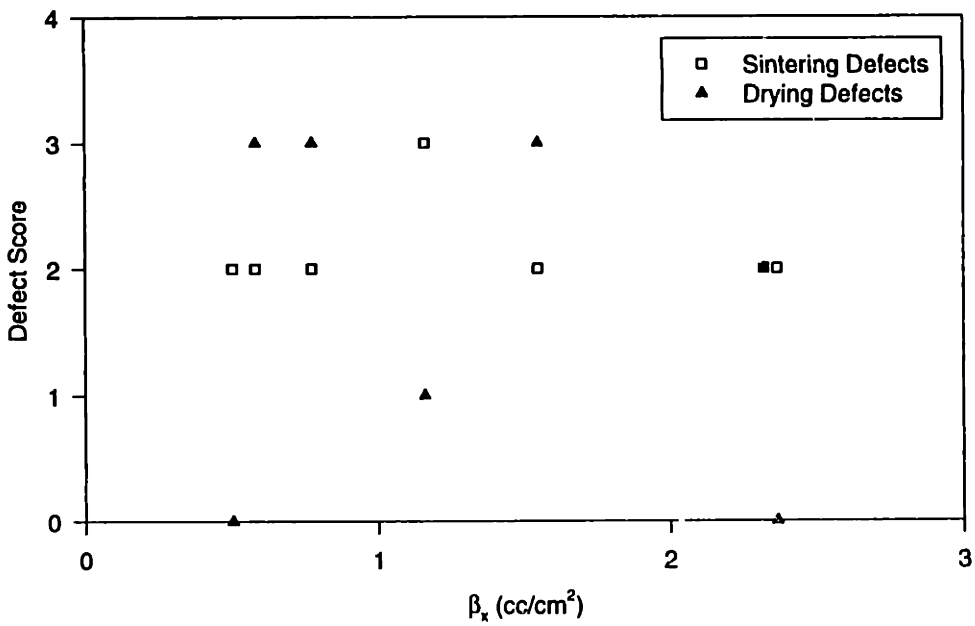

Figure 5.13: Defect vs. βx for PLLA (131,000)

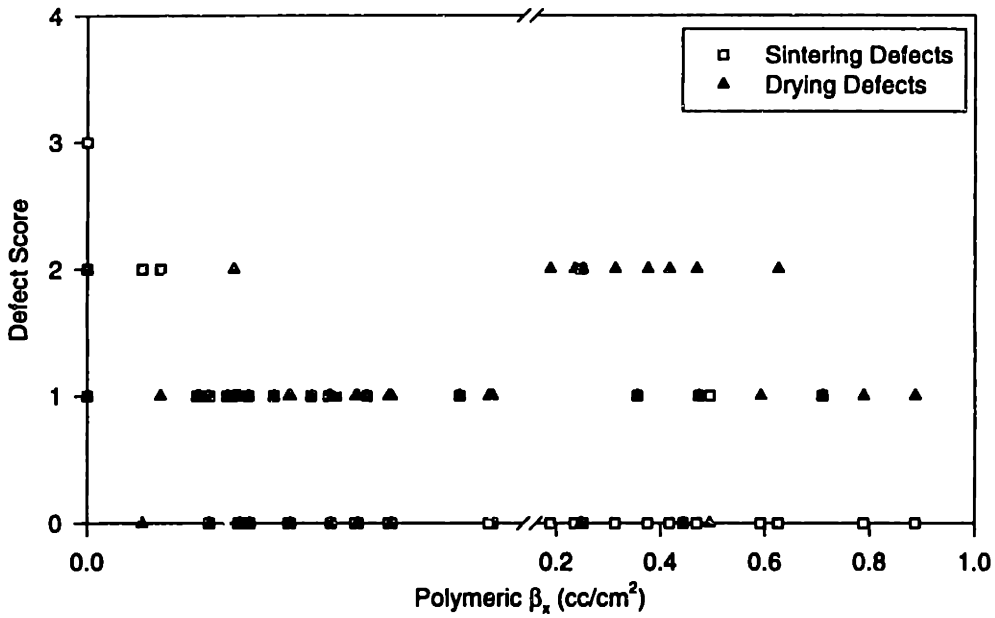

Figure 5.14: Defect vs. polymeric βx for PLGA (85:15 100,000) and chloroform

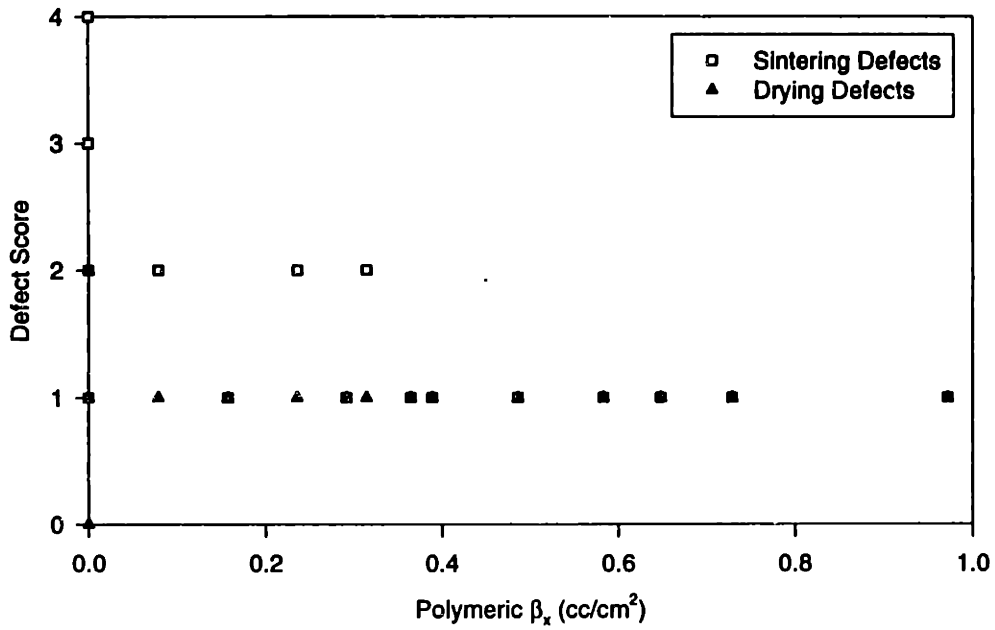

Figure 5.15: Defect vs. polymeric βx for PLGA (85:15 100,000) and acetone

5.3.6 Effect of processing parameters on defects

The previous section showed that material properties, such as particle solubility, play an important role in defect formation. The data can be analyzed to determine the role of printing parameters on defect formation. Figure 5.14 showed that defect-free structures are possible with PLGA (85:15 100,000) and certain polymeric binders. The data for one binder, 2.5% PCL, is extracted out of Figure 5.14, and re-plotted in Figure 5.16 as "defect vs. β_x". The plot would simply re-scale if "defect vs. polymeric β_x" was plotted, since only one binder is represented. The effects of binder saturation on defect formation can be readily seen. Increased β_x, as expected, lead to significant decrease of sintering defects, and minor increase in drying defects. More importantly, there is a range of β_x within which both sintering and drying defects are minimal (β_x values between 2 and 3cc/cm^2). The quantity β_x, as introduced earlier, is a grouped parameter representing the volume of binder deposited per unit area printed. The two quantities which make up β_x are BPULL and line spacing. It is important to determine the relative importance between BPULL and line spacing in terms defect formation. This can be easily accomplished by introducing another data representation scheme. Each data point shown on Figure 5.17 represents a sintering score of one SEM. The data points are assigned various symbols according to the sintering defect scores as shown in the legend of Figure 5.17. The critical line spacing seems to be 50 μm for PLGA (85:15 100,000). The significance is that when 2.5% PCL (45,000)/chloroform solution is printed into PLGA (85:15 100,000) particles at below 50 μm line spacing, defect-free devices can be at lower BPULL. The plot in Figure 5.17 clearly shows that line spacing is more significant than BPULL in sintering defect reduction. The length scale of a 3DP droplet is about 60 μm, and the typical particle size range of the powder is 45-75 μm. The 50 μm line spacing (center-to-center) should result in a 10 μm overlapping of binder droplets. One possible conclusion is that, for this materials system, 10 μm overlapping is necessary for achieving high density stitching by depositing more solid through the nozzle.

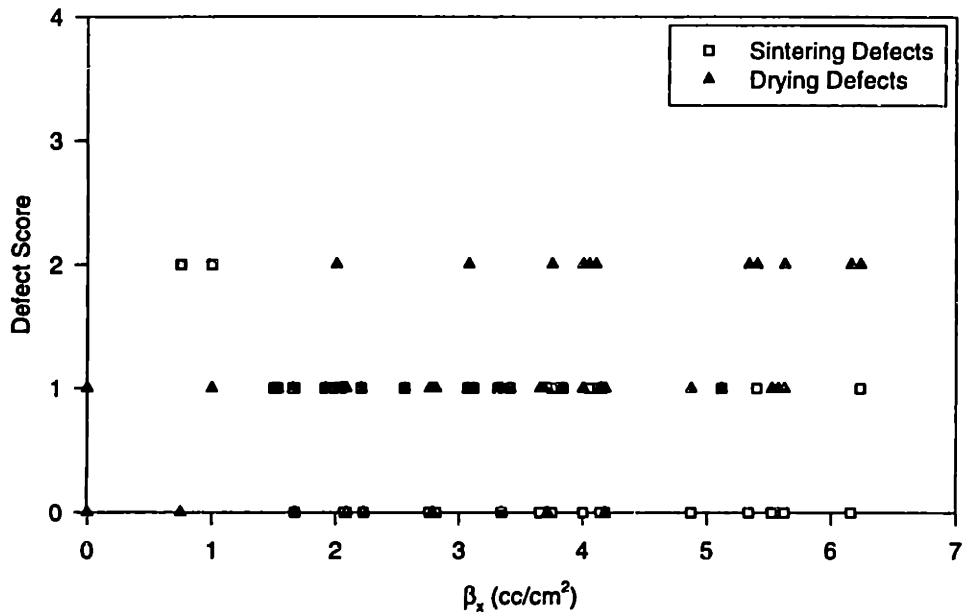

Figure 5.16: Defect vs. βx for PLGA (85:15 100,000) and 2.5% PCL/$CHCl_3$

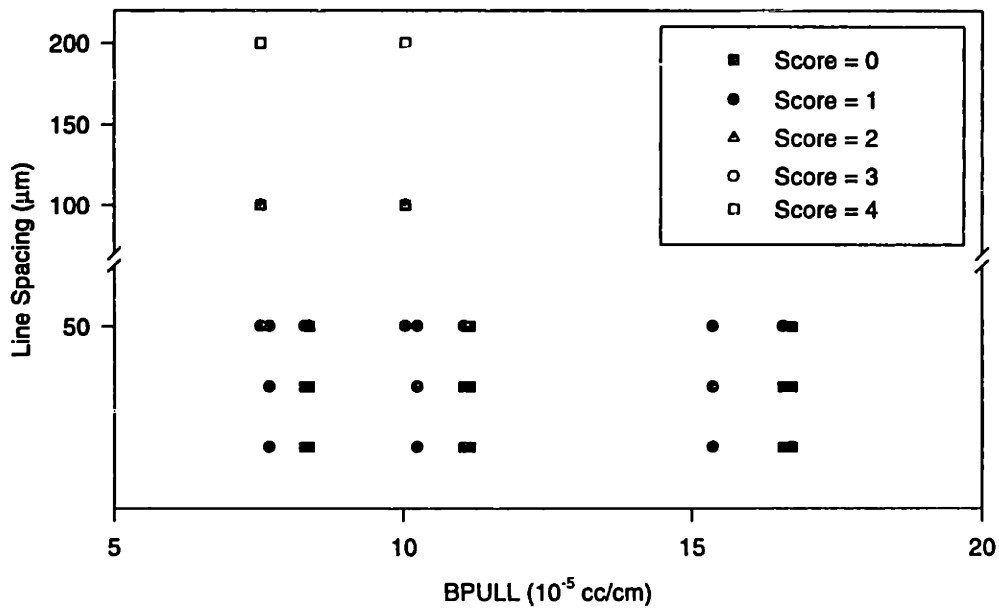

Figure 5.17: Line spacing vs. BPULL for PLGA (85:15 100,000) & 2.5% PCL/$CHCl_3$

Figure 5.18 represents devices made by printing two powder sizes of PLGA (85:15 100,000) with 2.5% PCL in chloroform. The two particle size range of interest are 45-75 μm, and 75-150 μm. The data reveal that the same (or better) defect scores can be obtained with lower β_x values if the powder bed particle size is smaller. This is indicative of improved dissolution of the smaller particles.

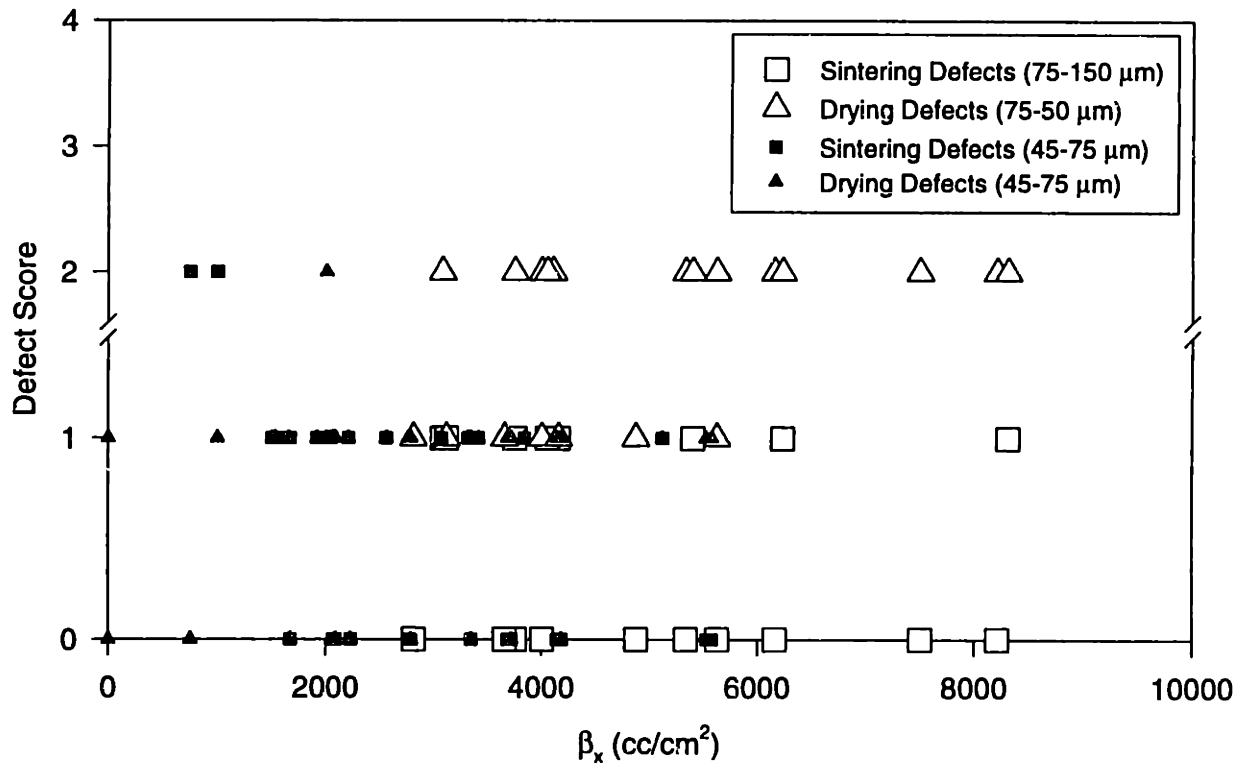

Figure 5.18: Effect of particle size on defect score vs. βx for PLGA (85:15 100,000)

5.4 DISCUSSION

Similar analyses are done for other combinations of powder, binder, and processing conditions. The effects of powder and binder composition on defect formation are summarized in Table 5.3. The effects of printing parameters on microstructure are listed in Table 5.4. Less sintering defects are associated with lower molecular weight particles. This is in agreement with Figure 3.15, which showed that dissolution time is highly sensitive on molecular weight. The data reveal that improved defect scores can be obtained with lower β_x values if the powder bed particle size is smaller. This finding is expected based on the particle size vs. dissolution time plot in Figure 3.7, and the dissolution evaporation plot shown in Figure 4.13. The time scale for dissolution of the finer particles are significantly less than that for the larger particles. This finding is expected based on the particle size vs. dissolution time plot in Figure 3.7, and the dissolution dissolution evaporation plot shown in Figure 4.13. The time scale for dissolution of the finer particles are significantly less than that for the larger particles.

Molecular Weight
- Decreased sintering defects associated with lower MW PLA
- Decreased drying defects associated with higher MW PLGA

PLA/PLGA Mixture Ratio
- Decreased sintering defects associated with lower PLA/PLGA Ratio
- Decreased drying defects associated with higher PLA/PLGA Ratio

L:G Blend Ratio
- Decreased sintering defects associated with lower L:G Ratio
- Decreased drying defects associated with higher L:G Ratio

Polymer Composition in Binder Solution
- % Polymer in binder has no direct effect on sintering defects
- PCL and low MW PCL are more effective in defect reduction than low MW PLA or PLGA
- Decreased defects associated with PCL, low MW PCL-PCL binders
- Increased drying defects associated with low MW PLGA binder

Polymer Composition in Powder Bed
- 100,000 MW PLGA (65L:35G) can be processed to make defect-free devices
- PCL offers a wide range of printing conditions for making defect-free devices

Particle Size
- Smaller particles (<75 μm) result in devices with better print resolution and lower binder requirement

Table 5.3: Effects of composition on microstructure

Layer Thickness

- Decreased lamination defects by decreasing layer thickness (optimal=150mm)
- Decrease sintering defects by decreasing layer thickness
- Powder spreading becomes difficult below 150 mm
- Increase drying defects for PLLGA

Saturation: Flow Rate, Print Speed, Line Spacing, Layer Thickness, Print Style

- Decreased lamination defects and sintering defects with increased saturation
- Increased drying defects with increased saturation

Line Spacing

- More important than BPULL (repeated printing) in defect reduction

Table 5.4: Effects of printing parameters on microstructure

6. POROUS STRUCTURES BY 3DP™

6.1 BACKGROUND

Microporous ceramic and metal parts have not been fabricated by 3DP™ because of the emphasis toward industrial applications for these materials. Highly microporous constructs are particularly important in tissue engineering applications which involve cell ingrowth. Most tissue engineering matrices for successful cell transplantation must maximize cell mass per unit volume (cell density), vascularization, nutrient delivery, and metabolic waste elimination. The scaffolds should exhibit structural components which can achieve these functional requirements. Three structural hierarchical levels have been reported for tissue engineering matrices: macroscopic shape (1-1,000 mm), oriented channels (0.1-1 mm), and microporosity (0.01-0.1 mm)[81]. Three dimensional printing™ has been used for fabricating complex, highly porous constructs possessing all three structural hierarchies[82]. 3DP™ also have the additional capability to control three dimensional spatial distribution of bioactives such as drugs, nutrients, cell adhesion modifiers, and growth factors[83].

Although there is insufficient data in the literature to suggest what the optimal range of dimensions should be for each hierarchy, the ability of 3DP™ to exert delicate control over these hierarchical dimensions had not been demonstrated or optimized. The capability of 3DP™ to exert control over microstructure and surface texture is particularly important for tissue engineering applications. It should be emphasized that porous polymeric matrices are also important in some drug delivery systems[84,85,86], and in 3-D structures which release bioactive agents[87]. Section 6.2 reviews some of the creative and novel approaches for fabricating porous structures. Section 6.3 describes the various 3D printing™ strategies for producing highly porous structures possessing all three structural hierarchie. The experimental data, and the relationship between processing parameters, materials interactions, and microstructure will also be analyzed in section 6.4 and section 6.5.

6.2 CURRENT APPROACHES FOR POROUS STRUCTURES

6.2.1 Solvent based techniques

Many techniques rely on the use of organic solvents during processing steps. All of them, therefore, require solvent extraction/removal steps prior to implantation. Mikos et al. used particulate leaching to fabricate highly porous PLLA foams[88]. Wake et al. combined solvent casting and particulate leaching to fabricate pliable foams with PLGA and PEG blends[89]. The pore size of the foams ranged from 71 to 154 μm, and the porosity ranted from 80 to 94%. There have been many attempts at achieving simultaneous control over macroscopic shape and microporosity. Lo et al. recently fabricated PLLA foams by phase separation from homogeneous naphthalene solutions. These highly porous porous matrices were used for both cell culture and sustained release of drugs and proteins, although 0.2% residual naphthalene remained after vacuum[90]. Mooney et al. fabricated porous PLGA films by particulate leaching and formed the films into tubular scaffolds for engineering of tubular vascularized tissues[91]. Beumer et al. used sequential solvent casting technique to fabricate bilayered matrices with porous tissue-side layer for demal ingrowth and a dense outer layer for keratinocytes adhesion[92]. Manual molding of polymeric fibers and fabrics into anatomical shapes have generated much excitement and interest in tissue engineering[93,94]. 3 dimensional lamination of pre-cut layers to form macroscopic shape have been described[95], although such approaches are not easily amenable to large scale manufacturing.

6.2.2 Non-solvent based techniques

No solvents are required for scaffolds which contained little or no polymers. Porous glass ceramic implants, for example, can be easily fabricated by pressing a mixture of fine ceramic powder and foaming agent to form the external shape, and then sintering to achieve an interconnected matrix[96]. Liu fabricated porous hydroxyapatite granules by a drip-casting process, and produced granules with porosity ranging from 24 to 76 vol%, and pore size ranging from 100-400 μm[97]. A solvent-free approach for porous polymeric structures was recently described where PLGA disks were exposed to high pressure CO_2 (5.5 Mpa) for 72 hours at room temperature. The reactor was then

rapidly de-pressurized, resulting in thermodynamic instability and CO_2 gas bubble formation[98]. PLGA sponges with 100 μm pores with 93% porosity were reported, but some optimization of the technique is required to generate interconnected microporosity.

6.3 3D PRINTING™ STRATEGIES FOR POROUS STRUCTURES

None of the fabrication techniques described in the previous section offer simultaneous control over all three levels of structural hierarchy. This section describes three different possible approaches by 3DP™ to fabricate microporous structures with defined micro-architecture and macroscopic shape. All three involve the use of leachants for controlling microporosity. The ideal leachant should be insoluble in the printing binder, but readily soluble in aqueous environment. NaCl crystals and gelatin are examples of practical leachants. The simplest approach is to mix polymer and leachant powder uniformly in desired volumetric ratios, and deposit either pure solvents or polymeric solutions into the powder mix. The second approach is to first coat the leachant particles with polymer, and then deposit either pure solvents or polymeric solutions into the composite powder. The leachant-polymer composite can be produced by coacervation techniques developed in this laboratory. The third approach is to deposit polymer solutions into a bed composed only of leachant powder.

Simple mixture of the two (leachant and polymer) powders may, in some instances, produce inadequate particle bonding and insufficient mechanical properties. This is particularly true when larger polymer particles are used, if the polymer dissolution rate is low, or the solvent evaporation rate is high. The use of polymeric solutions is preferred since their increased viscosity generally result in less binder migration than the pure solvents. Binder migration can deteriorate print resolution and interfere with powder removal. The polymer can also be distributed more uniformly by printing it as a solution than mixing it as particles with the leachant. The density difference between NaCl (2.165 g/cm^3) and polymer (~1.1 g/cm^3) powders may also result in non-uniform distribution during spreading.

The use of polymeric solutions, however, may be practical only with low molecular weight polymers (<100,000 MW), and only in low concentrations, due to

rheological constraints. The maximum polymer concentrations for reliable jetting through a 45 μm continuous-jet nozzle are listed in Table 6.1 for various polymers. Mechanical requirements, depending on the final application, may necessitate the use of higher molecular weight polymers in higher volume content. The use of nozzles with larger orifices, such as 70 μm and 127 μm, have been attempted to deliver higher polymer content through the printhead. The high binder flowrate associated with these larger nozzles resulted in extensive ballistic destruction of the powder bed. The high polymer content requirement is perhaps best satisfied with the first two approaches. Printing into a powder bed containing a mixture of polymer & leachant is also advantageous over a leachant-only powder bed for fabricating low porosity (<85%) structures. The third approach (leachant only powder bed) may require multiple printing and drying cycles for each layer, which may be too inefficient for large scale manufacturing of structures with such high-polymer content.

For all printing strategies, increased mechanical properties are expected with increased polymer content of the printed structures, but excessive binder deposition may result in uncontrolled binder migration (bleeding) and deterioration of print resolution. Section 6.4 describes the experimental observation from printing polymeric binders into leachant-only powder beds, and summarizes the relationship between processing conditions, materials parameters, microstructure, and structural integrity. Section 6.5 summarizes the findings from printing into polymer-leachant powder bed mixtures.

6.4 POLYMER SOLUTIONS INTO PURE LEACHANT BEDS

6.4.1 Materials and methods

NaCl crystals are cold milled and classified into the following particle size ranges: 45-75 μm, 75-150 μm, and 150-180 μm. PLGA (85:15 100,000 MW) is dissolved in chloroform to prepare 2% (w/w) solutions. Various combinations of 3DP™ machine parameters (Table 6.2) were used to fabricate thin strips (5 mm wide, 50 mm long, 1.5 mm thick) with each of the leachant particle size range. The thin strips were dried by placing them into N_2 glove box for 48 hours, and into vacuum for 48 hours.

Leachant removal was achieved by immersing the strips in individual vials of deionized water for 2 hours in an automated shaker rotating at 200 rpm. The strips were then placed into a desiccator for 48 hours, and into vacuum for 48 hours. Microstructural analysis of porous samples should, ideally, include quantitative description of overall porosity and pore size. Preliminary experiments, however, with mercury intrusion porosimetry indicated gross data distortion attributable to the collapse of these highly porous polymer samples. The compressible volume was erroneously included in the intrusion volume, and overestimating the intrusion volume. This results in gross miscalcalculations of other important parameters. Recovery and examination of the tested sample revealed the absence of mercury in the sample core.

Final pore size was determined by SEM, and porosity was determined by mass-density calculations. The mass of the each strip was recorded before and after particulate leaching. The final porosity of the dried, leached strips can be computed by using the following equation:

$$P_f = \frac{V_{final\ sample} - V_{polymer}}{V_{final\ sample}}$$

where $V_{final\ sample} = k^3 \cdot V_{initial\ sample}$

$$k = \frac{width\ of\ final\ sample}{width\ of\ initial\ sample}$$

$$V_{polymer} = \frac{mass\ of\ leached\ strip}{density\ of\ polymer\ (1.1)}$$

$$V_{salt} = \frac{mass\ of\ unleached\ strip\ -\ mass\ of\ leached\ strip}{density\ of\ salt\ (2.165)}$$

Polymer	Solvent	Wt. %
PEO (100,000)	chloroform	1%
PLGA 85:15 (100,000)	chloroform	2%
PLGA 50:50 (50,000)	chloroform	2.5%
70% PLGA (50:50 4,500) & 30% PLLA (147,000)	chloroform	2.5%
50% PLGA (50:50 50,000) & 50% PLLA (27,000)	chloroform	3%
PCL (45,000)	chloroform	5%
PEG (14,000)	chloroform	7.5%
Dimethylamonoethyl methacrylate ester (150,000) & Methacrylic acid ester (Eudragit E100)	ethanol	20%
Ammonio methacrylate copolymers (150,000) (Eudragit RS PO)	acetone	20%
LPS-PCL (9,000)	chloroform	20%
PEG (3,400)	chloroform	20%
PLA (2,000)	chloroform	25%

Table 6.1: Polymer concentrations for reliable jetting through a 45 μm nozzle

Layer thickness	# print / layer	Printspeed	Line spacing
150 μm	1	37.5 cm/s	24 μm
	3	75 cm/s	50 μm
		115 cm/s	74 μm
		150 cm/s	100 μm
			150 μm
			200 μm

Table 6.2: Printing parameters for fabricating porous strips

Strips printed with excessive binder density are associated with increased binder migration, deteriorated edge definition, and poor resolution. The actual widths of the as-printed strips were measured with a digital caliper, and were compared with the theoretical strip widths. The theoretical strip widths, in turn, can be derived as follows:

$$theoretical\ \ width = 300 + (n-1)\cdot \Delta x$$

where n = number of lines printed per strip

Δx = line spacing (center to center) [microns]

The equation above would give the thinnest strips that can be realistically achieved, and any additional bleeding would be undesirable. The "300" in the above equation accounts for the 150 μm thick wall proximal to the first center line, and the 150 μm thick wall distal to the n^{th} center line. 150 μm is used since 300 μm is the thinnest polymeric *wall* achieved by 3DP™. Bleeding scores are assigned to the as-printed strips prior to particulate leaching according to the criteria listed in Table 6.3.

Bleeding score	Extent of bleeding
4	Severe binder bleeding (> 0.5 mm)
3	Moderate binder bleeding (0.20 - 0.5 mm)
2	Minor binder bleeding on both edges (<0.20 mm)
1	Minor binder bleeding on one edge (<0.20 mm)
0	No bleeding

Table 6.3: Bleeding scoring system for as-printed strips

Distortion scores are assigned to the wet, leached strips according to Table 6.4. A distortion score of 4 indicates extensive and irreversible distortion. Such strips tend to curl up around the forceps during removal from the water, and remains as a "blob" on the drying container. A score of 3 indicates moderate and reversible distortion. The original shape of these strips can be regained if the strips are properly and carefully manipulated. A "2" score denotes strips that are slightly distorted, and the shapes are easily regained. Scores of "1" represent strips that distort only slightly in water, and recover their originally shapes automatically. A distortion score of "0" indicates no/minimal distortion. Strips with distortion scores 2, 3, and 4 are unacceptable.

The distortion scores are plotted against various printing parameters to determine the appropriate processing conditions and final porosity for fabricating highly porous structures by 3DP™. Microstructural analysis of the leached, dried strips was

accomplished with scanning electron microscopy. The actual widths of the leached strips were also measured with the digital caliper, and were compared with those of the as-printed strips. The scaling factor *k* accounts for the dimensional change in width due to leaching, and is assumed to be isotropic. This assumption is necessary because the actual height and length of leached strips cannot be easily determined due to distortion during leaching. The scaling factor *k* is then used to estimate the volume and final porosity of the leached strips.

Distortion score	Distortion
4	Severe, irreversible distortion
3	Moderate, reversible distortion
2	Slight, reversible distortion
1	Slight, reversible distortion
0	No / minimal distortion

Table 6.4: Distortion scoring system

6.4.2 Observations

Figure 6.1 illustrates that two ranges of pore sizes can be observed in 3DP™ devices, primary pores (>10 μm), and secondary pores (<10 μm). Primary pores are essentially controlled by the salt particle size used in the 3DP™ powder bed. Secondary pores (Figure 6.2) are observed on the walls which surround the primary pores.

A number of factors may be responsible for the formation of secondary pores. The smooth, well defined borders of the secondary pores suggest that they were formed during printing, rather than being produced during the leaching procedure. The round borders also suggest that their formation may be related to poor wetting between the polymeric solution and the NaCl powder. A more likely possibility is that there may simply be insufficient amounts of polymer for the formation of solid films around the NaCl particles. This last possibility is supported by Figure 6.3, which shows that the secondary pores can be eliminated by printing chloroform into a powder bed consisted of 40 % (v/v) polymer.

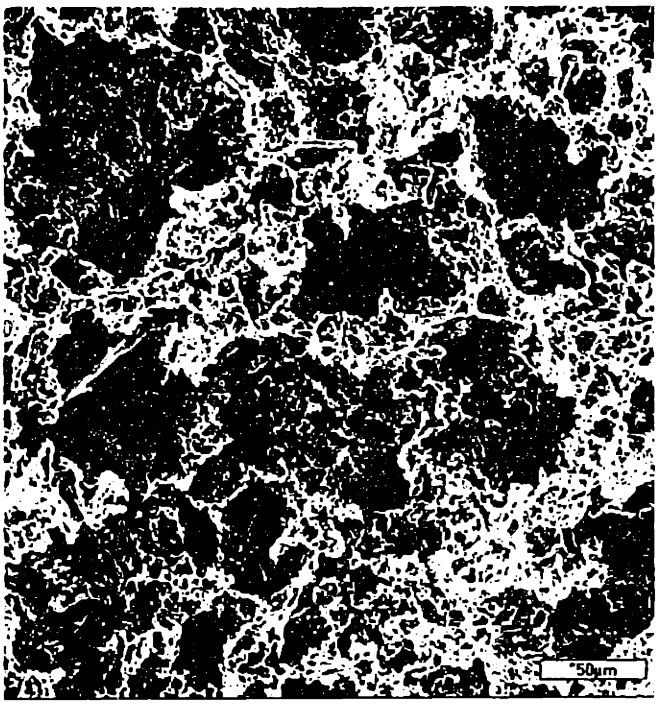

Figure 6.1: 1° and 2° pores

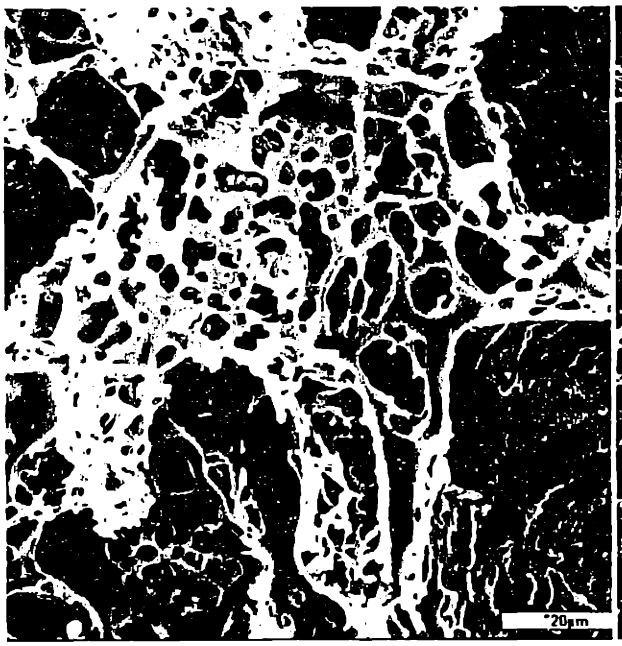

Figure 6.2: Secondary pores

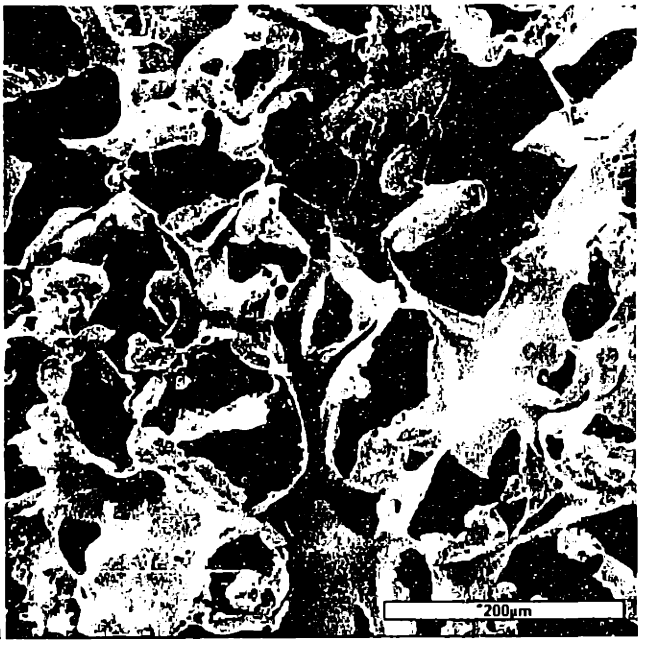

Figure 6.3: Absence of 2° pores

The plot in Figure 6.4 shows the distortion vs. PPULL (polymer printed per unit line length) for single printing per layer of 45-75 μm salt powder, triple printing per layer of 45-75 μm salt powder, and triple printing per layer of 75-150 μm salt powder. The data confirms that distortion score is improved with increasing polymer concentration. PPULL is affected by two printing parameters, printspeed and line spacing. The plot in Figure 6.5 shows that by re-plotting the same data as distortion vs. PPULL/line spacing (polymeric β_x), the minimum polymeric β_x for obtaining minimal distortion during leaching seems to be 60 mg/cm^2 for PLGA (85:15 100,000MW).

The strip widths decreased by approximately 1% during leaching. The scaling factor *k* was determined to be 0.99. The final volume is therefore assumed to be 97% that of the as-printed volume. This dimensional change corresponds to a 0.5% change in final porosity. Figure 6.6 shows the distortion as a function of final porosity for single printing per layer of 45-75 μm salt powder, triple printing per layer of 45-75 μm salt powder, and triple printing per layer of 75-150 μm salt powder. The data suggests that structures with >96% porosity can not be made with PLGA 85:15, 100,000 MW by 3DP™ due to excessive distortion during particulate leaching. It should be noted that all of the strips represented in Figure 6.4 have minimal bleeding, i.e. bleeding score = 0.

Figure 6.7 shows the distortion and bleeding scores for the polymeric β_x for single printing per layer of 45-75 μm, 75-150 μm, and 150-180 μm salt powder. It appears that bleeding occurs at polymeric $\beta_x > 85$ mg/cm^2, while significant distortion occurs when β_x falls below 60 mg/cm^2. The optimal processing window is, therefore, between 60 - 85 mg/cm^2 for single printing PLGA (85:15 100,000 MW).

6.4.3 Discussion

Two ranges of pore sizes can be observed in 3DP™ devices, primary pores (>10 μm), and secondary pores (<10 μm). Primary pores are essentially controlled by the salt particle size used in the 3DP™ powder bed. Under-sized primary pores can inhibit cell penetration during seeding, whereas excessively large pores tend to hinder cell-retention. The optimal pore size range is expected to increase with larger overall device thickness.

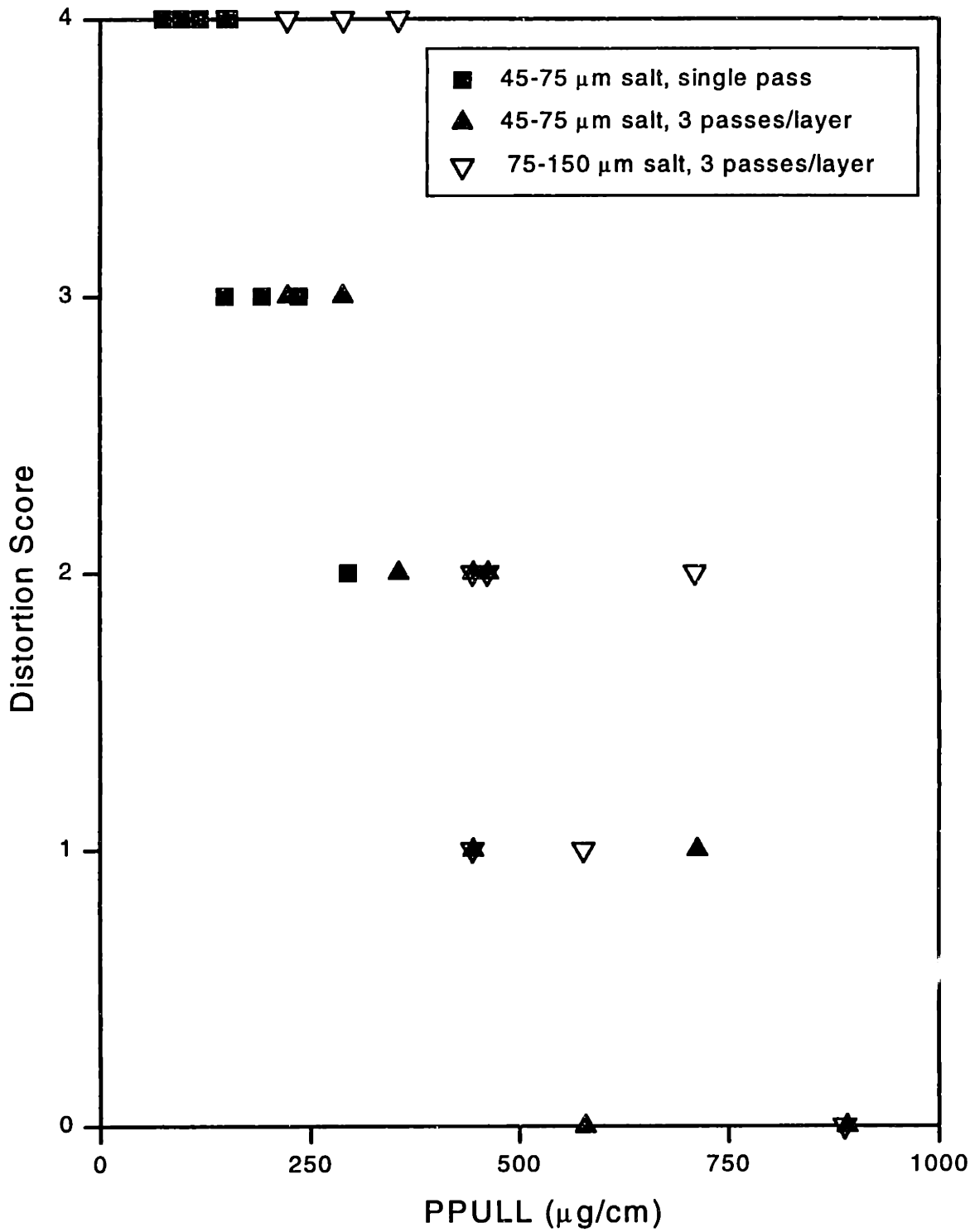

Figure 6.4: Distortion vs. polymer concentration

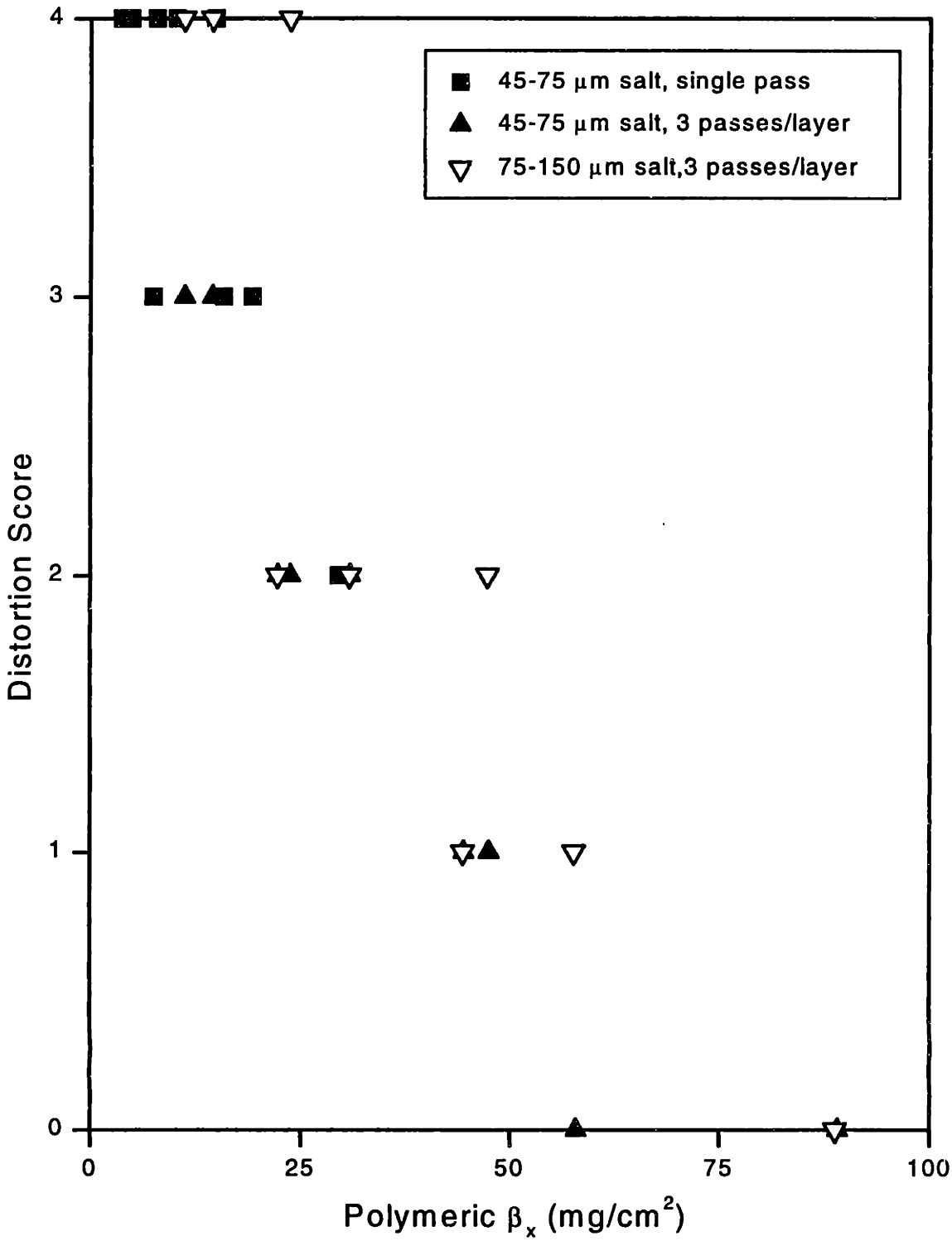

Figure 6.5: Distortion vs. polymeric β_x

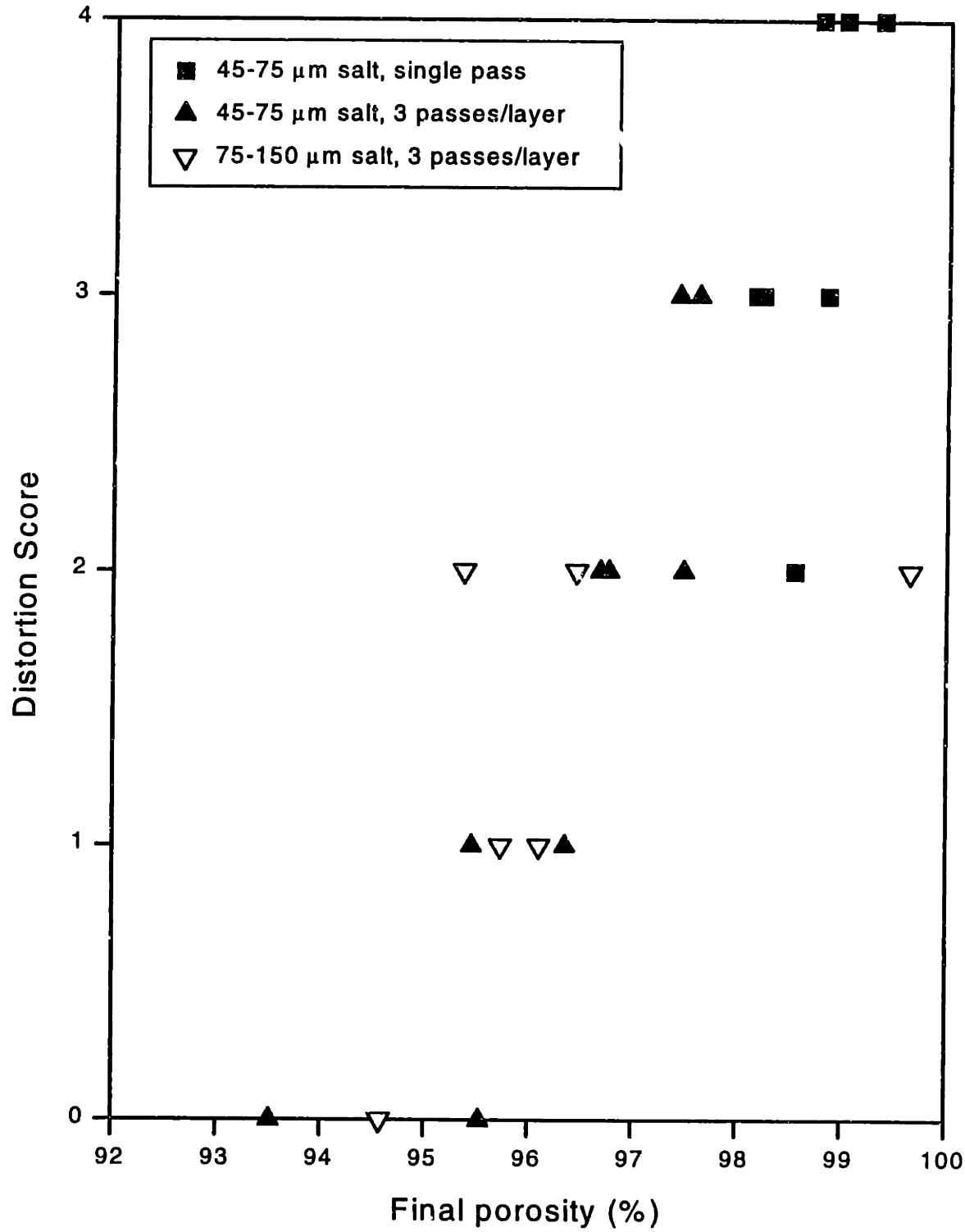

Figure 6.6: Distortion vs. porosity

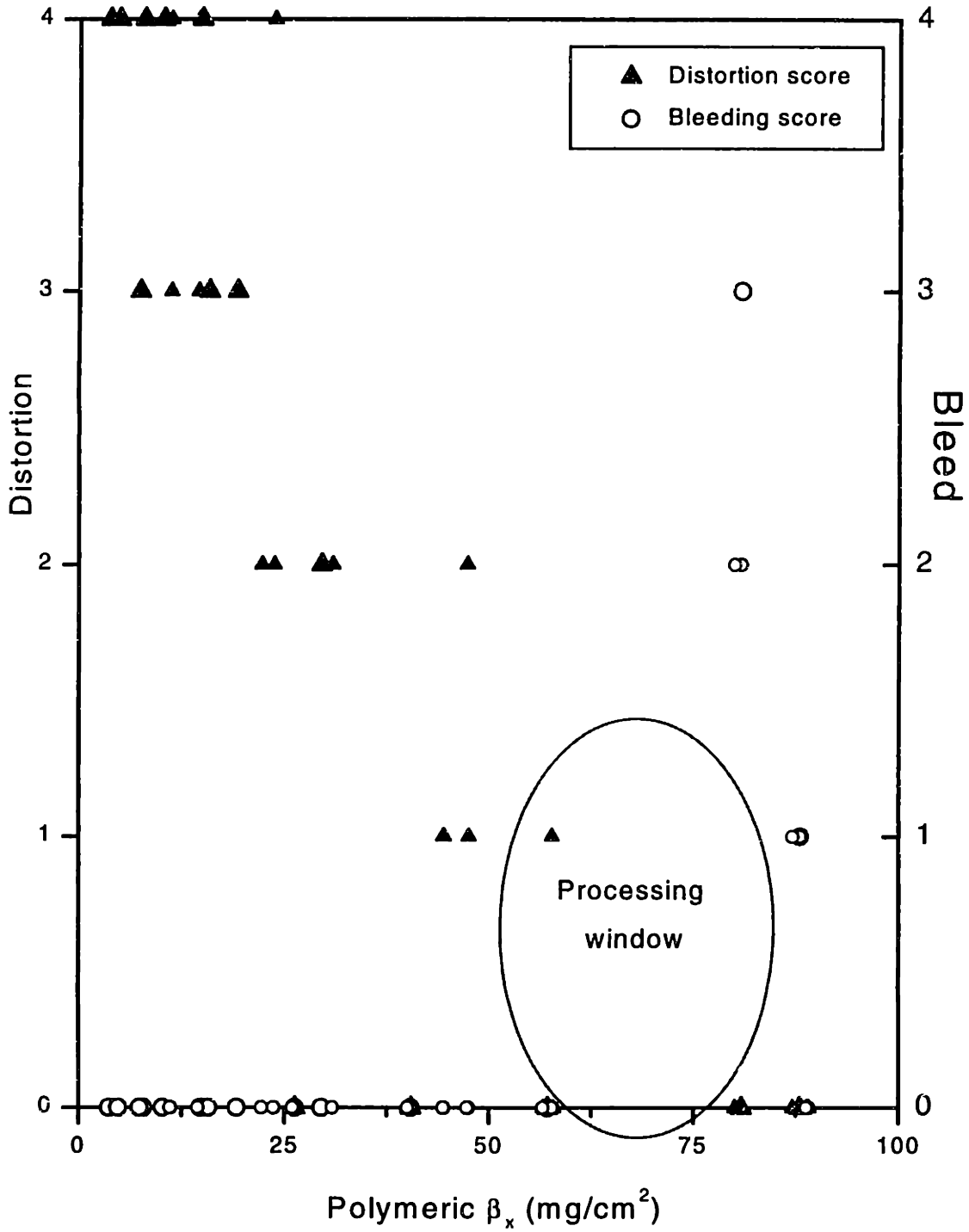

Figure 6.7: Distortion & bleeding vs. polymeric β_x (<100 mg/cm^2)

Figure 6.6 suggests that the mechanical integrity of the 3D printed™ strips depend strongly on porosity, and only weakly on pore size. This is consistent with the common assertion that the single most important determinant for mechanical properties of cellular solids is overall porosity[99]. The leachant-particle size ranges used for this study, 45-75 μm, 75-150 μm, and 150-180 μm did not seem to affect the distortion score or bleeding scores. This is not surprising since it is known that most mechanical and thermal properties of cellar solids depend only weakly on cell size. Cell shape, isotropy, and wall connectivity may be actually more important than cell size[99]. Mechanical integrity requirements may, however, impose constraints on maximum pore size. Distortion score may be affected by larger salt particles (>180 μm), but such large particles would not be used since the typical layer thickness values for 3DP™ are below <150 μm. Secondary pores are observed on the walls which surround the primary pores. Secondary pores connect the adjacent, larger pores, and may be beneficial during initial cell seeding and cell maturation. Secondary pores may also facilitate nutrient/waste transport by allowing liquid state diffusion through the polymeric walls. The etiology of their formation is thought to be multifactorial.

All of the strips represented in Figure 6.4 - Figure 6.6 have minimal bleeding, i.e. bleeding score = 0. The zero bleeding score may be attributed to the print style. Multiple printing of each layer can increase β_x without excessive binder migration by allowing more evaporation time and decreasing the overall binder deposition rate. Single printing can only increase β_x by either decreasing printspeed or line spacing, effectively increasing the binder deposition rate without allowing for additional evaporation time. The processing window shown in Figure 6.7 may be extended (increasing polymeric β_x) by multiple printing over the same layer, with allowance for evaporation to minimize bleeding.

6.5 PRINTING INTO POLYMER-LEACHANT MIXTURE

6.5.1 Materials and methods

PLGA (85:15 100,000 MW) pellets were cryogenically milled, dried in vacuum for 72 hours, and classified into the following particle size ranges: <45 μm, 45-75 μm, and 75-150 μm. NaCl crystals were cold milled and classified into two particle size ranges: 45-75 μm, and 75-150 μm. Six combinations of polymer-salt mixture were thus obtained, with the polymer-salt mixture ratio kept at 60:40 v/v in all cases. Pure, fresh chloroform was used for binder. Three printspeed (75 cm/sec, 112.5 cm/s, and 150 cm/s), and three interline spacing (100 μm, 150 μm, and 200 μm) were programmed to nine fabricate thin strips (5 mm wide, 50 mm long, 1.5 mm thick) with each of the six polymer-salt mixtures. The material and printing parameters for this experiment are listed in Table 6.5. All strips were dried by placing them into N_2 glove box for 48 hours, and into vacuum for 48 hours. Additional post processing steps to extract the residual chloroform to below regulatory specifications were not performed for these samples since they will not be implanted.

Leachant particles 60% v/v NaCl	Polymer particles 40% v/v PLGA	Printspeed (cm/s)	Line spacing (μm)
45-75 μm	< 45 μm	75	100
75-150 μm	45-75 μm	112.5	150
	75-150 μm	150	200

Table 6.5: Material and printing parameters for printing into polymer-leachant bed

Leachant removal was achieved by immersing the strips into individual vials of deionized water for 2 hours in an automated shaker rotating at 200 rpm. The strips were then placed into a desiccator for 48 hours, and into vacuum for 48 hours. Samples were then sectioned, coated, and prepared for microstructural analysis by scanning electron microscopy. Preliminary experiments with mercury intrusion porosimetry with these porous polymer samples also involved overestimation of the intrusion volume.

6.5.2 Observations

The SEMs suggest that the resultant pore sizes are essentially determined by the initial salt particle size, as expected. The final polymeric wall microstructure, however, may be dependent on initial polymer particle size and printing parameters. The surface morphology of the polymeric walls ranged from solid, smooth appearances, to rough, irregular texture interspersed with incompletely dissolved polymer particles.

Figure 6.8 shows an SEM of a sample produced by printing chloroform at 150 cm/sec with 100 μm line spacing, into a powder bed mixture of 60% v/v 75-150 μm salt, and 40% v/v <45 μm PLGA. The solid, smooth texture is readily evident. A few particles are still evident, but most of the particles have dissolved. The general appearance is that of a smooth wall texture. The pore sizes are generally within the range of the initial salt sizes (75-150 μm). A few micropores, or secondary pores, are present. Figure 6.9 shows an SEM of a sample produced by printing chloroform at 150 cm/sec with 100 μm line spacing, into a powder bed mixture of 60% v/v 75-150 μm salt, and 40% v/v 75-150 μm PLGA. Numerous incompletely dissolved polymer particles can be readily observed. The particle dimensions of the partially dissolved particles are similar to that of the initial salt size, indicating that very little dissolution has occurred. Figure 6.10 shows an SEM of a sample produced by printing chloroform at 75 cm/sec with 200 μm line spacing, into a powder bed mixture of 60% v/v 75-150 μm salt, and 40% v/v 75-150 μm PLGA. These printing parameters should result in the same binder saturation as the sample shown in Figure 6.9, but more polymer particles are exhibited in Figure 6.10. This observation suggests that between the 2 printing parameters, interline spacing may play a stronger role in particle dissolution than printspeed.

Figure 6.11 shows an SEM of a sample produced by printing chloroform at 150 cm/sec with 100 μm line spacing, into a powder bed mixture of 60% v/v 45-75 μm salt, and 40% v/v 45-75 μm PLGA. A few particles are still evident, but the smooth wall texture is readily apparent. Several 1° pores on the order of 45-75 μm, and numerous micron-sized 2° pores can be observed. The origin of the 2° pores is likely to be the inclusion of numerous micron-sized salt particles during particle classification.

Figure 6.8: Smooth wall texture with 75-150 µm pores

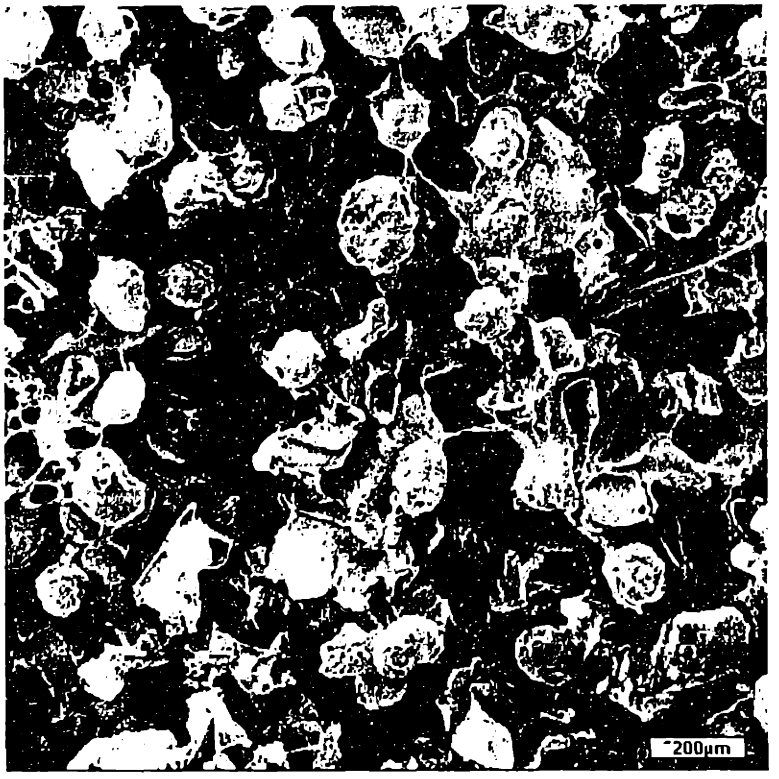

Figure 6.9: Incompletely dissolved particles (100 µm line spacing)

Figure 6.10: Incompletely dissolved particles (200 µm line spacing)

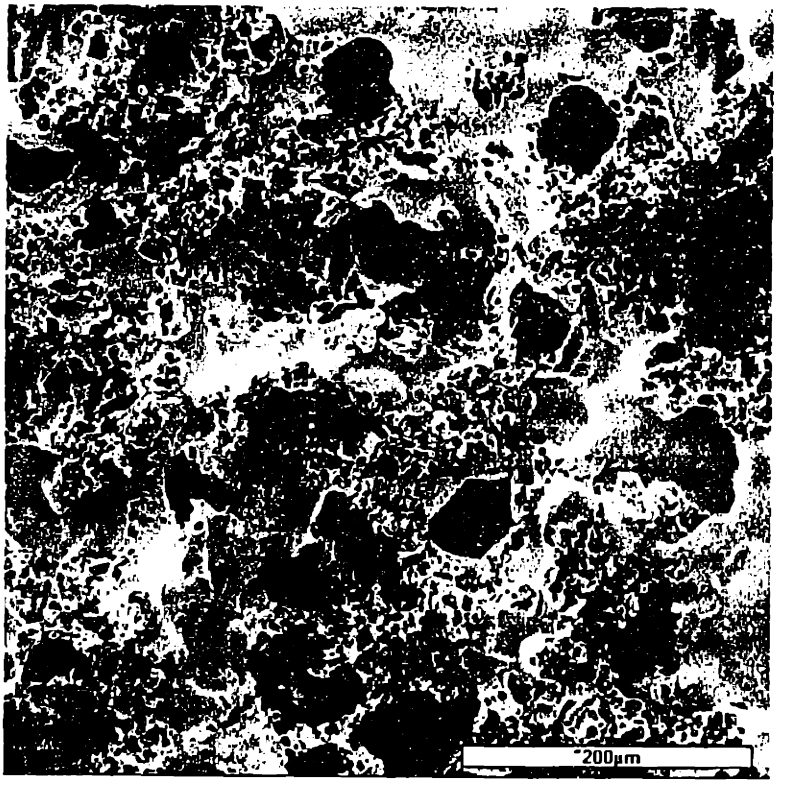

Figure 6.11: Smooth wall texture with 45-75 µm 1°pores and 2° micropores

6.5.3 Discussion

The pore wall structure derived by printing into polymer-leachant mixture is expected to be quite different than obtained by printing into pure leachant. Dissolution of polymeric particles is critical for determining the final microstructure in the former approach. No polymer dissolution occurs during the latter approach, since polymer solution is printed into a leachant-only powder bed. The microstructure in the latter approach appears to depend on other factors, such as the amount of binder deposited.

Many incompletely dissolved polymer particles are observable in the scanning electron micrographs of samples constructed with polymer particle size range of 75-150 μm (Figure 6.9 and Figure 6.10). The degree of dissolution increased for these samples, as expected, with increasing binder saturation. Three parameters contribute to binder saturation: binder flow rate, print speed, and interline spacing. Only the two latter parameters need to be considered since the log files confirmed that constant binder flow rate throughout the experiment. The results in this section suggest a stronger influence by interline spacing on microstructure. Decreasing interline spacing may facilitate particle dissolution in two ways. The most apparent effect is the associated increase in binder saturation. This effect alone, however, is not sufficient to explain the microstructure difference between samples printed with equal binder saturation, but with different interline spacing and compensating printspeed. A more subtle, but perhaps more important effect, is the increased time duration at which the polymer particles are exposed to a "critical" volume fraction of solvents. The binder deposited for two adjacent lines may migrate and mix better if the migration distance is shorter. The fresh binder from the second line may be enough to "supplement" the binder for the first line to induce further particle dissolution by increasing exposure time to a "critical" volume fraction of solvents. This suggest that spatial solvent density is less influential in determining microstructure than the kinetics competition between particle dissolution and solvent evaporation.

It is interesting that while numerous incompletely dissolved particles are observed with polymer particle size range of 75-150 μm, the same printing parameters was able to dissolve most particles in the 45-75 μm range. Insignificant improvement

was observed with using <45 μm polymer particles. These observations are in agreement with those obtained from the particle dissolution experiments. It was described in chapter 3 that an "optimal" particle size exists for particles which dissolve with gel formation, and that no improvement (decrease) in dissolution time is expected below this "optimal" dimension. Figure 3.7 showed that the "optimal" particle size for PLGA (85:15 108,000) particles dissolving in chloroform is about 75 μm, with a t_{min} of 1.25 sec. Very similar limits are expected with PLGA (85:15 100,000). Section 4.6 considered the relative rates of particle dissolution and solvent evaporation. Figures 6.8, 6.9, and 6.11 are used in the dissolution-evaporation plot in Figure 4.14 to illustrate the influence of the relative kinetics on microstructure formation.

The effects of material properties and machine parameters on microporosity and wall surface texture were examined in this chapter. This provides a rationale for the development of design rules for the fabrication of three-dimensionally complex, microporous tissue engineering scaffolds with controlled micro-architecture (see Chapter 8).

7. 3DP™ DRUG DELIVERY DEVICES

7.1 BACKGROUND

A lot of fascinating research in drug delivery focus on the development of new biomaterials with improved chemical and physical properties to exert better control of drug delivery. Except for delivery systems which are targeted at life threatening ailments, many of the research efforts have a large regulatory hurdle awaiting them. Considerably less research efforts have been devoted to refining existing pharmaceutical manufacturing processes in order to maximize the potentials of existing, FDA-approved biomaterials. The origin of this dichotomy may be the fact that no existing manufacturing technique, pharmaceutical or industrial, offers automated control over spatial distribution of matter, local composition and microstructure.

Conventional pharmaceutical manufacturing processing methods of various drug delivery systems have been reviewed by Chien[100]. The processes typically begin by blending the drug with the polymer according to pre-determined mixture ratios. The uniform blend can then be injection molded or extruded to manufacture polymeric matrix devices. The methods of drug incorporation into the matrix have been shown to affect consistency of release kinetics. When compared to compression molding techniques, hot melt[101] and injection molding[102] techniques created matrices of increased density and homogeneity. One limitation of current manufacturing techniques of polymeric matrix devices is that unless the manufacturing process is significantly complicated, drug release rate decreases as a function with time. Constant release rates are needed for drugs possessing a narrow range of therapeutic index. Various approaches have been proposed to achieve constant release rates in polymer matrix devices. One approach utilizes geometric configurations that produce increase in surface area with time. Cylindrical rods with internal pie shapes, inwardly-releasing hemispheres, and cylindrical donut, are examples of the surface area[103] method. An alternative approach is to modify the rate of initial drug release. An example of this approach includes coating the devices with low permeability material, which decreases the initial release rate.

3DP™ is unique among advanced, CAD-based manufacturing techniques in two important ways. 3DP™ is the only SFF technology with well documented demonstration of producing functionally gradient materials by selective deposition of matter. It is also, by far, the most flexible among all SFF technologies in terms of materials systems that can be processed. These attributes, plus the ability to control local composition, microstructure, and spatial positioning, makes 3DP™ an attractive candidate as a pharmaceutical manufacturing technique. Design and fabrication of medical devices for drug delivery is one of two major focuses at the MIT 3DP™ biomaterials research program.

3DP™ offers several unique built strategies for obtaining zero order release kinetics. Different diffusion gradients may be printed at any location within the device, either by changing the binder composition or by varying the microstructure of the diffusion barriers. A highly specific release profile can be produced by depositing the appropriate amount drugs at precise locations within the gradient. Obviously, 3DP™ is not limited to zero order release. 3D Printing™ can produce multiple diffusion gradients within a single device, resulting in complicated, chronopharmacological drug release profiles not easily achieved with conventional processing techniques. Devices for hormonal replacement therapy could, for example, be made which mimic the physiological cyclic rhythms; zero order release for a specific amount of time, after which no release, when a period of quiescence occurs. Cyclic release profiles can be produced by repeating units in recurring sequences throughout the device. Alternatively, release of multiple drugs in rhythmic cycles can be achieved by setting up units of gradients that release different drugs at different time point.

Section 7.2 describes the early experiments[104] which demonstrated unprecedented level of control in release profiles by manipulating spatial composition of printed matter, local composition and microstructure. Section 7.4 illustrates how 3DP™ can work with conventional excipient materials to fabricate oral dosage forms. Section 7.3 presents some preliminary data for fabricating implantable contraceptive devices.

7.2 CONCEPT DEMONSTRATION DEVICES

7.2.1 Materials and methods

The polymeric material used in these experiments were poly-ε-caprolactone (PCL), MW 10,000-20,000 (Polysciences, Inc., Warrington, PA, USA; lot no. 434850), acid modified poly-ε-caprolactone LPS-60HP, (PCL-LPS) MW <9,000 (Union Carbide Chemicals & Plastics Company, Inc., Danbury, CT, USA; lot no. 2043), and polyethylene oxide (PEO), MW 100,000 (Polysciences, Inc., Warrington, PA, USA; lot no. 426741).

PCL is supplied in pellets and extrusions, therefore cryogenic milling is required to prepare PCL fine powder. After cooling in liquid nitrogen, the frozen PCL pellets are placed into a Ultra Centrifugal Mill (Glen Mills Inc., Clifton, N J). Milled powder is then allowed to dry and return to room temperature in nitrogen gas environment, prior to being sieved through a series of mesh. PEO is supplied in fine powder form, and the as-supplied powder is similarly sieved. For these experiments, powder particle size range of interest are 45-75 μm and 75-150μm.

The PCL-LPS and PCL are dissolved in chloroform to prepare, respectively, 20% (w/w) PCL-LPS solutions and 5% (w/w) PCL solutions. The glass bottle containing the appropriate binder solution is placed in a stainless steel pressurized reservoir. 20-40 psi is usually adequate to force binder to flow through a 7 μm stainless steel filter (Nupro Company, Willoughby, Ohio, Model SS-2TF2-7). A nozzle with 45 μm orifice is connected at the output end via a series of Viton tubing and connectors. As the binder is forced out of the nozzle, small droplets of binder, with diameter on the order of 60-80 μm are formed. The pressurized reservoir/binder assembly is place on a PM4800 DeltaRange balance (Mettler Instrument Corp., Hightstown, NJ, USA). The change in total weight with time represents the actual flow rate of the binder.

7.2.2 Device design and 3DP™ build strategy

The model device used for this study was designed to demonstrate control of drug release profiles by controlling position, composition, and microstructure. A diagram of

the device is shown in Figure 7.1. The top and bottom of the tabular device are composed of relatively non-resorbable PCL while the interior layers are composed of PEO bound by printing binders solutions so as to form perpendicular walls in the interior of the device. Dyes are deposited in selected locations with the device during the build procedure. Hydrolytic degradation of PCL occurs much slower than that of PEO. Thus, the top and bottom sheets of dense PCL serve as barriers against dye diffusion during resorption, and dye diffusion is confined to the plane of the device since the top and bottom are relatively non-resorbable.

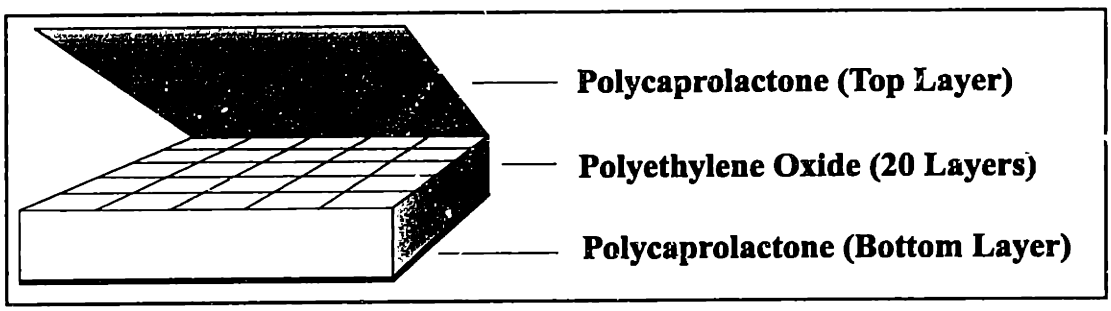

Figure 7.1: Model drug delivery device

The device design in Figure 7.1 was also designed to overcome several current limitations of ink-jet printing of solvents. Organic solvents are more difficult to print with drop-by-drop control using the continuous jet-printing method that we currently practice because of their high electrical resistivity and flammability. We, therefore, decided that our preliminary experiments should consist of selective printing of lines to form the walls of the device and manual deposition of the dyes. Continuous flow of binder solution through a 45 micron orifice plate was maintained during processing. Two types of patterns were printed into the powder bed to construct the device in Figure 7.1. Top and bottom layers of the device were constructed by printing individual lines across the powder bed in the fast axis direction followed by small steps in the slow axis direction. In this way, a thin solid layer could be fabricated on the top and bottom of the device. A cellular-type pattern was printed in the intermediate layers of the device. Widely separated lines were printed in the fast axis direction to fashion what would

ultimately be one set of vertical walls in the final device. Perpendicular walls were made by rotating the piston once on each layer so that perpendicular lines in could be printed with the same print head velocity. Dyes were selectively placed within the structure by stopping the build sequence before the final layer was constructed and depositing dye solutions using a micropipette within the desired cell of the device shown in Figure 7.1. Future versions of the solvent capable 3DP™ machine will permit drop-by-drop control and multiple binder printing so that piston rotation and manual drug placement will not be necessary.

A typical build sequence is described as follows. First, a bead of PCL powder is spread into a thin layer on the piston. A solid sheet of PCL is then formed by depositing droplets of 20% PCL-LPS/chloroform binder solution onto the PCL powder. As the binder contacts the thin layer of PCL powder, PCL particles bind to each other according the pattern of the printhead motion. Lines of PCL are formed by moving the printhead in a linear fashion. A dense PCL sheet is formed (see Figure 7.2) by repeatedly printing lines directly adjacent to each other. The piston is then lowered and the 3D Printing™ machine is ready for the next layer of powder. Layer number two begins by spreading a bead of PEO powder on top of the freshly printed PCL layer. A square grid pattern of 5 cells by 5 cells can be made by printing a set of 6 lines in one direction at 3 mm interline spacing, and then repeating another set of 6 lines in a direction 90° to the first set by rotation of the piston. This layer is repeated for a total of twenty layers to construct twenty-five cells which serve as drug reservoirs. Next, 8 µl of the appropriate dye is deposited into the unprinted powder within each selected cell according to the pattern shown in Figure 7.3a. A top layer of dense PCL is printed after drying of dye solution to seal the cells in the same manner as the first layer.

Figure 7.2: SEM of dense PCL sheet formed by printing lines of 5% PCL in $CHCl_3$

Three other types of devices were constructed to illustrate control of the release rate control of the wall composition, device anisotropy, and microstructure. A demonstration of the effect of binder composition was performed by constructing a device similar to that shown in Figure 7.3a, except that this second device was printed with 5% PCL/ chloroform as the binder (see Figure 7.3b). Any difference between the two devices reflects the difference between the two binder materials. The device shown in Figure 7.3c was printed with the same binder material for both print directions, but the microstructure of the walls varies with orientation. The walls in Figure 7.3c are chemically identical but physically different. Six lines are printed in one direction with the printhead moving at normal traverse velocity. Then six lines are printed at a much lower print speed in the perpendicular direction. The slower printspeed allows the printhead to deposit more volume of binder per unit length of line. As expected, low magnification SEM shows that the second set of lines are wider than the first set of lines (see Figure 7.4). Walls of two different thickness are built by repeating this layer 20 times. Figure 7.3d represents a different device with microstructural control. In this case, the binders are kept the same, as is the width of the walls in both direction. Each of the six walls in one direction are formed by printing four lines closely together in one direction. Each of the walls in the second direction are formed by printing only two lines, separated from each other by

unprinted PEO powder. Finally, control devices were fabricated with identical wall composition and microstructure in both directions, as well as symmetrical spatial distribution of both dyes (Figure 7.3e).

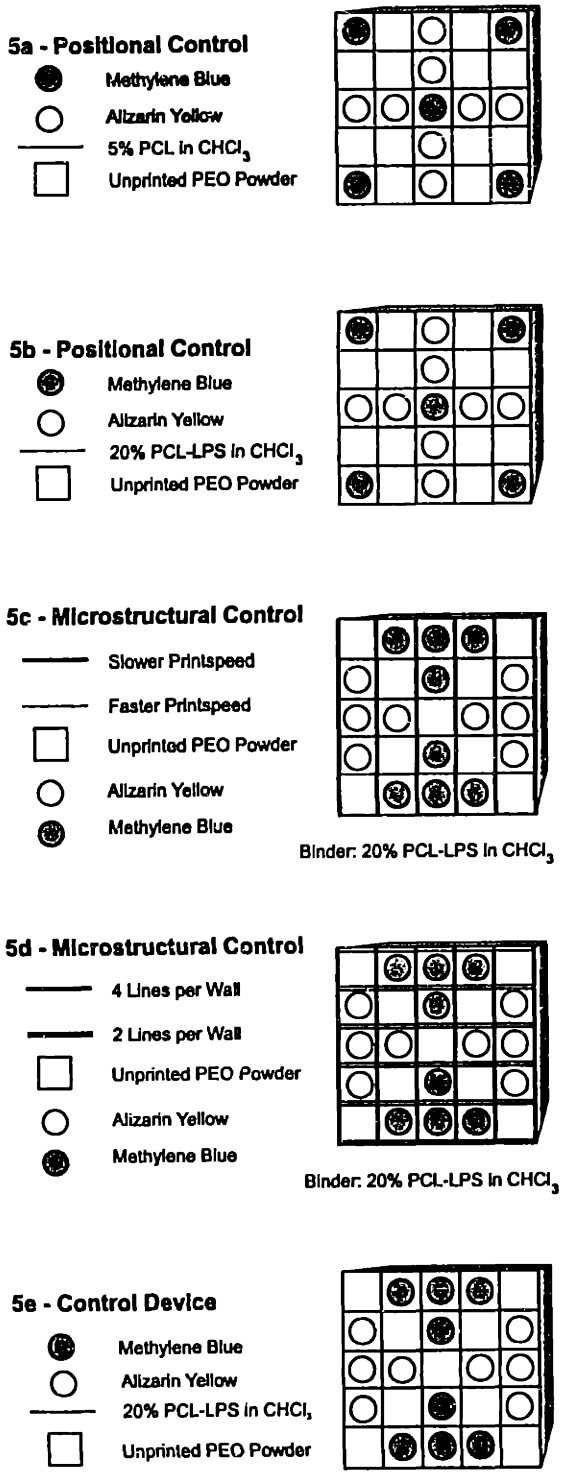

Figure 7.3: Design of test devices

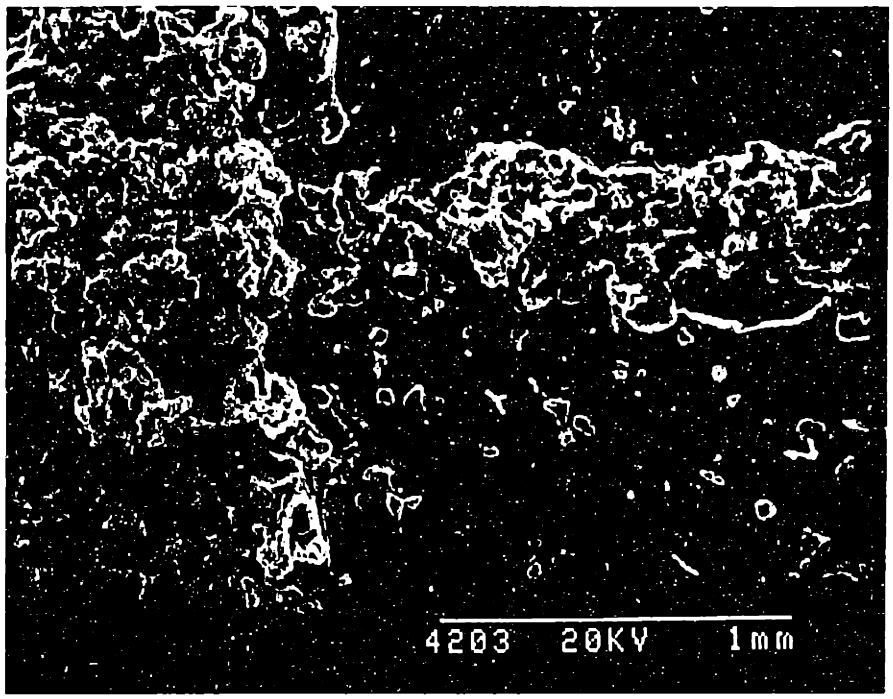

Figure 7.4: SEM of sectioned device as diagrammed in Figure 7.3c

All devices were allowed to dry in vacuum for 7 days, and their release rates were characterized by placing single devices into individual beakers filled with 10 ml water. The release of methylene blue and alizarin yellow from the devices was conducted at room temperature (20°C). The appropriate sample collection schedule was determined in separate, preliminary experiments in order to maintain sink conditions. At the appropriate time intervals, the devices are removed and placed into fresh 10 ml water. The 10 cc samples are stored in individual vials, and then transferred into Ultra-Vu disposable polystyrene cuvettes (Baxter Diagnostics Inc., Deerfield, IL) for spectrophotometric analysis. Absorbance for methylene blue (664 nm) and alizarin yellow (353 nm) was measured for all samples on a DU-640 spectrophotometer (Beckman Instruments Inc., Fullerton, CA). At the completion of the release, any remaining device was dried, sectioned, and prepared for scanning electron microscopic (Hitachi Instruments Inc., San Jose, CA) examination.

7.2.3 Observations

Control devices were constructed to establish a baseline release profile with which other devices will be compared. The blue and yellow dyes were deposited in the symmetrical pattern as shown in Figure 7.3e. The release profile for this device is expressed in terms of release rate (μg/hr) vs. time, and is shown in Figure 7.5. As expected, the two dyes are released at identical rates to within the statistical error of the experiment. Both release curves appear to exhibit a large release rate at t = 4 hours, and a second, smaller burst of release at t = 8 hours. The second burst is most likely attributed to dye distribution along the inner level of the device.

The release profile of the devices shown in Figure 7.3a (printed with 20% LPS-PCL/chloroform) clearly exhibit two maxima in the methylene blue release rate and a relatively constant release rate of alizarin yellow (Figure 7.6). The second burst of methylene blue release is statistically significant for these devices. The difference in release patterns between figures 7 and 8 can only be attributed to the different spatial distributions of the dyes within the devices, since all walls in this device are constructed with the same binder using the same printing parameters. Figure 7.7 shows that the similar devices printed with 5% PCL/chloroform (Figure 7.3b) have similar release profile, differing in release rates and time scale. The second burst of the PCL devices is less evident than that of the LPS-PCL devices (Figure 7.6), suggesting a different release mechanism.

Figure 7.8 shows the release profile for devices prepared according to Figure 7.3C. Methylene blue is released at an initially higher rate than alizarin yellow. The two dyes were deposited in symmetrical cells within the device. Therefore, any difference in release profile reflects the difference in printing parameters used to construct the device. In this case, the difference can be attributed to difference in wall thickness, since the positioning of the two dyes is symmetrical and the wall composition is constant throughout the device. The walls vary in thickness depending on the printing parameters used. Walls built with slower print speed on each layer are thicker than walls built with higher traverse velocity due to difference in binder per unit line length. Walls prepared

with larger amounts of binder per unit line length (slower printing speed) also have substantially higher density, as observed by SEM. The release pattern of the device shown in Figure 7.3d is depicted in Figure 7.9. The blue dye is released immediately, while the yellow dye is released after an initial lag time of 4 hours. With these devices, the difference in release rate reflects the difference in wall density, which is determined by print style.

The mechanism for release in PCL devices is readily apparent by microstructural observation of the device components after release. The behavior of the horizontal PCL sheets and vertical PEO side walls were substantially different. Six PCL plates were placed in water for 0, 1, 12, 24, 48, and 96 hours. SEM micrographs in Figure 7.10 show that the 96-hour specimen retains the dense, non-porous structure of as-printed PCL sheet. SEM micrographs in Figure 7.11and Figure 7.12 depict the PEO walls (printed with 5% PCL/ chloroform) before and after dye release, respectively. Most of the PEO particles are no longer visible after dye release and a porous microstructure is evident. No PEO walls printed with 20% PCL-LPS/chloroform were available after dissolution for SEM observation, since complete erosion of those walls took place during the release. Only the dense PCL sheets of these devices remain at the end of experiment, and they were similar to that shown in Figure 7.10.

Devices printed with 20% PCL-LPS/chloroform (Figure 7.3a, Figure 7.6) behaved primarily according to a biodegradation type mechanism. Erosion of PEO particles from the surface of the device was visually observed during dissolution. Dissolution of the PEO/PCL-LPS walls was completed within 15 hours, leaving behind only the top and bottom PCL plates. Mass transport occurred mainly in the x- and y- directions since the top and bottom solid PCL sheets did not dissolve within the time scale of these experiments. The erosion proceeded from the surface of the device toward the interior and gradually released the dyes as the erosion front progress toward the center of the device.

Similar devices (Figure 7.3b, Figure 7.7) built with the 5% PCL/chloroform binder probably functioned by a combination of mechanisms. Surface PEO particles

which were not coated with PCL binder underwent dissolution upon initial exposure to water. After approximately 5 hours, swelling of the PEO/PCL walls was visually noticeable. After about 20 hours, significant swelling of the PEO/PCL walls was experimentally observed. The top and bottom PCL sheets did not exhibit any swelling. These mechanism combined to facilitate the diffusion of the dyes into the external media. In this system, the control of release profile was strictly related to the position of dye location within the device. As expected, the blue dye exhibited a pulsatile release pattern with two bursts of dye release.

The device from Figure 7.3c shows that wall thickness affects release rates. This is expected regardless of mechanism. For the diffusion model, increased wall thickness can re related to increased diffusion distance, and increased tortuousity of the diffusion path. For the erosion model, increased wall thickness results in increased duration of slower degradation rate, assuming that the printed walls' degrade faster than the unprinted regions.

The device shown in Figure 7.3d demonstrates that for walls of equal thickness and composition, modification of internal wall microstructure can affect the release rate. Here, dyes limited by solid walls (4 connected lines per wall) were released at a slower rate than dyes limited by semi-solid wall (2 lines per wall, spaced 400μm apart).

It should be noted that walls of different microstructure can also be built by simply using different binders. For example, solvents which are more efficient in binding the powder material together can be printed in one direction, creating microstructurally dense walls in that direction. In the other direction, walls can be built by using binders in which the powder material is less soluble. These walls would then be more porous. If the two binders are similarly in solubility rate, then the second set of walls should allow faster release rates. No mechanical mixing was conducted to obtain these release rates. The release rates are expected to increase if mixing was conducted, and the time scale of the experiments would be reduced. The increase in release rate should be less significant for devices which are diffusion-limited.

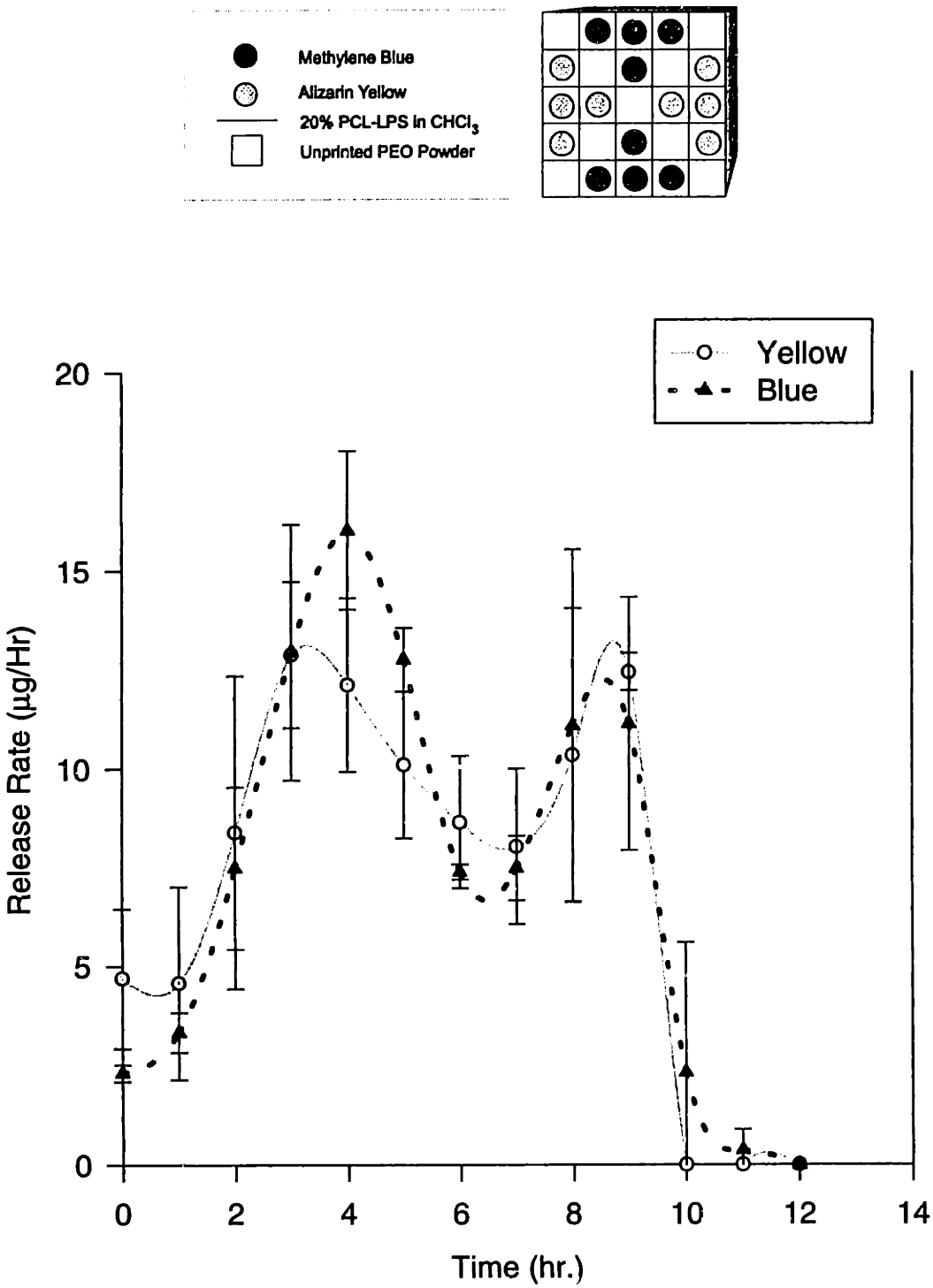

Figure 7.5: Release rate profile of control device depicted in Figure 7.3e

Positional Control - Asymmetric spatial distribution Identical walls

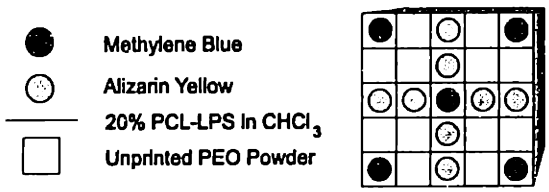

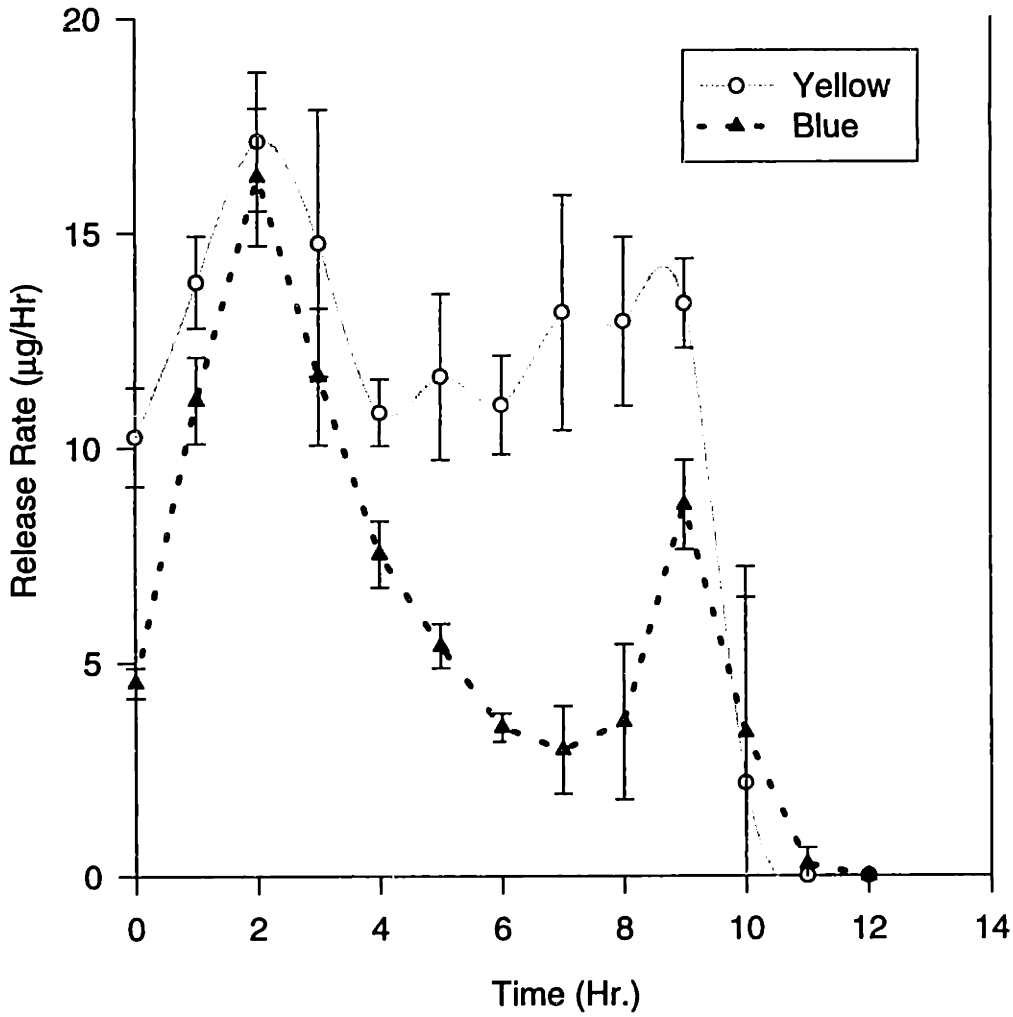

Figure 7.6: Release rate profile for device depicted in Figure 7.3a

Positional Control - Asymmetric spatial distribution Identical walls

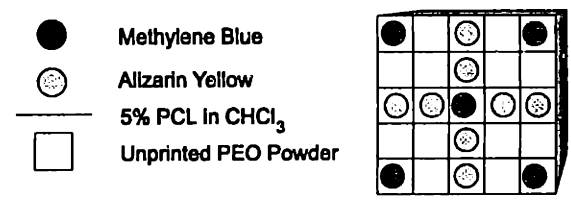

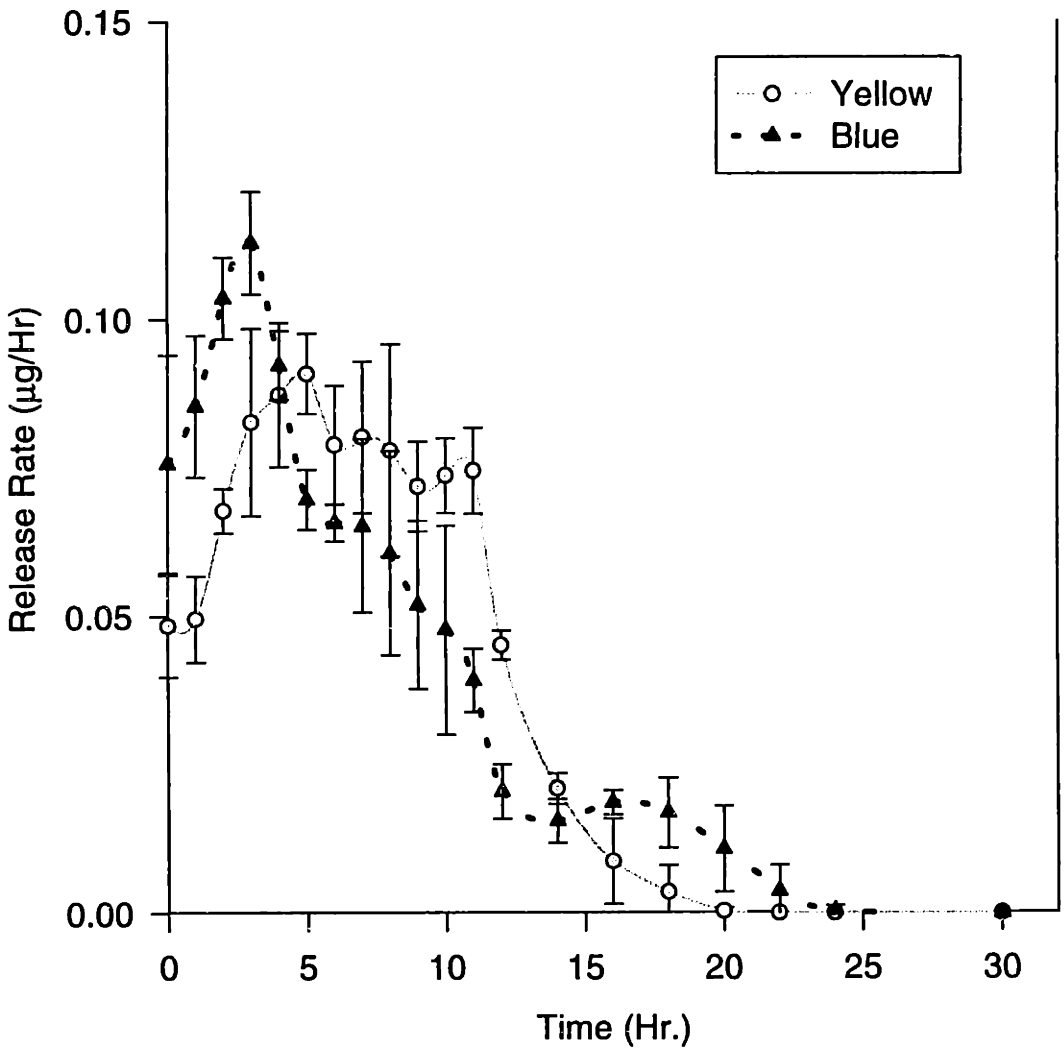

Figure 7.7: Release rate profile for device depicted in Figure 7.3b

Microstructural Control - Symmetric spatial distribution
Varying wall thickness walls

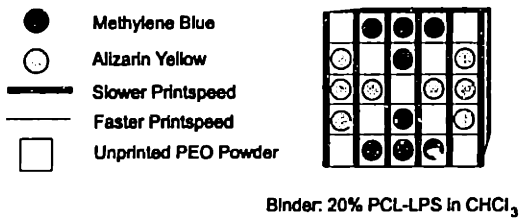

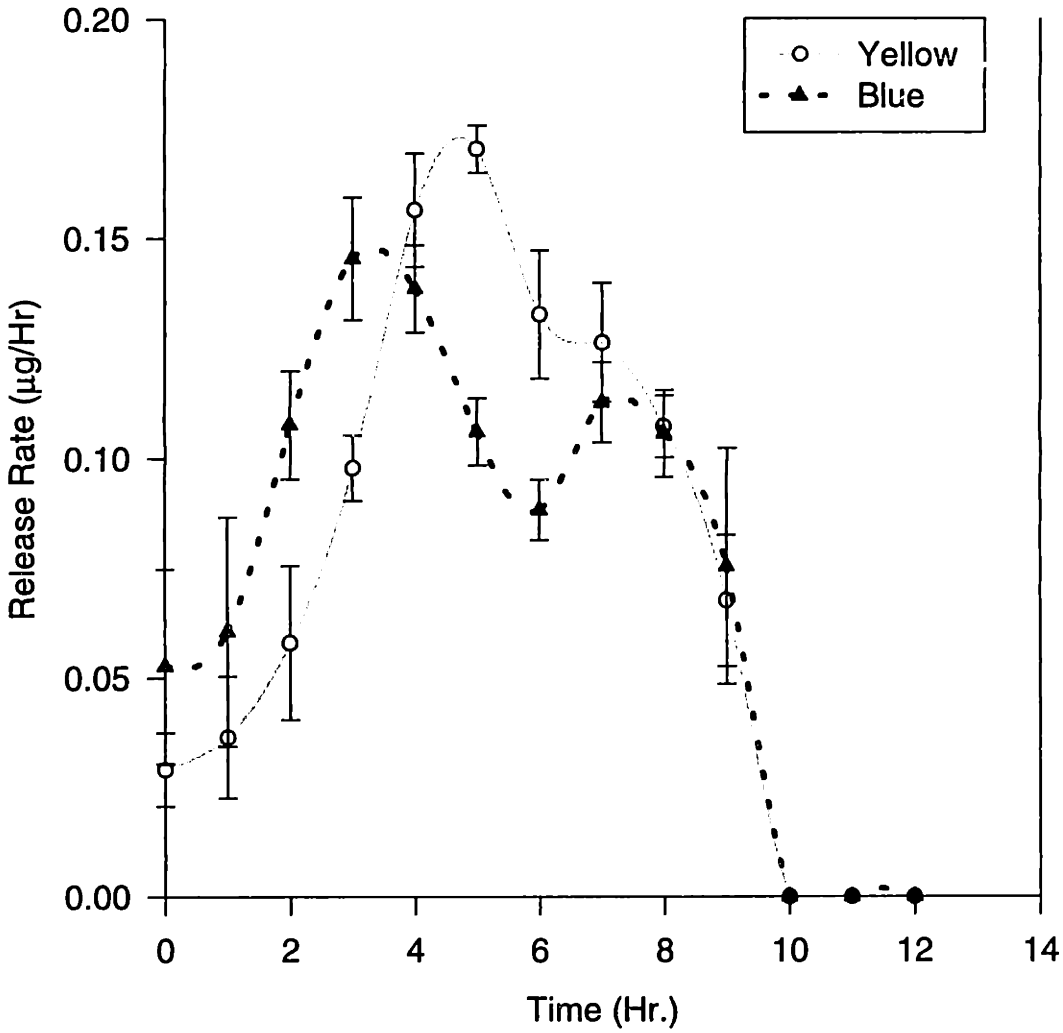

Figure 7.8: Release rate profile for device depicted in Figure 7.3c

Microstructural Control - Symmetric spatial distribution
Varying wall microstructure

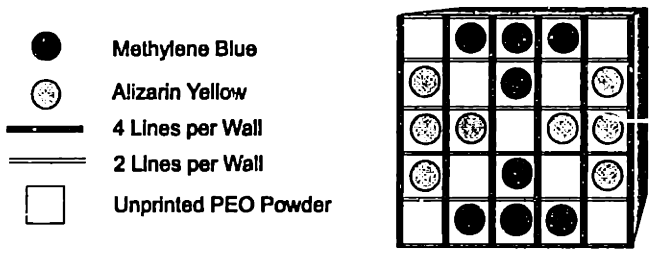

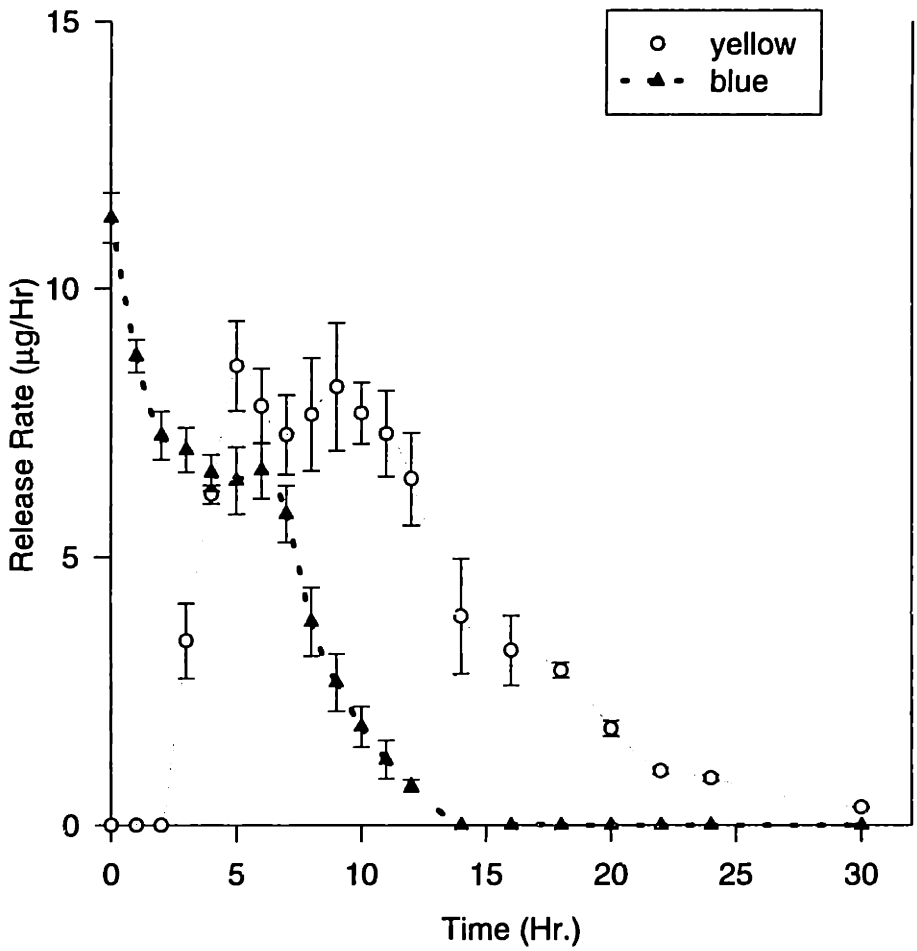

Figure 7.9: Release rate profile for device depicted in Figure 7.3d

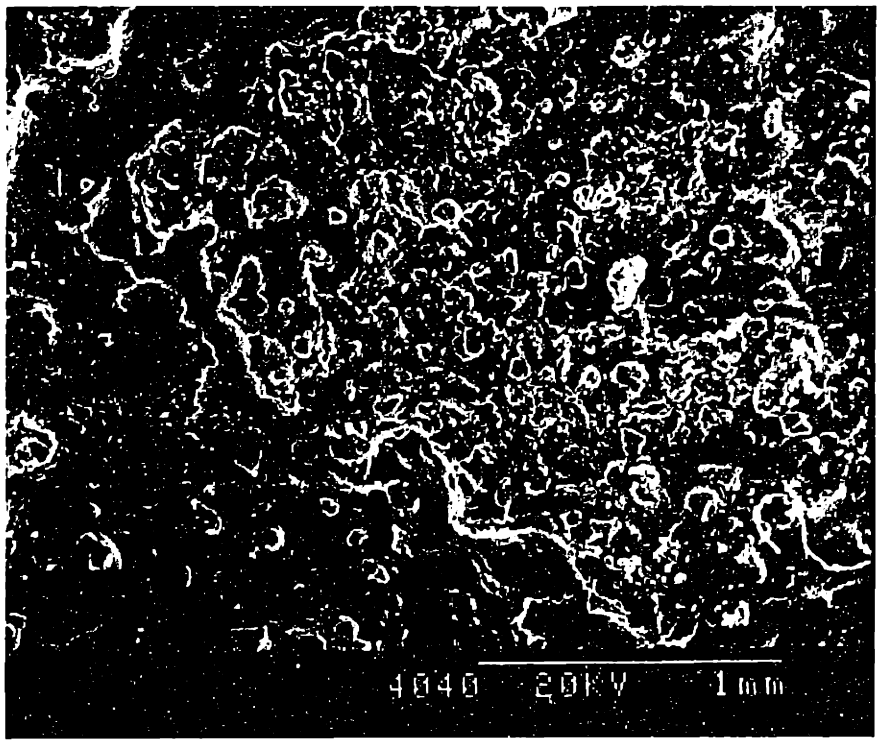

Figure 7.10: SEM of PCL sheet after 96-h in water (pH 6.0)

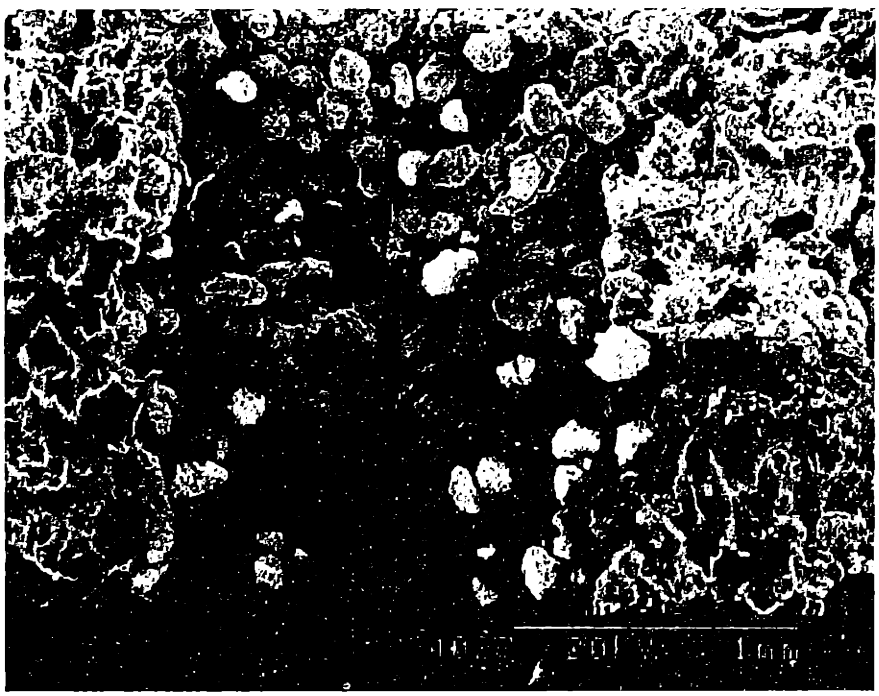

Figure 7.11: SEM of PEO-PCL matrix before water immersion

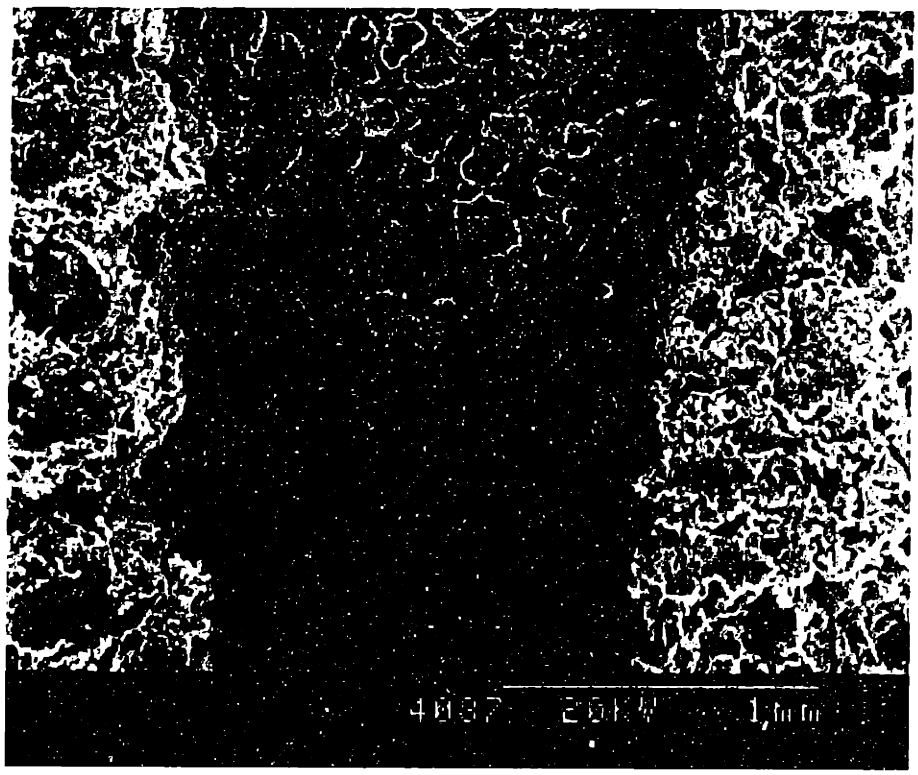

Figure 7.12: SEM of PEO-PCL matrix after 96-h water immersion

7.2.4 Discussion

The most common mechanism of drug release from polymeric systems is by diffusion. Mathematical models which simulate diffusion of drugs through a polymer network have been described[105]. The drug is distributed within a polymer matrix in a matrix device. If the drug is dissolved in the device, the final drug concentration is below the saturation solubility of the drug in the polymer. If the drug is dispersed as particles within the polymer, the final drug concentration is above the saturation solubility. Drug permeability is controlled by choice of the polymer.

3D Printing™ offers several unique built strategies for obtaining zero order release kinetics. Different diffusion gradients may be printed at any location within the device, either by changing the binder composition or by varying the microstructure of the diffusion barriers. A highly specific release profile can be produced by depositing the appropriate amount drugs at precise locations within the gradient. Obviously, 3D Printing™ is not limited to zero order release. 3D Printing™ can produce multiple

diffusion gradients within a single device, resulting in complicated drug release profiles not easily achieved with conventional processing techniques. Devices for hormonal replacement therapy could, for example, be made which mimic the physiological cyclic rhythms; zero order release for a specific amount of time, after which no release, when a period of quiescence occurs. Cyclic release profiles can be produced by repeating units in recurring sequences throughout the device. Alternatively, release of multiple drugs in rhythmic cycles can be achieved by setting up units of gradients that release different drugs at different time point.

It should be noted that although all devices fabricated for this report were printed with chloroform-containing binder, the 3DP™ process is not limited to the use of chlorinated solvents. Alcohols and non-halogenated solvents, such as acetone, have been used successfully to fabricate 3DP™ polymeric parts. All devices reported in this study were dried in vacuum for 7 days prior to water immersion, but a small amount of residual chloroform probably remained. Chlorinated solvents are undesirable in terms of potential health risks, and regulatory approval, but recent studies with critical point CO_2 drying demonstrate that chloroform can be removed to below USP specifications. The type of polymer also plays an important role in solvent retention. Some polymer, such as polycaprolactone, do not retain chloroform vigorously. Lyophilization is adequate to extract chloroform to below USP levels from PCL devices. A more detail description of these solvent removal techniques is presented in Section 2.6 of this thesis.

One concern of implantable drug delivery devices is the possibility of device rupture after implantation, leading to massive drug overdose. The mechanical properties of the devices in these experiments have not been studied, since they were designed only to demonstrate the 3DP™ capabilities. Mechanical properties must be among the key criteria in material selection for future, real devices. Polymers which swell when exposed to water, for example, are undesirable for implantable devices due to increased probability for rupture. Polymers such as polycaprolactones, polylactides, polyglycolides, and their co-polymers, exhibit less swelling than PEO and devices composed of these materials are less likely to rupture.

This preliminary work suggests that 3D Printing™ can reproducibly fabricate delivery devices with controlled release profiles by asserting three modes of control: three dimensional position. microstructure, and composition. Although only PEO and PCL powders are used in these experiments, virtually any material that can be processed into powdered form can be used in 3D Printing™.

7.3 ORAL DOSAGE FORMS

7.3.1 Background

3DP™ represents a fundamentally new approach to develop and manufacture novel drug delivery systems. This flexible technology can impact pharmaceutical manufacturing in three specific areas: controlled release, dosage control, and rapid formulation. The results presented in the previous section successfully demonstrated release profiles can be controlled in 3DP™ by modulating the tablet geometry, spatial distribution of the drugs, and the release barrier thickness, composition, and microstructure. The devices used in those experiments, however, were designed to confine drug diffusion to the horizontal plane for concept demonstration purposes only. The devices were not designed for real-world, practical drug delivery systems. The materials used, although biocompatible, were not recognized USP grade pharmaceutical materials. The dyes were manually deposited into each microreservoir by micropipettes. The latter limitation motivated the development and integration of drop-on-demand printing technology with 3DP™. In addition to accelerating the build sequence, selective droplet generation is advantageous for depositing drugs because of reduced waste. The modular nature of DOD systems is also important because for minimizing cross-contamination. DOD systems work at lower frequency range than continuous jet systems because the meniscus at the nozzle must be restored and the chamber refilled before the next droplet can be fired. The slower throughput per nozzle is overcome by having multiple nozzles per cartridge.

This section illustrates the 3DP™ development process for fabrication of oral dosage forms (ODF) with real drugs, and with USP grade pharmaceutical excipients. Drug deposition will be automated by drop-on-demand printing. Issues relevant to DOD

printing, such as droplet reproducibility and dosage accuracy, have been addressed in section 2.4.4. Thermal stability of the drugs during nozzle activation, have not been studied. The other two areas of potential impact, dosage control and rapid formulation, will also be explored.

7.3.2 Thermal stability of drugs during DOD nozzle activation

One obvious concern with thermal DOD systems was whether the heat generation during nozzle firing would damage the drug molecules being printed. The surface resistor within each DOD nozzle can reach a peak temperature of 400°C within 10^{-6} second, and typical pulse widths are less than 3 μm seconds. It is known that many drugs are thermally unstable at temperatures below their T_m, and significantly below the DOD resistor surface temperature (400°C). The question is not whether the DOD peak temperature exceeds that of the drug decomposition temperature, but whether the peak temperature is maintained for long enough time for decomposition to occur. This question was addressed by printing a drug which is known to be thermally unstable and monitoring its degradation after printing. Epinephrine has a melting temperature of 212°C[106], and has been reported in the medical literature to degrade at 60C with a concomitant color change from transparent to reddish brown[107].

Church et al. reported complete degradation of USP injectable epinephrine[108] solutions (1:10,000) after 169 hours of constant heat (65°C) exposure, and 31% degradation after 672 total hours of cyclic heating (8 hr/day at 65°C). Epinephrine degradation was reported to depend on sodium metabisulfite concentration and the duration of cyclic heating. The same investigators also reported on the effect of epinephrine concentrations on thermal stability[109]. 672 total hours of cyclic heating (8 hr/day at 70°C) did not result in significant degradation of highly concentrated epinephrine solutions (1:1,000), but resulted in 64% degradation of a more diluted solution (1:10,000). Significant loss (~30%) of cardiovascular potency was determined by blood pressure and heart rate responses in conscious rats. 1:10,000 epinephrine solution may be a good choice for DOD testing since a small temperature difference of only 5°C (65°C vs. 70°C) apparently resulted in a two-fold increase in epinephrine

degradation. The thermal stability of the concentrated epinephrine solution maybe due to lower pH. This pH effect may be related to the increased thermal stability of sodium metabisulfite (anti-oxidant).

1 mg epinephrine (Sigma Chemicals) was placed in 20 cc deionized water, and the mixture was sonicated for 15 minutes to accelerate dissoluion. The mixture was then centrifuged at 2500 rpm for 15 minutes to separate all undissolved matter. 2 cc supernatant was placed in silica glass cuvette (control) for UV-vis measurement. Another 5 cc of the supernatant was placed in a glass vial and placed into a 60°C water bath for 1 minute (heated sample). Another 10 cc supernatant was placed into a DOD cartridge and printed directly into a second silica glass cuvette (printed sample). A LabView program was developed to customize the signal waveform in terms of frequency, pulse width, amplitude, and duration. An electronic circuit was developed to facilitate individual nozzle selection. It was found that for each material, there is a narrow range of operational conditions for pulse width and signal amplitude. A wide range of signal frequencies could be used for most materials, ranging from 100 Hz to 10 kHz. The DOD operating conditions used for epinephrine were 5 kHz, 2.2 μsec, 24 v. The samples were scanned in the UV vis spectrophotometer at various time points up to 3 hours.

UV-vis spectra for control epinephrine are shown in Figure 7.13. A small absorption peak at 280 nm is detected. No major peak shift was observed, and no visually discernible color change was observed in this unheated, unprinted sample. A major color change from clear to pinkish brown was observed in the heated sample, even though it was only heated at 60°C for 1 minute. A slight shift in UV-vis spectra can be observed after 1 minute, and maximum color change was obtained after approximately 90 minutes (Figure 7.14). No color change was observed in the printed solution, which is consistent with the lack of spectral shift as shown in Figure 7.15.

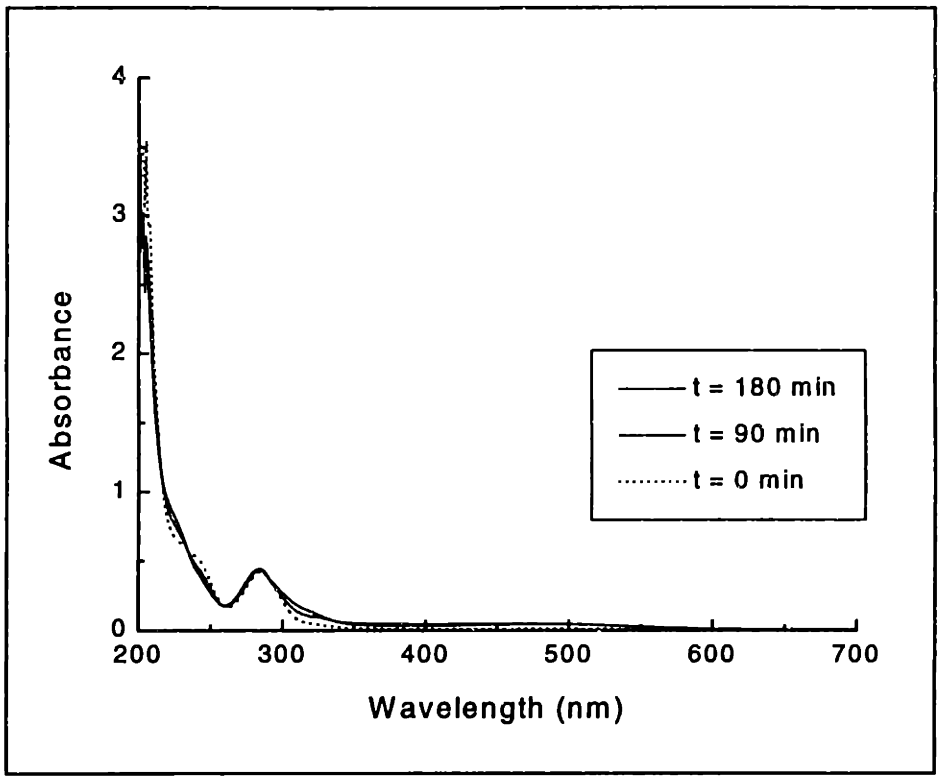

Figure 7.13: UV-vis spectra for control epinephrine (unheated, unprinted), 0-3 hr

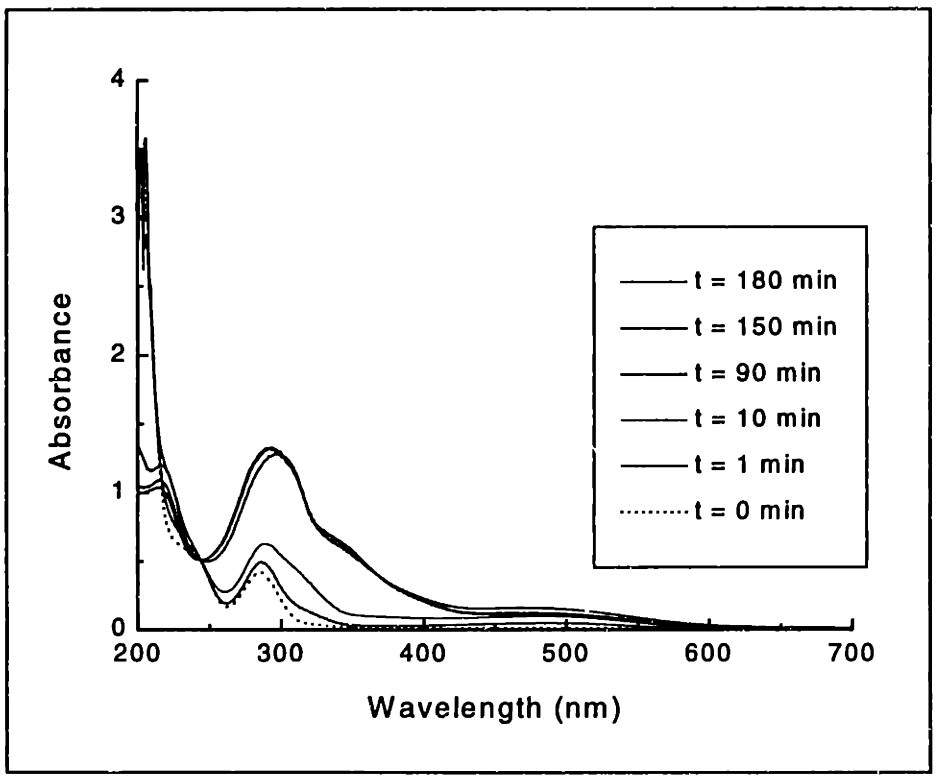

Figure 7.14: UV-vis spectra for heated epinephrine, 0-3 hr (60°C for 1 minute)

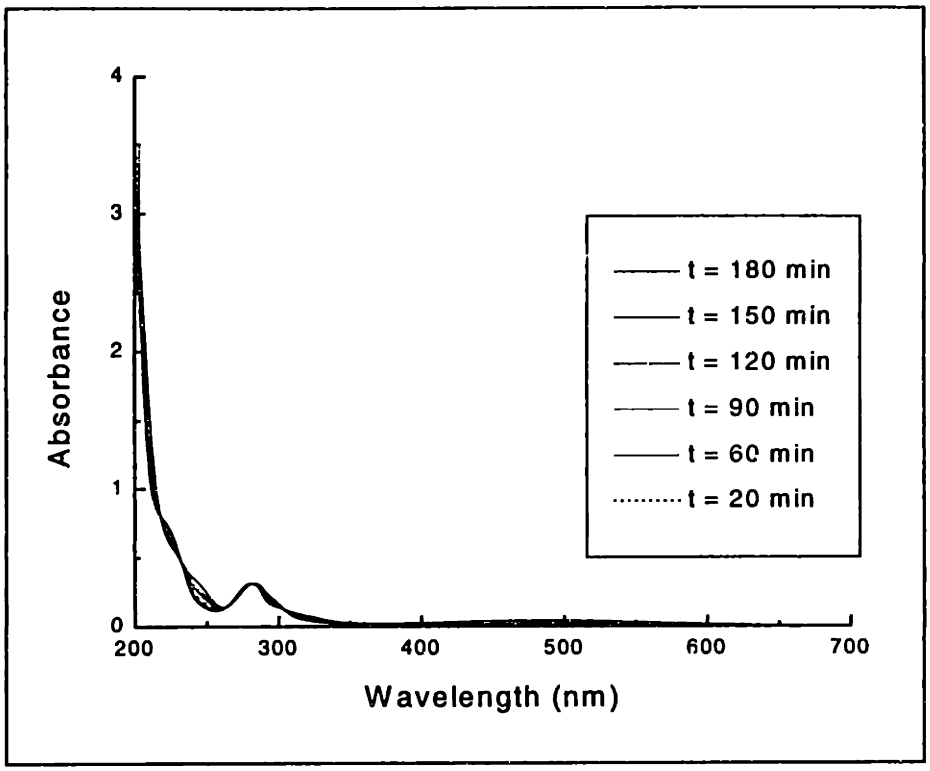

Figure 7.15: UV-vis spectra for printed epinephrine, 0-3 hr (5 kHz, 2.2 μsec, 24 v)

Preliminary UV-vis data with epinephrine suggested that thermal inkjet printing resulted in less thermal breakdown of the epinephrine molecule than heating for 1 minute at 60°C. The UV-vis spectra of the DOD printed epinephrine solution revealed only a single peak near 280 nm, as specified by the British Pharmacopia [vol. 14, 1973]. The UV-vis spectra of the 60°C sample turned pinkish brown, and an second absorption peak was detected. It is possible, however, that although the catechol chromophore responsible for the absorption peak is not affected by the printing process, other side groups of the epinephrine may be altered by the DOD process without wholesale degradation. Other analytical techniques such as will be used to better characterize the DOD printed epinephrine. Heller et al. showed that in a basic aqueous environment, epinephrine can be oxidized to produce hydroxyindole, which fluoresces in the visible range[110]. This method has been used for assaying epinephrine content in physiological fluids and in dosage forms. Quantitative HPLC protocols have also been developed[111]. Additional experiments are required to fully establish the heating effects of thermal inkjet printing on drug stability. Drop-on-demand inkjet printheads which rely on non-thermal activation

technologies, such as peizoelectric energy, are commercially available. These printheads would eliminate the question of thermal stability.

7.3.3 ODF construction

Prototype oral dosage forms were constructed as shown in Figure 7.16. The pill is 8.5 mm in diameter, and 5 mm in height. The binder solution used was a ethanol-based solution of Eudragit E100 (Rohm Pharma), which is a pH dependent copolymer with good solubility at low pH. The excipient powder was a microcrystalline cellulose (PH-101, FMC), with an average particle size of 50 microns. The bottom and top sections were made by printing binder only with continuous jet. Each sections consisted of 10 layers of 150 μm thickness. The middle section contained binder and drug. The binder was deposited with a CJ printhead, and the drug was deposited by a DOD printhead. A 17% drug solution was prepared and placed into a DOD cartridge. 4.5 mg of drug was deposited into each pill. Three groups of 8 pills were printed, and their printing parameters are listed in Table 7.2. The only variable among the 3 groups was the binder interline spacing. Group A was printed with the tightest interline stitching, which translates into the highest binder saturation and best inter-particle binding at 100μm. Group A ODFs are expected to exhibit the slowest release onset. All pills were dissolved in pH 3.5 media in a rotary shaker at 200 rpm. Samples were collected at predetermined time points which were determined in preliminary trials. Samples were centrifuged at 2500 rpm for 15 minutes. The supernatant was analyzed for drug release.

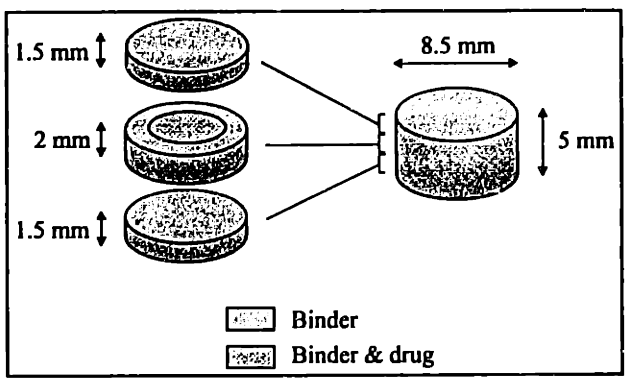

Figure 7.16: ODF design

	Group A	Group B	Group C
Binder flow rate	1.12 cc/min	1.12 cc/min	1.12 cc/min
Printhead velocity	112.5 cm/sec	112.5 cm/sec	112.5 cm/sec
Interline spacing	100 μm	125 μm	150 μm

Table 7.1: Printing conditions for ODF experiment

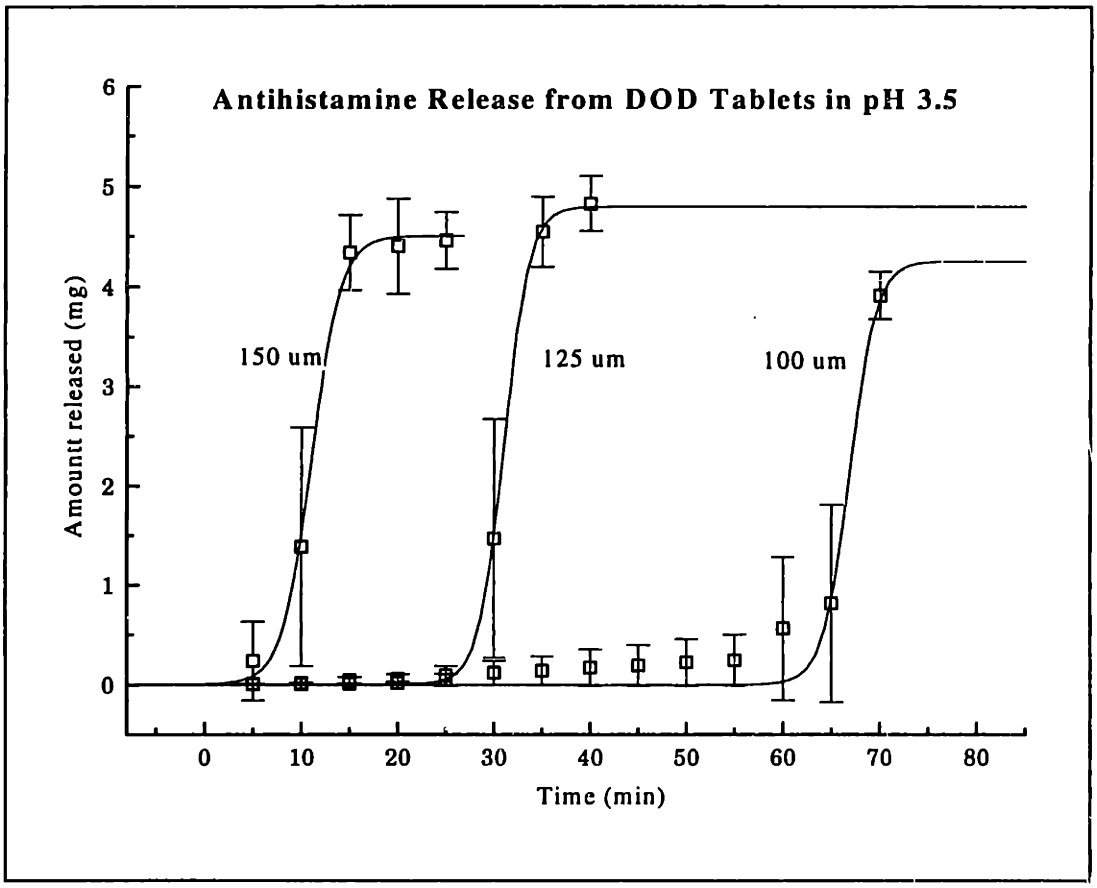

Figure 7.17: Cumulative release profiles for 100, 125, 150 μm interline spacing

Group C devices released after only 5 minutes of testing. Groups B and A, exhibited delay periods of 25 minutes and 60 minutes, respectively. The slopes of the 3 release curves suggest identical release rates for the 3 groups (Figure 7.17). It appears that binder saturation has a significant effect on delay onset of release, but negligible effects on release rate. This is consistent with the visual observation that the tablets dissolve predominantly by a erosion mechanism. Loose microcrystalline cellulose particles were observed to detach from the tablet as the acrylic binder dissolved. Devices

with higher binder saturation, therefore, provided longer delay time. The steep slopes suggest that drug release commenced as soon as the erosion front reached the drug reservoir. Some drugs may have diffused or leaked out before the erosion front reached the drug reservoir of Group C devices. Binder saturation would affect release rate if these ODF's released by diffusion. Powder-binder systems which bind by cohesive mechanisms (Chapter 3) are more likely to produce diffusion based release, depending on the dissolution media. Powder-binder systems which bind by adhesive mechanisms can also release by diffusion if the binder phase remain intact, but dissolution is only limited to the particles. This simple experiment demonstrates that device performance can be drastically affected by minute changes in 3D Printing™ parameters. In this case, a 25 μm decrease in line spacing resulted in a 35 minute extension in release onset.

7.4 IMPLANTABLE DRUG DELIVERY DEVICES

7.4.1 Background

Existing oral contraceptives are inconvenient, require daily dosing, and are highly susceptible to large fluctuations in blood levels of the therapeutic agent. Implantable contraceptive devices are designed for continuous release of steroids over a long period of time to improve patient convenience and compliance, and to minimize dosage fluctuation associated with other route of drug administration. The first commercially available contraceptive implant system is Norplant, which is a set of 6 hollow silastic capsules 34 mm in length, and 2.41 mm in outer diameter. Each hollow capsule, 1.57 mm inner diameter, is filled with 36 mg of levonorgestrel crystals, for a total dosage of 216 mg. The silastic capsules are implanted subdermally by trained physicians in a fan-shaped pattern through a trocar on the medial side of the upper arm. As of 1995, the system has been used by >1,000,000 women in over 20 countries[112,113]. A number of other systems are currently under development and/or clinical testing. Their physical dimensions and dosage information are summarized in Table 7.2.

Each of the systems listed in Table 7.2 provide relatively constant release of a single therapeutic agent, which does not mimic normal physiological hormonal production pattern. The ideal hormonal delivery system would be chronopharmacologic

in behavior, releasing more than one drug according to physiological patterns[114]. Five of the six systems listed are constructed from non-bioresorbable materials such as silicone rubber and ethylene vinylacetate, and surgical retrieval is required for these systems. Only Capronor is constructed with a biodegradable polymer.

	Norplant	Norplant 2	ST-1435
# Rods	6	2	1
Length	34 mm	44 mm	44 mm
Diameter	2.41 mm		
Matrix	silastic capsules	silastic rods	silastic rod
Hormone	levonorgestrel	levonorgestrel	nestorone progestin
Dosage (total)	216 mg	14 mg	
Release Rate	30 µg/day	70-80 µg/day	45 - 50 µg/day
Duration	5 years	3 years	> 2 years
	Implanon	**Uniplant**	**Capronor**
# Rods	1	1	1
Length	40 mm	35 mm	25 or 40 mm
Diameter	2 mm		2.4 mm
Matrix	ethylene vinylacetate	silastic capsule	polycaprolactone rod
Hormone	3-keto-desogestrel	nomegestrol acetate	levonorgestrel
Dosage	67 mg	38 mg	12 or 21.6 mg
Release Rate	60 µg/day	75 µg/day	30 µg/day
Duration	2 years	1 year	1 year

Table 7.2: Specifications of 6 implantable contraceptive systems

7.4.2 Device construction

The steroid containing devices are printed with the optimal printing conditions to fabricate defect free devices. They are similar in overall build strategy as the control release devices which contain amaranth. The materials used construction of each layer

are shown in Figure 7.18. Four groups of devices are constructed out of each matrix material to determine the effect of layer thickness, and the number of "releasing layers" on the release profile. An decrease in layer thickness corresponds, theoretically, to a denser microstructure, and hence a slower release rate. An increase in the number of "releasing layers" should result in a increase in the initial lag time, during which no release occurs.

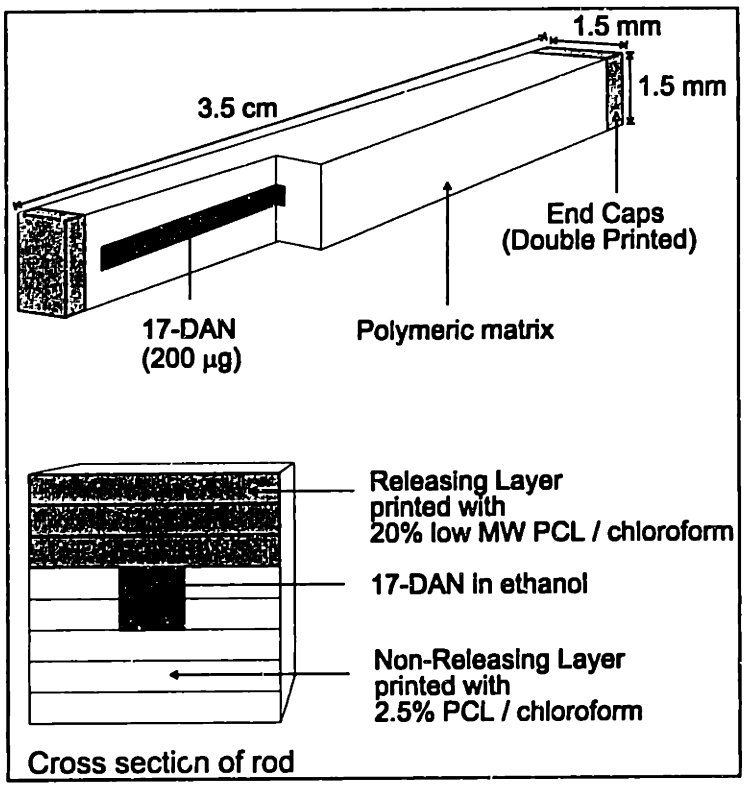

Figure 7.18: Implantable contraceptive device design

The matrix material used for constructing the polymeric matrix of the initial steroid-containing prototypes are PLGA powders (PLGA 85:15 100,000 MW; 45-75 µm). A second set of steroid-containing prototypes are constructed with PCL (45,000 MW; 45-75 µm) due to the slow release kinetics of steroids through PLGA. In both cases, the non-releasing layers are printed with a polymeric binder solution of 2.5% PCL (45,000 MW) in chloroform, using the appropriate printing parameters for the respective powder materials. After the non-releasing layers are printed, the reservoir in each device is printed with drug solution containing 8.5 w/w % 17-DAN in ethanol. The printing is then paused for approximately 30 minutes to allow adequate drying of the drug solution. The

devices are completed by printed the releasing layers are printed with 20% low MW PCL (9,000 MW) in chloroform. The devices are allowed to dry to minimize the amounts of residual solvents, and then placed in vials containing 20 cc 0.5% Tween 20 in water. The vials are placed in a automatic shaker rotating at 200 rpm.

Four groups of PCL devices are printed to determine the effect of layer thickness, and the number of "releasing layers" (see Figure 7.18) on the release profile. Two groups of devices are printed with 200 μm layer thickness, one group containing two releasing layers on top, and one group containing three releasing layers. Each group consists of 10 PCL devices. 2 similar groups of PCL devices are printed with 150 mm layer thickness. All devices are placed in nitrogen glove box for three days, conventional vacuum for 2 days, and then lyophilized for 2 days. 1 device from each group is randomly taken for SEM analysis in order to determine the effect of layer thickness on the microstructure in these devices. All remaining devices are placed in vials 20 cc 0.5% Tween 20 / water solutions. The vials are placed in a automatic shaker rotating at 200 rpm.

7.4.3 Drug assay

A solution of 17-DAN in 0.5% Tween 20/DI water is filtered and placed into a silica cuvette, and the cuvette is scanned from 190 to 300 nm to obtain the absorbance spectra in the UV-vis spectrophotometer (Beckman DU-640). Standard solutions of 17-DAN in 0.5% Tween 20/water are prepared and allowed to reach complete solubility in 24 hours. Beer-Lambert plots are constructed for the optimal wavelength determined above, and the recommended wavelength of 254 nm.

Numerous combinations of HPLC operating parameters are tested with two HPLC columns in order to identify the optimal parameters for analyzing 17-DAN release. Isopropanol:water and methanol:water are tested as mobile phase with a Zorbax-CN column (Du Pont), and water:tetrahydrofuran:methanol is tested as mobile phase with a hydrophobic C-18 column. Once the optimal parameters are identified, standard solutions of 17 DAN in 0.5% Tween 20/water at 2, 4, 6, 8, 10, 20, 30, 40, and 50 μg/cc are prepared and allowed to reach equilibrium for 24 hours. The solutions are then filtered through 0.45 μm disposable filter (Millex-HV, Millipore). The HPLC column is

then purged and equilibrated with the mobile phase for 2 hours. 50 µl of each standard dilution are injected, and the entire sequence repeated 6 times.

The spectra in Figure 7.19 indicates the existence of a maxima at 244 nm. The standard solutions are analyzed at 244 nm and 254 nm, and Beer-Lambert plots are constructed for the two wavelengths as shown in Figure 7.20. The experimental molar extinction coefficient for 17-DAN at 244 nm and 254 nm are ε=20,662, and ε=16,021, respectively, with 244 nm exhibiting a larger extinction coefficient. The optimal HPLC protocol for 17-DAN is identified, and the protocol is accurately enough to resolve both isomers of 17-DAN. HPLC protocol parameters and chromatogram of 17-DAN are shown in Figure 7.21.

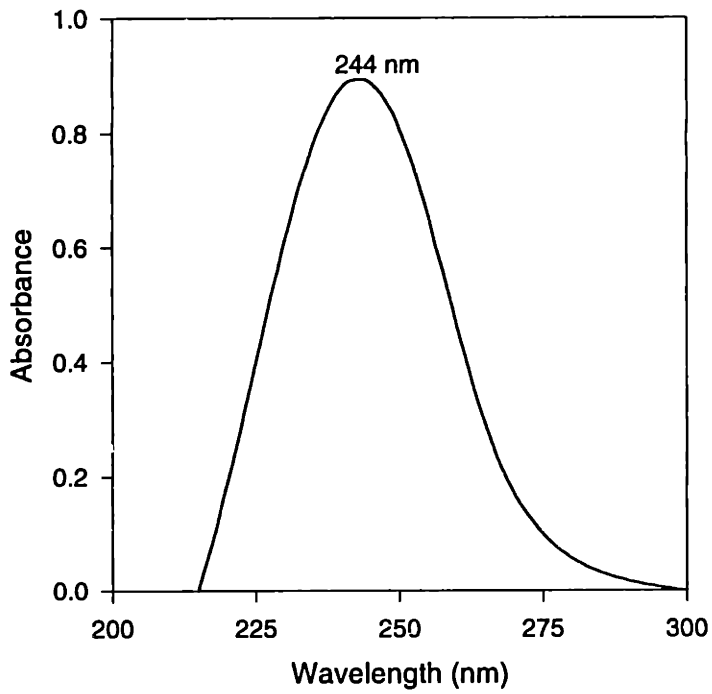

Figure 7.19: UV-spectra of 17-DAN

The r^2 values at both detection wavelengths (>0.99) suggest that both wavelengths can be used for reliable detection of 17-DAN by an UV-detector in concentration range of 1- 20 µg/ml. The experimental molar extinction coefficient for 17-DAN at 244 nm and 254 nm are ε=20,662, and ε=16,021. The use of 244 nm results in a 25% higher molar extinction coefficient, which is expected since this wavelength corresponds to the peak of

the absorbance spectra. The r^2 value for 254 nm is surprisingly good considering that this wavelength corresponds to the steep vertical part of the spectra. These experimental extinction coefficients are in agreement with those of other similarly structured steroids. Reported values for Norgestrel (ε=16,900 at 242 nm) and Norgestrienone (29,100 at 342) are similar to that determined experimentally for 17-DAN.

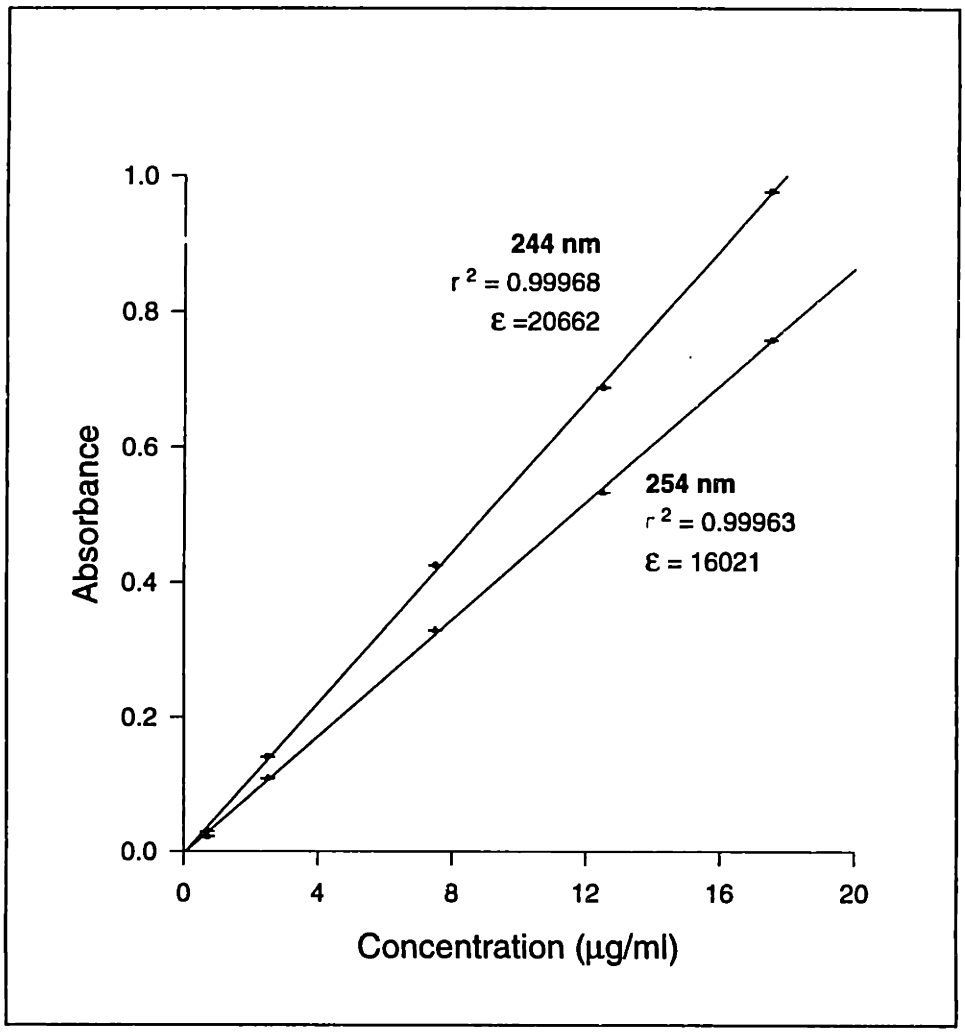

Figure 7.20: Beer-Lambert plot for 17-DAN at 244nm and 254 nm

The extinction coefficients can be used to determine the detection limit for 17-DAN in a solution of known volume. If a device is placed in a vial containing 10 cc 0.5% Tween 20/water, the detection limits are 1.79 µg and 2.31 µg, at 244 nm and 254 nm, respectively. These detection limits correspond to 0.025% and 0.033%, respectively, of 17-DAN solubility in that volume of 0.5% Tween 20/water. The detection wavelength of

244 nm should be used because of the reasons described above. 254 nm may be preferred, however, in cases where other substances in the vial have strong absorbance in the lower end of the UV range, and interferes with the 17-DAN spectra at 244 nm detection wavelength. The breakdown products from the polymeric matrix material, as well as Tween 20 itself, are expected to interfere at this UV range.

High performance liquid chromatography is the preferred analytical technique to assay for 17-DAN release from real devices due to the large number of potential sources for UV-vis detection interference. A hydrophobic column (C-18) is attached to a Waters HPLC unit. Mobile phase is a mixture of water, tetrahydrofuran, and methanol at 65:25:10 volume ratios. The mobile phase mixture is sonicated for 5 minutes, and then deaerated under vacuum and moderate stirring. Freshly degassed mixture is immediately used to purge the HPLC system and then equilibrate for 30-60 minutes, at a flow rate rate of 2 ml/min. The column is at ambient temperature. The multi-channeled UV detector is set to detect at 230 nm and 244 nm, and the raw data obtained at 244 nm is used for all subsequent assays. The raw data from 230 nm is stored, in case the need arise to re-evaluate the data due to other unexpected sources of interferences. The HPLC chromatogram and the conditions used to obtain it are shown in Figure 7.21. The supplied 17-DAN powder exist in an equilibrium mixture of *syn* and *anti* isomers. The resolution of the two isomers is reported to be critical for the reliable determination of 17-DAN content in the solution, and is highly dependent on the tetrahydrofuran content in the mobile phase[115]. The chromatogram below suggests that the listed conditions can result be used to obtain reliable data.

Standard solutions of 17 DAN in 0.5% Tween 20/water at 2, 4, 6, 8, 10, 20, 30, 40, and 50 μg/cc are prepared and allowed to reach equilibrium for 24 hours. The solutions are then filtered through 0.45 μm disposable filter (Millex-HV, Millipore). After equilibrating and purging the column, 50 μl of each standard dilution are injected, and the entire sequence was repeated 6 times. Clean peaks were obtained for each dilution, and the areas under both isomer peaks are integrated and summed to produce a total area vs. concentration plot for all standard injections (Figure 7.22). The slope of the linear regression is 671,992 μV*sec/μg/cc, and will be used to determine the

concentrations of the unknown. The good linearity (r^2 = 0.999) support the use of the HPLC operating parameters listed in Figure 7.21, in the 17-DAN concentration range of 2 to 50 µg/cc.

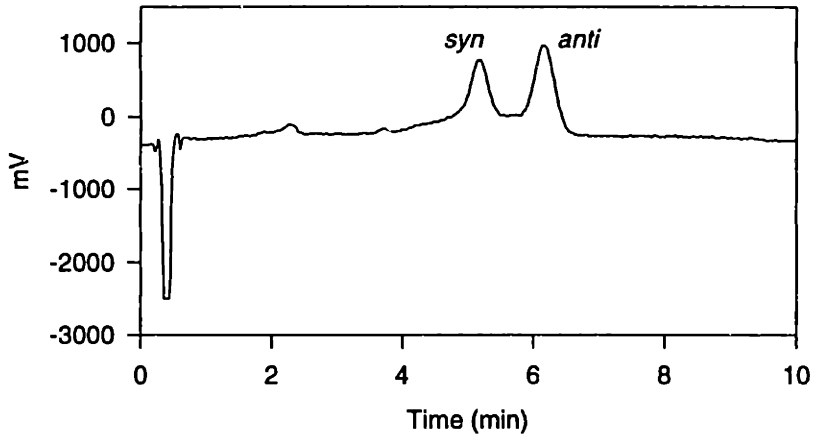

HPLC:	Waters (Division of Millipore)
Column:	C-18
Mobile Phase:	65:25:10 H_2O:THF:Methanol (filtered & degassed)
Flow Rate:	2.0 ml/min
Column Temp:	20 °C
Injection Volume:	50 µl
Detection:	UV at 244, 0.100 AUFS
Retention Time:	syn-isomer: 5.5, anti-isomer: 6.5 minutes

Figure 7.21: HPLC protocol and characteristic chromatogram for 17-DAN

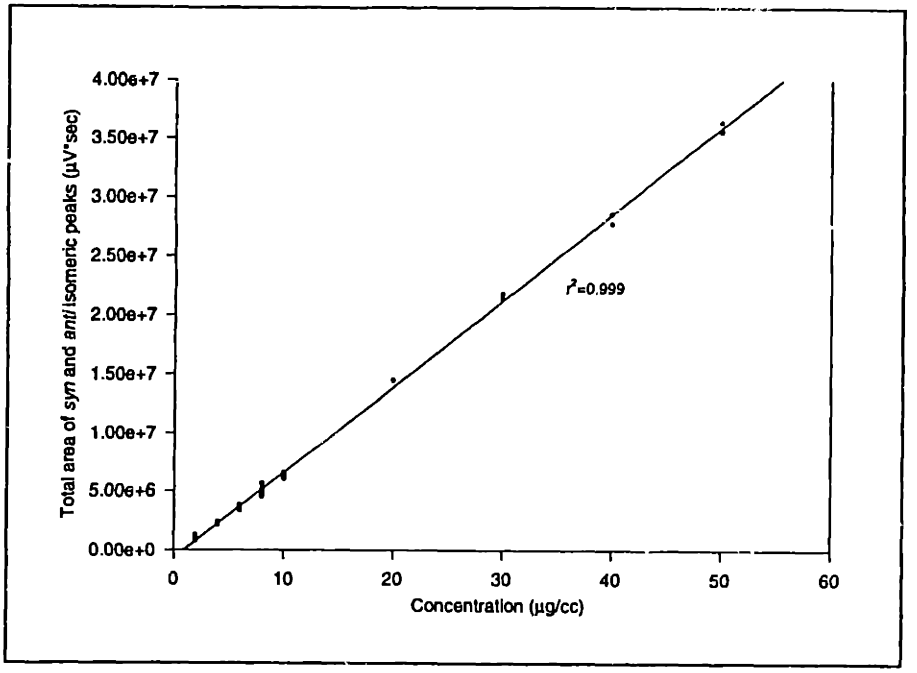

Figure 7.22: HPLC calibration plot of 17-DAN standards

7.4.4 Device performance

Figure 7.23 shows the release profiles for both groups printed with 200 µm layer thickness. After an initial lag time of 2 to 3 days, both groups released at similar initial rates. Devices printed with two releasing layers show initial release rates of 4.2 µg/day from days 2 to 8, while devices printed with 3 releasing layers show initial release rates of 3.6 µg/day. The steady state release rates of the two groups, taken to take place after day 8, are almost identical. The 2-layered group has steady state release rate of 0.85 µg/day, and the 3-layered group released at 0.88 µg/day during the same period.

Figure 7.24 shows the release profiles for both groups printed with 150 µm layer thickness. The 2-layered and 3-layered groups printed with 150 µm behaved similar to the corresponding groups printed with 200 µm layer thickness. Devices printed with two releasing layers show initial release rates of 3.2 µg/day from days 2 to 8, while devices printed with 3 releasing layers show initial release rates of 2.7 µg/day. The steady state release rates of the two groups, are slightly different. The 2-layered group has steady state release rate of 0.82 µg/day, and the 3-layered group released at 0.64 µg/day during the same period. Scanning electron micrographs (Figure 7.25) of

representative devices from both groups demonstrate that 150 μm devices are associated with very few porosity, while the 200 μm devices are associated with a few, but minor porosity.

A decrease in layer thickness should correspond, theoretically, to denser microstructure, and hence slower release rate. Scanning electron micrographs (Figure 7.25) of representative devices from each group support the hypothesis that the 150 μm devices are associated with very little porosity, while the 200 μm devices have a more porous microstructure. Comparing the release data from the 200 μm and the 150 μm layer thickness groups, the 150 μm group released at slightly lower initial rates than those from the 200 μm group, further supporting the idea that thinner layer thickness results in denser microstructure, and therefore lower release rates.

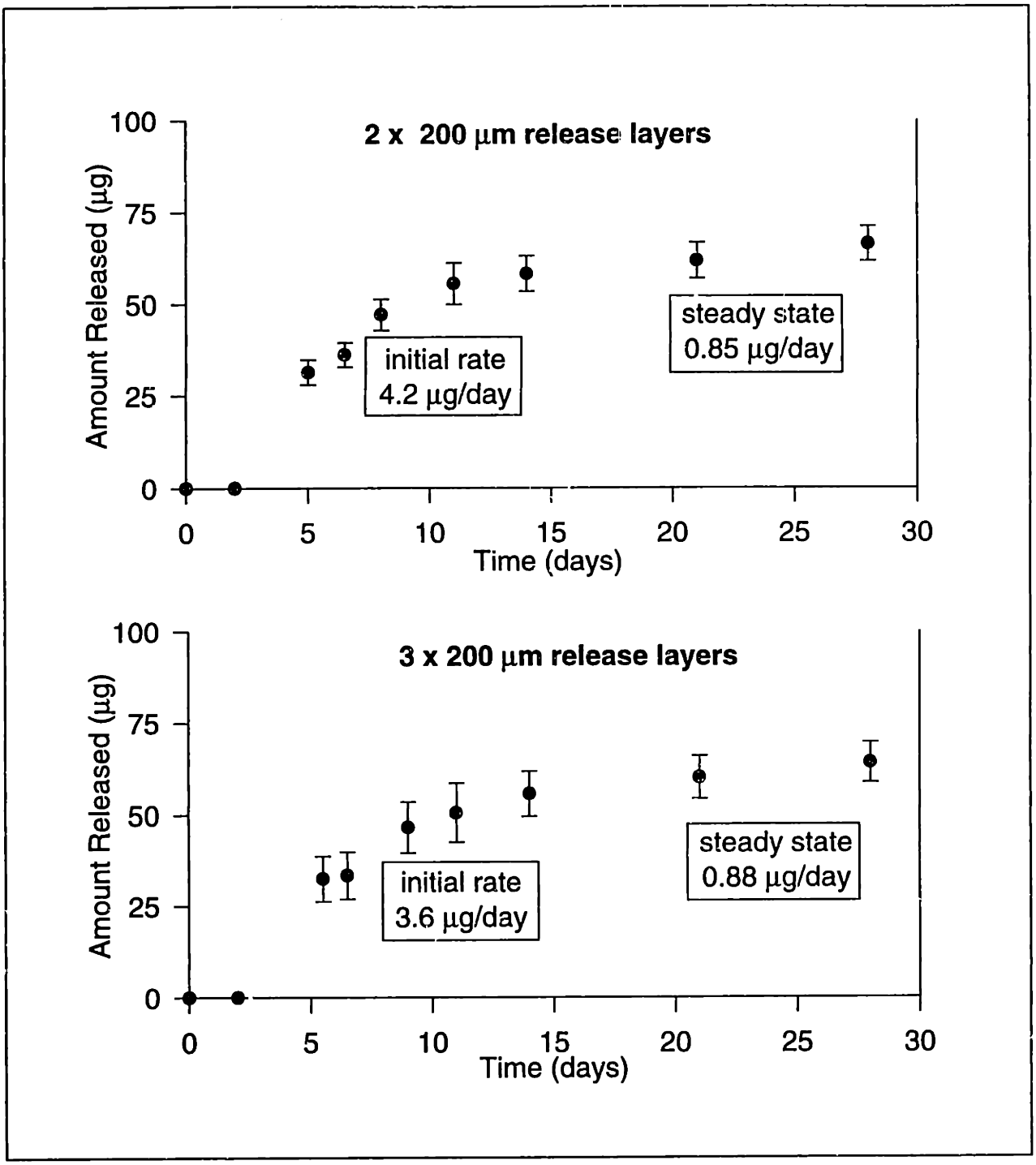

Figure 7.23: Release profiles for PCL devices printed with 200 µm layer thickness

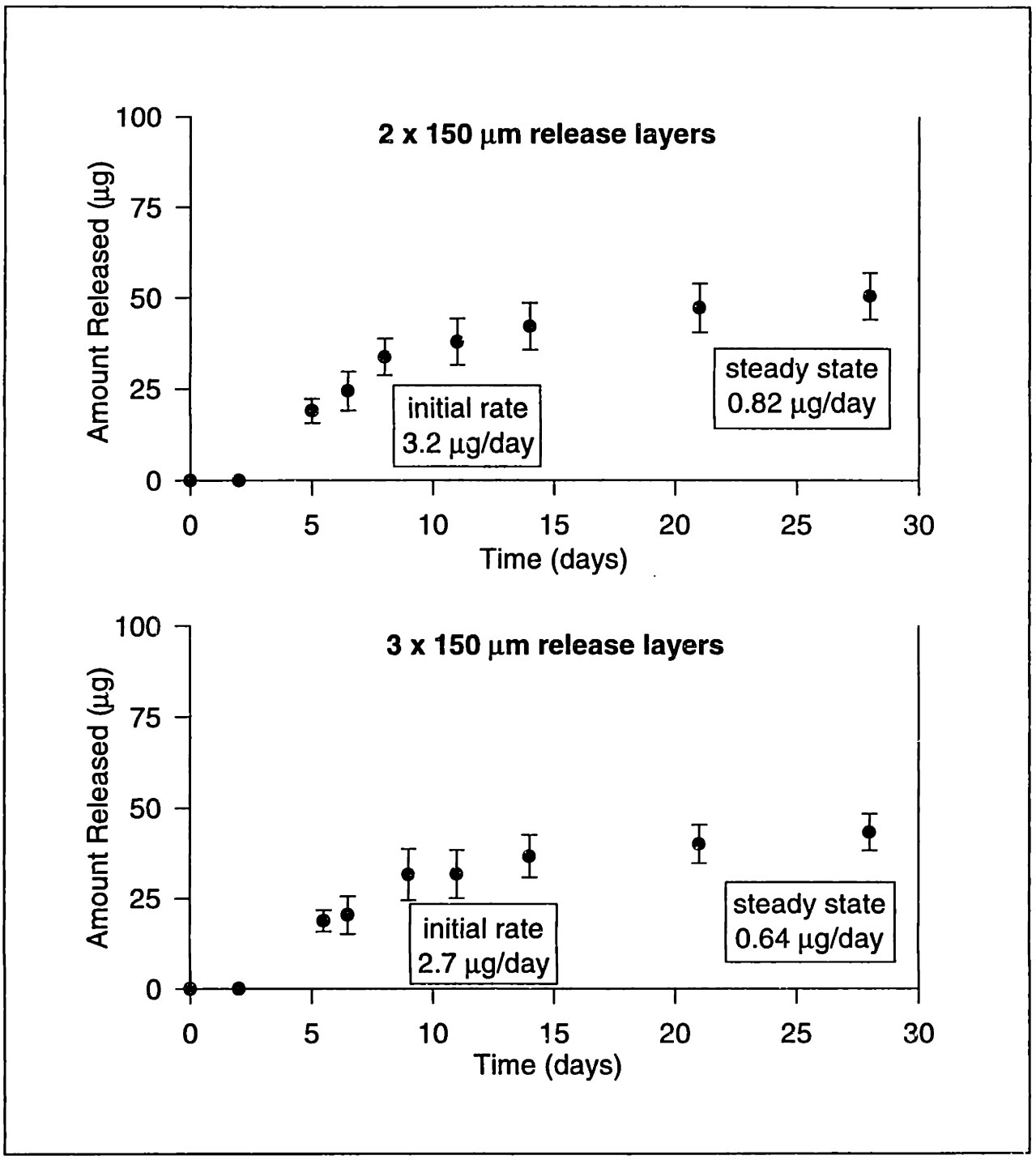

Figure 7.24: Release profiles of PCL devices printed with 150 µm layer thickness

Figure 7.25: SEMs of devices printed with 200 μm (left) and 150 μm (right)

It should be emphasized that the data suggest very good reproducibility in terms of sample performance. The standard errors among devices are on the order of 10-15 μg/day, which is quite good considering the fact that each group contains only 10 samples. The actual amount of 17-DAN / ethanol deposited within each layer in the reservoir can be easily obtained by the following equation:

$$\text{Amount of 17 - DAN deposited [}\mu\text{g]} = \frac{n F_v l C}{V}$$

where n = number of printhead passes over printed length

F_v = volumetric flowrate of drug solution [ml/sec]

l = printed length [cm]

C = concentration of drug solution [μg/ml]

V = printspeed [cm/sec]

All five variables can theoretically be used to control the amount of steroid printed in each device. The goal is to maximize the amount of drug printed into each device. The geometry of the device design, however, places an upper limit on the amount of drug that can be placed into each device since the implants must be less than 35 mm long. The

volumetric flowrate can be raised to increase the amount of printed drug, but there is a maximum flowrate beyond which the resolution of the printed part would deteriorate. The flowrate is also not a good parameter for controlling the amount of drug deposited because it is not practical to change the flowrate during a program run. The printspeed is much easier to control, and it can be used to precisely vary the amount of drug deposited. The increased amount of drug loading can be achieved by decreasing the printspeed. The minimum printspeed, however, is also constrained by print resolution. The concentration of the drug solution can be increased without affecting the device design or resolution. The concentration is constrained, however, by the solubility limit of the drug in the solvent, and by the viscosity of the drug-solvent solution. Solutions with viscosity greater than 50 cp are associated with jet instability and nozzle clogging problems. The last variable is the number of passes a printhead makes over the same reservoir region. If the drug is dissolved in a solvent with sufficiently high vapor pressure, then the solvent can evaporate quickly, and a second pass of the same solution can add more drug to the reservoir without affecting the resolution of the device. The precise amount of drug deposited can therefore be controlled by modulating all 5 parameters within their respective limits as discussed above.

7.4.5 Effect of matrix composition on 17-DAN release

The transport of steroids through polymeric matrices can be highly dependent on the polymeric matrix composition. These experiments are designed to compare the release behavior of 17-DAN through polymeric devices constructed with PLGA and PCL. Devices are printed with PLGA polymer (100,000 MW, 85L:15G) powder similar to the PCL devices, as described in Figure 7.18. The PLGA devices are printed with smaller line spacing (40 μm) than are the PCL devices (100 μm), and the PLGA devices are printed with slower printspeed (100 cm/sec) than the PCL devices (150 cm/sec). These printing conditions result in higher binder volume per unit volume of printed region for the PLGA devices, which are needed for defect-free PLGA devices. Steroid containing PLGA thin films are made by adding 17-DAN a solution of PLGA / chloroform, and allow for drug dissolution. Similar films are made with PCL / chloroform solutions. The PLGA rods and films are allowed to dry, and then placed into aqueous solutions

containing 0.5% Tween 20. Samples from the dissolution vials are analyzed or the presence of 17-DAN by HPLC according to the protocol described in Figure 7.21. Figure 7.26 shows the HPLC chromatogram obtained from a sample solution after two months of "release" from a steroid-containing prototypes constructed with PLGA (100,000 MW, 85L: 15G, 45-75 μm) powder. The chromatogram is in marked contrast with that shown in Figure 7.21. The characteristic peaks from the syn- and anti- isomers are not present, suggesting that even after >60 days in water, no detectable amount of 17-DAN is released from the PLGA printed devices. By keeping the binder compositions constant, and changing only the matrix powder material from PLGA to PCL (45,000 MW), a dramatically different release behavior is obtained.

Figure 7.27 shows that after only 5 days in water, the two isomeric peaks can be easily detected. The data suggests that the release of steroidal compounds, such as 17-DAN, is much faster in PCL matrices than in PLGA matrices.

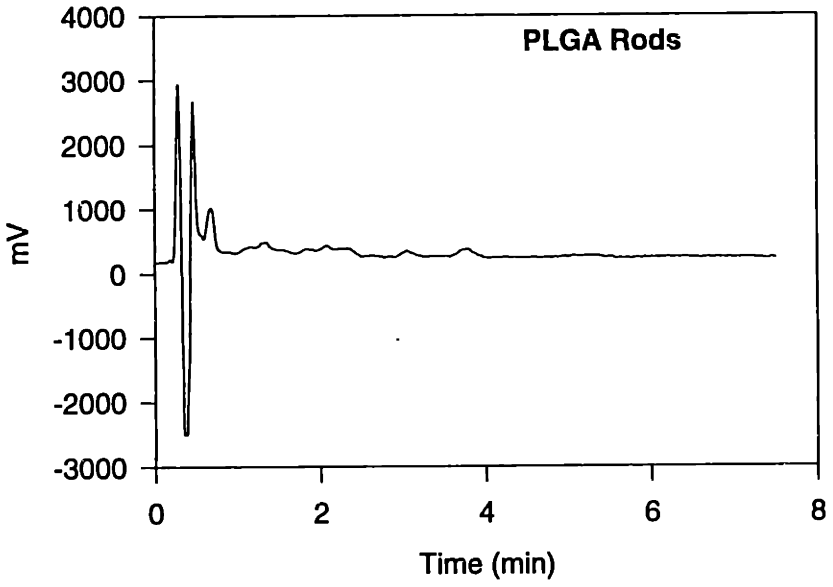

Figure 7.26: HPLC chromatogram of PLGA devices after 2 months in water

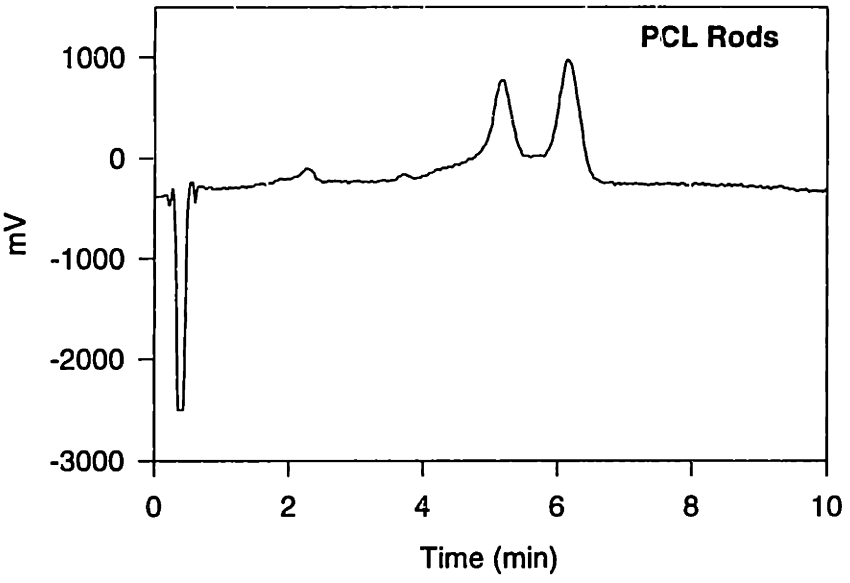

Figure 7.27: HPLC chromatogram of PCL devices after 5 days in water

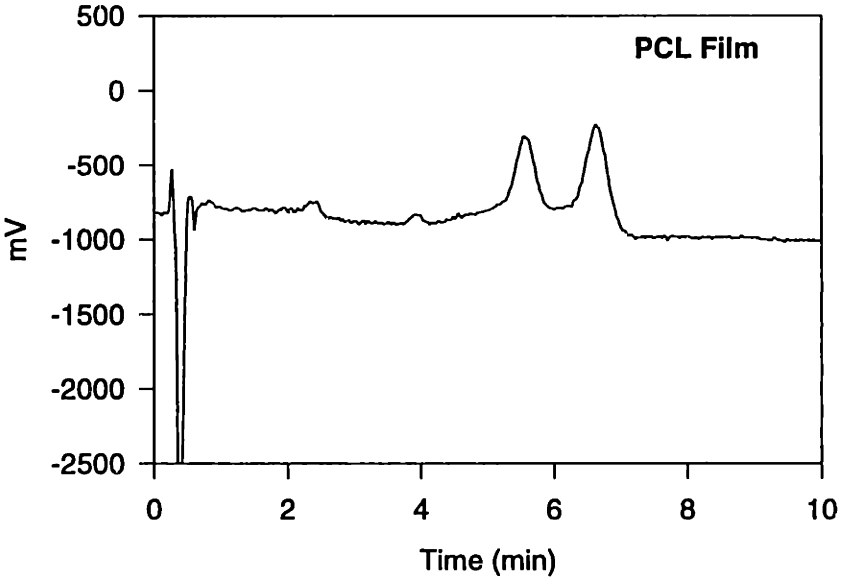

Figure 7.28: HPLC chromatogram of PCL thin film after 30 days in water

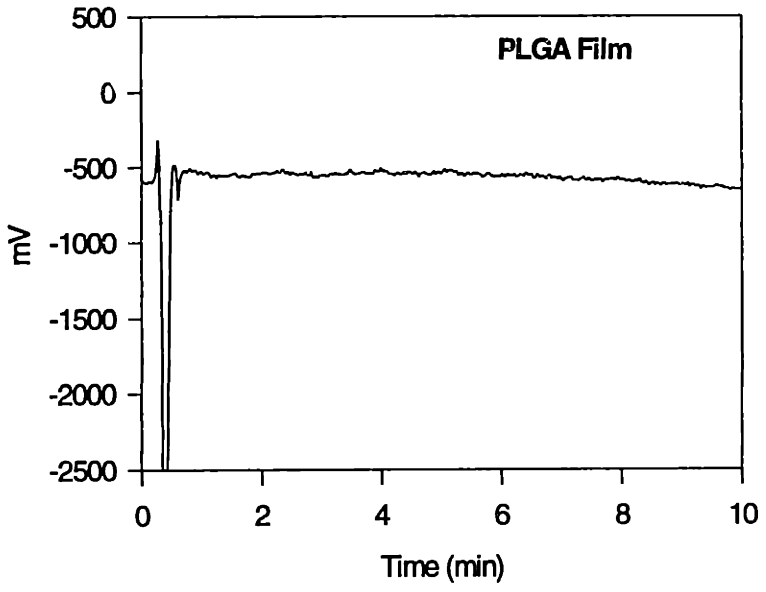

Figure 7.29: HPLC chromatogram of PLGA thin film after 30 days in water

The above findings are consistent with the thin film experiments designed to compare the release kinetics of 17-DAN from PLGA and PCL. Figure 7.29 showed that release of steroid from PLGA film is non-detectable even after 30 days, in good agreement with Figure 7.26. The release of 17-DAN from PCL film is easily detectable, as shown in Figure 7.28, and is consistent with the chromatogram shown in Figure 7.27. One contribution for the dramatic difference in release kinetics may be the difference in glass transition temperature of the polymers. The Tg of PLGA is approximately 60°C, slightly above ambient temperature (20°C) at which the release is conducted. The Tg of PCL is -60°C, which is significantly lower than room temperature. Polymers at temperatures above their Tg's are expected to exist in a non-glassy, rubbery state. Drug permeability in rubber polymers is expected to be significantly higher than the permeability of the same drug through the glassy state. Polymers such as PLGA, which exist in the glassy state at 20°C, are expected to have significantly lower drug permeability. Good correlation exists between Tg and the permeability of similar polymers[116]. It is interesting to note that despite retaining 3-4 wt % residual solvents, the

PLGA matrix is not plasticized sufficiently to cause a significant increase in steroid permeability. It is possible that the residual chloroform may be leached out of the PLGA matrix faster through liquid water than by evaporation and diffusion in the gaseous state.

A second contribution for the faster release profile from PCL matrix may be the difference in solubility of 17-DAN in PCL. Pitt et al reported silimar permeabilities of progesterone in PCL and in silicone rubber, even though the diffusivity of progesterone in silicone rubber (450 cm^2/sec) is two orders of magnitude higher than that of progesterone in PCL (3.6 cm^2/sec). The difference in this case is the large solubility of progesterone in PCL (17 mg/g), relative to solubility in silicone (0.57 mg/g). The solubility of steroids in PLGA is expected to be on the same order of magnitude as in PLA, which is significantly lower than steroid solubility in PCL. The combination of solubility and diffusivity determines the permeability of the drug. The solubility of progesterone in poly (DL-lactic acid) is similarly low, about (0.65 mg/g). The diffusivity of progesterone in poly (DL-lactic acid), 5.1×10^{-3} cm^2/sec, is about five orders of magnitude lower than that of silicone rubber[116]. This combination of low solubility and very slow diffusivity results in a very low progesterone permeability in poly (DL-lactic acid).

8. 3DP™ TISSUE ENGINEERING SCAFFOLDS

8.1 BACKGROUND

This chapter reviews some of the contributions 3DP™ has made toward liver regeneration. About 30,000 Americans die from end-stage liver disease each year,[117] and liver transplantation is currently the only established successful treatment for end-stage liver failure. The severe scarcity of donor organs, particularly in the pediatric population, has become a major limitation to liver transplantation. Langer and Vacanti introduced the idea of constructing tissue engineering matrices from artificial bioabsorbable polymers to regenerating liver tissues.[118,119] Earlier studies have demonstrated hepatocyte survival on synthetic polymeric discs in peripheral tissues,[120,121] improved survival of transplanted hepatocytes with hepatotrophic stimulation using portacaval shunt and partial hepatectomy,[122] partial correction of single enzyme liver defects,[123] and reorganization of hepatocytes and sinusoidal endothelium co-cultured under continuous flow conditions in vitro.[124] One major lingering problem has been the insufficient survival of transplanted hepatocytes, possibly due to mass transport limitations of oxygen/nutrients and metabolic wastes[125]. The mass transport problem has limited the overall scaffold dimensions, particularly for liver regeneration due to high metabolic requirements of the hepatocytes. Mass transport is the major reason that although the regeneration of various tissue types have been reported, the regeneration of thick structures has not been demonstrated in the literature. By offering simultaneous control over macroscopic shape, oriented channels, microporosity, and local composition, 3DP™ offers unique opportunities to fabricate complex scaffolds with intrinsic vascular network for engineering of thick organs.

The feasibility to fabricating thick scaffolds was assessed in a preliminary study.[126] 3DP™ was used to create 90 complex biodegradable scaffolds from polylactide-co-glycolide (53,000 MW 65L:35G). Polymer constructs consisted of multiple vascular-like channels with an internal diameter of 500 μm and wall thickness of 300 μm. Bovine aortic endothelial cells were isolated and seeded into 50 devices. Hepatocytes were isolated from adult Lewis rats using a collagenase digestion, and 40 additional matrices were seeded with a co-suspension of 2.5×10^6 endothelial cells and 2.5×10^7 hepatocytes

(1:10 endothelial:hepatocyte). All cells were cultured using standard techniques. Cell-polymer constructs remained *in vitro* from 18 hours to 5 weeks. Specimens were fixed, stained, labeled, and analyzed histologically. Phase contrast microscopy of cell-polymer constructs revealed cell adhesion to the 3D printed™ matrices and development of a confluent cell layer. Fluorescence microscopy demonstrated that, at four weeks, endothelial cells had intrinsically remodeled the channels of the polymer matrices into endothelial-lined rounded channels resembling a native vascular network. Scanning electron microscopy confirmed endothelial cells had assumed the continuous pavement-like lining of a native vessel. The endothelial cell-hepatocyte co-culture demonstrated remodeling over time with hepatocytes adjacent to the walls of the polymer channels lined by an endothelial cell monolayer. Histotypic reorganization was observed to occur on the scale of 500 μm. This initial *in vitro* work demonstrated that 3DP™ can fabricate thick, complex, pre-vascularized structures with favorable cellular response, and is suitable for fabricating tissue engineering matrices. The results, however, were obtained under static flow conditions.

The next logical step involved the design and fabrication of complex, three dimensional devices which will be seeded and tested under flow conditions in bioreactors. Section 8.2 describes the experiments to ascertain the effect of microporosity and bioreactor flow rate on seeding density of a co-culture of endothelial cells and hepatocytes.

8.2 EFFECTS OF MICROPOROSITY AND FLOW

8.2.1 Materials and methods

Non-microporous and microporous devices were fabricated by 3DP™ with the sequential stencils technique (Section 2.3.6). The devices consisted of 5 channel sections and 4 pillar sections, as shown in the schematic diagram in Figure 8.1. Each channel section consisted of 5 individual channel layers at 200 μm layer thickness each, and each pillar section consisted of 4 individual pillar layers at 150 μm each. Unprinted regions in the pillar layers form the radial channels in the pillar sections. Unprinted regions in the

channel layers line up with the unprinted regions in the pillar layers to form the axial channels.

Non-microporous structures were produced by printing chloroform through the stencils onto a powder bed containing 45-75 μm particles of PLGA (85:15 100,000). Microporous devices with pore size distribution of 45-75 μm were constructed. These devices were produced by printing chloroform into a 45-75 μm powder mixture containing 60% v/v salt and 40% v/v PLGA (85:15 100,000) particles. Printing parameters used are listed in Table 8.1. The as-printed 45-75 μm devices are shown in Figure 8.2. Note the axial and radial channels throughout the devices (Figure 8.3). The actual thickness of each channel section is 900 μm in height, and that for each pillar section is 600 μm. The overall device length is 6.9 mm, with an outer diameter is 7.6 mm.

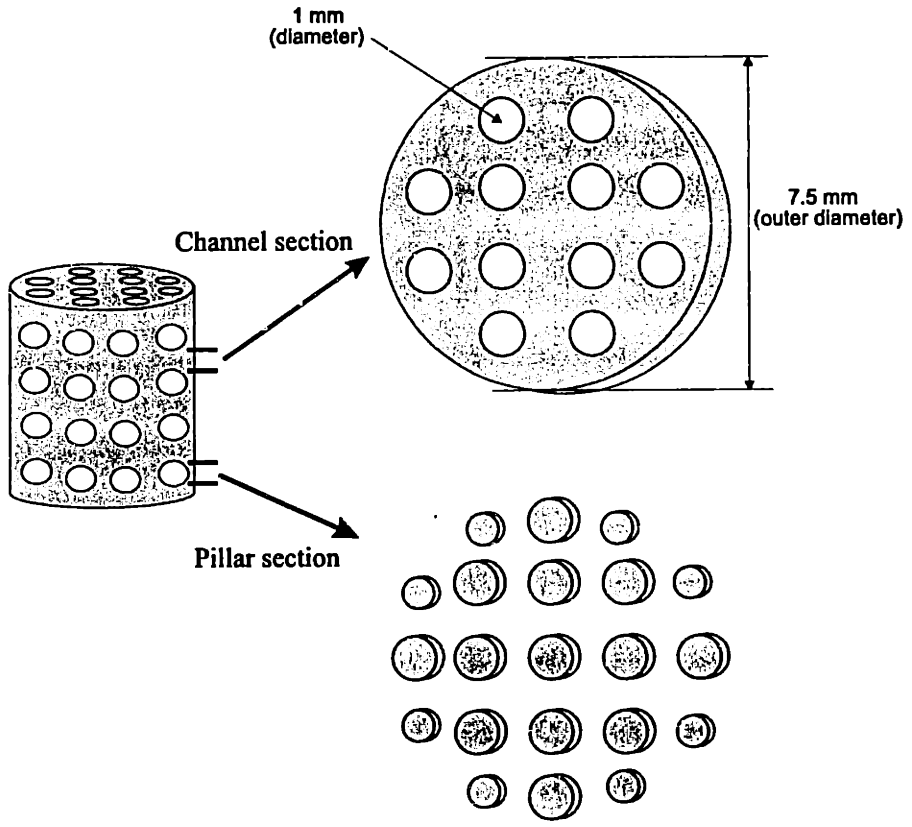

Figure 8.1: Schematic for liver devices

Powder:	PLGA (85:15 100,000) 45-75 μm
Binder:	Chloroform
Flowrate:	1.5 g/min
Printspeed:	100 cm/sec
Layer thickness (channel layers):	200 μm
Layer thickness (pillar layers):	150 μm
Line spacing (all layers):	100 μm

Table 8.1: 3DP™ parameters for printing devices shown in Figure 8.2

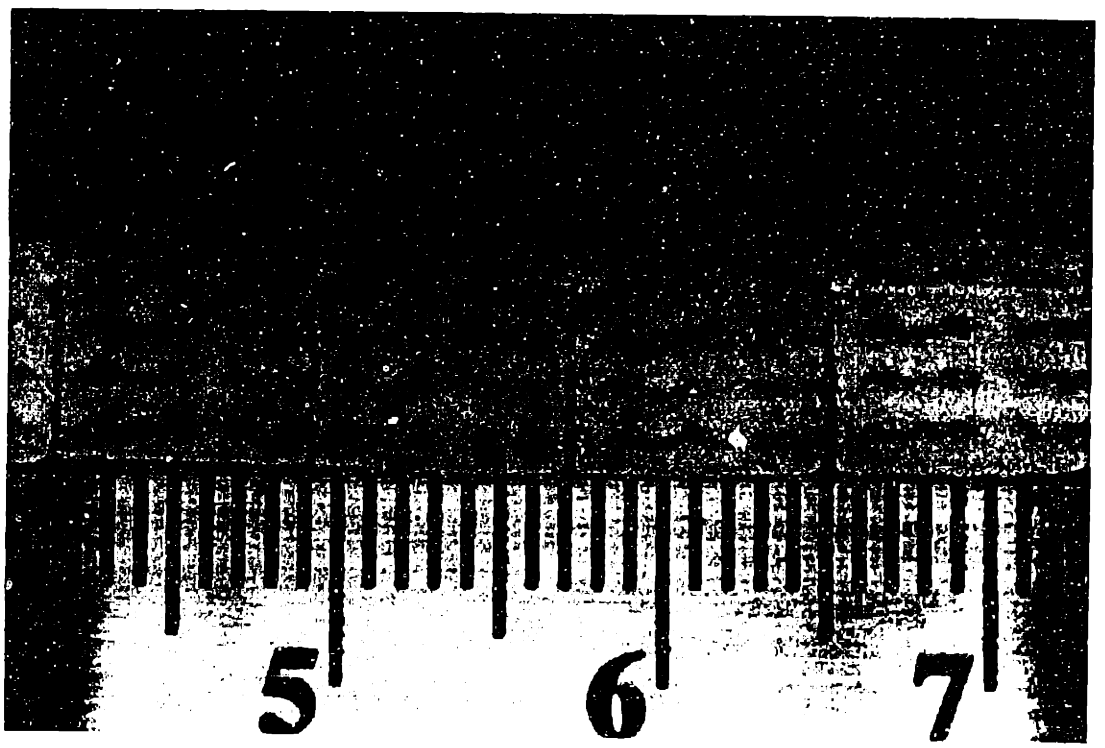

Figure 8.2: 3D Printed 60:40 salt:PLGA devices with 45-75 μm particle size

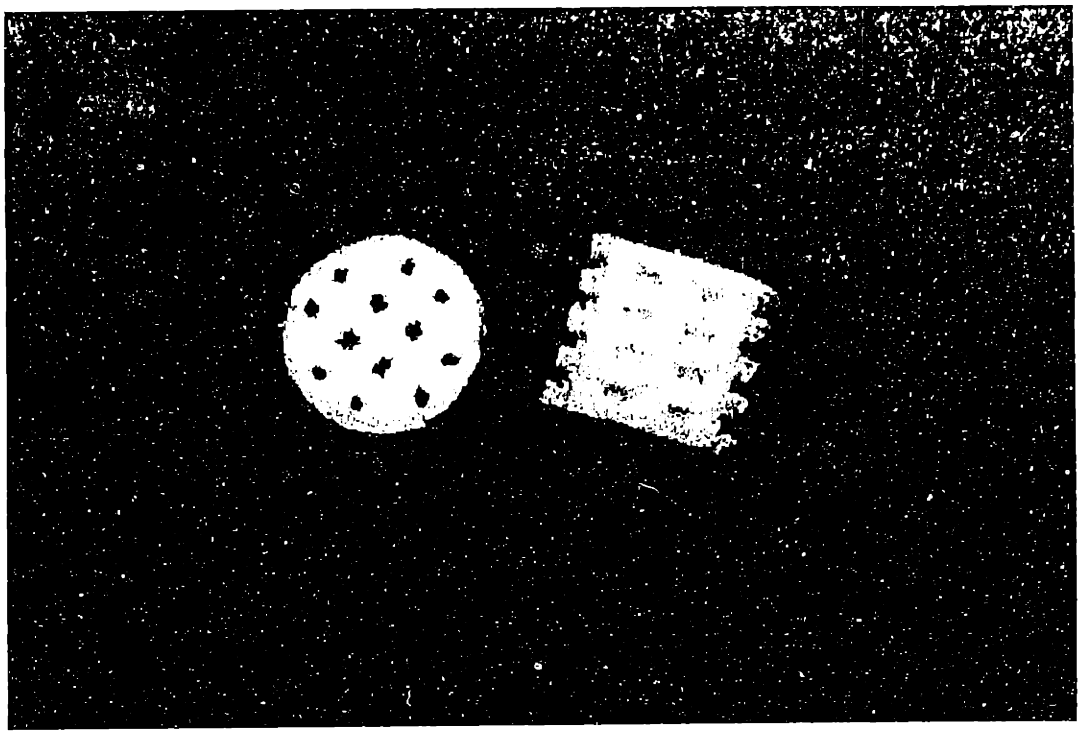

Figure 8.3: Axial and radial channels of 60:40 salt:PLGA devices

Chloroform extraction was achieved by critical point CO_2. Manual powder removal from the un-printed channels was achieved from all devices. Powder removal was significantly easier with the salt-polymer devices. The difference in powder removal may be attributed to the reduced lateral migration of the polymeric liquid primitive during printing, which may be due to the presence of salt. The devices were sterilized with ethylene oxide. The salt particles in the devices were leached out after EO sterilization by immersing the devices in water for 24 hours.

Perfusion bioreactor systems were setup according to Figure 8.4, which also illustrates the ideal cell distribution in the microporous devices under continuous flow bioreactor conditions. Non-microporous PLGA devices (with no salt particulates) were seeded for 48 hours in two bioreactors to qualitatively evaluate the effect of reactor flow rate on hepatocyte adhesion and viability. The first reactor design has a flow rate of approximately 1.2 cc/min, and holds only 1 device along a series loop. The second reactor design has a lower flow rate of approximately 0.7 cc/min, which is achieved by branching the main tubing line into 3 parallel device holders. With the exception of the device holder, the second reactor is essentially a commercially available bioreactor.

Microporous PLGA devices (60:40 v/v salt:polymer) were also seeded for 48 hours in the high flow bioreactor The devices were removed at the end of 48 hours, critical point dried, and sectioned for SEM analysis.

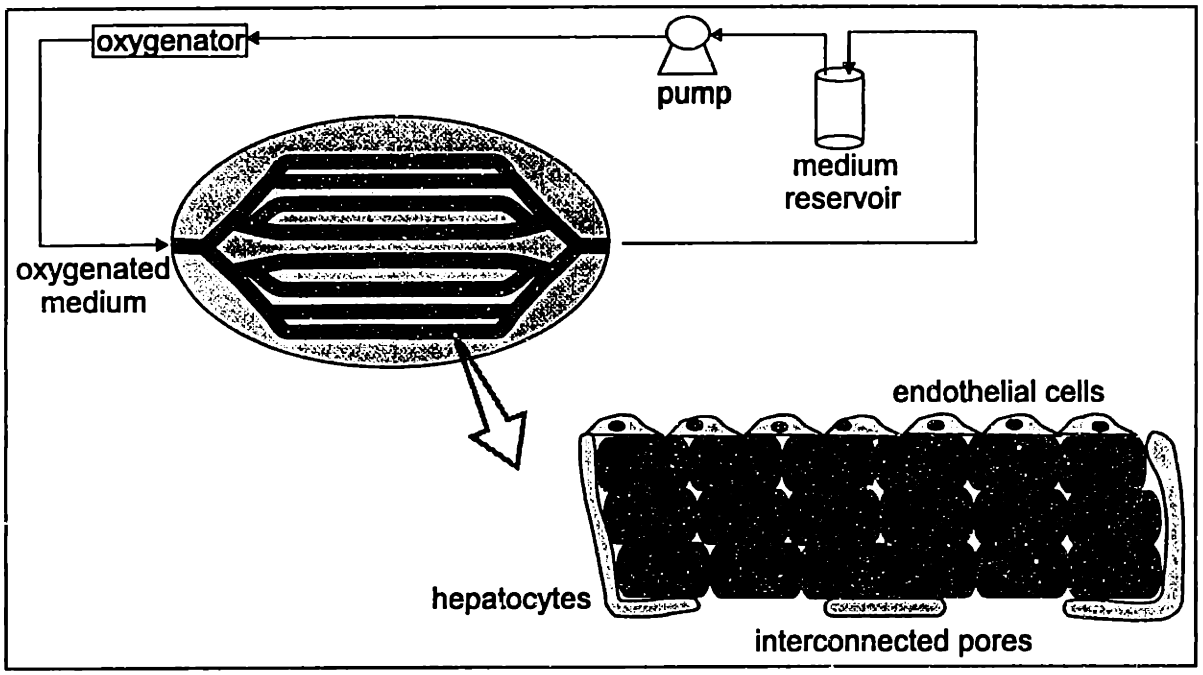

Figure 8.4: Perfusion bioreactor system

8.2.2 Observation

8.2.2.1 Non-microporous, high flow rate (1.2 cc/min)

Significantly less cell coverage and adhesion was observed in non-microporous devices which were exposed with the higher flow rate (1.2 cc/min). Figure 8.5 shows the low magnification of one such device. This section is produced by cutting the device along the section formed by vertical pillars, and orienting the electron beam from the inside of the device. The polymer particles are clearly identifiable in this scale, suggesting that the particles were not very well sintered with the printing conditions used. The cells are too small to be observed at this low magnification.

More cells are expected to be observable at higher magnifications in between the pillars, and few or none at the pillars. This was found to be generally true, except that

very few cells were observable in general. Figure 8.6 is a high magnification view of the device in between the pillars, showing a mixture of endothelial cells, hepatocytes, and extracellular matrix around PLGA particles. The hepatocytes in Figure 8.6 appear to have smooth surfaces, and the endothelial cells appear spread out. The two cell types are in close approximation with each other. Figure 8.7 shows a higher magnification of the endothelial cells and hepatocytes. The hepatocytes shown in this SEM appear to have rough, porous cell walls. The endothelial cells appeared spread out. More hepatocytes with rough, porous cell walls can be seen in Figure 8.8. The porous cell walls may suggest the lack of cell viability. In contrast to the hepatocytes in Figure 8.6, the hepatocytes in these two SEM's appear isolated from each other and from the endothelial cells. Their lack of viability and rough surface morphology may be related to their isolation from other cells.

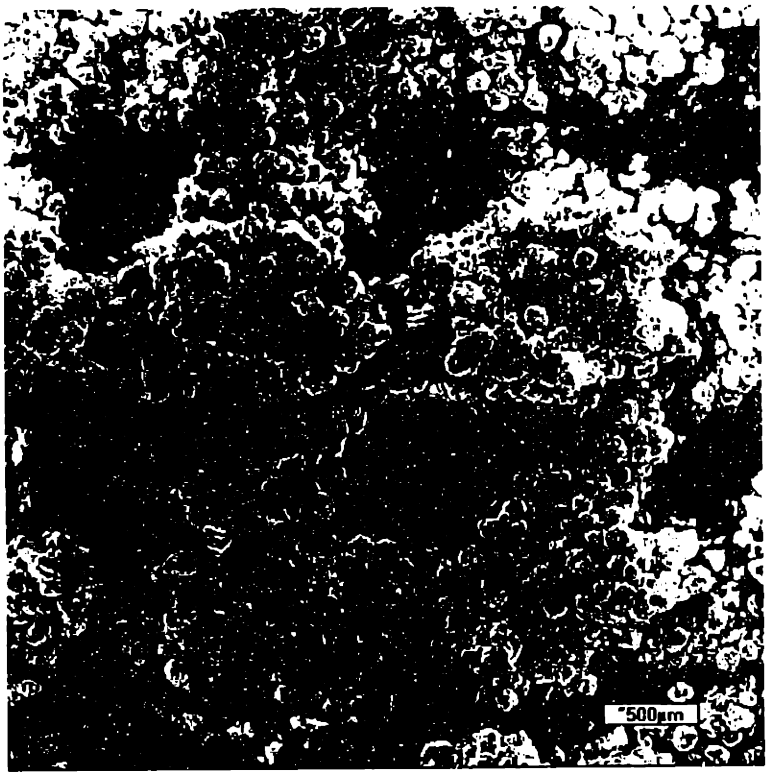

Figure 8.5: Low magnification view of device, showing axial channels and pillars

Figure 8.6: High magnification view of polymer surface between pillars

Figure 8.7: Endothelial cells, matrix, and rough, porous hepatocytes

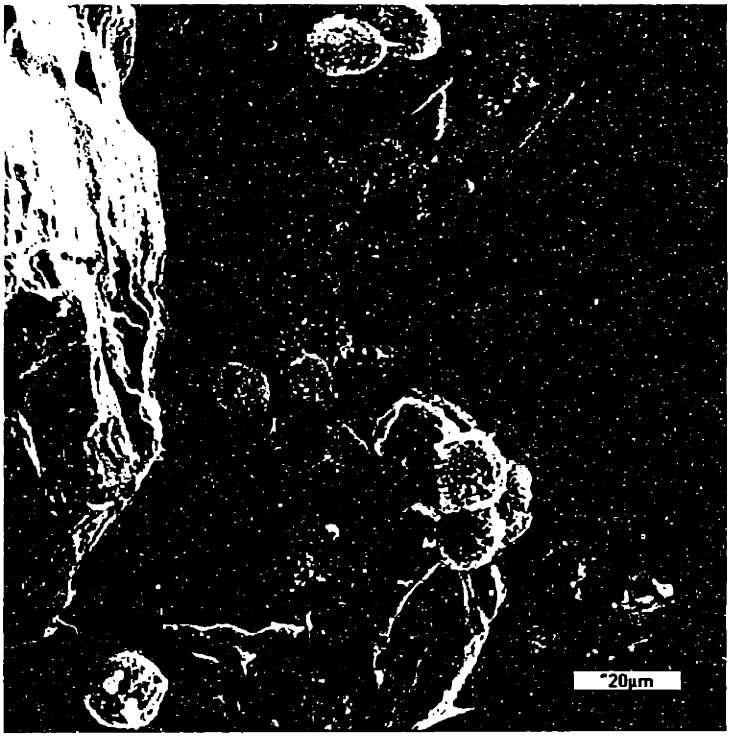

Figure 8.8: Numerous rough, porous hepatocytes on PLGA particles

It must be emphasized that although Figure 8.6-Figure 8.8 show cells in the devices, very few cells are observed in general from this device (high bioreactor flow rate). Most of the observed hepatocytes have porous surface texture which suggest poor cell viability. The cause of cell death may be due to excessively high flow rate in the bioreactor, insufficient seeding time under static conditions, or device contamination. Another possibility is that the device surfaces shown in these figures are perpendicular to the flow directions, resulting in excessive turbulence along those surfaces. It is possible that more cells may be found along the axial channels. Figure 8.9 is a low magnification view of a channel section, showing the channels and the channel walls. No cells can be observed in this low magnification. More cells are expected to be along the channel surfaces, and very few cells are expected in between the channels. Only a few cells could be found in the channels of this device (high bioreactor flow rate), and they are shown in Figure 8.10. The cells and matrix material can be easily identified, and the hepatocytes appear to be organized in small groups.

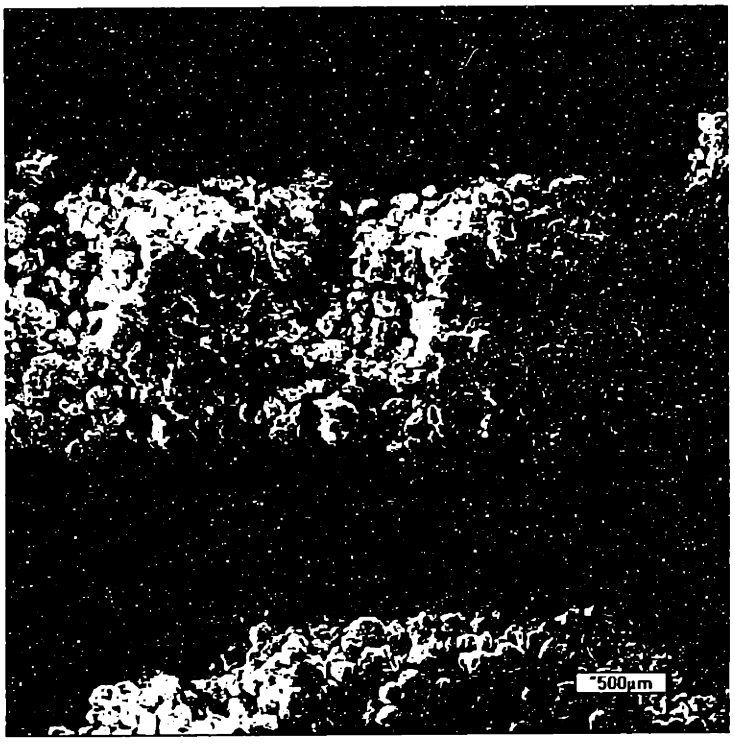

Figure 8.9: View of the channel section, showing channels and channel walls

Figure 8.10: Endothelial cells and hepatocytes along the channel surface

8.2.2.2 Non-microporous, low flow rate (0.7 cc/min)

The effect of bioreactor flow rate can be determined by evaluating identical devices which were placed in a slower flow rate bioreactor. Figure 8.11 is a low magnification view of a channel section, showing the channels and the channel walls. No cells can be observed in this low magnification, but higher magnification may reveal more cells. Figure 8.12 shows a medium magnification view of a channel surface, showing numerous cells adhering to the polymer particles. Figure 8.13 and Figure 8.17 are higher magnification views of the cells, demonstrating histotypic reorganization with hepatocytes adjacent to the polymer surface, and endothelial cells and matrix covering the hepatocytes.

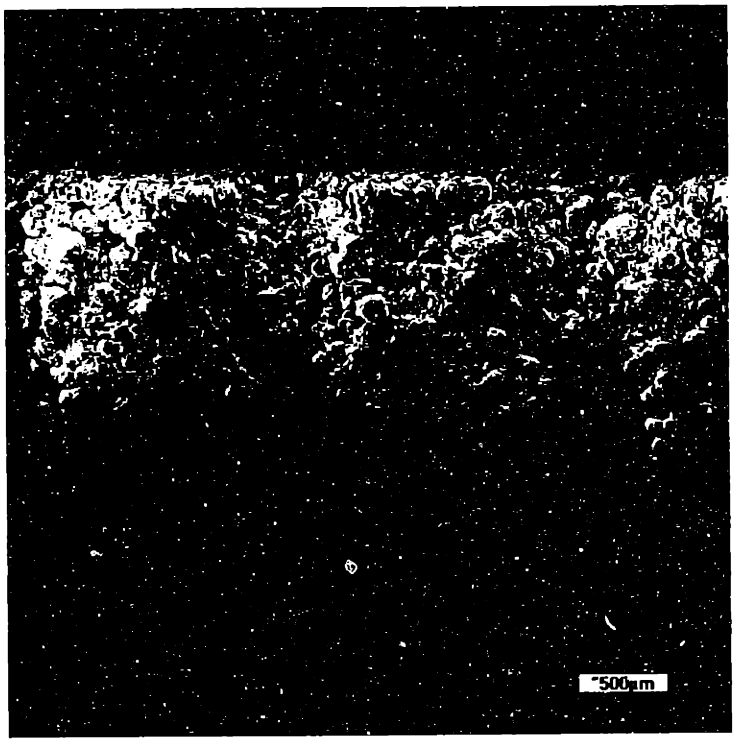

Figure 8.11: Channel section, showing channels and channel walls

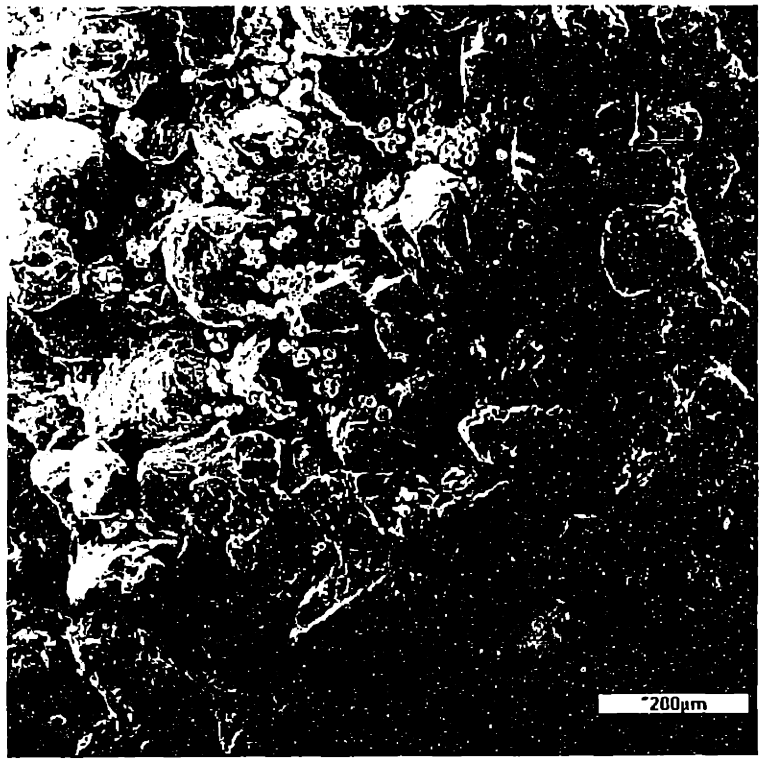

Figure 8.12: Aggregates of hepatocytes along channel surface

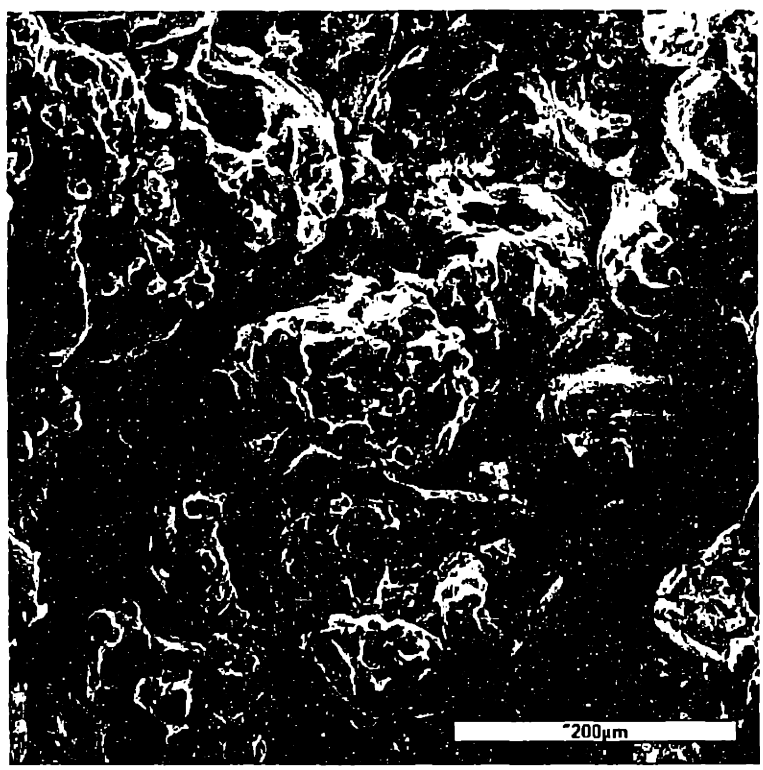

Figure 8.13: Endothelial cells and hepatocytes along the channel surface

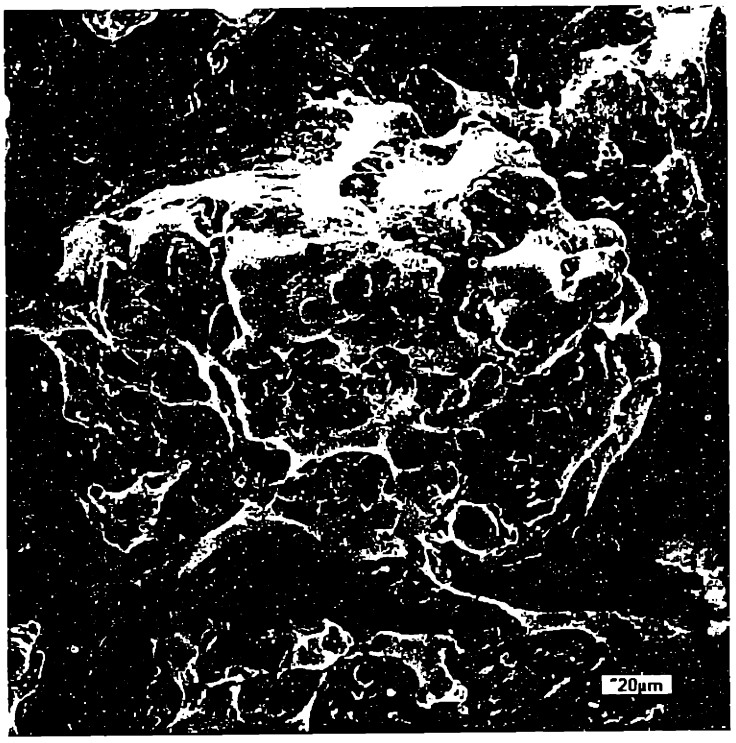

Figure 8.14: Endothelial cells and hepatocytes on the surface of a PLGA particle

One interesting observation is the presence of isolated cells between the PLGA particles which make up the channel walls. Figure 8.15 shows the different cell density found between particles which make up the channel walls, and that found along the channel surface. It can be seen that significantly more cells adhered to the channel surface. Higher magnification (Figure 8.16) of the cells in the channel walls show isolated cells which did not exhibit the same histotypic organization as that seen in Figure 8.12 through Figure 8.14. The presence of cells between polymer particles in the channel walls suggest that although no microporosity was designed for these matrices, some degree of interconnected microporosity does exist. Microporous devices produced by particulate leaching should result in significantly higher cell count.

8.2.2.3 Microporous, high flow rate (1.2 cc/min)

Figure 8.17 shows the electron micrographs (low and high magnification) of the microporous devices prior to particulate leaching. These devices were built with 45-75 µm powder. The axial channels can be clearly seen in the low magnification SEM, and they are on the order of 900-1,000 µm in diameter.

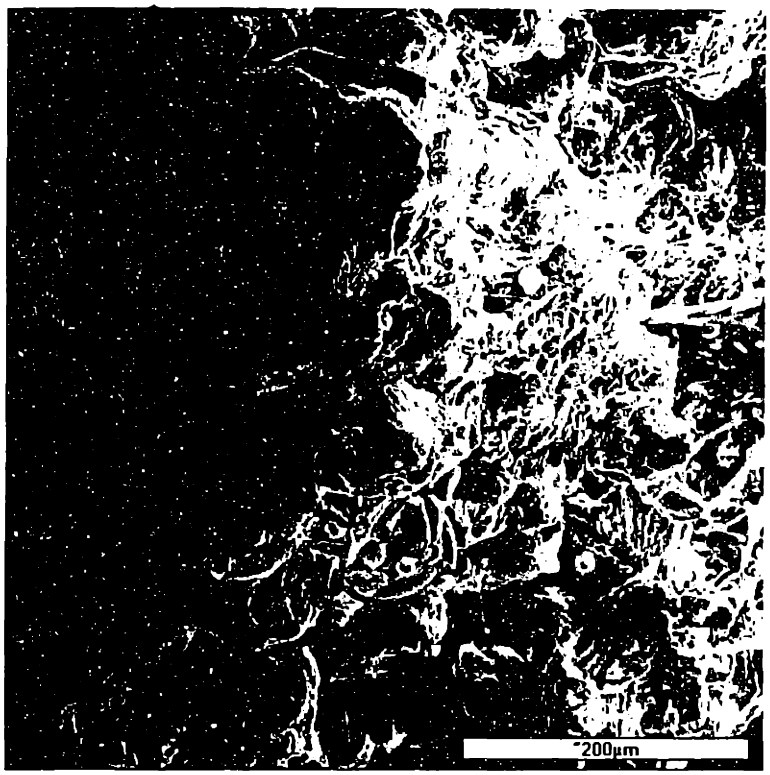

Figure 8.15: Channel wall (left) than the channel surface (right)

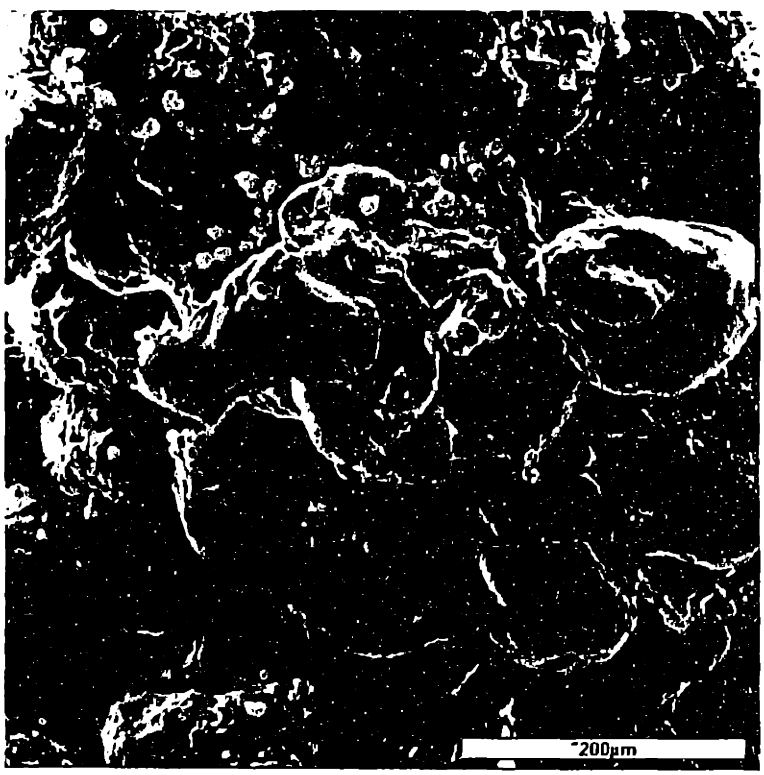

Figure 8.16: Isolated hepatocytes on PLGA particles along a channel wall

The walls between the channels range from 800 to 900 μm. High magnification revealed adhesive binding of the salt particles by dissolving the polymers. Good, complete polymer particle dissolution probably occurred since no polymer particles are noticeable. It appears that a majority of the salt particles are smaller than 45 μm. The salt particles may have been crushed to a smaller size during manual mixing with PLGA particles in the mortar and pestle. Perhaps another mixing technique should be employed to avoid the powder size reduction problem. The resultant microporosity may be too small to be beneficial for aggregates of hepatocytes, which are on the order of 25-40 μm in diameter. Subsequent removal of salt particles resulted in dramatic microstructural changes. Figure 8.18 shows the micrograph of the 45-75 μm devices after 24 hours of particulate leaching. 1° and 2° pores are readily identifiable in these microporous devices. The SEM shown in Figure 8.19 illustrates extensive coverage of cells along the surfaces of the channel layer of the microporous devices. The SEM's shown in Figure 8.20 and Figure 8.21 illustrate cell penetration into the bulk of the microporous devices. The extend of cell penetration into the microporous device is significantly more than that into the non- microporous device.

8.3 DISCUSSION

Devices with all three levels of structural hierarchy were constructed by 3DP™: macroscopic shape, oriented channels, and microporosity. This preliminary work confirms that cell penetration into microporous devices was significantly more than that into non-microporous devices under flow conditions. Technical protocols for *reproducible* biochemical assays are being optimized for quantifying cell function and viability. Various biochemical assays of hepatocyte metabolites are being evaluated to measure cell function. Several histological staining techniques are being evaluated to better determine cell viability. 3DP™ devices with even higher total porosity are being constructed to further increase cell penetration. The upper limit on total porosity will be constrained by mechanical force requirements. Future devices will be seeded into bioreactor for longer residence time (7 days minimum) to assess their true potential.

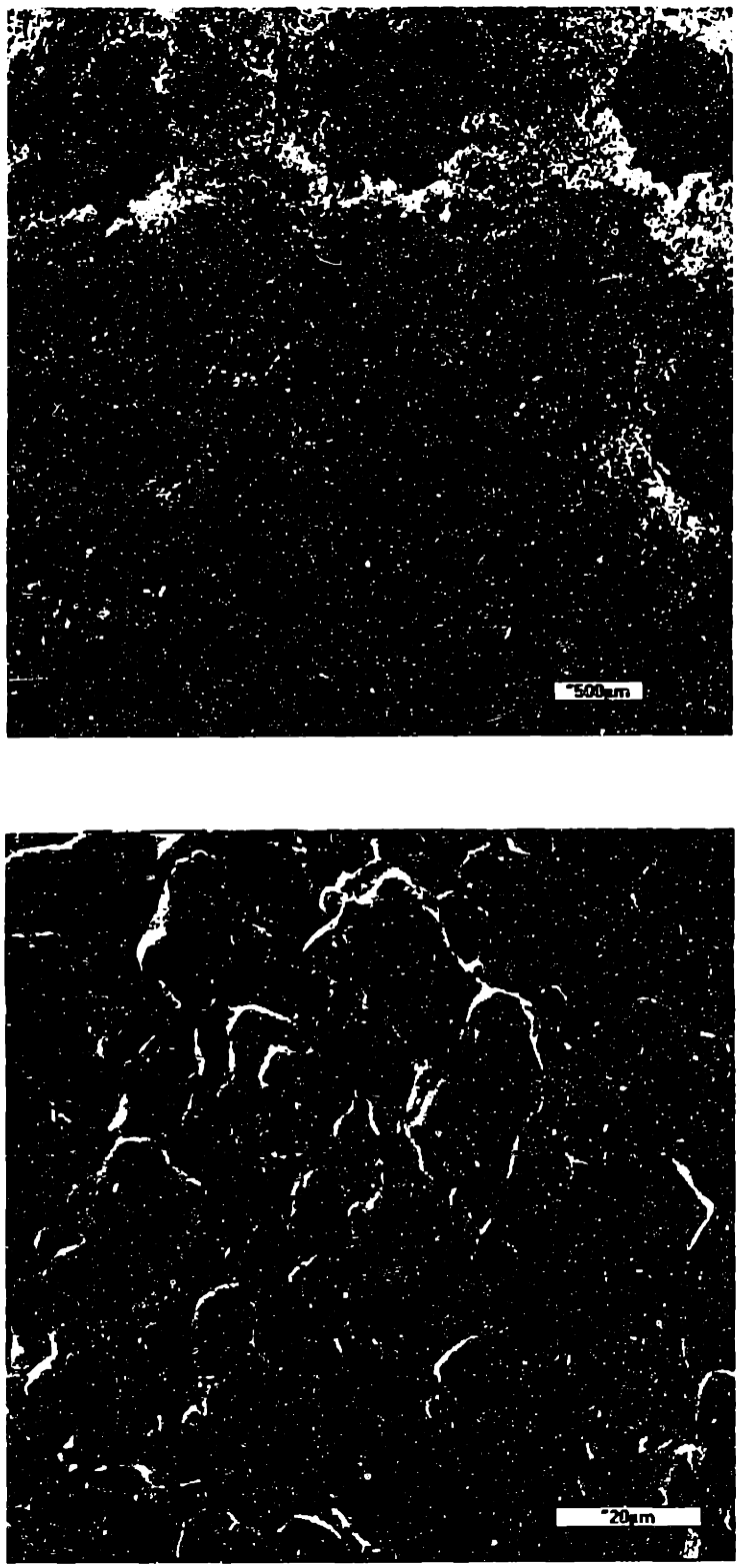

Figure 8.17: Low (top) and high (bottome) magnification of unleached device

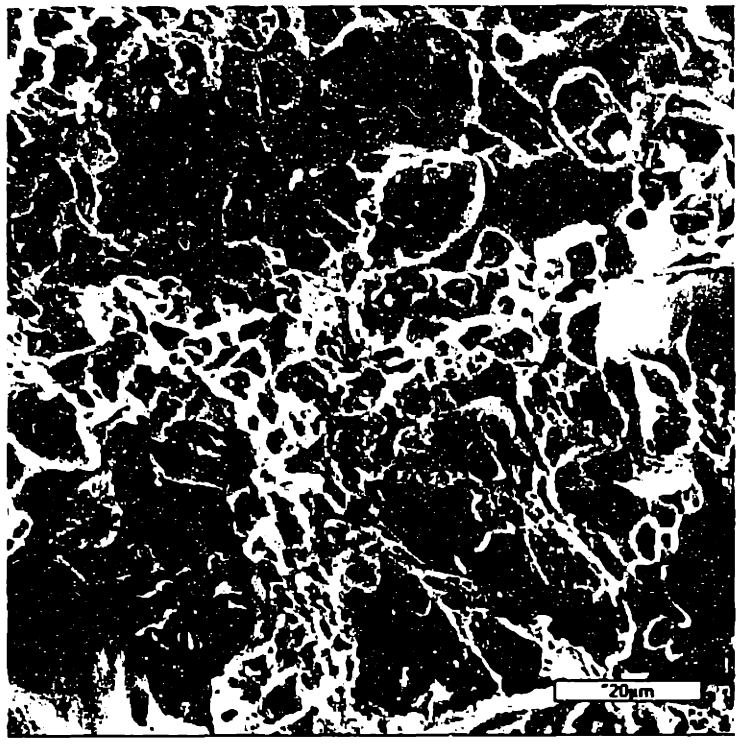

Figure 8.18: Microporous 45-75 µm salt:PLGA device after leaching

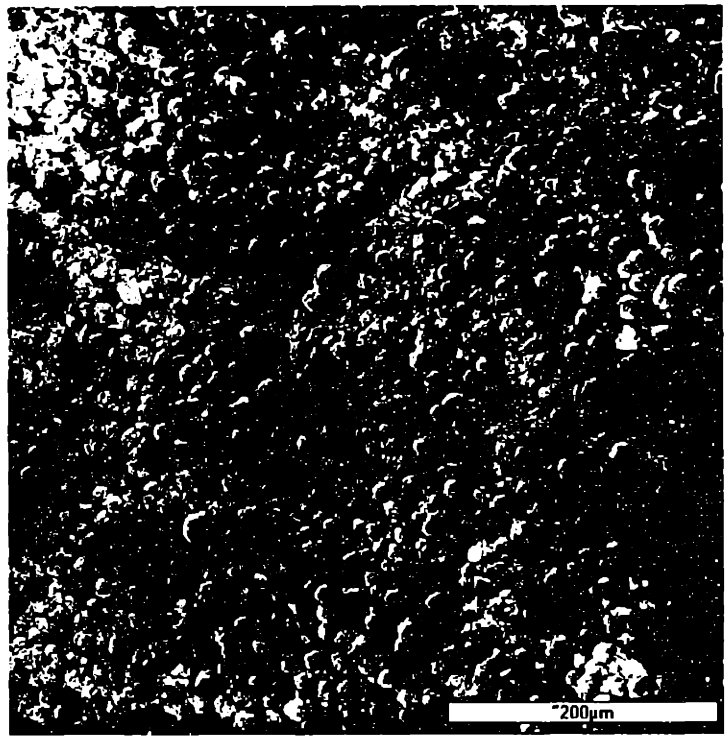

Figure 8.19: Extensive cell coverage on microporous channel layer surfaces

Figure 8.20: Cell penetration into the bulk of the microporous device

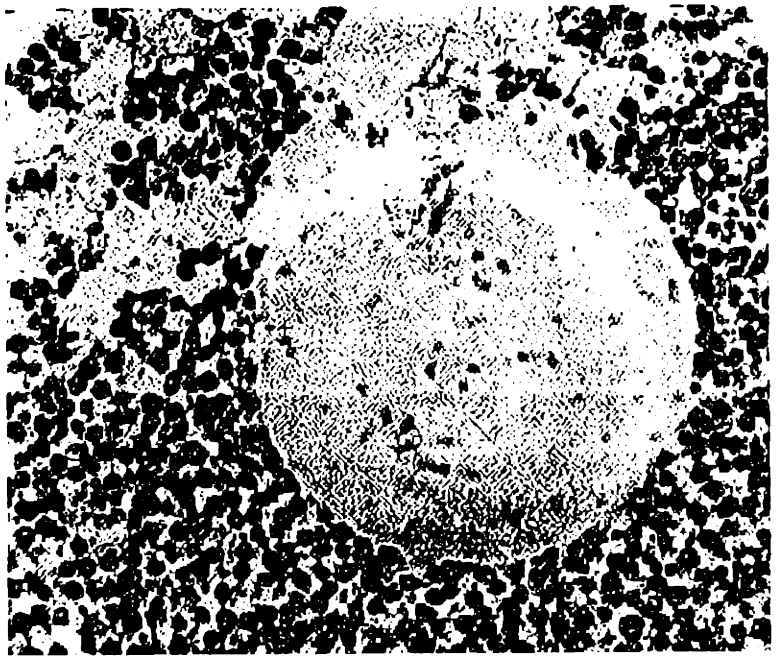

Figure 8.21: Cell penetration into the bulk of the microporous device

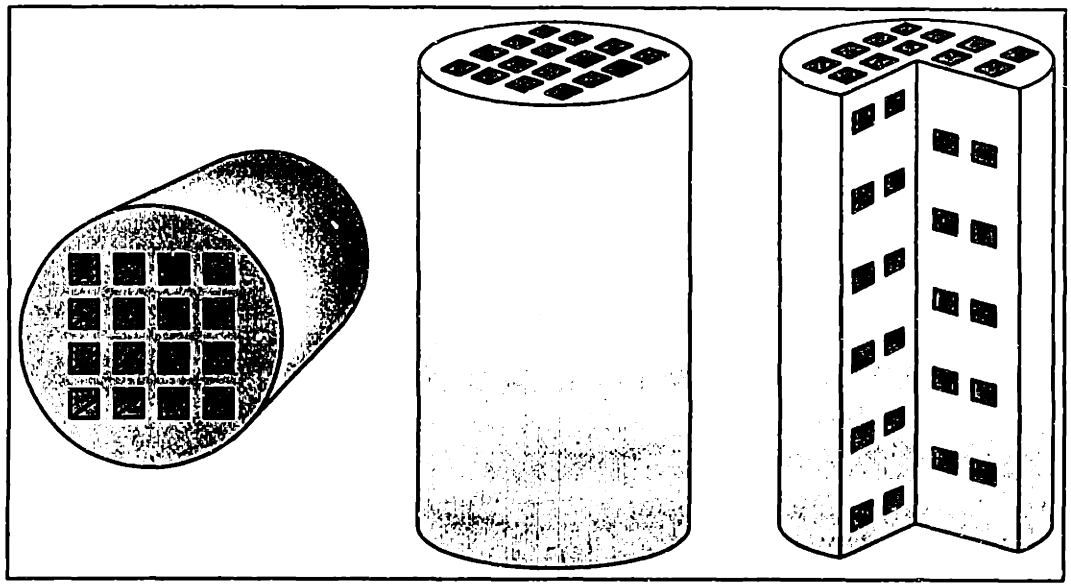

Figure 8.22: 3DP™ devices with open axial channels and closed radial channels

9. Conclusions

The manner by which 3DP forms structures - by selective deposition of multiple matter, affords unprecedented flexibility to manipulate local composition, and offers many new design possibilities for biomedical devices. Dense, defect-free structures are desirable for many drug delivery applications. Tissue engineering matrices, on the other hand, require interconnected channels and microporous structures. The common theme for achieving these different requirements is the need to understand the binding mechanisms during 3D Printing™.

One of the most important attributes of 3DP™ is its flexibility in material selection. Virtually any powder material and low viscosity liquid can be processed by 3DP™. It turns out that all of the materials combinations encountered in this research program can be conveniently categorized according to their powder-liquid binding mechanisms. Four types of binding mechanisms have been observed, and they have meaningful implications on printing strategy and device performance. The degradation mechanism of the printed structure, which plays a crucial role in determining release rate of drug delivery devices, depends on the type of binding mechanism. Bulk erosion due to simultaneous binder dissolution and particle disassociation would result in rapid drug release. Slower, Fickian transport is expected for devices with intact matrices. Intermediate release rate is expected for devices with evolving porosity. Selective dissolution of the binder from printed structures which were formed by the adhesion mechanism results in unbinding and scattering of the particles. An example of this is the water dissolution of aqueous latex binder and subsequent scattering of microcrystalline cellulose particles. Selective dissolution of the particles, on the other hand, from "adhesive" bound structures leaves behind a porous matrix composed only of the binder material. An example of this is the water dissolution of sodium chloride particles and development of an interconnected, porous polylactide structure. Particle scattering is unique to the adhesion mechanism.

The other three binding mechanisms are considered to be cohesive binding mechanisms, as they involve chemical and physical alteration of the powder particles.

Selective dissolution of the binder from cohesively bound structures does not result in scattering of the bound particles. Presence of the binder is not always necessary for particle binding during cohesive binding. The binder used in most cohesive binding are, in fact, pure solvents. Selective dissolution of the particles from cohesively bound structures also leaves behind a porous matrix with higher inter-pore connectivity than can be derived from adhesive bound structures. An example of this is the water dissolution of low molecular weight polyethylene glycol particles and formation of an interconnected porous polylactide structure.

Binding mechanisms also have important implications on printing strategies. It may be theoretically impossible to achieve full density *directly* during printing if the binding mechanism is adhesive in nature. The inter-particle void space must be completely saturated with binder material in order to achieve fully dense structures, since the particles do not contribute to void filling. Repeated printing over the same layer is also mandatory, since the solid content in the binder is limited. Repetitive printing is inefficient because the printhead must raster over the same region multiple times, and adequate time must be allotted for liquid drying between successive repetitions in order to preserve print resolution. Drying time may be reduced by heating, increasing ventilation rate, or choosing binders with higher evaporation rates.

Achieving full density *directly* during printing may be possible with cohesive binding mechanisms. There are two sources of void filling material in cohesive mechanisms - binder and particles. The key contribution here is the re-distribution of physically modified particle materials into the adjacent void spaces. Repetitive printing may still be required to introduce additional volume of materials, depending on the packing density of the powder and solid concentration in the binder. The contribution from dissolved particles should, however, reduce the number of repetitions. Repetitive printing alone is not likely to fill all the voids if the particles do not dissolve, since the solids in the binder are carried with a solvent which occupy finite volume. Dissolution/re-precipitation is expected to contribute the most material to void filling among the three cohesive mechanisms, since the dissolved polymer can flow and redistribute. The contribution to void filling for the swelling and chemical reaction

mechanisms depend on the flowability of the swollen state, and the nature and extent of the chemical reaction, respectively.

Dissolution-re-precipitation is the predominant binding mechanism for bioerodable polymers, and four important stages have been identified in this mechanism: 1) ballistic impact, 2) imbibition and drainage, 3) dissolution/swelling, and 4) reprecipitation. The relative time scale between binder imbibition and particle dissolution are critical in determining feature size. Binder viscosity is expected to increase significantly during binder migration if the time scale for particle dissolution is short relative to binder imbibition and drainage. Binder viscosity can be assumed to be constant during binder imbibition, however, if the opposite is true. Time scale analysis and experimental observations with high speed photography revealed that droplet impact ($\sim 10^{-4}$ sec) and binder migration ($\sim 10^{-2}$ sec) are completed before significant particle dissolution ($\sim 10^{0}$ to 10^{2} sec) occurs. These findings suggest that binder viscosity is not expected to increase appreciably during binder migration. The practical implication is that particle dissolution does not contribute to printed feature size, which can be better controlled by printing more viscous binder into finer particles. The polymeric solutions are intrinsically more viscous in this approach. It should be emphasized that smaller particles do not form finer features because they dissolve faster and increase binder viscosity during binder migration. They improve resolution because the extra particles along the edges contribute less to the overall feature size.

Two mechanisms of particle dissolution were observed. Some particle-solvent systems dissolve by crack propagation and particle fragmentation. PCL (30,000) particles were found to develop cracks with smaller molecular weight solvents such as acetone (58 g/mole) but not with higher molecular weight solvents such as chloroform (119 g/mole). This two-fold difference in molecular weight, and lower solubility of PCL (30,000) in acetone, may contribute to the cracking seen with PCL-acetone and the gelling observed with PCL-chloroform. The predominant mechanism for bioerodable polyesters is dissolution with gel layer formation. 3 distinct regions can be observed during this mechanism of dissolution. A polymer rich zone of the particle becomes progressively small with time, while the swollen gel region expands radially outward. The third region

is the solvent-rich liquid surrounding the particles. Five events are involved with this type of dissolution: 1) solvent ingression into the polymer particle, 2) particle swelling, 3) chain disentanglement (reptation), 4) chain disengagement from the solvent-gel interface, and 5) chain diffusion. Reptation is the process by which individual polymeric chains "free" themselves from the entangled swollen polymer network. Some polymer-solvent combinations required a minimim dissolution time, which was found to scale with polymer molecular weight ($t_{min} \propto Mw^{2.5}$ for PLLA /chloroform). The power dependence has been reported to be 3.2 for polystyrene-cyclohexane, and about 2.9 for PMMA-benzene. These findings support the hypothesis that the minimum dissolution time represents the reptation time, which depends on factors such as molecular weight and molecular structure.

The "minimum" dissolution time is associated with an "optimal" particle size, and particles below this optimal size do not seem to dissolve significantly faster than the "minimum" dissolution time. These findings have important implications for 3DP™. Powder processing for polymeric materials is inefficient at best, particularly for very fine powder. A 75 μm "optimal" particle size for PLGA (85:15 108,000) implies that there is no need to expand great efforts in producing sub-45 micron powder from this polymer, since no improvement in particle dissolution will be achieved. The use of sub-45 micron powder of this polymer may also cause powder spreading problems due to electrostatic charging, resulting in poor powder bed uniformity. The minimum dissolution time defines critical amount of time that adequate amounts of solvents must be available in the powder bed to achieve dissolution. If solvent evaporates before this minimum time, complete dissolution will not be achieved. The minimum dissolution time ranges from 1 to 20 seconds for PLGA and PLLA, depending on molecular weight. Larger particles can require minutes for complete dissolution.

Evaporation time depends both on the volume available for evaporation and the evaporation rate. Evaporation rate was determined for solvents representing a wide range of vapor pressure, and the data shows that evaporation rate of solvents from pure liquid surfaces scaled linearly with vapor pressure. Ventilation results in a 3 to 4 fold increase in evaporation flux by increasing the mass transfer coefficient. These evaporation rates

were combined with simple transport models to show that significant chloroform evaporation occurs in flight between nozzle exit and powder impact. The model predictions are in good agreement with experimental data obtained with high magnification stroboscopic video which was synchronized with droplet formation frequency.

Powder bed evaporation experiments show that complete evaporation from the particulate surfaces can require up to 10^0 to 10^3 sec after impact. The extent of particle dissolution depended on the relative timescale of dissolution and evaporation. Dissolution-evaporation plots were constructed from simple analytical models for predicting microstructure based on materials properties such as dissolution rate and evaporation kinetics, as well as printing parameters such as flow rate, printspeed, and line spacing. Microstructural analysis of polymeric parts produced convincing arguments that dissolution-evaporation controls microstructural formation during 3D Printing™. Additional studies with printing dense structures showed increased sintering defects with larger particles for which the evaporation timescale is shorter than that required for complete particle dissolution. Dense structures were successfully produced by selecting the appropriate printing variables which correspond to the particle size and polymer-solvent combination. Additional studies with printing highly porous structures showed that granular pore wall surfaces were obtained larger particles for which the evaporation timescale is shorter than that required for complete particle dissolution. The observations in both studies (dense and porous structures) are in good agreement with the dissolution-evaporation plots derived from the dissolution and evaporation experiments.

The ability to fabricate dense structures was exploited for constructing drug delivery devices. Simple devices with visible dyes demonstrated unprecedented level of control in release profiles by manipulating spatial composition of printed matter, local composition and microstructure. FDA-approved materials were processed by 3DP™ to fabricate oral dosage forms (ODF) and implantable contraceptive devices with FDA-approved drugs. The data in both studies illustrate that small changes in 3DP™ process variables can have significant effects on release profiles. The major current limitations for drug delivery application are dosage and device dimension. Most human drug

delivery applications impose practical limitations on device dimensions, which translate into limited volume for drug loading. Another constraint on device dimension is print resolution, which depends on factors such as particle size, powder bed packing density, imbibition kinetics, and binder viscosity. Typical feature size of lines and walls range from 300 to 500 μm, and they subtract from the available volume for drug loading and limit the number of compartments within a device. The drug is currently delivered into the devices in liquid form, hence drug solubility plays a major role in determining maximum dosage. Dosages on the order of 10 mg may represent the practical upper limit for moderately soluble drugs in ODF's of typical dimensions. The dosage limit is best addressed by developing alternative drug deposition strategies which do not depend on drug solubility, such as slurry printing and powder delivery.

3DP™ was used fabricate thick, complex scaffolds with controlled macroscopic shape, oriented channels, and microporosity. Successful seeding of such thick, complicated scaffolds have not been previously reported due to mass transport limitations. Initial data show that hepatocytes/endothelial cells can penetrate, survive, and function within these complex structures. The major current process limitation for 3DP™ scaffolds is channel dimension, which depends on print resolution and powder removal. Powder removal from straight, short (1cm length), and wide (>500 μm diameter) channels can be accomplished by shaking or pressurized air. Narrower and longer channels require impractical manual powder removal with delicate instruments. Fine, long channels with tortuous flow paths have not been accomplished by 3DP™. One novel approach may be to deposit a channel template which "reserve" the channel lumen and prevent powder from occupying during powder spreading, and is then selectively etched away after printing, thus revealing the open lumen. This strategy is currently limited by print resolution, but adaptation of new ink-jet technologies which offer reliable printing of ultrafine droplets (<30 μm diameter) may be adequate to provide the proper channel dimensions for many tissue engineering applications.

Appendix A - Diffusion through a stagnant gas film

This appendix addresses the effect of a potential stagnant boundary layer over the evaporating dish used in section 4.3. The dish is 14.6 cm in diameter, and 1.5 cm in height. The reported evaporation rates in Figure 4.4 and Table 4.2 would be underestimates if a significantly thick stagnant layer exists over the liquid surface, although the dish with aspect ratio was selected specifically to minimize the stagnant boundary layer effect. 100 cc solvent in this dish with this diameter should occupy 0.6 cm in height. The thickness of the glass bottom is approximately 0.4 cm, hence the vertical distance between the top rim of the dish and the liquid surface should be approximately 0.5 cm.

The mass transfer rate of liquid *A* at the liquid surface through a stagnant film of gas *B* is given by the equation[127]:

$$N_{Ao} = \frac{cD_{AB}}{\delta \dfrac{x_{B\delta} - x_{Bo}}{\ln\left(x_{B\delta}/x_{Bo}\right)}}\left(x_{Ao} - x_{A\delta}\right) \qquad \text{(A-1)}$$

where c = concentration = P/RT

D_{AB} = diffusivity of vapor A in B (0.075 cm^2 / s for chloroform in air)

δ = distance between top of dish and the liquid level (0.5 cm)

x_{Ao} = mole fraction of A at liquid surface ($x_{Ao} = P_{sat}/P$; P_{sat} = 159 mm Hg)

x_{Bo} = mole fraction of B at liquid surface ($x_{Bo} = 1 - x_{Ao}$)

$x_{A\delta}$ = mole fraction of A at top of dish ($x_{A\delta} = 0$)

$x_{B\delta}$ = mole fraction of B at top of dish ($x_{B\delta} = 1$)

Equation A-1 can be rewritten as:

$$N_{Ao} = \frac{D_{AB}P_{sat}}{RT\delta \dfrac{1 - x_{Bo}}{\ln\left(1/x_{Bo}\right)}} \qquad \text{(A-2)}$$

Substituting the appropriate values into equation A-2:

$$N_{AO} = 1.4\ \mu mol/s*cm^2 \quad (at\ 300°K)$$

This value is slightly less than the measured (1.7 $\mu mol/s*cm^2$) evaporation rate, but the two values are on the same order of magnitude. It should be pointed out that similar evaporation rates were obtained from additional evaporation experiments in which liquid chloroform was filled up to within 1mm from the top of the rim. These findings suggest that the stagnant boundary layer did not significantly affect the evaporation rates reported in Figure 4.4 and Table 4.2.

This analysis does not consider the evaporative cooling effects on evaporation rate. It also ignores free-convection effects, since chloroform gas is expected to be heavier than the ambient gases above.

BIBLIOGRAPHY

1. Burns, M. (1993). Automated Fabrication : *Improving Productivity In Manufacturing*, PTR Prentice Hall, Englewood Cliffs, NJ.

2. Kochan, D. (1993). *Solid Freeform Manufacturing : Advanced Rapid Prototyping*, Elsevier, New York, NY.

3. Yoo, J., (1996). Fabrication and microstructural control of advanced ceramic components by three dimensional printing. *Ph.D. Thesis, Department of Materials Science and Engineering, Massachusetts Institute of Technology, Cambridge, Massachusetts.*

4. Levy, R. A., G.Sashidhar, and R.H. Crawford, (1992). Preliminary experience with selective laser sintigraphic (SLS) models of the human temporal bone. *Proceeding of solid freeform fabrication symposium, University of Texas at Austin, Austin, Texas, August 3-5, 1992.*

5. Clair, J. J., (1996). Stereolithography and the biomedical engineering. *Journal of materials processing technology.* **57**(3-4): 393.

6. Feygin, M., B. Hsieh, (1991). Laminated Object Manufacturing (LOM): A Simpler Process, in *Proceedings of the Solid Freeform Fabrication Symposium* (Austin, TX, August, 1991) The University of Texas at Austin, TX., p. 123.

7. Bill, J. S., J.F. Reuther, W. Dittmann, N. Kubler, J.L. Meier, H. Pistner, G. Wittenberg, (1995). Stereolithography in oral and maxillofacial operation planning. *International journal of oral and maxillofacial surgery* **24**(1-2): 98.

8. Grolman, W., P.F. Schouwenburg, B. Verbeeten Jr, M.F. deBoer, C.A. Meeuwis, (1995). Three-dimensional models of the tracheostoma using stereolithography. *Journal for oto-rhino-laryngology and its borderlands* **57**(6): 338.

9. Schmitt, S. M., D.A. Chance, (1995). Fabrication of titanium implant-retained restorations with nontraditional machining techniques. *Int J Prosthodont* **8**(4): 332-336.

10. Deckard, C., J. Beaman, (1987). Recent Advances in Selective Laser Sintering, in *Proceedings of the Fourteenth Conference on Production Research and Technology, University of Michigan, MI.*; pp. 447-452.

11. Vail, N. K., J.W. Barlow, H.L. Marcus, (1993). SiC preforms for metal infiltration by selective laser sintering of polymer encapsulated powders, in. *Proceedings of the SFF Symposium, University of Texas, Austin, TX.*; p. 204.

12. Levy, R. A., S. Guduri S, R.H. Crawford, (1994). Preliminary experience with selective laser sintering models of the human temporal bone. *Am J Neuroradiology* **15**(3): 476-477.

13. Wales, R., B. Walters, (1991). Fast, Precise, Safe Prototypes with FDM, in. *Proceedings of the SFF Symposium, University of Texas, Austin, TX.* p. 115.

14. Sachs, E. M., M.J. Cima, P. Williams, D. Brancazio, and J. Cornie, (1992). Three-Dimensional Printing: Rapid Tooling and Prototypes Directly from a CAD Model. *J. Eng. Ind.* **114**: 481-488.

15. Sachs, E., M.J. Cima, J. Bredt, A. Curodeau, (1992). CAD-Casting: The Direct Fabrication of Ceramic Shells and Cores by Three Dimensional Printing. *Man. Rev.* **5**(2): 117-126.

16. Cima, M. J., E. Sachs, L.G. Cima, J.Yoo, S. Khanuja, S.W. Borland, B. Wu, and R.A. Giordano, (1994). Computer-Derived Microstructures by 3D Printing: Bio- and Structural Materials. *Proceedings of the SFF Symposium,* University of Texas, TX.; pp. 181-190.

17. Yoo, J., M.J. Cima, E. Sachs, S. Suresh, (1995). Fabrication and Microstructural Control of Advanced Ceramic Components by Three Dimensional Printing, in *Ceramics Engineering and Science Proceedings,* G.N. Pfendt (Editor); pp. 755-762.

18. Wu, B. M., S.W. Borland, R.A. Giordano, L.G. Cima, Emanuel M. Sachs, M.J. Cima, (1996). Solid free-form fabrication of drug delivery devices. *Journal of Controlled Release* **40**: 77-87.

19. Savart, F., (1833). Memoire sur la constitution des veines liquides lancees par des orifices circulaires en mince paroi. *Ann. Chim. Phus.* **53**: 337-45.

20. Rayleigh, F. R. S., (1878). On the stability of jets. *Proc. London Math. Soc.* **10**(4): 4-13.

21. McCarthy, M.J. and N.A. Molloy (1974). Review of stability of liquid jets and the influence of nozzle design. *The Chemical Engineering Journal* **7**(1): 1-20.

22. Goldin, M., J. Yerushalmi, R. Pfeffer, and R. Shinar (1969). Breakup of a laminar capillary jet of a viscoelastic fluid. *J. Fluid Mech.* **38**: 689-711

23. Williams, P.A. (1988). Three dimensional printing: A new process to fabricate prototypes directly from CAD models. *M.S. Thesis, Department of Mechanical*

Engineering, Massachusetts Institute of Technology, Cambridge, Massachusetts. pp 117-118

24. Hendricks, C.D. and J.M. Schneider (1962). Stability of a conducting droplet under the influence of surface tension and electrostatic forces. *Am J. Physics* **31:** 450-453

25. Fillmore, G.L., W.L. Buehner, and D.L. West (1977). Drop charging and deflection in an electrostatic ink jet printer. *IBM J. Research and Development* **21**(1): 37-47

26. Lauder, A. J., (1992). Microstructure and Particle Arrangement in Three Dimensional Printing. *M.S. Thesis, Department of Materials Science and Engineering, Massachusetts Institute of Technology, Cambridge, Massachusetts.*

27. Bredt, J. F., (1996). Binder Stability and Powder/Binder Interaction in Three Dimensional Printing. *Ph.D. Thesis, Department of Mechanical Engineering, Massachusetts Institute of Technology, Cambridge, Massachusetts.*

28. Fan, T. L., (1995). Droplet-powder impact interaction in three dimensional printing. *Ph.D. Thesis, Department of Mechanical Engineering, Massachusetts Institute of Technology, Cambridge, Massachusetts.*

29. Heinzl, J., and C.H. Hertz (1985). Ink-jet printing. In *Advances in Electronics and Electron Physics, vol. 65.* Academic Press, p. 112

30. Giritlioglu, B., (1995). The Effect of Print Style on Mechanical and Microstructural Properties of Structural Ceramic Parts via Three Dimensional Printing. *M.S. Thesis, Department of Materials Science and Engineering, Massachusetts Institute of Technology, Cambridge, Massachusetts.*

31. Caradonna, M.A., (1997). The fabrication of high packing density ceramic powder beds for the three dimensional printing process. *M.S. Thesis, Department of Mechanical Engineering, Massachusetts Institute of Technology, Cambridge, Massachusetts*

32. German, R.M. (1989). Capillarity and liquid interactions with packed particles, in *Particle Packing Characteristics.* Metal Powder Industries Federation, Princeton, NJ; p. 333

33. Chang, L.S., (1988). Spreading of ink droplets on paper: a kinetic model. *Proceedings: the fourth International Congress on Advances in Non-Impact Printing Technologies, March 20-25, 1988, Fairmont Hotel, New Orleans, Louisiana/Society of Photographic Scientists and Engineers; Annette Jaffe, ed.*; p. 320-324.

34. Borland, S. W., (1995). Characterization of fundamental and reticulated biomedical polymer structures fabricated by three dimensional printing. *M.S. Thesis, Department of Chemical Engineering, Massachusetts Institute of Technology, Cambridge, Massachusetts.*

35. Washburn, E. W.,(1921). The dynamics of capillary flow. *Physics Review* **17**: 273.

36. Marmur, A., (1988). Drop penetration into a thin porous medium. *J. Colloid andInterface Sci.* **123**(1): 161-169.

37. Marmur, A., (1988). The radial capillary. *J. Colloid and Interface Science* **124** (1): 301-308.

38. Borhan, A., K.K. Rungta, (1993). An experimental study of the radial penetration of liquids in thin porous substrates. *J. Colloid and Interface Science* **158**: 403-411.

39. Kissa, E., (1981). Capillary sorption in fibrous assemblies. *J. Colloid and Interface Sci.* **83**: 265-272.

40. Gillespie, T., (1958). The spreading of low vapor pressure liquids in paper. *J. Colloid and Interface Sci.* **13**: 32-50.

41 Cooper, W. J., P.D. Drasicky, and F. Rodriguez, (1986). Dissolution rates of poly(methyl methacrylate) films in mixed solvents. *J. Applied Polymer Science* **31**: 65-73.

42 Reinhardt, M., K. Pfeiffer, and H.J. Lorkowski, (1994). Polymer dissolution. I. On the dissolution behavior of copolymers of methyl methacrylate and methacrylic acid. *J. Applied Polymer Science* **51**: 297-301.

43 Huang, S. J., (1995). Polymer Waste Management -- Biodegradation, incineration, and recycling. *Journal of Macromolecular Science. Pure and applied chemistry.* **32**(4): 593.

44 Matsuda, M., S. Asada, K. Webber, J. Lynch, and EB Nauman, (1994). Application of selective dissolution to the recycling of commingled automotive plastics. *SAE Transactions: Journal of Materials & Manufacturing* **103**: 792-807.

45 Papaspyrides, C. D., S. Gouli, and J.G. Poulakis, (1994). Recovery of poly (methyl methacrylate) by the dissolution /reprecipitation process: a model study. *Adv. Polym. Technol.* **13**(3): 213-218.

46 Saito, R., K. Ishizu, T. Fukutomi, (1992). Crosslinking of the inner poly(methyl methacrylate) core of poly(alpha -methylstyrene-b-methyl methacrylate) micelles in a selective solvent: IV. Reaction rate effects. *Polymer (UK)* **33**(8): 1712-1716.

47 Wang, and J.C. Chen, (1996). Chemical modification and crystalline polymer particle filled epoxy resins. *Journal of advanced materials* **27**(4): 25.

48 Langer, R.S., (1990). New methods of drug delivery. *Science* **249**: 1473-1624.

49 Ju, R. T., P.R. Nixon, M.V. Patel, and D.M. Tong, (1995). Drug release from hydrophilic matrices. 2. A mathematical model based on the polymer disentanglement concentration and the diffusion layer. *J. Pharmaceutical Science* **84**(12): 1464-1477.

50 Narasimhan, B., Nicholas A. Peppas, (1997). Molecular analysis of drug delivery systems controlled by dissolution of the polymer carrier. J. Pharmaceutical Sciences **86**(3): 297-304.

51 Langer, R.S., (1995). Biomaterials and biomedical engineering. *Chemical Engineering Science* **50**(24): 4109-4121.

52 Bredt, J.F., (1996). Binder Stability and Powder/Binder Interaction in Three Dimensional Printing. *Ph.D. Thesis, Department of Mechanical Engineering, Massachusetts Institute of Technology, Cambridge, Massachusetts*; p. 176-179

53 Fan, T. L., (1995). Droplet-powder impact interaction in three dimensional printing. *Ph.D. Thesis, Department of Mechanical Engineering, Massachusetts Institute of Technology, Cambridge, Massachusetts;* pp. 66-74.

54 Washburn, E. W. (1921). The dynamics of capillary flow. *Physics Review* **17**: 273-283.

55 Chang, L. S., (1988). Spreading of ink droplets on paper: a kinetic model. *Proceedings: the fourth International Congress on Advances in Non-Impact Printing Technologies, March 20-25, 1988, Fairmont Hotel, New Orleans, Louisiana/Society of Photographic Scientists and Engineers; Annette Jaffe, ed.*; p. 320-324.

56 Ueberreiter, K., and F. Asmussen, (1962). Velocity of dissolution of polymers. *J. Polymer Science* **57**: 187-198.

57 Brochard, F., P.G. de Gennes, (1983). Kinetics of polymer dissolution. *PhysicoChem. Hydrodynamics* **4**: 313-322.

58 Ranade, V. V. and R. A. Mashelkar (1995). Convective diffusion from a dissolving polymeric particle. *AIChE Journal* **41**(3): 666-676.

59 Astarita, G. and S. Joshi, (1978). A class of mathematical model for sorption of swelling solvents in glassy polymers. *Poly. Eng. Sci.* **18**: 388

60 Clift, R., J.R. Grace, and M.E. Weber, (1978). In *Bubbles, Drops and Particles.* Academic Press, New York.

61 Devotta, I., V.D. Ambeskar, A.B. Mandhare, and R.A. Mashelkar, (1994). The life time of a dissolving polymeric particle. *Chemical Engineering Science* **49**(5): 645-54.

62 Hixon A., J. Crowell (1931). *J. Ind. Eng. Chem.* **23**:923

63 Otsuka M., and Y. Matsuda (1996). Comparative evaluation of mean particle size of bulk drug powder in pharmaceutical preparations by Fourier-transformed powder diffuse reflectance infrared spectroscopy and dissolution kinetics. *J. Pharmaceutical Sciences* **85** (1): 112-116

64 DeGennes, P. G., (1976). Dynamics of entangled polymer solution - I. The Rouse model. *Macromolecules* **9**: 587-593.

65 Doi, M., Sam F. Edwards, (1986). *The Theory of Polymer Dynamics*; Oxford University Press.

66 Papanu, J. S., D.S. Soane (Soong), A.T. Bell and D.W. Hess, (1989). Transport models for swelling and dissolution of thin polymer films. *J. Applied Polymer Science* **38**: 859-895.

67 Ouano, A. C., J.A. Carothers, (1980). Dissolution dynamics of some polymers: solvent-polymer boundaries. *Polymer Engineering Science* **20**: 160-166.

68 Manjkow, J., J.S. Papanu, D.W. Hess, D.S. Soane (Soong), and A.T. Bell, (1987). Influence of processing and molecular parameters on the dissolution rate of poly-(methyl methacrylate) thin films. *J. Electrochem. Soc.* **134**(8): 2003-2007.

69. Lide, D.R. (1995), in *Handbook of Organic Solvents*, CRC Press

70. Budavari, S. (1989). *The Merck Index*, 11th edition.

71. Crank, J. (1950) *Proc. Phys. Soc.* **63**: 484

72. Yoo, J., (1993). Structural Ceramic Components by 3D Printing. *Solid Freeform Fabrication Symposium Proceedings, Univ. of Texas, Austin, TX*: pp. 40-50.

73. Khanuja, S. S., (1996). Origin and Control of Anisotropy in three Dimensional Printing of Structural Ceramics. Ph.D. Thesis, Department of Materials Science and Engineering, Massachusetts Institute of Technology, Cambridge, Massachusetts.

74. Nammour, D., (1995). Fabrication of Glass-Ceramic Components via 3DP. *M.S. Thesis, Department of Materials Science and Engineering, Massachusetts Institute of Technology, Cambridge, Massachusetts.*

75. Patel, V. R., M.M. Amiji, (1996). Preparation and characterization of freeze-dried chitosan- poly(ethylene oxide) hydrogels for site-specific antibiotic delivery in the stomach. *Pharm Res.* **13** (4): 588-593.

76. Sato, T., M. Kanke, H.G. Schroeder, P.P. DeLuca, (1988). Porous biodegradable microspheres for controlled drug delivery. I. Assessment of processing conditions and solvent removal techniques. *Pharm Res* **5** (1): 21-30.

77. Lo, H., S. Kadiyala, S.E. Guggino, K.W. Leong, (1996). Poly(L-lactic acid) foams with cell seeding and controlled- release capacity. *J Biomed Mater Res* **30**(4): 475-484.

78. Leenslag, J. W., A.J. Pennings, R.R.M. Bos, F.R. Rozema, and G. Boering, (1987). Resorbable materials of poly(L-lactide). VI. Plates and screws for internal fixation. *Biomaterials* **8**: 70-73.

79. Vainionpaa, S., J. Kilpikari, J. Laiho, P. Helevirta, P. Rokkanen, and P. Tormala, (1987). Strength and strength retention in vitro, of absorbable, self-reinforced polyglycolide (PGA) rods for fracture fixation. *Biomaterials* **8**: 46-48.

80. Giordano, R. A., B.M. Wu, S.W. Borland, L.G. Cima, E.M. Sachs, and M.J. Cima, (1996). Mechanical properties of dense polylactic acid structures fabricated by three dimensional printing. *J. Biomaterial Science, Polymer Edition* **8** (1): 63-75.

81. Griffith-Cima, L. G., (1996). Hierarchical Devices for Tissue Engineering. *211th American Chemical Society National Meeting.* March 24-48, New Orleans, La.

82. Griffith-Cima, L. G., B. M. Wu, M.J. Cima, B. Chaignaud, J.P. Vacanti, (1997). In Vitro Organogenesis of Liver Tissue. Accepted by *Annals of the New York Academy of Science* (in press).

83. Park, A., B.M. Wu, M. J. Cima, L.G. Griffith, (1997). Integration of surface modification and 3D fabrication techniques to prepare patterned poly(L-lactide) scaffolds allowing regionally selective hepatocyte and fibroblast adhesion. Submitted to the *Journal of Biomaterials Science - Polymer Edition* (7 Feb, 1997).

84. Freese, A., B.A. Sabel BA, W.M. Saltzman, M.J. During, and R. Langer, (1989). Controlled release of dopamine from a polymeric brain implant: in vitro characterization. *Exp Neurol* **103**(3): 234-238.

85. Patel, V. R., M.M. Amiji, (1996). Preparation and characterization of freeze-dried chitosan- poly(ethylene oxide) hydrogels for site-specific antibiotic delivery in the stomach. *Pharm Res.* **13**(4): 588-593

86. Sato, M. Kanke, H.G. Schroeder, P.P. DeLuca, (1988). Porous biodegradable microspheres for controlled drug delivery. I. Assessment of processing conditions and solvent removal techniques. *Pharm Res* **5**(1): 21-30.

87. Lo, H., S. Kadiyala, S.E. Guggino, K.W. Leong, (1996). Poly(L-lactic acid) foams with cell seeding and controlled- release capacity. *J Biomed Mater Res* **30**(4): 475-484.

88. Mikos, A. G., A.J. Thorsen, L.A. Czerwonka, Y. Bao, R. Langer, D.N. Winslow, and J.P. Vacanti, (1994). Preparation and characterization of poly(L-lactic acid) foams. *Polymer* **35**: 1068-1077.

89. Wake, M. C., P.K. Gupta, A.G. Mikos, (1996). Fabrication of pliable biodegradable polymer foams to engineer soft tissues. *Cell Transplant* **5**(4): 465-473.

90. Lo, H., S. Kadiyala, S.E. Guggino, K.W. Leong, (1996). Poly(L-lactic acid) foams with cell seeding and controlled- release capacity. *J Biomed Mater Res* **30**(4): 475-484.

91. Mooney, D. J., G. Organ, J.P. Vacanti, R. Langer, (1994). Design and fabrication of biodegradable polymer devices to engineer tubular tissues. *Cell Transplant* **3**(2): 203-210.

92. Beumer, G. J., C.A. van Blitterswijk, M. Ponec, (1994). Degradative behaviour of polymeric matrices in (sub)dermal and muscle tissue of the rat: a quantitative study. *Biomaterials* **15**(7): 551-559.

93. Cima, L. G., J.P. Vacanti, C.A. Vacanti, D. Ingber, D. Mooney, R. Langer, (1991). Tissue engineering by cell transplantation using biodegradable polymer substrates. *J. Biomechanical Engineering* **113**: 143-151.

94. Vacanti, C. A., L. G. Cima, D. Ratkowski, J. Upton, and J.P. Vacanti, (1992). "Tissue engineering of new cartilage in the shape of a human ear using specially configured polymers seeded with chondrocytes", in. *Tissue-Inducing Biomaterials,* L.G. Cima, Ed.; Materials Research Society, Pittsburgh pp. 323-330.

95. Mikos, A. G., G. Sarakinos, S.M. Leite, J.P. Vacanti, and R. Langer, (1993). Laminated three-dimensional biodegradable foams for use in tissue engineering. *Biomaterials* **14**: 323-330.

96. Lin, F. H., Y.Y. Huang, M.H. Hon, S.C. Wu, (1991). Fabrication and biocompatibility of a porous bioglass ceramic in a Na2O-CaO-SiO2-P2O5 system. *J Biomed Eng* **13**(4): 328-334.

97. Liu, D. M., (1996). Fabrication and characterization of porous hydroxyapatite granules. *Biomaterials* **17**(20): 1955-1977.

98. Mooney, D. J., D.F. Baldwin, N.P. Suh NP; J.P. Vacanti, R. Langer, (1996). Novel approach to fabricate porous sponges of poly(D,L- lactic-co-glycolic acid) without the use of organic solvents. *Biomaterials* **17**(14): 1417-22.

99. Gibson, L. J., M.F. Ashby., (1988). In *Cellular solids : structure & properties*, 1st ed.; Oxford [Oxfordshire] ; New York : Pergamon Press.

100. Chien, Y. W., (1985). Polymer-controlled drug delivery systems: science and engineering, in. *Polymeric Materials in Medication* (ed. C.G. Gebelein, C.E. Carraher), Plenum Press, New York, pp. 27-46.

101. Masters, D. B., C.B. Berde, S. Dutta, T. Turek, and R. Langer, (1993). Sustained local anesthetic release from bioerodible polymer matrices: A potential method for prolonged regional anesthesia. *Pharmaceutical Research* **10**: 1527-1532.

102. Leong, K. W., B.C. Brott, R. Langer, (1985). Bioerodible polyanhydride as drug-carrier matrices. I. Characterization, degradation, and release characteristics. *J. Biomedical Materials Research* **19**: 941-955.

103. Hsieh, D. S. T., W.D. Rhine, R. Langer, (1983). Zero-order controlled-release polymer matrices for micro- and macromolecules. *Journal of Pharmaceutical Sciences* **72**: 17.

104. Wu, B. M., S.W. Borland, R.A. Giordano, L.G. Cima, Emanuel M. Sachs, M.J. Cima, (1996). Solid free-form fabrication of drug delivery devices. *Journal of Controlled Release* **40**: 77-87.

105. Balazs, A. C., D.F. Calef, J.M Deutch, R.A. Siegel, and R.Langer, (1985). The role of polymer matrix structure and interparticle interactions in diffusion-limited release, in. *Polymeric Materials in Medication* (ed. C.G. Gebelein, C.E. Carraher), Plenum Press, New York; pp. 87-101.

106. *Merck Index* (1989). 11th edition; p. 3570.

107. Valenzuela, T. D., E.A. Criss, W.M. Hammargren, K.H. Schram, D.W. Spaite, H.W. Meislin, J.B. Clark, (1989). Thermal stability of prehospital medications. *Ann Emerg Med* **18**(2): 173-176.

108. Church, W. H., S.S. Hu, A.J. Henry, (1994). Thermal degradation of injectable epinephrine. *Am J Emerg Med* **12**(3): 306-9.

109. Grant, T. A., R.G. Carroll, W.H. Church, A. Henry,N.H. Prasad, A.A. Abdel-Rahman, E.J. Allison, (1994). Environmental temperature variations cause degradations in epinephrine concentration and biological activity. *Am J Emerg Med* **12**(3): 319-322.

110. Heller, E. F., R.B. Setlow, E. Mylon, (1949). *Am. J. Physiol.* **161**: 268.

111. Fu, C. C., M.J. Sibley, (1977). Quantitative high-pressure liquid chromatographic determination of epinephrine in pharmaceutical formulations. *J. Pharm Sci* **66**(3): 425-426.

112. Peralta, O., S. Diaz, and H. Croxatto, (1995). Subdermal contraceptive implants. *J. Steroid Biochemistry and Molecular Biology* **53**(1-6): 223-226.

113. Sam, A. P., (1992). Controlled release contraceptive devices: a status report. *J. Controlled Release* **22**: 35-46.

114. Lamberg, L., (1996). Time of day medicine dose is taken may boost its efficacy, cut toxicity. *JAMA* **275**(15): 1143-1144.

115. Lane, P. A., D.O. Mayberry, R.W. Young, (1987). Determination of norgestimate and ethinyl estradiol in tablets by high-performance liquid chromatography. *J. Pharmaceutical Sciences* **76**(1): 44-47.

116. Pitt, C. G., T.A. Marks, A. Schindler, (1980). Biodegradable drug delivery systems based on aliphatic polyesters: application to contraceptives and narcotic antagonists; in. *Controlled release of bioactive materials.* R. Baker (Ed). Academic Press, New York, 1980.

117. American Liver Foundation, (1988). *Vital Statistic of the United States* **2**(Part A).

118. Langer, R., J.P. Vacanti, (1993). Tissue engineering. *Science* **260**: 920-926.

119. Vacanti, J. P., M.A. Morse, W.M. Saltzman, A.J. Domb, A. Perea-Atayde, R. Langer, (1988). Selective cell transplantation using bioabsorbable artificial polymers as matrices. *J. Pediatric Surgery* **23**: 3-9.

120. Mooney, D. J., P.M. Kaufmann, K.M. McNamara, J.P. Vacanti, R. Langer, (1994). Transplantation of hepatocytes using porous, biodegradable sponges. *Transplantation Proceedings* **26**: 3425-3426.

120. Mooney, D. J., P.M. Kaufmann, K.M. McNamara, J.P. Vacanti, R. Langer, (1994). Transplantation of hepatocytes using porous, biodegradable sponges. *Transplantation Proceedings* **26**: 3425-3426.

121. Mooney, D. J., S. Park, P.M. Kaufmann, K. Sano, K.M. McNamara, J.P. Vacanti, R. Langer, (1995). Biodegradable sponges for hepatocyte transplantation. *J. Biomedical Materials Research* **29**: 959-965.

122. Kaufmann, P. M., K. Sano, S. Uyama, T. Takeda, J.P. Vacanti, (1996). Heterotopic hepatocyte transplantation: Assessing the impact of hepatotypohic stimulation. *Transplantation Proceedings* **26**: 2240-2241.

123. Takeda, T., T.H. Kim, S.K. Lee, R. Langer, J.P. Vacanti, (1995). Hepatocyte transplantation in biodegradable polymer scaffolds using the Dalmatian dog model of hyperuricosuria. *Transplantation Proceedings* **27**: 635-636.

124. Lee, H., R.A. Cusick, J.M. Pollok, H. Utsunomiya, P.X. Ma, R. Langer, J.P. Vacanti, Formation of hepatocyte spheroids on biodegradable polymers under continuous flow conditions; accepted for publication

125. Kim, S. S., H. Utsunomiya, J.A. Koski, B.M. Wu, M.J. Cima, J. Sohn, K. Mukai, L.G. Griffith, J.P. Vacanti, Survival and function of hepatocytes on a novel three dimensional synthetic biodegradable polymer scaffold with an intrinsic vascular network, submitted to *Annals of Surgery.*

126. Chaignaud, B., B.M. Wu, H. Lee, H. Utsunomiya, L.G. Cima, J. Vacanti, (1996). Complex 3-Dimensional Tissues Engineered with a Vascular Network Using a New Technology of Solid Free Form Fabrication. *27th Annual Meeting of the American Pediatric Surgical Association,* May 19-22, San Diego, Ca.

127. Bird R.B., E,S. Warren, E.N. Lightfoot, (1960). Concentration distributions in solids and in laminar flow, in *Transport Phenomena.* Wiley & Sons, New York. pp. 522-526